

UWB Antennas and MIMO Antenna Arrays  
Development for Near-Field Imaging

Yu-Che YANG



# UWB Antennas and MIMO Antenna Arrays Development for Near-Field Imaging

Proefschrift

ter verkrijging van de graad van doctor  
aan de Technische Universiteit Delft,  
op gezag van de Rector Magnificus prof. ir. K. C. A. M. Luyben,  
voorzitter van het College voor Promoties,  
in het openbaar te verdedigen op donderdag 20 oktober 2011 om 12.30 uur

door

Yu-Che YANG

elektrotechnisch ingenieur  
geboren te Taipei, Taiwan

Dit proefschrift is goedgekeurd door de promotor:

Prof. DSc. A. G. Yarovoy

Samenstelling promotiecommissie:

Rector Magnificus	voorzitter
Prof. DSc. A. G. Yarovoy	Technische Universiteit Delft, promotor
Prof. dr. ir. A. Neto	Technische Universiteit Delft
Prof. ir. F. le Chevalier	Technische Universiteit Delft
Prof. dr. ir. A.B. Smolders	Technische Universiteit Eindhoven
Prof. dr. J.-Y. Dauvignac	Université de Nice-Sophia Antipolis
Prof. dr.-ing. habil. R. S. Thomä	Technische Universität Ilmenau

This research was partly supported by FP6 project Radiotect (COOP-CT-2006-032744)

ISBN/EAN 978-94-6186-011-8

UWB Antennas and MIMO Antenna Arrays Development for Near-field Imaging.  
Dissertation at Delft University of Technology.  
Copyright © 2011 by Yu-Che Yang.

*All rights reserved. No parts of this publication may be reproduced or transmitted in any form or by any means, electronic or mechanical, including photocopy, recording, or any information storage and retrieval system, without permission in writing from the author.*

*To my child,  
Rozen*



# **Table of Contents**

<b>1.</b>	<b>Introduction.....</b>	<b>1</b>
1.1	Background of the research.....	1
1.2	State-of-the-art in UWB arrays and research motivation .....	3
1.2.1	State-of-the art in time domain UWB imaging arrays.....	3
1.2.2	State-of-the-art in UWB antenna element development ....	4
1.3	Research objectives.....	5
1.4	Challenges .....	6
1.5	Approaches.....	7
1.6	Novelties and achievements .....	9
1.7	Research framework .....	10
1.8	Thesis outline .....	10
<b>2.</b>	<b>Measurement facilities and techniques.....</b>	<b>17</b>
2.1	Introduction .....	17
2.2	Measurement challenges.....	17
2.3	Antenna gain and radiation patterns measurement setups .....	18
2.3.1	Anechoic chamber measurement setup .....	18
2.3.2	Free space measurement setup .....	20
2.4	S-matrix calibration technique .....	21
2.5	Data post-processing techniques .....	23
2.5.1	Three-antenna gain calculation .....	23
2.5.2	Mix-mode S-parameter measurement .....	24
2.5.3	Time-gating technique .....	25
2.6	Conclusions .....	27
<b>3.</b>	<b>Microwave UWB antenna development and analysis .....</b>	<b>31</b>
3.1	Introduction .....	31
3.2	Novel ASP antenna design .....	32
3.2.1	Description of the antenna geometry.....	32
3.2.2	Antenna design approach.....	32
3.2.3	Choice of substrate material and thickness .....	33
3.2.4	Physical analysis of the antenna behavior.....	33
3.2.5	Interim conclusions.....	36
3.3	Antenna performance analysis .....	38
3.3.1	Reflection coefficient analysis.....	38
3.3.2	Radiation patterns analysis .....	39
3.3.3	Time domain behavior analysis .....	44
3.4	Antenna coupling .....	44
3.4.1	Antenna coupling measurement setup .....	44
3.4.2	Antenna cross-talk analysis .....	45
3.4.3	Antenna scattering coupling .....	48
3.5	Conclusions.....	49

<b>4.</b>	<b>K-band LTCC differentially-fed UWB antenna analysis and development .....</b>	<b>53</b>
4.1	Introduction.....	53
4.2	Antenna concepts.....	53
4.2.1	Initial antenna concepts .....	53
4.2.2	K-band LTCC antenna concepts.....	54
4.3	Antenna investigation and optimization.....	55
4.3.1	Impact of the LTCC material to the antenna radiation .....	56
4.3.2	Influence of the elliptical dipole axis and separation .....	58
4.3.3	Study on the multi-stair case shield .....	59
4.3.4	Realization of the metal shield .....	60
4.3.5	Feeding network design.....	63
4.3.6	Interim conclusion.....	63
4.4	Experimental verifications .....	64
4.4.1	Antenna connectorization .....	64
4.4.2	Reflection coefficient analysis.....	67
4.4.3	Gain and radiation patterns analysis.....	69
4.4.4	Time domain analysis .....	74
4.5	Manufacturing variation analysis .....	75
4.5.1	Process variation .....	75
4.5.2	Variation of the relative permittivity .....	76
4.5.3	Variation of the substrate height .....	77
4.5.4	Interim Conclusion .....	77
4.6	Integrated LTCC antenna .....	77
4.7	Conclusions .....	78
<b>5.</b>	<b>M-band differentially-fed UWB antenna analysis and development .....</b>	<b>81</b>
5.1	Introduction.....	81
5.2	Antenna concept .....	82
5.3	Antenna investigation and optimization.....	83
5.4	Antenna balun and shield design.....	87
5.4.1	Antenna balun design .....	87
5.4.2	Antenna shield design .....	88
5.5	Experimental verification and analysis.....	91
5.5.1	Manufactured antenna .....	91
5.5.2	Antenna reflection coefficient measurement and analysis.....	92
5.5.3	Antenna broadside gain measurement .....	96
5.5.4	Antenna radiation patterns measurement.....	97
5.5.5	Manufacturing variations.....	100
5.6	Integrated antenna design .....	100
5.7	Conclusions .....	101
<b>6.</b>	<b>UWB MIMO Sparse Arrays for Near-Field Imaging.....</b>	<b>103</b>



6.1	<b>Introduction .....</b>	<b>103</b>
6.2	<b>UWB array performance evaluation and presentation .....</b>	<b>103</b>
6.2.1	UWB antenna array pattern calculation .....	103
6.2.2	UWB antenna array PSF representation .....	104
6.3	<b>Existing 2-D imaging array design approaches.....</b>	<b>107</b>
6.4	<b>Investigation of UWB antenna array behavior .....</b>	<b>108</b>
6.4.1	Sidelobe behavior with respect to element spacing.....	108
6.4.2	Impact of antenna mutual coupling.....	109
6.5	<b>MIMO antenna array design.....</b>	<b>113</b>
6.5.1	Linear MIMO array design based on linear uniformly spaced effective array approach.....	113
6.5.2	Linear MIMO array design based on optimization algorithm.....	115
6.5.3	Two-dimensional MIMO antenna array design .....	116
6.6	<b>Application-driven UWB antenna array design .....</b>	<b>117</b>
6.6.1	System specifications .....	118
6.6.2	One-dimensional MIMO array design using the effective array approach .....	118
6.6.3	One-dimensional array design using the optimization algorithm approach.....	120
6.6.4	Two-dimensional UWB antenna array design.....	122
6.7	<b>Experimental verification.....</b>	<b>124</b>
6.7.1	Coupling behavior analysis.....	125
6.7.2	Measured PSF.....	128
6.7.3	Image of distributed targets in free space.....	130
6.8	<b>Conclusions .....</b>	<b>133</b>
7.	<b>Conclusions and recommendations .....</b>	<b>137</b>
7.1	Results and novelties of this research .....	137
7.2	Dissemination and utilization of the results .....	139
7.3	Recommendations .....	140
	<b>Appendix A Introduction to equipment used .....</b>	<b>143</b>
A.1	Programmable network analyzer .....	143
A.2	24-port switch .....	143
A.3	Antenna probes .....	146
A.4	Customized mini-SMP to 2.4mm adaptor .....	147
	<b>Appendix B Introduction to LTCC .....</b>	<b>149</b>
B.1	Introduction to LTCC technology .....	149
B.2	LTCC Process.....	150
B.3	Material properties used in this thesis .....	153
B.4	LTCC manufacturing terminology .....	154
B.5	Design rules.....	155
	<b>Appendix C List of antennas parameters .....</b>	<b>157</b>

C.1	Microwave antenna parameters .....	157
C.2	K-band antenna parameters .....	157
C.3	M-band antenna parameters .....	158
<b>Appendix D Projection slice method and element shadowing effect.....</b>		<b>161</b>
<b>Appendix E Experimental verification of 1-D MIMO array .....</b>		<b>163</b>
<b>List of Acronyms .....</b>		<b>167</b>
<b>Summary.....</b>		<b>169</b>
<b>Samenvatting .....</b>		<b>173</b>
<b>Author's publications.....</b>		<b>177</b>
<b>Acknowledgement .....</b>		<b>179</b>
<b>About the Author .....</b>		<b>181</b>

## List of Figures

Figure 1.1 Research line .....	5
Figure 2.1 Antenna far-field measurement setup with the cylindrical scanning.....	20
Figure 2.2 UWB antenna array PSF measurement setup in anechoic chamber (a) Antenna measurement setup in DUCAT (b) Antenna measurement setup in FHR (c) Array PSF measurement setup in DUCAT .....	20
Figure 2.3 Example free space measurement setup.....	21
Figure 2.4 Error box model of PNA S-matrix measurement.....	22
Figure 2.5 Manufactured TRL calibration standards (a) TRL calibration standards of the connector-MS line and balun (b) TRL calibration standards of the connector-MS line...	23
Figure 2.6 Time domain reflection coefficient (a) Time domain coefficient of thru (b) Time domain reflection coefficient of AUT and time-gate.....	23
Figure 2.7 Three-antenna gain measurement setup .....	24
Figure 2.8 S-parameters of a differentially-fed antenna .....	25
Figure 2.9 Synthesized differential mode and common mode reflection coefficient.....	25
Figure 2.10 Typical measured raw signal and its spectrum before and after time gating (a) Typical measured raw signal and time gate (b) Spectrum of the measured signal before and after time gating .....	27
Figure 3.1 Proposed antenna geometry (a) Antenna layered view (b) Antenna top view ....	32
Figure 3.2 Impedance loci of different aperture length $A_L$ (a) $A_L = 6$ mm (b) $A_L = 7$ mm (c) $A_L = 8$ mm.....	34
Figure 3.3 Impedance loci of different aperture width $A_W$ (a) $A_W = 0.5$ mm (b) $A_W = 0.6$ mm (c) $A_W = 0.7$ mm .....	35
Figure 3.4 Impedance loci of antenna with different upper patch length $L_2$ (a) $L_2 = 3.6$ mm (b) $L_2 = 4.6$ mm (c) $L_2 = 5.6$ mm .....	36
Figure 3.5 Impedance loci of the antenna with different lower patch length $L_1$ (a) $L_1 = 3.5$ mm (b) $L_1 = 4.5$ mm (c) $L_1 = 5.5$ mm.....	36
Figure 3.6 Impedance loci of different feeding stub length (a) $L_S = 2.2$ mm (b) $L_S = 2.5$ mm (c) $L_S = 2.8$ mm .....	37
Figure 3.7 Impedance loci of different fork separation distance (a) $F_S = 3$ mm (b) $F_S = 4$ mm (c) $F_S = 5$ mm.....	37
Figure 3.8 Fabricated ASP antenna.....	38
Figure 3.9 Predicted and measured reflection coefficient of the antenna .....	39
Figure 3.10 Antenna radiation pattern measurement (a) E-plane (b) H-plane .....	40
Figure 3.11 Measured and predicted antenna gain (a) broadside gain (b) backside gain (c) co-polar and cross-polar gain.....	41
Figure 3.12 Predicted and measured normalized radiation pattern. Blue lines denote the E-plane radiation patterns, and red lines denote the H-plane radiation patterns. The solid lines are measured radiation patterns, “-*-“ lines are CST predicted patterns, and “-o-“ lines are FEKO predicted patterns. (a) 10 GHz (b) 12 GHz (c) 15 GHz (d) 18 GHz ....	42
Figure 3.13 (a) Normalized radiation patterns at the E-plane (b) Normalized radiation patterns at the H-plane .....	43
Figure 3.14 Radiated pulses at different angles in the E- and H- plane and the fidelity function as a function of angle (a) E-plane (b) H-plane (c) Fidelity function value .....	43
Figure 3.15 Normalized radiated pulse of the antenna .....	44
Figure 3.16 Measured group delay of the antenna .....	44
Figure 3.17 Measurement setup for antenna aligned along their H-plane or E-plane (a) antenna aligned along the H-plane (b) antenna aligned along the E-plane .....	46

Figure 3.18 Measurement setup of the antenna cross talk and scattering coupling (a) Antenna cross-talk measurement setup (b) Scattering coupling measurement setup....	46
Figure 3.19 Measured antenna cross talk level (a) Antennas are aligned along the H-plane (b) Antennas are aligned along the E-plane .....	47
Figure 3.20 Measured and simulated antenna coupling when antennas were aligned along their H-plane and E-plane (a) Antennas were aligned along their H-plane (b) Antennas were aligned along their E-plane .....	47
Figure 3.21 Envelop of time domain cross talk.....	48
Figure 3.22 Scattering coupling when the antennas are aligned along the E-and the H-plane (a) Antennas are aligned along the H-plane (b) Antennas are aligned along the E-plane .....	49
Figure 3.23 Time domain received signal with vicinity of another antenna (a) Antennas are aligned along their H plane, antenna separation = 2 cm (b) Antennas are aligned along their E plane, antenna separation = 6 cm.....	49
Figure 4.1 Shielded butterfly-dipole antenna (a) Side view of the shielded antenna (b) Top view of the shielded antenna (Courtesy of [9]) .....	54
Figure 4.2 The K-band antenna concept structure (a) Antenna shield concept. (b) Antenna feeding concept.....	55
Figure 4.3 Normalized E-field distribution of the antenna on different substrates. Frequency 25 GHz. Absolute value. (a) Antenna in the free space (b) Antenna on Roger the RT/5880 substrate (c) Antenna on the LTCC substrate .....	57
Figure 4.4 Reflection coefficient of the antenna on different substrates.....	57
Figure 4.5 Reflection coefficient of the antenna on LTCC substrate with different thickness.....	57
Figure 4.6 Reflection coefficient of the antenna on LTCC substrate with different size.....	57
Figure 4.7 Normalized E-field distribution of the LTCC antenna with thin substrate and small substrate (a) Normalized E-field distribution of the LTCC antenna with thin substrate (b) Normalized E-field distribution of the LTCC antenna with small substrate. Frequency 25GHz, absolute value of the total electric field. ....	58
Figure 4.8 Layout of the elliptical dipole .....	58
Figure 4.9 Antenna reflection coefficient of different dipole dimensions (a) Reflection coefficient of different X axis length (b) Reflection coefficient of different Y axis length .....	59
Figure 4.10 Impedance loci of different antenna flare separation.....	59
Figure 4.11 Multi-staircase shield profile.....	61
Figure 4.12 Reflection coefficient of antennas with different shield profiles .....	61
Figure 4.13 3D Radiation pattern of the antenna with and without shield at 25GHz (a) Antenna without shield (b) Antenna with shield.....	61
Figure 4.14 Interleaved via fence .....	62
Figure 4.15 Reflection coefficient comparison of the antenna with solid metal shield and realistic metal shield .....	62
Figure 4.16 Antenna gain of the gridded shield and solid shield .....	62
Figure 4.17 Radiation patterns comparison of the antenna with solid metal shield and realistic metal shield in the E- and the H-plane, frequency = 26 GHz (a) E-plane (b) H-plane .....	62
Figure 4.18 Reflection coefficient of the antenna with and without feeding structure .....	63
Figure 4.19 Antenna schematic.....	64
Figure 4.20 CPS-CPSWG-MS line transition .....	65
Figure 4.21 Reflection coefficient and insertion loss of the CPS-CPSWG-MS line transition .....	65
Figure 4.22 Layout of the balun.....	66
Figure 4.23 Balun performance (a) Reflection coefficient and insertion loss (b) Phase difference .....	66

Figure 4.24 Simulated reflection coefficients of the antennas with different feeding .....	67
Figure 4.25 Realized antenna (a) Antenna with balun-fed (b) Antenna with differential-fed	67
Figure 4.26 Measured antenna reflection coefficient (a) Antenna fed differentially (b) Antenna fed by balun .....	69
Figure 4.27 Reflection coefficient comparison of the differentially-fed and balun-fed antenna .....	69
Figure 4.28 Differential mode and common mode reflection coefficient.....	69
Figure 4.29 Antenna broadside and backside gain (a) Comparison of broadside gain (b) Comparison of backside gain (c) Comparison of co- and cross-polar gain .....	71
Figure 4.30 Balun-fed Antenna radiation patterns at the E-and the H-plane (a) 25 GHz, E-plane (b) 25 GHz, H-plane (c) 28 GHz, E-plane, (d) 28 GHz, H-plane.....	72
Figure 4.31 Differentially-fed antenna radiation patterns at the E- and the H-plane (a) 25 GHz, E-plane (b) 25 GHz, H-plane (c) 28 GHz, E-plane (d) 28 GHz, H-plane .....	73
Figure 4.32 Comparison of the antenna radiation patterns with different feeding .....	74
Figure 4.33 Antenna TX-RX impulse response.....	75
Figure 4.34 Antenna TX-RX group delay .....	75
Figure 4.35 Reflection coefficient of manufactured antennas (a) Differentially-fed antennas (b) Balun-fed antennas .....	76
Figure 4.36 Antenna reflection coefficients with respect to different relative permittivity.....	76
Figure 4.37 Antenna reflection coefficients with respect to different substrate thickness.....	77
Figure 4.38 Layout of the integrated antenna .....	78
Figure 5.1 The conceptual M-band differentially-fed LTCC antenna (a) Side view (b) Feeding aperture (c) Top view (d) Antenna with simple shield .....	83
Figure 5.2 Impedance locus of the initial values .....	85
Figure 5.3 Impedance locus of $TL=TW=PL=PW=0.65\text{mm}$ .....	85
Figure 5.4 Impedance loci of different $L_1$ .....	86
Figure 5.5 Impedance loci of different $L$ .....	86
Figure 5.6 Impedance loci of different $W_1$ .....	86
Figure 5.7 Impedance loci of different $W_2$ .....	86
Figure 5.8 Impedance of different $TW$ .....	86
Figure 5.9 Impedance loci of different $PW$ .....	86
Figure 5.10 Simulated antenna reflection coefficient and gain (a) Simulated reflection coefficient (b) Simulated gain.....	87
Figure 5.11 Balun layout .....	88
Figure 5.12 Reflection coefficient and the insertion loss of the balun .....	88
Figure 5.13 Antenna with and without shield .....	90
Figure 5.14 Simulated E-field at the antenna surface at 60 GHz (a) Antenna without shield (b) Antenna with shield.....	90
Figure 5.15 Simulated reflection coefficient of the antenna with and without shield with different size (a) Simulated reflection coefficient of the unshielded antenna with different size (b) Simulated reflection coefficient of the shielded antenna with different size .....	91
Figure 5.16 Simulated broadside antenna gain of the antenna with and without shield.....	91
Figure 5.17 Manufactured unshielded and shielded antenna (a) Manufactured unshielded antenna (b) Manufactured shielded antenna.....	92
Figure 5.18 Measured antenna reflection coefficient using the SOLT calibration standards	93
Figure 5.19 Reflection coefficient of the TRL thru standard port 1 .....	93
Figure 5.20 Time domain response of the TRL thru standard.....	94
Figure 5.21 Reflection coefficient of the antenna with and without shield calibrated by TRL calibration (a) antenna without shield (b) antenna with shield.....	94
Figure 5.22 time domain reflected signal of the unshielded and shielded antenna measured using SOLT calibration (a) Unshielded antenna (b) Shielded antenna .....	95

Figure 5.23 Comparison of gated antenna reflection coefficient and the predicted antenna reflection coefficient (a) Unshielded antenna (b) Shielded antenna .....	95
Figure 5.24 Antennas time domain reflection coefficient after calibration (a) Unshielded antenna measured using the TRL calibration (b) Shielded antenna measured using the TRL calibration (c) Unshielded antenna measured using the SOLT calibration and time gating (d) Shielded antenna measured using the SOLT calibration and time gating .....	96
Figure 5.25 Measured and predicted gain of the antenna with and without the shield (a) Unshielded antenna measured with the SOLT calibration (b) Shielded antenna measured with SOLT calibration (c) Unshielded antenna measured with the TRL calibration (d) Shielded antenna measured with the TRL calibration .....	98
Figure 5.26 Predicted co- and cross-polar gain.....	99
Figure 5.27 Measured and nominal standard-gain-horn gain.....	99
Figure 5.28 Radiation patterns of the shielded antenna at the E-plane and the H-plane (a) E-plane (b) H-plane .....	99
Figure 5.29 Radiation patterns of the unshielded antenna at the E-plane and the H-plane (a) E-plane (b) H-plane .....	100
Figure 5.30 Reflection coefficients of different unshielded and shielded antennas measured using the TRL calibration (a) Reflection coefficients of different unshielded antennas (b) Reflection coefficients of different shielded antennas .....	100
Figure 5.31 Manufactured integrated M-band antenna with MMICs.....	101
Figure 6.1 Example of a 1-D UWB antenna array PSF calculated by the modified Kirchhoff migration .....	105
Figure 6.2 Different PSF representation of a 1-D array (a) Range used to calculate the averaged PSF (b) Averaged PSF of a 1-D array (c) Maximum projected PSF of a 1-D array .....	106
Figure 6.3 An example of a 3-D PSF of a 2-D array.....	106
Figure 6.4 2-D projections of the 3-D PSF onto different planes (a) Projection onto the XZ plane (b) Projection onto the YZ plane (c) Projection onto the XY plane .....	107
Figure 6.5 PSF of one-dimensional equally spaced antenna array with different element spacing, fractional bandwidth = 57%.....	109
Figure 6.6 Antenna array model considered for mutual coupling analysis .....	111
Figure 6.7 Sensitivity function of each loop .....	111
Figure 6.8 Distribution of total electrical field around a single loop at 3.6 GHz.....	111
Figure 6.9 Frequency domain footprint of the array with and without element interaction (a) With element interaction (b) Without element interaction .....	112
Figure 6.10 Time domain footprint of the array with and without element interaction (a) Without element interaction (b) With interaction .....	112
Figure 6.11 Focused time domain footprint with and without element interaction (a) Without element interaction (b) With element interaction, blue line indicates -3 dB contour and black line indicates -10 dB contour.....	113
Figure 6.12 PSF of the MIMO array and its equivalent SIMO array for target at different range (a) target located at 1 m (b) target located at 4 m .....	115
Figure 6.13 Flow chart of PSO method .....	116
Figure 6.14 Example of a grid in 2D array plane formed by placing the equivalent array at the vertical and horizontal axes.....	117
Figure 6.15 Different linear MIMO array configuration (a) TX antennas located at the edge of the array (b) TX antennas located at the center of the array .....	119
Figure 6.16 PSF of the effective SIMO array and different factorized linear MIMO configuration.....	119
Figure 6.17 Fitness function value trace of the PSO .....	121
Figure 6.18 PSO optimized MIMO array topology .....	121

Figure 6.19 PSF of the PSO optimized MIMO array and the mask.....	121
Figure 6.20 Grid of antenna positions .....	123
Figure 6.21 Designed 2D MIMO antenna topologies (a) Array topology 1 (b) Array topology 2.....	123
Figure 6.22 Simulated PSF of array topology 1 and array topology 2 (a) Simulated PSF of array 1 (b) Simulated PSF of array 2 .....	124
Figure 6.23 Manufactured prototypes of array 1 and array 2 (a) Prototype of array 1 (b) Prototype of array 2 .....	125
Figure 6.24 Target response between T1 and R1 before and after background subtraction (a) Response of T1-R1 pair before background subtraction (b) Response of T1-R1 pair after background subtraction.....	126
Figure 6.25 Frequency domain sensitivity function of R1 and R11 in different environments (a) Sensitivity function of R1 in different environments (b) Sensitivity function of R11 in different environments .....	127
Figure 6.26 Time domain sensitivity function of R1 and R11 in different environments (a) Sensitivity function of R1 in different environments (b) Sensitivity function of R11 in different environments .....	127
Figure 6.27 Measured PSF of array 1 and array 2 when the target is located at center (a) Measured PSF of array 1 (b) Measured PSF of array 2.....	129
Figure 6.28 Measured PSF of array 1 and array 2 when the target is located at (-250,-250) (a) Measured PSF of array 1 (b) Measured PSF of array 2 .....	129
Figure 6.29 Cross-range measurement of array 1 and array 2 (a) Cross-range measurement of array 1 (b) Cross-range measurement of array 2.....	129
Figure 6.30 Down-range measurement of array 1 and array 2 (a) Down-range measurement of array 1 (b) Down-range measurement of array 2 .....	130
Figure 6.31 2D and 3D images of a vernier caliper (a) Position of the vernier caliper (b) 2D image generated by array 1 (c) 2D image generated by array 2 (d) 3D image generated by array 1 (e) 3D image generated by array 2 .....	132
Figure 6.32 2D and 3D images of a pistol (a) Position of the pistol (b) 2D image generated by array 1 (c) 2D image generated by array 2 (d) 3D image generated by array 1 (e) 3D image generated by array 2 .....	132





## **List of Tables**

<b>Table 6-1 Advantages and disadvantages of the deterministic approach and stochastic approach .....</b>	<b>122</b>
---	------------



# 1. Introduction

## 1.1 Background of the research

Ultra-wide band (UWB) radar can be claimed to be the most promising radar system of the future [1] thanks to many distinctive advantages such as *improved down-range measurement accuracy*, classification capabilities, immunity to narrow band interference, and decrease the radar “dead zone” [2]. Widely used definition of UWB is based on the Federal Communications Commission (FCC) regulation [3], which says that the operational fractional bandwidth (impedance bandwidth) at -10 dB level has to be larger than 20%, or the absolute bandwidth (determined at the same level) is larger than 0.5 GHz. This bandwidth can be located at different frequency bands according to the application requirements. For example, if a UWB radar operates at around 1 GHz, its radiation can penetrate walls or ground and detect objects behind. On the other hand, if it operates at center frequency over 10 GHz with bandwidth over 10 GHz, it can detect small objects hidden under cloths. Due to their advanced capabilities, UWB radars have found their place in a *wide range of applications* such as ground penetration radar (GPR) [4], non-destructive testing (NDT) for civil engineering, archaeology [4], drug industry [5], surveillance radar [6][7], through-the-wall radar for security personnel involved in anti-terrorist operations [8][9][10][11], search and rescue radar to detect human avalanche victim [12] or people trapped in fire or buried under rubble after an earthquake [13].

The large absolute operational bandwidth results in fine down-range resolution. Simultaneous processing of multiple radar measurements done across certain scene allow for radar beam focusing and might result in a fine cross-range resolution [13]. It has been shown that combination of both approaches can provide high-resolution 3-D images of the objects for classification and identification [14]. *There are numerous applications where UWB imaging arrays can bring large added value to UWB radar systems.* The early applications of UWB imaging are the GPR imaging [15] and the (airborne) synthetic aperture radar (SAR) (such as [16] and [17]). In recent years, the UWB imaging radar became of interest for a wide range of application. Due to its non-ionizing nature, it poses no known health issue to human beings at moderate power levels, so it has been considered as an alternative to the X-ray mammography for the breast cancer detection [18][19][20][21]. It also provides great value for the security and safety sector. Some through-the-wall imaging (TWI) radar can image scene behind walls providing extra information for security personnel [8][9][10][11]. It has also great value at security checkpoints such as airports to detect weapons or unauthorized objects on a human body concealed under common clothes [22][23][24] (which generally refers to concealed weapon detection radar, or CWD radar).

The operational band of the UWB imaging radar depends on the applications and system requirements. For example, TWI UWB radars often operate at lower microwave range (say from 1 GHz to 4 GHz) because only at this frequency can the electromagnetic (EM) wave penetrate walls with reasonably small losses. The CWD imaging radar, on the other hand, works at higher frequencies (for example, 10 GHz

to 20 GHz), or mm-wave range (such as 60 GHz to 70 GHz). Different operational frequency bands have different advantages and disadvantages. The mm-wave UWB imaging radar can provide very high-resolution image, but the technology at this frequency band is not mature (comparing to technology at microwave frequency band), which complicates the antenna as well as the electronics design. In addition, mm-wave UWB imaging radar raises ethical and privacy issues as the resolution of the images provided is so high that not only weapons will be imaged but also private part of the human body [25][26]. The microwave UWB imaging radar, on the other hand, can only provide lower resolution images. Such a resolution is already sufficient to image common weapons such as pistols or knives but it would not present human body details. Moreover, the technology at microwave frequency range is mature, thus a microwave UWB imaging system is relatively simpler and cheaper than a mm-wave UWB imaging system.

In order to obtain 3-D images by means of UWB radars, radar data should be acquired over 2-D planar or cylindrical aperture (such data set is called C-scan) over target area. There are several ways to obtain a C-scan. The simple way is to use a single transmit-receive antenna pair and move it over the 2-D aperture with two dimensional mechanical system. This approach only requires very simple antenna system, but the mechanical scanning is time consuming. As a result, it takes considerable time (from hours to a few seconds in the most advance systems) to acquire a C-scan. As a result, the refresh rate of image is low and the radar cannot provide real time image of moving targets. To speed-up the data acquisition and increase the image refreshing rate, the single antenna pair can be replaced by an antenna array, such as in [27], where the image is obtained by one dimensional transmit/receive antenna *array pair* to obtain a linear scan (B-scan) of an object electronically and use one dimensional mechanical scan in orthogonal direction to obtain the C-scan. The drawback of this approach is that it requires a large number of antennas, which leads to heavy weight, complicated radio-frequency (RF) front end electronics, and high cost. In [28], the one-dimensional transmit/receive *antenna pair array* is replaced by one single transmit antenna and several receiving antennas. The B-scan is obtained by electrically steering the beam, and the C-scan is obtained by one dimensional mechanical scanning perpendicular to the array. This can simplify the whole antenna system, reduce the weight and complexity, and reduce the cost. Nevertheless, the methods mentioned above all require mechanical scanning, which is the bottleneck of the imaging system with respect to the refresh rate. To obtain real-time images, a dedicated 2-D array is necessary, because it can directly measure and obtain a C-scan in one snapshot, which greatly improves the data acquisition time.

Despite the fact that generation of high-resolution radar 3-D images in real-time is of great interest, *it is still not possible to do this at the current technology stage of development*. The major problem is how to combine fast data acquisition (via decreasing number of measurements) with a reasonable image quality (via imaging sparse data sets). Two essential items are still missing: dedicated antenna systems for sparse C-scan acquisition and fast high-quality imaging algorithms. While the imaging algorithms is out of scope of this study, both the cm- and mm-wave UWB antennas and antenna arrays for high-resolution imaging radar applications are investigated in this thesis . For the cm-wave UWB imaging radar, an array system including the array topology and element is developed. For the future mm-wave

UWB imaging radar, prototype mm-wave antenna elements for an imaging array are developed.

## 1.2 State-of-the-art in UWB arrays and research motivation

As mentioned above, this thesis research is focused on 2-D UWB antenna arrays for near-field imaging application. The array requires a large operational bandwidth (at least several GHz, which determines the down-range resolution), low side- and grating lobe level (which determines the dynamic range of the image), narrow footprint (this determines the cross-range resolution, and the requirement depends on application), large enough scanning angle (e.g.  $\pm 60^\circ$ ) to cover the area of interest and a relatively small number of elements (to make realization of a whole system feasible). The number of elements should be as small as possible to reduce the cost, weight, and data flow; however it should be sufficient in order to produce images of reasonable quality.

The peculiarity of the UWB imaging applications mentioned above is that the imaging object is typically situated in the near- or intermediate zone of the array. So for these applications, near- field performance of the array is of importance.

Development of an array can be split in three issues: selection of an array topology, selection of antenna elements and research on coupling between elements in the array and its influence on the array performance. The antenna elements for the array should satisfy multiple requirements and constraints, which sometimes prevents the use of existing UWB antennas in dedicated arrays. They not only need sufficient impedance bandwidth, but also should have good radiation characteristics, time domain performance, and reasonable size. The antenna effects such as coupling, dispersion, and ringing should also be minimized because they will degrade the image quality and may obscure smaller objects, making detection and classification difficult.

### 1.2.1 State-of-the art in time domain UWB imaging arrays

Most of the UWB array analyses are done in time domain. The preliminary physical investigations of UWB array behavior have been reported in studies such as [29][30][31][32]. In [29], the mathematical formulation of the time domain UWB array has been exploited and developed. In [30], the steady-state concepts such as beam width, directivity, gain, effective receiving area, Fresnel and Fraunhofer regions are extended to transient UWB arrays using time domain analysis. In [31], important comparisons between narrow band arrays and UWB arrays are given, and it indicated that the UWB sparse arrays do not suffer from the grating lobe problem. In [32], far-field linear UWB array behavior in time-domain was discussed. In [33][34][35][36][37][38], UWB array pulse forming has been investigated. The above mentioned studies did not consider the antenna coupling. The investigation of antenna coupling effects has been reported in [39] and [40]. These theoretical investigations provide solid theoretical background of UWB array behavior and design guide.

Although several studies have been devoted to explore the physical behavior of the UWB array, the experimental realization of the UWB array remains a relatively untouched area. There are a few experimental 1-D or 2-D UWB arrays for different applications. In [28] a 1-D array for GPR applications is presented, some 1-D arrays for the TWI radar application is discussed in [8] and [41], a 2-D UWB square array

used in radio astronomy application is presented in [42], a hemispherical 2-D array for breast cancer detection is shown in [21], and a 2-D array for TWI application is presented in [11]. However, these arrays are either 1-D, which needs the aid of mechanical scanning to obtain images, or they are 2-D with non-optimized topology such as square or circular. Very limited information is known on properties of the radiated UWB field in the near-zone and optimization of the UWB array topology to achieve certain performance in the near-zone has never been discussed.

The discussions on how to design 2-D UWB array can be found in the ultrasonics society. In [43], the design and analysis of 2-D transducer sparse array has been reported. It demonstrated that by using the transducer arrays are capable to achieve grating lobe free array pattern with the sparse array configuration. The idea of the transducer array has also been discussed in [31]. In this thesis these concepts are extended to the electromagnetic UWB array and applied to investigation of arrays for short-range high resolution imaging arrays.

### 1.2.2 State-of-the-art in UWB antenna element development

The very first of the UWB antenna can be traced as early as Hertz's spark gap (1888) [44]. Over the years many different types of UWB antennas have been proposed in the antenna society. After 2002 when the FCC permitted the commercial use of the UWB band, there are many more different UWB antennas developed. A good introduction of UWB antenna development can be found in [44] and [45].

However, most of the existing antennas cannot fulfill the element requirement for impulse UWB array application. The antenna should not only have sufficient impedance bandwidth, the radiation patterns and gain should also be stable within the operational bandwidth. The radiation patterns of the antenna is required to be uni-directional with wide beamwidth to illuminate the area of interest and large front-to-back ratio (FBR) to isolate the elements and the electronics behind. The antenna should be non-dispersive or dispersive in a controllable way at all directions of interest so it is possible to compensate the dispersion. The antenna interaction should also be controlled as it can disrupt the array performance. Last but not least, the antenna is preferable to be small, flat, and light, to reduce the antenna size and weight.

Popular UWB antenna types such as TEM horn [45], helix antenna [46], bi-conical antenna [44][46], frequency independent antenna [44][46], UWB dipole-like antenna such as elliptical dipole or bow-tie antenna [44], UWB monopole antenna [44][47][48][49], magnetic loop antenna [46][50], and Vivaldi antenna [51] all have their limitations and are not suitable for this application. The TEM horn and the helix antennas are bulky and have narrow beamwidth. The frequency independent antennas are dispersive. The broadband dipole and monopole antennas have omnidirectional or quasi-omni directional radiation pattern. The Vivaldi antennas have very broad bandwidth with good FBR, but the end-fire radiation nature makes them not ideal for broadside array application. All these characteristics prevent from using them. International Research Center for Telecommunications and Radar (IRCTR) has developed a shielded elliptical dipole antenna which has large bandwidth, large FBR, and good linearity [52]. It was successfully re-designed to be operated at K-band presented in Chapter 4. However, at microwave frequencies the back shield is bulky, thus it is not suitable for the microwave array application. Microstrip types of

antennas are most promising element candidate for microwave UWB imaging array application as they are flat, and potentially can provide sufficiently large bandwidth with desired radiation characteristics.

### 1.3 Research objectives

The research objectives of this thesis are development of design approach for sparse MIMO 2-D UWB antenna arrays for short-range high-resolution imaging and experimental verification of the developed approach on a number of UWB arrays for different imaging applications. Particularly, complete UWB MIMO sparse antenna array system including array topology and suitable antenna elements working at microwave range will be developed. Antenna elements prototype working at mm-wave range will also be developed for the future mm-wave ultra-high resolution imaging radar application. The research line is illustrated in Figure 1.1.

For the array design, the following research activities should be performed: derivation of an optimal array topology based on system requirements, development of an antenna element, embedding of the antenna element in this topology and study of antenna element mutual coupling and, finally, experimental verification of the focusing properties of the complete array.

Development of an antenna element for an array include following steps: determine the possible antenna types, obtain comprehensive understanding of the physical processes of the antenna geometry to the antenna performance, optimize the antenna impedance matching, optimize antenna radiation characteristics, and experimental verification of the antenna performance.

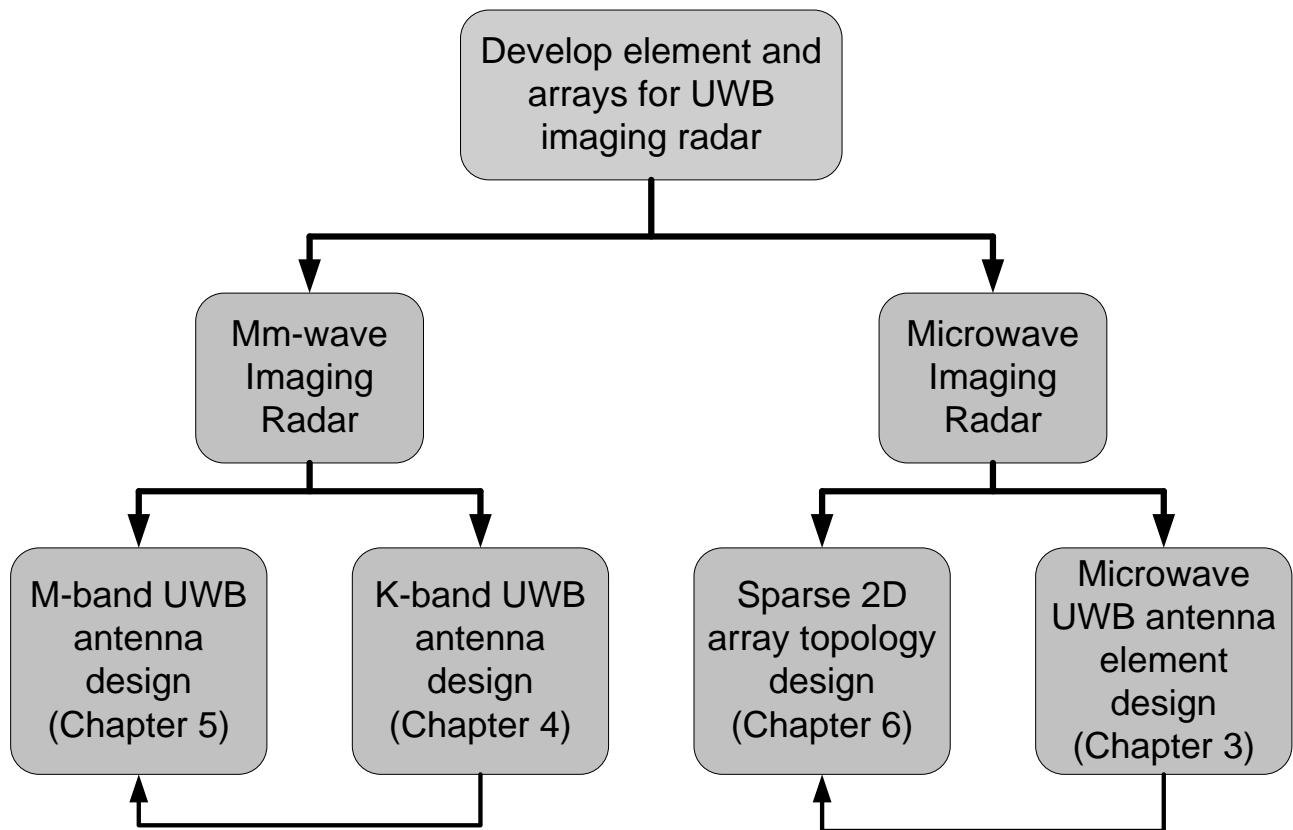


Figure 1.1 Research line

## 1.4 Challenges

In this thesis several challenges have been addressed.

- Development of a radiating element for an imaging array operating in the bandwidth 10-18 GHz. The antenna requirements are dictated by the radar's specifications, which prevents from using the common UWB antennas. Specifically, the antenna elements not only need to have sufficient impedance bandwidth, but also meet strict requirements on the radiation characteristic and time domain behavior. The antennas should radiate at its broadside, have stable gain across the operational band, and have sufficient beamwidth. The antenna should be uni-directional and radiate toward broadside to protect the electronics behind as well as to reduce the interference from the electronics. The antennas should have small group delay and have low late-time ringing. Additionally, the imaging application requires that the antenna coupling should be controlled such that when the antennas are embedded into the array, the coupling would not degrade the array performance. The size of the antennas is desired to be small (smaller than half wavelength at the centre frequency), light weight, and flat. All these constrain should be carefully dealt.
- Development of M-band differential UWB antenna in low-temperature co-fired ceramic (LTCC) technology. The advantage of the LTCC technology is that the LTCC material provides low loss and stable material properties at mm-wave frequencies. Furthermore, the LTCC material is a layered structure, so it suit well for realization of 3-D structures with passive components. As a result, the LTCC technology is suitable for mm-wave integrated system-on-chip (SOC) and was chosen to realize the M-band antenna. Despite of numerous advantages of the LTCC technology, for UWB antenna development the technology has a significant drawback – the high value of the substrate dielectric permittivity. This typically limits the antenna bandwidth and makes UWB antenna design in this technology particularly challenging. Furthermore, LTCC technology does not allow for solid metallization walls and thus leakage of electromagnetic energy through perforated metal walls should be taken into account. Antenna connectorization is also not straightforward in LTCC technology. Finally, as LTCC manufacturing technology is not yet standardized the manufacturing tolerances are much larger than those in PCB technology and should be taken into account by the antenna design. In order to better understand constrains of the LTCC technology, we have first developed an antenna working in K-band (20 GHz to 40 GHz) because at this band the manufacturing as well as the measurement technologies are relatively mature. The knowledge obtained from the development of the K-band antenna is then used to reduce the risk of development of the M-band antenna.
- Measurement of the K-band and the M-band differential antenna performances also poses great challenges. Firstly, the antennas are as small as (or even smaller than) the commercially available connectors, thus the antenna substrate needs to be enlarged to incorporate the connectors, which increases the spurious radiation. In addition, the limited LTCC substrate size prevents the spatial separation of the antenna and the connector, so the reflection from the interface of the connectors and the antenna as well as the spurious radiation from connectors cannot be time-gate out. Although it is possible to measure the antenna reflection coefficient using on-wafer probe [53][54], to measure the



antenna radiation pattern and gain special equipment (which is not available to us) is necessary. As a result dedicated antenna measurement procedures should be developed. To de-embed the effect of the feeding structure, calibration procedure for the measurement should be developed as well.

- Design of 2-D UWB antenna array for imaging applications is a novel research area. Only very few discussions on array topology design and antenna element coupling issues in the literature. The 2-D array is desired to have narrow footprint, low sidelobe level, and small number of elements. However, these performance requirements are often contradictory to the requirement of small element numbers, as the footprint size is mainly obtained by large aperture size and low sidelobe level is related to dense element spacing. But large aperture size and dense spacing indicates large number of antenna elements. How to overcome these contradictions and find a good balance between footprint size, sidelobe level, and element number is very challenging. In addition, it was found that the antenna element interaction will alter the footprint in the near-field and degrades the antenna array performance [55]. Therefore, it is important to consider this fact when designing the array topology and antenna element. Finally, different 2-D element arrangement might have the same radiation patterns along certain axes but different patterns along other axes within the scanning area. Global optimization over the array performance within the scanning area may be performed. Although this may insure the best performance, it will dramatically increase the design complexity. Trade-off between the antenna array performance and complexity of the array as well as optimal positioning of the antenna elements within the array aperture are real challenges in 2-D UWB antenna design.

## 1.5 Approaches

In this research several approaches have been utilized to overcome the challenges and achieve the research objectives.

- The development and analysis of antennas (the microwave antenna, the K-band antenna, and the M-band antenna) follows similar steps. Firstly the antenna type is selected based on system requirements and accurate full-wave numerical antenna model based either on the Method of Moment (MoM) [46] or the finite integral technique (FIT) [56] for generic antenna geometry is created. Secondly, the models have been used to evaluate the relationship between the antenna's physical dimensions and the antenna performance as well as to analyze the antenna behavior. Thirdly, based on the found relationship antenna performance optimization has been done. The model has also been used to evaluate the impact of the manufacturing limitation to the performance of the antenna. Finally, experimental verification of the antenna performance is performed.
- Since LTCC technology is not standardized and impact of manufacturing tolerances in this technology on M-band antenna performance might be essential, it has been decided to develop K-band antenna in LTCC technology first and investigate on the example of this antenna influence of manufacturing tolerances on antenna performance. By evaluating the impact of manufacturing variation of the K-band antenna, we can have better understanding of the LTCC technology. Therefore the experiences and analysis done in the K-band

antenna can be used to adjust the M-band antenna design. By doing so the risk of the development of the M-band antenna can be reduced. Furthermore, K-band antenna has been used to develop reliable measurement techniques for differentially-fed LTCC antennas.

- To analyze the array performance in the near field, numerical models of the topologies with ideal elements (isotropic radiators without coupling) have been used. The array performance is evaluated by its point spread function (PSF) at a certain distance. The PSF is obtained by using modified Kirchhoff Migration algorithm. The PSF can be viewed as the array beam pattern and the array cross-range resolution and the sidelobe level can be extracted from the PSF.
- To achieve fine cross-range resolution, low sidelobe level, and small number of antennas, the concept of multiple transmit antennas and multiple receive antennas (MIMO) has been adopted. It has been demonstrated that by using the MIMO array topology, one can achieve fine cross-range resolution and low sidelobe level with considerably less amount of the antenna elements. In addition, by using the MIMO array, the element spacing can be much greater than a wavelength at the lowest operational frequency with only slight rise of sidelobe level, which reduces the effect of element coupling.
- As direct design of a 2-D MIMO array topology is very difficult, we utilized the concepts of effective array and array projection. The concept of effective array is that by spatial convolve the transmit sub-array and the receive sub-array, we can obtain an array with 1 transmit antenna and  $N$  receive antennas where  $N$  is the sum of number of transmit antennas and receive antennas. Although this concept is only applicable to the far-field region of UWB arrays, and for near-field array region it is not entirely true, for the UWB pulse interference area (the main lobe), this concept can still be applied [31]. The concept of element project is that the array PSF on a certain axis is same as PSF of the 1-D array whose topology is same as the projection of the 2-D array topology onto that axis. With these 2 concepts we can firstly design a 1-D linear array with 1 transmit antenna and  $N$  receive antennas whose PSF meets the requirements, then from this 1-D array we find a 1-D MIMO array whose effective aperture is the designed 1-D array, and then from this 1-D MIMO array we find corresponding 2-D MIMO arrays which gives the same 1-D MIMO topology on the principal axis.
- The 2-D array topology obtained by using the above mentioned method is not unique. Different element arrangement can give the same PSF on the principal axes, but different behaviors on other axes. In addition, different element arrangement leads to different inter-element spacing and different element relative orientation, which influences the coupling level between elements and the coupling effects to the antenna performance. As a result, it is important to investigate the influence of antenna coupling to the antenna array performance. Traditionally people only concentrate the study on the impact of active coupling, but it is shown that even when the antennas are operated in the passive mode, the antenna coupling will alter the sensitivity function and eventually change the array foot print, which leads to higher side lobe level or ringing. By understanding the effects of coupling to the array performance, we can either design an element which has small coupling or to find an optimal element arrangement which reduces the element coupling effect.

## 1.6 Novelties and achievements

In this thesis we have dealt with novel problems of antenna elements and antenna array design for real-time high-resolution near-field imaging. This has resulted in several novel scientific results which have not been discovered by other parties at the time of performing the research. Additionally, the research has led to a number of scientific results that give important contributions to the thesis. The main novelties and major scientific achievements are list below:

### Main novelties of the research problems:

- In this thesis we have dealt with novel problems regarding 2-D sparse antenna array design for real-time high-resolution short-range UWB imaging radar. We have not only investigated the array topology design principles but also verified the proposed principles through experiments.
- Challenges of develop differentially-fed mm-wave UWB antenna using the LTCC technology have been taken in this thesis, which results in two novel mm-wave antenna designs.

### Main novel scientific results:

- A low profile aperture stacked patch 10-18 GHz UWB antenna has been specifically designed for the proposed 2-D MIMO arrays. This antenna has hemispherical radiation pattern, good total efficiency ( $>90\%$ ), and small group delay, which is very suitable for the time-domain UWB array. They have been integrated with the proposed array topology to experimentally verify the simulated array performance, and the influence of the real antenna effect such as coupling and non-linearity has been evaluated.
- A differentially-fed, shielded elliptical dipole UWB antenna using the LTCC technology has been developed. Effects of high dielectric constant nature of the LTCC material to the antenna performance have been investigated. To increase the bandwidth of the antenna, stair-case shield has been developed to avoid resonance of rectangular or circular shield. The impedance bandwidth of the antenna is from 25 GHz to 30 GHz with good gain, high efficiency ( $>95\%$ ), and radiation pattern. To avoid resonances and increase the antenna bandwidth, a stair-case shield has been implemented. However, due to manufacturing limitations, solid shield is not possible to realize. We have demonstrated that the solid shield can be replaced by the metal grid and connected interleaved via fences. Special design of the feeding structure has been proposed to connect the elliptical dipole to the outside of the shield.
- An M-band ASP antenna with novel differential feeding structure has been developed. The differential feeding is realized by using a parallel transmission line to couple the energy to the aperture instead of the microstrip line. Due to high dielectric constant, the surface wave problem is severe and the radiation patterns are deformed. A metal cage is designed to surround the radiation patch which greatly alleviates the surface problem while keeping the impedance bandwidth. The antenna geometry is simple and low profile, thus it is easy to manufacture. We have achieved large impedance bandwidth from 50 GHz to above 78 GHz (44%), which has never been seen in the literature for this type of antenna and the LTCC material. The radiation patterns are stable within this

bandwidth and the gain is of about 3.5 dBi to 8 dBi with radiation efficiency larger than 80%.

- Development of measurement procedure to measure the differentially-fed K-band and the M-band antennas. Mix-mode S-parameters were used to measure the reflection coefficient of the differential input. By using the mix-mode S-parameters we can have better insight of how the differential mode reflection coefficient and the common mode reflection coefficient behave, and how the mode conversion behaves.
- 1-D MIMO array has been developed based on (particle swarm optimization) PSO. The PSO was used to optimize the array PSF, and by applying different masks and weight functions, we can trade the cross-range resolution with the side-lobe level.
- Two theoretical 2-D real-aperture MIMO antenna arrays based on the same 1-D MIMO array working from 10 GHz to 18 GHz have been developed to examine the proposed approach. In simulations both arrays can provide -10 dB cross-range resolution of 5 cm, but due to different element arrangement, one topology outperforms the other in the sense that it has 4 dB lower sidelobe level.

## 1.7 Research framework

This research is mainly done under the framework of the European Union project Radiotect (Ultra Wideband Radio Application for Localisation of Hidden People and Detection of Unauthorised Objects) which started on 1<sup>st</sup> of January 2007 and involves several universities and small-medium enterprises. The partners are: Delft University of Technology, Technische Universität Ilmenau, Technická univerzita v Košiciach, Vrije Universiteit Brussel, MEODAT Messtechnik, Ortung und Datenverarbeitung GMBH, Geozondas Ltd, INGMETAL, IRK-Dresden, Swedish Rescue Services Agency, and Stephen Crabbe Consulting.

The main goals of the Radiotect project is to develop a through-the-wall imaging (TWI) radar, a concealed weapon detection (CWD) imaging radar, imaging algorithms for the UWB radar, and explore the feasibility of extending the radar to the M-band. Nevertheless, the research tasks of this thesis are focused on developing the antenna array system for the CWD radar, and develop the antenna element for the M-band radar.

## 1.8 Thesis outline

The thesis is organized in the following chapters:

- **Chapter 2** — *Measurement facilities and techniques*. This chapter discusses the measurement challenges, setups, calibration techniques, and data post processing techniques.
- **Chapter 3** — *Microwave UWB antenna analysis and development*. This chapter presents the analysis and development of the 10-18 GHz antenna element. The Aperture Stacked Patch (ASP) antenna has been chosen as the basic element type. Antenna mutual coupling has been specifically investigated to evaluate its impact to the antenna array.

- **Chapter 4** — *K-band LTCC differentially-fed UWB antenna analysis and development.* This chapter discusses the development of the K-band LTCC antenna. This antenna is mainly served as an intermediate step of developing the M-band LTCC antenna. This is because the measurement equipments and techniques for the M-band are very expensive or even unavailable, especially for the differentially-fed antennas. Thus, by designing and measuring at relatively matured K-band, we can gain experiences and consequently reduce the risk of developing the M-band antenna.
- **Chapter 5** — *M-band differentially-fed UWB antenna analysis and development.* This chapter describes the analysis and development of the M-band LTCC antenna and its experimental verification. Based on the analysis in chapter 3 and 4, we have selected the ASP antenna as the basic antenna type for the M-band antenna as well. Nevertheless due to the high relative permittivity of the LTCC material, strong surface wave is excited. We have proposed by adding a simple rectangular-shaped shield, the surface wave problem can be alleviated and the antenna performance can be improved.
- **Chapter 6** — *UWB Sparse Arrays for Near-Field Imaging.* This chapter gives the fundamental research of the UWB antenna array. In this chapter, properties of 2-D UWB antenna array are examined, and approaches of how to develop 2-D UWB array topologies are introduced. Two application- based 2-D MIMO array topologies are developed based on introduced approaches and are experimentally verified.
- **Chapter 7** — *Conclusions.* This chapter summarizes the results of this study and gives recommendations for future research.

## References

- [1] I. I. Immoreev, J. D. Tayler, P. E., "Future Radars", *Proc. IEEE Conf. on UWB Systems and Technologies*, p.p. 197-200, 2002.
- [2] I. I. Immoreev, PGS Dmitry V. Fedotov, "Ultra Wideband Radar Systems: Advantages and Disadvantages", *Proc. IEEE Conf. on UWB Systems and Technologies*, p.p. 201-206.
- [3] FCC (GPO) Title 47, Section 15 of the Code of Federal Regulations Subpart F: Ultra-wideband, 16 May, 2002.
- [4] D. J. Daniels, *Ground Penetrating Radar*, 2<sup>nd</sup> edition, United Kingdom, IEE, 2004
- [5] T. W. Wang, K. G. Deepak, M. N. Taib, N. K. Anuar, "Microwave non-destructive testing technique for characterization of HPMC-PEG 3000 films", *International Journal of Pharmaceutics*, vol. 343, issue 1-2, p.p. 122-130, October 2007.
- [6] R. J. Fontana, "Recent Applications of Ultra Wideband Radar and Communication Systems", *Ultra-Wideband, Short-Pulse Electromagnetics 5*, part 2, pp. 225-234, 2002.

- [7] A. Martinez-Vazquez and J. Fortuny-Guash, "UWB MIMO Radar Arrays for Small Area Surveillance Applications", *Proc. EuCAP 2007*, 2007.
- [8] G. Franceschetti, J. Tatoi, D. Giri, and G. Gibbs, "Timed Arrays and Their Application to Impulse SAR for 'Through-The-Wall' Imaging", *Ultra-wideband Short-Pulse Electromagnetics 7*, p.p. 199-205, 2007.
- [9] S. Nag, M. A. Barnes, T. Payment, and G. W. Holladay, "An Ultra-Wideband Through-Wall Radar for Detecting the Motion of People in Real Time", *Proc. of SPIE*, vol. 4474, p.p. 48-57, 2002
- [10] Available online: <http://www.cambridgeconsultants.com/prism200.shtml>
- [11] A. Beeri and R. Daisy, "High-resolution Through-wall Imaging", *Proc. of SPIE*, vol. 6201, art. No 62010J, 2006.
- [12] W. A. Chamma, H. Mende, G. Barrie, and R. Robinson, "Detection of Avalanche Victims Using Ultra-wideband Short-pulse Radar", *Ultra-wideband Short-Pulse Electromagnetics 7*, pp. 632-644, 2007.
- [13] A. G. Yarovoy, X. Zhuge, T. G. Savelyev, and L. P. Ligthart, "Comparison of UWB Technologies for Human Being Detection with Radar", *Proc. of 4<sup>th</sup> EuRAD*, pp. 295-298, 2007.
- [14] E. L. Mokole and P. Hansen, "Survey of Ultra-wideband Radar", *Ultra-wideband Short-Pulse Electromagnetics 7*, pp. 571-585, 2007.
- [15] A. G. Yarovoy, B. Sai, G. Hermans, P. van Genderen, L. P. Ligthart, A. D. Schukin, and I. V. Kaploun, "Ground Penetrating impulse radar for detection of small and shallow-buried objects", *Proc. IGARSS 99*, pp. 2468-2470, Hamburg, 1999.
- [16] H. Hellsten, "CARABAS-an UWB low frequency SAR", *IEEE MTT-S*, pp 1495-1498, 1992.
- [17] M. Ressler, L. Happ, L. Nguyen, T. Tuan, and M. Bennett, "The Army Research Laboratory Ultra-wideband Testbed Radars", *IEEE Radar conference 95*, pp. 686-691, 1995.
- [18] X. Li, E. J. Bond, B. D. Van Veen, and S. C. Hagness, "An overview of ultrawideband microwave imaging via space-time beamforming for early-stage breast cancer detection", *IEEE Antennas and Propagation Magazine*, vol. 47, no. 1, pp. 19-34, Feb. 2005.
- [19] M. Klemm, I. J. Craddock, J. A. Leendertz, A. Preece, and R. Benjamin, "Radar-Based Breast Cancer Detection Using a Hemispherical Antenna Array – Experimental Results", *IEEE Trans. on Antennas and Propagation*, Vol. 57, No. 6, pp. 1692-1704.
- [20] X. Zhuge, M. Hajian, A.G. Yarovoy, L.P. Ligthart, "Ultra-Wideband Imaging for Detection of Early-Stage Breast Cancer", *Proc. EuRAD*, Munich, Germany, 2007
- [21] I. J. Craddock, A. Preece, J. Leendertz, M. Klemm, R. Nilavaln, and R. Benjamin, "Development of a Hemi-spherical Wideband Antenna Array for

- Breast Cancer Imaging”, *Proc. EuCAP 2006*, November 2006.
- [22] D. M. Sheen, D. L. McMakin, and T. E. Hall, “Three-Dimensional Millimeter-Wave Imaging for Concealed Weapon Detection”, *IEEE Trans. on Microwave Theory and Techniques*, Vol. 49, No. 9, pp. 1581-1592.
  - [23] D. M. Sheen, D. L. McMakin, and T. E. Hall, “Near-Field Imaging at Microwave and Millimeter Wave Frequencies”, *IEEE MTT-S International Microwave Symposium Digest*, art. No. 4264177, pp. 1693-1696.
  - [24] R. R. Blasing, T.W. Grudkowski, S.T. Trospers, “Millimeter-wave Active Imaging System with Modular Array”, US patent 7119740 B2, Oct. 16, 2006.
  - [25] Available online: <http://www.prisonplanet.com/inverted-body-scanner-image-shows-naked-body-in-full-living-color.html>
  - [26] Available online: <http://www.wired.com/threatlevel/2011/02/scanners-part1/>
  - [27] R. J. Chignell, H. Dabis, N. Forst, and S. Wilson, “The Radar Requirements for Detecting Anti-personnel mines”, *Eighth Int. Conf. Ground Penetrating Radar*, SPIE vol. 4084, pp. 861-866, May 2000.
  - [28] A. G. Yarovoy, T. G. Savelyev, P. J. Aubry, P. E. Lys, and L. P. Ligthart, “UWB Array-Based Sensor for Near-Field Imaging”, *IEEE Trans. on MTT*, vol. 55, No. 6, June 2007.
  - [29] A. Shlivinski and E. Heyman, “A Unified Kinematic Theory of Transient Arrays”, in *Ultra-Wideband Short-Pulse Electromagnetics 5*, P. D. Smith and S. R. Cloude, Eds. New York: Kluwer Academic/Plenum Publisher, 2000, pp. 327-334.
  - [30] G. Franceschetti, J. Tatoian, and G. Gibbs, “Timed Array in a Nutshell”, *IEEE Trans. on Antennas and Propagation*, Vol. 53, No. 12, pp. 4073-4082, Dec. 2005.
  - [31] J. L. Schwartz and B. D. Steinberg, “Ultrasparse, Ultrawideband Arrays”, *IEEE Trans. on Ultrasonics, Ferroelectrics, and Frequency Control*, vol. 45, no. 2, March 1998.
  - [32] E. L. Mokole, “Behavior of Ultrawideband-Radar Array Antennas”, *IEEE International Symposium on Phased Array Systems and Technology*, pp. 113-118, 1996.
  - [33] M. Ciattaglia, G. Marrocco, “Time Domain Synthesis of Pulsed Arrays”, *IEEE Trans. on Antennas and Propagation*, Vol. 56, No.7, pp.1928-1938, 2008.
  - [34] D. H. Schaubert, S. Kasturi, A. O. Boryssenko, and W. M. Elsallal, “Vivaldi Antenna Arrays for Wide Bandwidth and electronic Scanning”, *Proc. 2<sup>nd</sup> EuCAP* 2007.
  - [35] M. Wang and S. Wu, “A Time Domain Beamforming Method of UWB Pulse Array”, *IEEE International Radar Conference*, p.p. 697-702, 2005.
  - [36] F. Anderson, W. Christensen, L. Fullerton, and B. Kortegaard, “Ultra-wideband beamforming in sparse arrays”, *IEE Proc. H: Microwaves, Antennas and Propagation*, vol. 138, issue 4, p.p. 342-346, 1991.

- [37] F. Dowla and A. Spiridon, "Spotforming with an Array of Ultra-wideband Radio Transmitters", *IEEE Conf. on Ultra Wideband Systems and Technologies*, p.p. 172-175, 2003.
- [38] M. G. M. Hussain and A. S. Al-Zayed, "Aperture-Sparsity Analysis of Ultrawideband Two-dimensional Focused Array", *IEEE Trans. on Antennas and Propagation*, Vol. 56, No. 7, pp. 1908-1918, 2008.
- [39] M. Ciattaglia and G. Marrocco, "Investigation on Antenna Coupling in Pulsed Arrays", *IEEE Trans. On Antennas and Propagation*, vol. 54, No. 3, March 2006.
- [40] G. Kotyrba and H. J. Chaloupka, "On Signal Distortion in Compact UWB Arrays due to Element Interaction", *IEEE AP-S International Symposium*, Vol 1A, pp. 614-617, 2005.
- [41] D. L. Sostanovsky, A. O. Boryssenko, and E. S. Boryssenko, "UWB Radar Imaging System with Two-element receiving Array Antenna", *Proc. 5<sup>th</sup> International Conf. of Antenna Theory and Techniques*, p.p. 357-360, 2005.
- [42] R. Maaskant, M. Popova, and R. van den Brink, "Towards the Design of a Low-cost Wideband Demonstrator Tile for the SKA", *Proc. EuCAP 2006*, 2006.
- [43] G. R. Lockwood and F. S. Foster, "Optimizing Sparse Two-Dimensional Transducer Arrays Using an Effective Aperture Approach", *IEEE Ultrasonic Symposium*, Vol. 3, pp. 1497-1501, 1994.
- [44] H. Schantz, *The Art and Science of Ultrawideband Antennas*, Norwood, MA, Artech House, 2005.
- [45] J.D. Taylor, *Introduction to Ultra-Wideband Radar Systems*, CRC Press, 1995.
- [46] C. A. Balanis, *Antenna Theory: Analysis and Design*, John Wiley & Sons, 1997.
- [47] K. P. Ray, P. V. Anob, R. Kapur, and Girish. Kumar, "Broadband Planar Rectangular Monopole Antennas", *Microwave and Optical Technology Letters*, Vol. 28, No. 1, pp. 55-59, 2005.
- [48] G. Kumar and K.P. Ray, *Broadband Microstrip Antennas*, Norwood, MA: Artech House, 2003, pp. 357-378
- [49] J. Liang, C. C. Chiau, X. Chen, and C. G. Parini, "Study of a Printed Circular Disc Monopole Antenna for UWB Systems", *IEEE Trans. on Antenna and Propagations*, Vol. 53, No. 11, pp. 3500-3504, 2005.
- [50] A. Yarovoy, R. de Jongh, and L. Ligthart. "Ultra-wideband sensor for electromagnetic field measurements in time domain", *Electronics Letters*, vol. 36, pp. 1679-1680, (2000).
- [51] P.J. Gibson, "The Vivaldi Aerial", *Proc. 9<sup>th</sup> European Microwave Conference*, 1979, p.p. 101-105.
- [52] A. Vorobyov, "Report on Antenna Back Side Shield Optimization for Elliptically Shaped Dipole Antenna", IRCTR Internal report.
- [53] S. Ranvier, M. Kyrö, C. Icheln, C. Luxey, R. Staraj, and P.



- Vainikainen, "Compact 3-D On-wafer Radiation Pattern Measurement System for 60GHz Antennas", *Microwave and Optical Technology Letters*, Vol. 51, No. 2, pp. 319-324, 2009.
- [54] J. A. G. Akkermans, R. van Dijk, and M. H. A. J. Herben, "Millimeter-wave Antenna Measurement", *Proc. of the 37th EuMC*, pp. 83-86, Oct. 2007.
- [55] B. Yang, A. G. Yarovoy, and L. P. Ligthart, "Performance Analysis of UWB Antenna Array for Short-range Imaging", *Proc. 2<sup>nd</sup> EuCAP*, 2007.
- [56] T. Weiland, "A Discretization Method for the Solution of Maxwell's Equations for Six-Component Fields", *Electronics and Communications (AEUE)*, vol. 31, no. 3, pp. 116–120, 1977.



## **2. Measurement facilities and techniques**

### **2.1 Introduction**

The antenna elements and array studies cannot be purely done theoretically. Experimental verification plays a vital role in the life cycle of antenna and array development. Although one needs experimental analysis to verify theoretical model, careless measurements may generate erroneous results and misled the analyst. Therefore, this chapter is devoted to describe the measurement setups, calibration techniques, and data post-processing techniques developed for this research.

The chapter starts with the measurement challenges faced in this thesis. The measurement setups to measure the antenna characteristics and antenna array performances are described in section 2.3. Calibration techniques are described in Section 2.4. Section 2.5 discusses the data post-processing techniques and Section 2.6 draws conclusions.

### **2.2 Measurement challenges**

The measurement challenges in this research mainly lay in the mm-wave measurements and can be described as impact of the measurement equipment on antenna parameters and accuracy of the radiated field measurements. The former challenge is due to the fact that the majority of the mm-wave antennas have dimensions of several millimeters only. These dimensions are so small that the influence and disturbance from the measurement equipment becomes so significant that it should be carefully compensated. In particular, antenna feeding techniques play an important role. The latter challenge is related to the probe compensation, measurements of the differentially fed antennas and impact of the measurement environment.

There are three main approaches to feed mm-wave antennas under test: using waveguides (e.g., [1][2][3]), using on-wafer probes (e.g., [4][5][6]), or using coax-connectors (e.g., [7][8][9]). Waveguide measurement is traditionally well known and robust, but is bulky and not easy to manipulate. On-wafer probe measurement is an emerging technology and becomes more and more popular in mm-wave measurements. It avoids the using of connectors, but it also brings many challenges and limitations. While the antenna reflection coefficient measurement is possible by using standard on-wafer measurement stations, the antenna gain and radiation patterns measurements have many limitations. The major limitation is that most of the existing on-wafer antenna radiation measurement setups require the feeding point and the antenna at the same side. This immediately prevents us from using the existing on-wafer mm-wave antenna measurement setups. Standard on-wafer probe station is not suitable to measure the antenna radiation either, because it is a large metal piece which will greatly disturb the radiation pattern. Besides, the contact of the on-wafer probe to the antenna input is difficult to make secure, so the vibration may cause unstable contact between the antenna and the probe when rotating the antenna to measure the radiation patterns. As a result, the measurement results are often non reproducible. Furthermore, scattering from the

probe station alters considerably the antenna radiation patterns. Finally, there is no well-developed calibration technology for the on-wafer probe.

The main disadvantage of the mm-wave antenna measurements using coax-connectors is that the dimension of an mm-wave antenna is generally smaller than most of commercially available coax-connectors. Hence, coax-connectors may bring many unwanted effects such as mismatching and spurious radiation [4]. However, the main advantage of using this measurement technique is that one can use standard Programmable Network Analyzer (PNA) without any additional measurement equipment. Moreover, the connector also provides secure connections which ensure the repeatable and stable measurement results that on-wafer probes does not. Furthermore, the mm-wave antennas we proposed have a shield to protect its radiation properties, thus the coax-connector may not have substantial influence to the antenna radiation properties.

After comparative analysis of all possible approaches, I have selected to measure mm-wave antennas using coax-connectors and to develop the calibration set-ups to calibrate out the impact of the connector on the antenna performance. The coax-connector used for the mm-wave LTCC antennas (both K-band and M-band) is the mini-smp connector. This connector works up to 65 GHz and is the smallest commercially-available connector (4.4 mm x 4.4 mm) we could find. The transition of the connector to the microstrip line is designed by the connector provider. For the K-band, this transition provides almost -20 dB reflection coefficient and 0 dB insertion loss. However, at the M-band no successful transition was designed. The best transition we could achieve only provides about -10 dB reflection coefficient and about -1 dB insertion loss (in simulation). The calibration technique is described in the section 2.4 and the post-processing techniques for the reflection coefficient measurements of differentially-fed antennas are presented in the section 2.5. The detailed measurement results of the M-band antenna can be found in Chapter 4 section 4.4 and Chapter 5 section 5.5.

For the radiated-field measurements I decided to use the standard measurement techniques which I have extended with the post-processing techniques to remove unwanted reflections from the environment. I have also used post-processing to compute the gain of a differentially fed antenna. The details of the set-ups are described in the next section, while the post-processing techniques are presented in the section 2.5.

## **2.3 Antenna gain and radiation patterns measurement setups**

To measure the antenna gain and radiation patterns, two different setups were used. The first setup is measuring the gain and radiation patterns in an anechoic chamber. The other measurement setup is measuring the gain and radiation patterns in free space, and then use time-gating technique described in section 2.5.3 to create a virtual interference free environment.

### **2.3.1 Anechoic chamber measurement setup**

Anechoic chamber is a room designed to stop reflections of electromagnetic waves to simulate an infinite-open space. This ensures that the measured antenna gain and radiation patterns will not be interfered with reflections from the side-walls of the room. Therefore, most of the measurements reported in this thesis are done in the anechoic chamber. IRCTR (International Research Centre for

Telecommunication and Radar) owns an anechoic chamber, which is called DUCAT (Delft University Chamber for Antenna Tests). This anechoic chamber has been used to measure the ASP antenna gain and radiation patterns in Chapter 3 and array PSF in Chapter 6. However, the measurement facilities in DUCAT can only measure up to 26 GHz. Therefore, the mm-wave antenna measurements reported in Chapter 4 and 5 were done in the anechoic chamber in Fraunhofer-Institut für Hochfrequenzphysik und Radartechnik (FHR). Both anechoic chambers have similar measurement setups except the one in FHR can work up to mm-wave frequencies.

Typical antenna far-field measurement setup with cylindrical scanning in an anechoic chamber is illustrated in Figure 2.1. The antenna under test (AUT) is positioned on a 360° rotational cylinder at a certain distance (in DUCAT this distance is fixed to 3.5 m with adjustable possibilities within 20cm and in FHR's anechoic chamber this distance can be varied) away from the reference antenna. The cylinder has 3 axes (X-, Y-, and rotation) and its position can be accurately controlled by the computer-controlled step motor. The reference antenna is a known characteristic antenna, and it acts as a transmit antenna.

To obtain the antenna absolute gain and radiation patterns, firstly a response calibration has been performed by directly connect the cable from Source OUT and RF IN. This determines the received power level of RF IN.

There are two methods to determine the gain of AUT. The first method is by measuring received power of the AUT at the broadside and compensates the reference antenna gain and free space loss, and then the absolute gain of the AUT at broadside can be determined. However, this method is less accurate as firstly the nominal gain of the standard gain horn may not be very accurate; secondly, the antennas may not be accurately aligned at their broadside thus the nominal reference antenna gain may not be used. A better method would be to use the 3-antenna method discussed in section 2.5.1. This is a robust antenna absolute gain measurement technique and does not need to know the absolute gain of each antenna.

After the broadside absolute gain is obtained, it can be used to calibrate the radiation patterns. The radiation patterns is measured by rotating the cylinder to measure the received power of the AUT at different angle and level all the received power at different angle such that the broadside received power is equal to the gain of the AUT previously measured. In such way, the absolute radiation patterns of the AUT can be obtained. Figure 2.2 (a) shows the measurement setup of antenna far-field measurement in DUCAT. Figure 2.2 (b) shows the antenna far-field measurement setup in FHR.

The antenna array measurement setup is shown in Figure 2.2 (c). To obtain multi-channel array measurement data, the 24-port switch is used together with the network analyzer. The target is located about 0.8m away from the array, and is supported by foam to reduce the reflection from the support. To have the most accurate result, full 2-port calibration using the e-cal set has been performed over all used switch ports. The measured raw data of each channel is then processed by the imaging algorithm discussed in Chapter 6 to generate the point spread function (PSF) of the array. This PSF can then be used to evaluate the array performance.

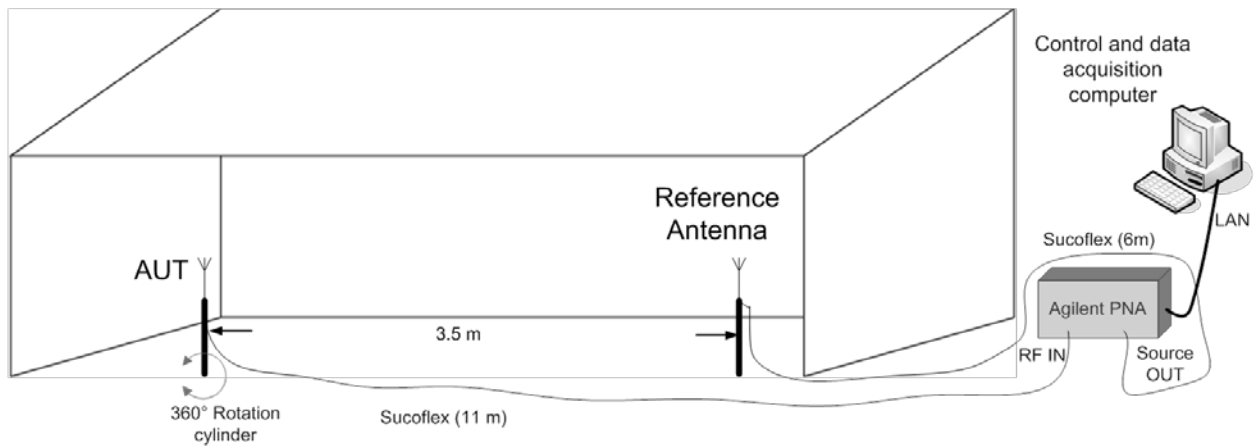
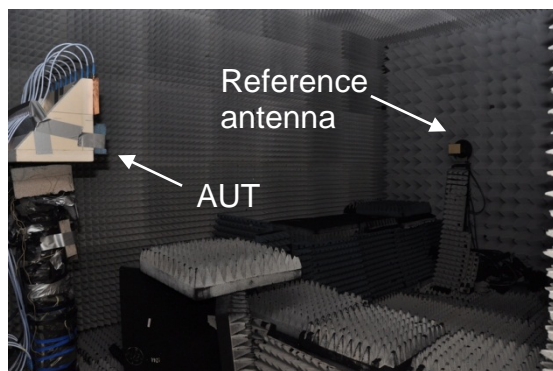
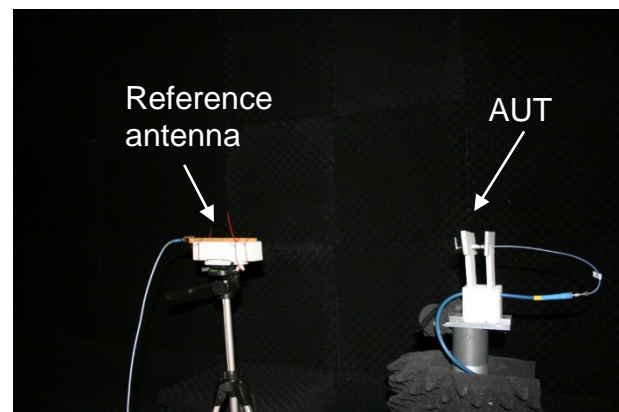


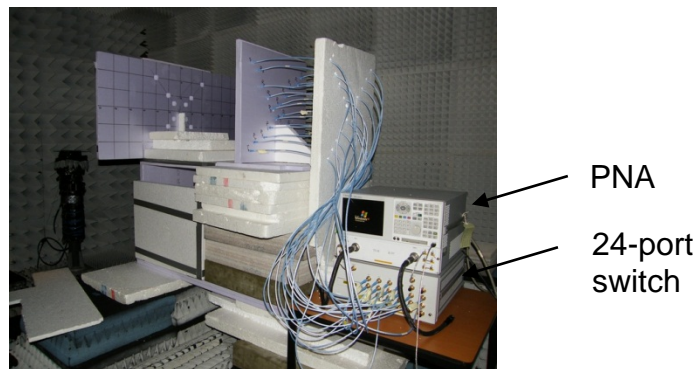
**Figure 2.1 Antenna far-field measurement setup with the cylindrical scanning**



(a) Antenna measurement setup in DUCAT



(b) Antenna measurement setup in FHR



(c) Array PSF measurement setup

**Figure 2.2 UWB antenna array PSF measurement setup in anechoic chamber (a) Antenna measurement setup in DUCAT (b) Antenna measurement setup in FHR (c) Array PSF measurement setup in DUCAT**

### 2.3.2 Free space measurement setup

Although anechoic chamber is widely used in antenna measurement and it does provide many advantages, the major drawback is that an anechoic chamber is very expensive, especially in the mm-wave frequency range. And even in an anechoic chamber the interference cannot be completely removed. One distinct feature of

impulse UWB system is that it deals pulses that have limited length in time. As a result, it is possible to measure the antenna in free-space and use time-gating technique to create a virtual interference free space. This avoids using expensive anechoic chamber and the measurement environment can be fairly easy to setup. An example free space measurement setup is shown in Figure 2.3. The details of data post-processing technique needed for the free space measurement setup are discussed in section 2.5.3. This measurement setup has been used in Chapter 5 to measure the M-band antenna radiation characteristics before we have access to an mm-wave anechoic chamber.

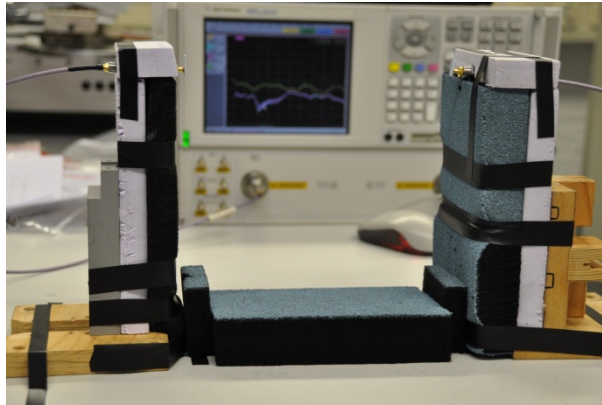


**Figure 2.3 Example free space measurement setup**

## **2.4 S-matrix calibration technique**

The true S-matrix of the device under test (DUT) is always embedded in errors caused by different sources (Figure 2.4). Some errors are repeatable and predictable over time and temperature. Such errors can be removed, whilst other errors (i.e. random errors) cannot be removed but can be reduced by averaging, using narrow IF bandwidth, or increasing power level [10]. The removable errors can be modeled as error boxes shown in Figure 2.4. The characteristics of the error boxes can be characterized by known standards. One of the most popular standards is the short-open-load-thru (SOLT) standards. The error boxes are then characterized by connecting the short, open, and matched load to Port 1 and Port 2 of the PNA respectively, and connecting Port 1 and Port 2 with a thru. After that the true S-matrix can be derived by de-embedding the error boxes from the measured S-matrix. This calibration technique is frequently used in micro-wave antenna measurements and array measurements. However, it is difficult to realize the perfect match load, thus the calibration in SOLT standard are normally limited to certain coaxial-type connectors.

Another popular calibration technique is the thru-line-reflect (TRL) calibration technique [11]. This technique requires 1) a short thru (in theory zero length, but in practice the length of thru should be long enough such that the launch spacing is larger than two wavelengths to avoid coupling between launchers), 2) a line that does not equal to half wavelength (and is normally quarter wavelength longer than the thru), and 3) an arbitrary reflect (such as an open or a short) [12]. The wavelength here refers to the center frequency of the operational band. These standards are easy to manufacture and can be applied to wide range of devices. Therefore, we have developed and manufactured the TRL calibration standards for mm-wave antennas to calibrate measurement errors. The manufactured TRL

calibration standards are shown in Figure 2.5. Figure 2.5 (a) shows the TRL calibration standards of connector-microstrip (MS) line and balun. Figure 2.5 (b) shows the manufactured TRL calibration standards particularly for connector-MS line. The connector-MS line TRL calibration standards are not only be used for calibration but also was used for checking the connector-MS line transition.

The de-embedding procedure using the TRL standards is briefly described below. By using the scattering transfer matrix or the T-matrix representation, the relationship between the measured T-matrix  $\mathbf{T}_M$  and the T-matrix of the DUT  $\mathbf{T}_{DUT}$  can be denoted as

$$\mathbf{T}_M = \mathbf{T}_{e_a} \mathbf{T}_{DUT} \mathbf{T}_{e_b} \quad (2.1)$$

where  $\mathbf{T}_{e_a}$  and  $\mathbf{T}_{e_b}$  are the T-matrixes of the error boxes  $e_a$  and  $e_b$ , respectively.

The  $\mathbf{T}_{e_a}$  and  $\mathbf{T}_{e_b}$  are obtained by measuring the thru, line and reflect standards, the  $\mathbf{T}_{DUT}$  can be calculated by

$$\mathbf{T}_{DUT} = \mathbf{T}_{e_a}^{-1} \mathbf{T}_M \mathbf{T}_{e_b}^{-1} \quad (2.2)$$

Detailed derivation of each error term can be found in [11][13].

Due to the large bandwidth of the probing wave (typically several GHz in this thesis), it is possible to separate the connectors reflection from the TRL standards measurement. With this knowledge, we can use time-gating technique to gate out the reflection from the connector and obtain the desired antenna reflection. Figure 2.6 (a) shows an example of time domain thru reflection coefficient. The connector used here is a 2.4 mm to 3.5 mm adaptor, concatenated with a 2.92 mm to mini-SMP connector. Four distinctive pulses can be identified. The first two reflections are corresponding to the 2.4 mm to 3.5 mm adaptor and the 2.92 to mini-SMP connector. The third one is from the mini-SMP to MS-line transition, and the fourth one is from the other mini-SMP to MS-line transition. The first three reflections are unwanted interferences to the reflection coefficient of the AUT, so time-gating such as Figure 2.6 (b) can be applied to eliminate most of the first three reflections. More details of this technique and its impact to the measured data can be found in Chapter 5 section 5.5.2.

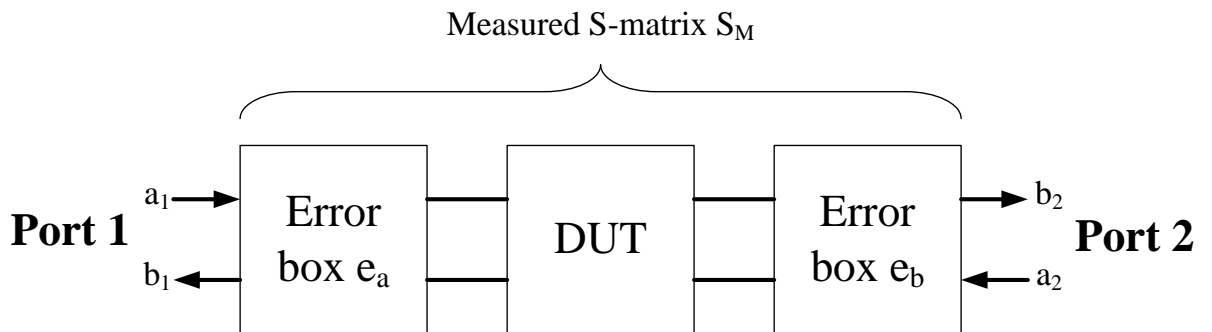
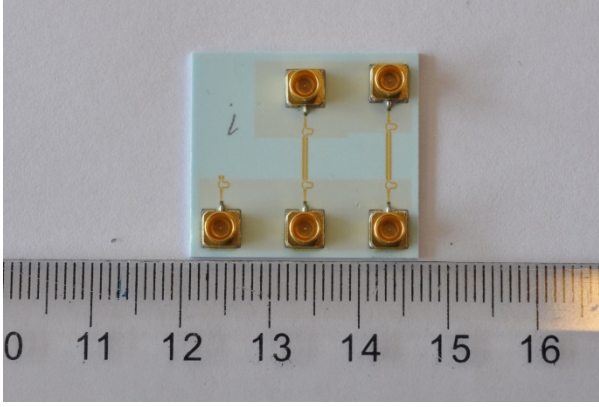
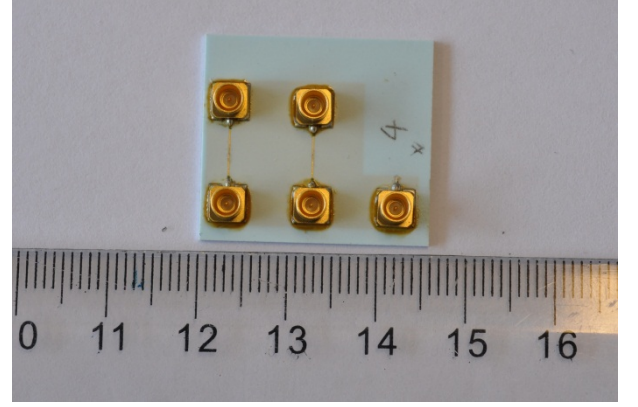


Figure 2.4 Error box model of PNA S-matrix measurement



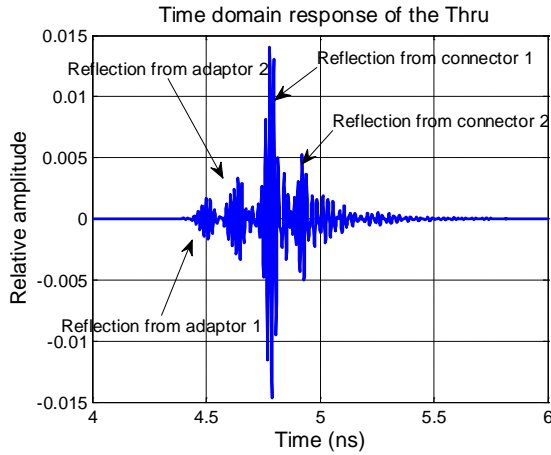


(a) TRL calibration standards of the connector-MS line and balun

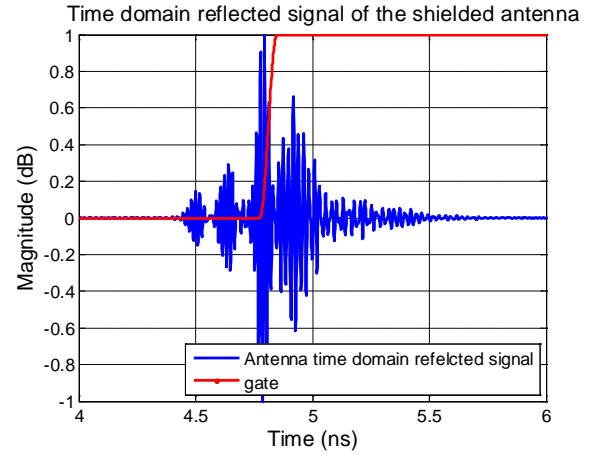


(b) TRL calibration standards of the connector-MS line

**Figure 2.5 Manufactured TRL calibration standards (a) TRL calibration standards of the connector-MS line and balun (b) TRL calibration standards of the connector-MS line**



(a) Time domain reflection coefficient of thru



(b) Time domain reflection coefficient of AUT and time-gate

**Figure 2.6 Time domain reflection coefficient (a) Time domain coefficient of thru (b) Time domain reflection coefficient of AUT and time-gate**

## 2.5 Data post-processing techniques

As discussed in section 2.3, to determine the gain of an antenna, we have used three-antenna gain calculation method. This technique will be discussed in section 2.5.1. In Chapter 4 we have developed and measured a differentially-fed antenna using the mix-mode S-matrix. This mix-mode S-matrix will be briefly described in section 2.5.2. Section 2.5.3 describes the time-gating technique, which is extensively used throughout this research.

### 2.5.1 Three-antenna gain calculation

A versatile approach to measure unknown antenna gain is the three-antenna gain measurement. The three-antenna gain measurement setup is shown in Figure 2.7. By knowing the distance  $D_1$ ,  $D_2$ , and  $D_3$ , and measure the transmission coefficients

$S_{12}$ ,  $S_{13}$ , and  $S_{23}$  (in dB), we can easily calculate the gain of three antennas  $G_1$ ,  $G_2$ , and  $G_3$  (in dBi) by:

$$G_1 = \frac{1}{2}(S_{12} + S_{13} - S_{23} - L_1 - L_2 + L_3) \quad (2.3)$$

$$G_2 = \frac{1}{2}(S_{12} - S_{13} + S_{23} - L_1 + L_2 - L_3) \quad (2.4)$$

$$G_3 = \frac{1}{2}(S_{23} - S_{12} + S_{13} - L_3 + L_1 - L_2) \quad (2.5)$$

where  $L_1$ ,  $L_2$ , and  $L_3$  are free space path loss of  $D_1$ ,  $D_2$ , and  $D_3$  (in dB) , respectively.

The major source of uncertainty of the three-antenna gain calculation method comes from the estimation of  $L_1$ ,  $L_2$ , and  $L_3$ . These distances shall be accurately measured from phase center to phase center, but normally phase center of an antenna is not easy to find and it may change as a function of frequency. This may cause a few dBi deviations to the measured antenna gain. To evaluate the accuracy of the measured antennas gains, a standard gain horn or a known-gain antenna can be used as one of the antennas. Thus, by comparing the gain measured by the 3-antenna method and its known gain, we can have a good estimation about the measurement error.

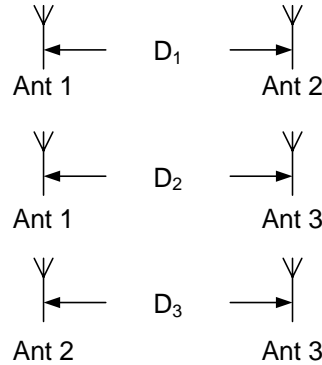


**Figure 2.7 Three-antenna gain measurement setup**

### 2.5.2 Mix-mode S-parameter measurement

Reflection coefficient is one of the important parameters of antenna characteristics. For singly-fed antennas, one-port measurement is sufficient to characterize the antenna reflection coefficient. For differentially-fed antennas, the antenna input may work in differential mode or common mode. Therefore, they are mostly characterized by the mix-mode S-parameters [14]. For a four-port device, a four-port PNA is necessary to characterize all the mix-mode S-parameters by the following relationship [15]:

$$s_{dd11} = \frac{1}{2}(s_{11} - s_{21} - s_{12} + s_{22}) \quad (2.6)$$

$$s_{dd21} = \frac{1}{2}(s_{31} - s_{32} - s_{41} + s_{42}) \quad (2.7)$$

$$s_{cc11} = \frac{1}{2}(s_{11} + s_{21} + s_{12} + s_{22}) \quad (2.8)$$

$$s_{cc21} = \frac{1}{2}(s_{31} + s_{32} + s_{41} + s_{42}) \quad (2.9)$$

where  $s_{dd11}$ ,  $s_{dd21}$ ,  $s_{cc11}$ ,  $s_{cc21}$  are differential and common-mode reflection and transmission coefficients. Since for a differentially-fed antenna only differential and common-mode reflection coefficients exist, it is possible to use a two-port PNA to measure the antenna differential and common-mode return loss using eq. (2.6) and eq. (2.8). An example of S-parameters of a differential antenna is illustrated in Figure 2.8. Since the antenna is a passive device, the S21 and S12 are identical. The S11 and S22, however, are not identical because the antenna together with the connectors is not symmetric. The synthetic differential mode reflection coefficient and common mode reflection coefficient are shown in Figure 2.9. The mix-mode S-matrix is used to measure the proposed differentially-fed antenna in Chapter 4 and more discussions of this technique can be found in section 4.4.2.

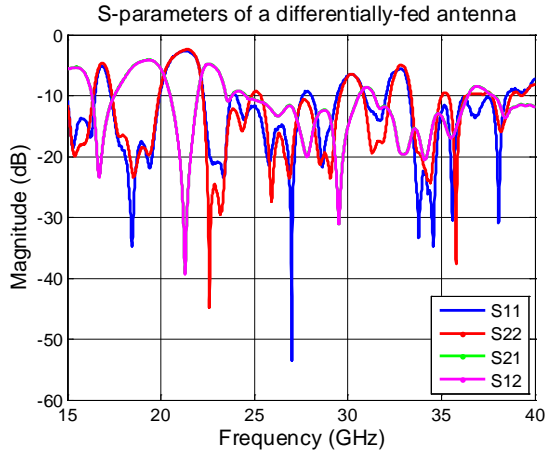


**Figure 2.8 S-parameters of a differentially-fed antenna**

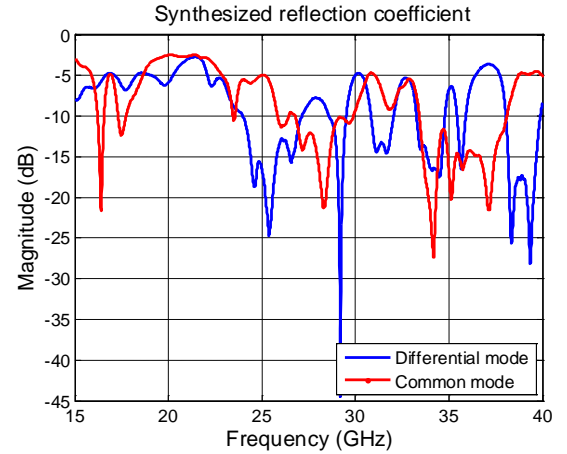


**Figure 2.9 Synthesized differential mode and common mode reflection coefficient**

### 2.5.3 Time-gating technique

Time-gating technique is the most important and most often used data post-processing technique throughout this thesis. Measurement data are inevitably contaminated by interferences even if the measurement is done in a relative interference-free area such as anechoic chamber. Thanks to the UWB nature of the system, the measured signals are all short pulses. Therefore, time-gating can be applied to eliminate interferences and create a virtual interference-free zone even in free space. The basic idea of this technique is to firstly transform the frequency domain measured raw data into time domain to perform time-gating, and then transfer back to frequency domain. However, limited measurement frequency range acted as a square window on the spectrum which introduces abrupt truncation to the spectrum. This abrupt truncation will cause severe ringing in transformed time domain signal. To smooth out the raw data, the following band pass filter is used:

$$w_f(f) = \begin{cases} w_{Hann,L}(f) & f_1 < f \leq f_2 \\ u(f) & f_2 < f \leq f_3 \\ w_{Hann,R}(f) & f_3 < f \leq f_4 \end{cases} \quad (2.10)$$

where  $f_1, f_2, f_3, f_4$  are the stop frequency 1, band pass frequency 1, band pass frequency 2, and stop frequency 2, respectively.  $w_{Hann,L}(f)$  and  $w_{Hann,R}(f)$  are the left and right hand side of a Hann window [17], and  $u(f)$  is a unity function. In addition, zero padding is used to increase the time resolution. The time domain window should also follow the same rule, that abrupt truncation should be avoided to avoid frequency domain ringing. To achieve smooth transition of the time domain window, Hann window is used and the time domain window is created similarly as the frequency BPF as following:

$$w_t(t) = \begin{cases} w_{Hann,L}(t) & t_1 < t \leq t_2 \\ u(t) & t_2 < t \leq t_3 \\ w_{Hann,R}(t) & t_3 < t \leq t_4 \end{cases} \quad (2.11)$$

where  $t_1, t_2, t_3, t_4$  are stop time 1, pass time 1, pass time 2, and stop time 2, respectively.  $w_{Hann,L}(t)$  and  $w_{Hann,R}(t)$  are the left and right hand side of a Hann window, and  $u(t)$  is a unity function. The time-gated signal then converted back to frequency domain by using FFT. Since the original spectrum is a single-sided spectrum, it can be viewed as the pre-envelop  $S_+(f)$  of the band-pass signal  $S(f)$  [15]. As a result, the band-pass signal can be obtained by

$$S(f) = \frac{1}{2} [S_+(-f)^* + S_+(f)] \quad (2.12)$$

where  $*$  denotes complex conjugate. The pre-envelop  $S_+'(f)$  of the time-gated signal can be calculated by

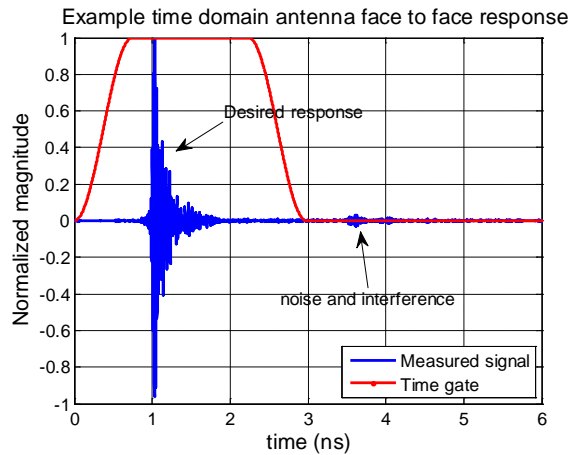
$$S_+'(f) = 2 * FFT \{ w_t(t) * IFFT \{ w_f(f) * S(f) \} \} \quad (2.13)$$

The impact of time-gating is demonstrated in Figure 2.10. A typical time domain antenna face to face measurement result (which might be the antenna gain or radiation pattern measurement results) is shown in Figure 2.10 (a) and its frequency domain counterpart is shown in Figure 2.10 (b). It can be seen in the time domain signal that there is not only the desired signal response but also interferences and noises throughout the whole time window. These interferences and noise cause ripple in the spectrum. The impact of the time-gating is that it gates out the unwanted interference but also at the same time reduces the noise. As a result, the gated spectrum is “cleaner” comparing to the original spectrum, as shown in Figure 2.10 (b).

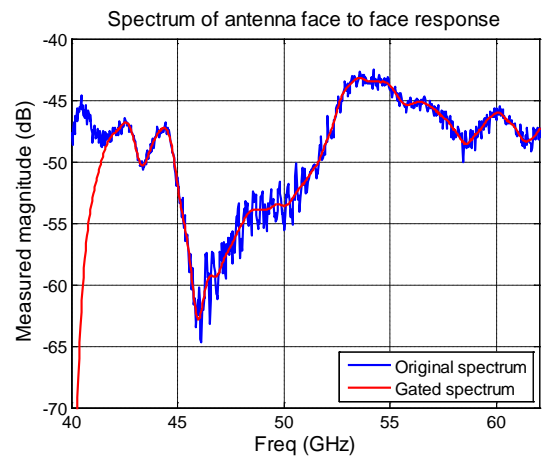
The impact of time-gating to the array received signal (Figure 2.10 (c) and (d)) is similar to what we have shown in Figure 2.10 (a) and (b). However, for the array received signal, the time-gating has another very crucial role: it removes the antenna cross talk. Without time-gating, antenna cross talk is not possible to be

completely removed and will generate severe clutters in the final image. By using the time-gating technique, the cross talk can be completely removed and consequently the image quality can be greatly improved.

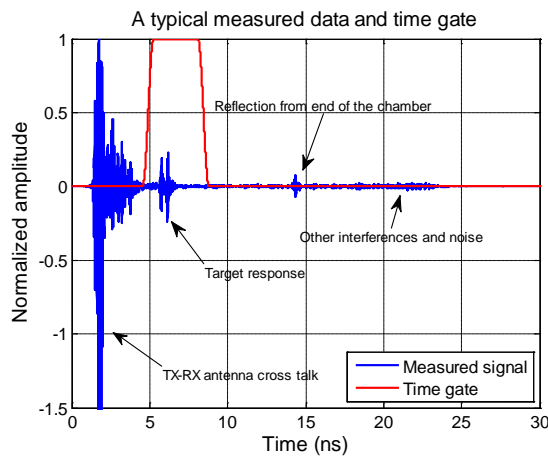
Another possible application of time-gating technique is to be used in reflection coefficient measurement. In Chapter 5 we find that the reflections from the adapters and connector-microstrip line transition are very strong, which obscures the true reflection of the antenna. Luckily these reflections can be separated in time. Thus, it is possible to use time-gating to gate out (or reduce) the unwanted reflections and keep only the desired signal (see chapter 5 section 5.5.2 for more discussion).



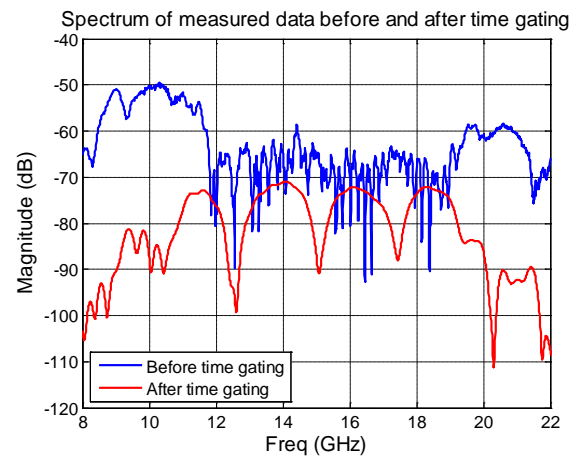
(a) Example of typical time domain antenna face to face response



(b) Spectrum of typical antenna face to face response



(c) Typical time domain array measured response



(d) Spectrum of typical array measured response

**Figure 2.10 Typical measured raw signal and its spectrum before and after time gating (a) Typical measured raw signal and time gate (b) Spectrum of the measured signal before and after time gating**

## 2.6 Conclusions

This chapter is devoted to discuss the current measurement challenges as well as introduction the measurement facilities and techniques used throughout this

research. The measurement facilities and techniques reported here are required to perform experimental verifications to the developed theories and systems which will be given in the following chapters.

To overcome the measurement challenges for the mm-wave antenna measurement and array measurement, I have developed a coax-to-microstrip transition for the M-band antenna, calibration procedure and coax calibration standards for SOLT and TRL measurements (I have used SOLT calibration for micro-wave range measurement while both SOLT and TRL calibration were used for mm-wave range calibration) and several data post-processing technique used throughout this work. The most important technique is the time domain gating technique. By using the time domain gating technique we can gate out undesired noise or interference, and “clean” the measured data for further processing. The second most important one is mixed-mode S-parameter measurement technique, which was used for the differentially-fed antenna measurements.

## Reference

- [1] M. Martínez Vázquez, S. Holzwarth, C. Oikonomopoulos-Zachos, and A. Rivera, “Wideband, Balanced-Fed 60GHz Antennas for Integrated Transceivers on LTCC Substrate”, *Proc. 4<sup>th</sup> EuCAP*, 2010.
- [2] B. Sanadgol, S. Holzwarth, A. Milano, and R. Popovich, “60 GHz Substrate Integrated Waveguide Fed Steerable LTCC Antenna Array”, *Proc. 4<sup>th</sup> EuCAP*, 2010.
- [3] C. Oikonomopoulos-Zachos, D. Titz, M. Martínez Vázquez, F. Ferrero, C. Luxey, and J. Jacquemod, “Accurate Characterisation of a 60 GHz Antenna on LTCC Substrate”, *Proc. 5<sup>th</sup> EuCAP*, 2011.
- [4] S. Ranvier, M. Kyrö, C. Icheln, C. Luxey, R. Staraj, and P. Vainikainen, “Compact 3-D On-wafer Radiation Pattern Measurement System for 60GHz Antennas”, *Microwave and Optical Technology Letters*, Vol. 51, No. 2, pp. 319-324, 2009.
- [5] R. N. Simons and R. Q. Lee, “On-Wafer Characterization of Millimeter-wave Antennas for Wireless Applications”, *IEEE Trans. on Microwave Theory and Techniques*, Vol. 47, No. 1, pp. 92-96, Jan. 1999.
- [6] J.A.G. Akkermans, R. van Dijk, and M.H.A.J. Herben, “Millimeter-wave antenna measurement”, *Proc. 37<sup>th</sup> EuMW*, pp.83-86, Oct. 2007.
- [7] Y. P. Zhang, M. Sun, and W. Lin, “Novel Antenna-in-Package Design in LTCC for Single-Chip RF Transceivers”, *IEEE Trans. on Antennas and Propagation*, Vol. 56, No. 7, pp. 2079-2088, July 2008.
- [8] A. E. I. Lammien, J. Säily, and A. R. Vimpari, “60 GHz Patch Antennas and Arrays on LTCC With Embedded-Cavity Substrates”, *IEEE Trans. on Antennas and Propagation*, Vol. 56, No. 9, pp. 2865-2874, Sep. 2008.
- [9] A. Panther, A. Petosa, M. G. Stubbs, and K. Kautio, “A Wideband Array of Stacked Patch Antennas Using Embedded Air Cavities in LTCC”, *IEEE Microwave and Wireless Components Letters*, VOL. 15, No. 12, pp. 916-918, Dec. 2005.

- [10] Agilent AN 1287-3 *Applying Error Correction to Network Analyzer Measurement*, Available: <http://literature.agilent.com/litweb/pdf/5965-7709E.pdf>
- [11] G. G. Engen and C. A. Hoer, "Thru-Reflect-Line: An Improved Technique for Calibrating the Dual Six-Port Automatic Network Analyzer", *IEEE. Trans. Microwave Theory and Techniques*, Vol. 27, No. 12, pp. 987-993, Dec. 1979
- [12] Agilent Network Analysis *Applying the 8510 TRL Calibration for Non-Coaxial Measurements*, Product Note 8510-8A, Available: [http://www.icmicrowave.com/pdf/Non\\_Coax\\_Meas\\_5091-3645E.pdf](http://www.icmicrowave.com/pdf/Non_Coax_Meas_5091-3645E.pdf).
- [13] P. J. Matthews and J. J. Song, "RF Impedance Measurement Calibration", Advanced Photon Sources LS Notes 223, available: [http://www.aps.anl.gov/Science/Publications/lsnotes/content/files/aps\\_1417957.pdf](http://www.aps.anl.gov/Science/Publications/lsnotes/content/files/aps_1417957.pdf)
- [14] D. E. Bockelmann and D. E. Eisenstadt, "Combined Differential and Common-Mode Scattering Parameters: Theory and Simulation", *IEEE Trans. on MTT*, Vol. 43, No. 7, pp. 1530-1539, July 1995.
- [15] B. Sewiolo, G. Vinci, G. Fischer, and R. Weigel, "Mixed-Mode S-Parameter Design of Ultra-Wideband Coupled-Line Baluns", *Proc. on ICEAA '09*, pp. 55-58, 2009.
- [16] S. Haykin, *Communication Systems 4<sup>th</sup> ed.*, New York: John Wiley & Sons, INC., 2001, pp. 725-727.
- [17] Oppenheim, A.V., and R.W. Schafer, *Discrete-Time Signal Processing*, Prentice-Hall, 1989, pp. 447-448.





## 3. Microwave UWB antenna development and analysis

### 3.1 Introduction

In this chapter, an antenna element for 10 GHz – 18 GHz microwave UWB near-field high-resolution imaging array is developed and analyzed. The antenna element meets demanding performance specifications imposed by the array application, such as:

- Low reflection coefficient ( $< -10$  dB) within the operational frequency band.
- Moderate gain of about 5 dBi to 10 dBi within the operational bandwidth and hemispherical uni-directional radiation patterns.
- Large front-to-back radiation ratio (FBR) ( $\sim 10$  dB) to minimize the unwanted interaction between the antenna and the RF electronics behind.
- Non-dispersive or dispersive in a controllable way at all directions of interest so it is possible to compensate the dispersion.
- Small, flat, and light, so that the array can be planar and light.

Analysis of the known antennas in Chapter 1 showed that the microstrip patch type antennas are the most suitable antenna type for near-field imaging array application as these antennas have flat profile and sufficient FBR. As discussed in that chapter, basic microstrip patch antennas are mostly narrow band [1]. By using the aperture stack patch technique, the antenna bandwidth can be extended to 50% to 70% with about 10 dB to 14 dB FBR [2]. As a result, the aperture stacked patch (ASP) antenna has been chosen as the antenna candidate for the UWB near-field high-resolution imaging array application.

The basic working principles of the ASP antennas were discussed in [2]. This type of antennas are widely used in several wideband radar applications such as [3][4][5]. However, to the author's best knowledge, existing ASP antennas use many layers [3][4] or complex aperture shapes [6][7] to achieve large bandwidth. This complicates the design and manufacturing of the antenna, and raises the cost. Furthermore, analysis on the time domain behavior of the ASP antennas and their coupling influence to the imaging array are rarely discussed in the literature. This analysis is crucial as the antenna is specifically designed for time domain imaging array. It was found that coupling alters the element sensitivity function, which might cause late time ringing and obscure the target response [13]. It also increases the sidelobe level. Therefore, we will particularly analyze these aspects of coupling behaviors in section 3.4. In Chapter 6 we discuss the 2-D antenna array built from the antennas developed in this chapter.

The chapter starts with discussion on the antenna development in section 3.2. The developed antenna was manufactured and its performances were experimentally verified and analyzed in section 3.3. Section 3.4 investigates the antenna coupling behavior. Section 3.5 concludes the chapter.

## 3.2 Novel ASP antenna design

### 3.2.1 Description of the antenna geometry

The basic antenna geometry is shown in Figure 3.1 (a) and (b). Unlike other ASP antennas which use many layers including normal PCB materials and foams, only two layers of antenna substrate and one layer of feed substrate were used. It consists of two radiating patches with length  $L_1$ ,  $L_2$ , and width  $W_1$ ,  $W_2$ . The antenna is fed by a microstrip line, and the field is coupled to the radiating patches via a radiating aperture with length  $A_L$  and width  $A_W$ .

Conventionally, the aperture-coupled microstrip antenna's matching with the feeding line is done by changing the aperture size. However, for the ASP antenna, the aperture acts as a radiator. Thus, its size cannot be varied independently [1]. The radiating aperture results in a high level of coupling which must be reduced to properly impedance match the antenna. A double fork structure was designed in which the impedance of each feed line at the aperture is nominally  $100\Omega$ . The two  $100\Omega$  lines are joined together by a reactive power combiner to form a  $50\Omega$  line which matches the source impedance [1]. The width of each feed line is calculated by the microstrip transmission line theory to obtain the desired nominal impedance.

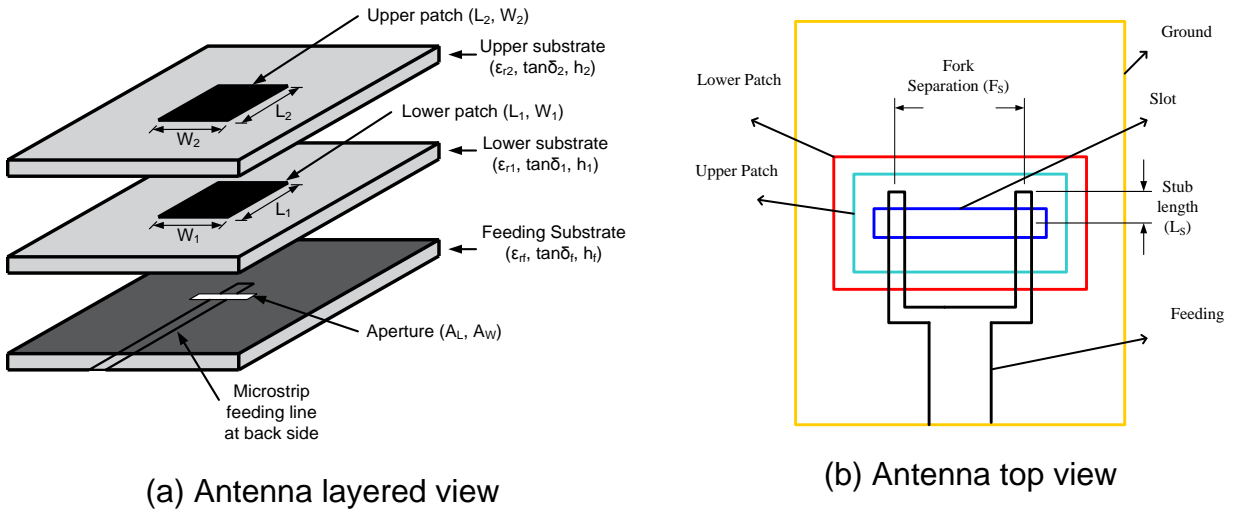


**Figure 3.1 Proposed antenna geometry (a) Antenna layered view (b) Antenna top view**

### 3.2.2 Antenna design approach

To design and optimize the ASP antenna, we first performed parametric study over the antenna geometry by using full-wave numerical models. Two numerical models based on different full-wave numerical methods were developed to perform the investigations and analysis. The first method is based on the frequency domain integral equations. The antenna structure is segmented into triangles, and each triangle is represented by an unknown equivalent surface current vector. The integral equations are solved by the Method of Moments (MoM) [9]. Commercially available EM simulator FEKO [10] was used to solve the integral equations and analyze the results. The second model was built based on Finite Integration Technique (FIT) [11], which is a time domain technique. The antenna is segmented into hexagons. The E-field and H-field on each hexagon is solved in time domain.

Commercially available EM simulator CST MWS [12] was used to solve and analyze this model.

Both antenna numerical models were verified internally by comparing the simulated results with different meshing size. For the FEKO model, non-uniform mesh was applied for different part of the structure. A meshing size of  $\lambda_g/15$  ( $\lambda_g$  is the wavelength in the substrate at 14GHz) was determined for the dielectric as the best trade-off between accuracy and computational load. A finer mesh,  $\lambda_g/30$ , was determined for the metallic part to improve the accuracy. For the CST model, a meshing size of  $\lambda_g/20$  has been determined to be the best tradeoff between accuracy and computational time. After internal check, the simulation results from both models were cross-checked against each other. Both results were very similar to each other which provided us the confidence on the accuracy of the theoretical model.

Although parametric study gave physical insight of the antenna behavior, it was difficult to obtain optimum performance by using parametric study alone because the parameters are coupled to each other. Therefore, we used optimization algorithm to aid the optimization process. With combination of parametric study and optimization algorithm approach, large bandwidth can be achieved with relatively simple and compact antenna profile. Detailed discussion and optimization is given in the next section.

### **3.2.3 Choice of substrate material and thickness**

To start the development of the antenna, the antenna substrate and feed substrate have to be determined first. According to the guidelines in [1] and [2], the dielectric constant of the antenna substrate should be as low as possible to increase impedance bandwidth and reduce the surface wave excitation. This is why plastic foams are widely used in this type of antenna. The drawback of plastic foams is that it is not easy to print metal patch on it. Thus, an additional PCB superstrate is needed, and this increases the cost. Therefore, in our design we have avoided plastic foam. The proposed antenna used two layers of commercially available Roger RT/duroid 5880 high frequency laminate with a relative permittivity  $\epsilon_r=2.2$  and loss tangent of 0.0009 @ 10 GHz as the upper and lower antenna substrate. Roger RT/duroid 5870 high frequency laminate with a relative permittivity  $\epsilon_r=2.33$  and loss tangent of 0.0012 @ 10 GHz was selected for the feed substrate. The thickness of the antenna substrate has to be thick enough to have wide bandwidth, but cannot be too thick to keep the good coupling level between patches. The thickness of the feed substrate is a trade-off between loss and spurious radiation. Thinner substrates result in less spurious radiation but more loss. We selected the thickness of the antenna upper and lower substrate to be 1.575 mm, and the thickness of the feed substrate was 0.508 mm. The length and the width of the substrate were both 17 mm in order to match the physical size of the connector.

### **3.2.4 Physical analysis of the antenna behavior**

The parametric study over the antenna's upper and lower patch width ( $W_2$ ,  $W_1$ ), length ( $L_2$ ,  $L_1$ ), aperture size ( $A_L$ ,  $A_W$ ), feeding fork length ( $L_S$ ), and fork separation ( $F_S$ ) was carried out to understand the antenna behavior. The antenna's wide-band characteristics are the result of coupled resonances which produces a loop in the impedance locus when plotted on a Smith chart. Therefore, the aim of the

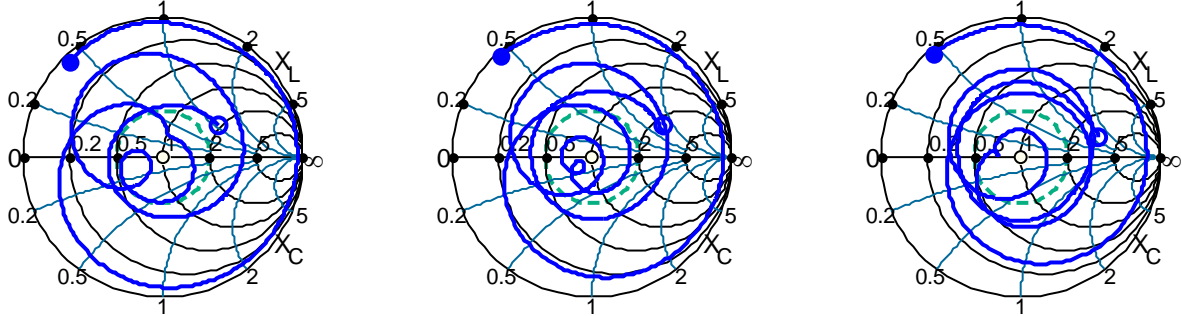
parametric study is to examine the behavior of the loops on the impedance locus and find the parameters that can help make the most part of the impedance locus within the VSWR=2 circle (reflection coefficient = -9.54 dB). The initial values of the parameters are given in appendix C.

### 3.2.4.1 Influence of the aperture length and width $A_L$ and $A_W$

To examine the influence of  $A_L$  and  $A_W$  on antenna input impedance, we plotted impedance loci on Smith Chart, shown in Figure 3.2 and Figure 3.3, respectively.

When  $A_L$  increases from 6 mm to 7 mm, the first loop becomes larger and shifts towards higher frequencies, and the second loop does not change much. When  $A_L$  increases to 8 mm, the first loop becomes small again (Figure 3.2). The increase of  $A_L$  not only changes the loop size, but also shifts the loops towards each other. These results indicate that  $A_L$  not only controls the coupling between the aperture and the lower patch but also controls the impedance matching. In addition,  $A_L$  cannot be too large, otherwise the aperture and the lower patch will be decoupled.

When we change  $A_W$  from 0.5 mm to 0.7 mm, the first loop becomes larger and stays at the same frequency range, but the second loop does not change. Since the dimension of the aperture mainly influences the coupling between the aperture and the lower patch, it can be claimed that the first loop is mainly caused by the coupling between the aperture and the lower patch because it is sensitive to change of aperture size. The second loop is insensitive to the variation of the aperture size, thus it is mainly caused by the mutual resonance between two patches.

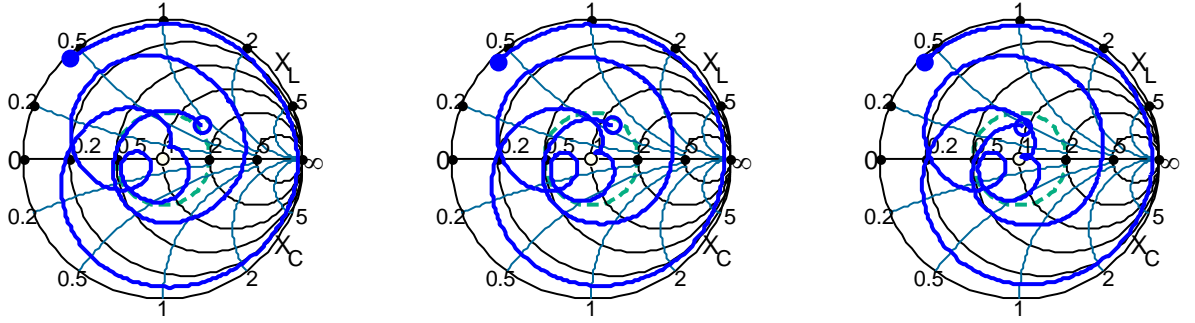


(a) Impedance locus of  $A_L = 6$  mm

(b) Impedance locus of  $A_L = 7$  mm

(c) Impedance locus of  $A_L = 8$  mm

**Figure 3.2 Impedance loci of different aperture length  $A_L$  (a)  $A_L = 6$  mm (b)  $A_L = 7$  mm (c)  $A_L = 8$  mm**



(a) Impedance locus of  $A_W$   
= 0.5 mm

(b) Impedance locus of  $A_W$   
= 0.6 mm

(c) Impedance locus of  $A_W$   
= 0.7 mm

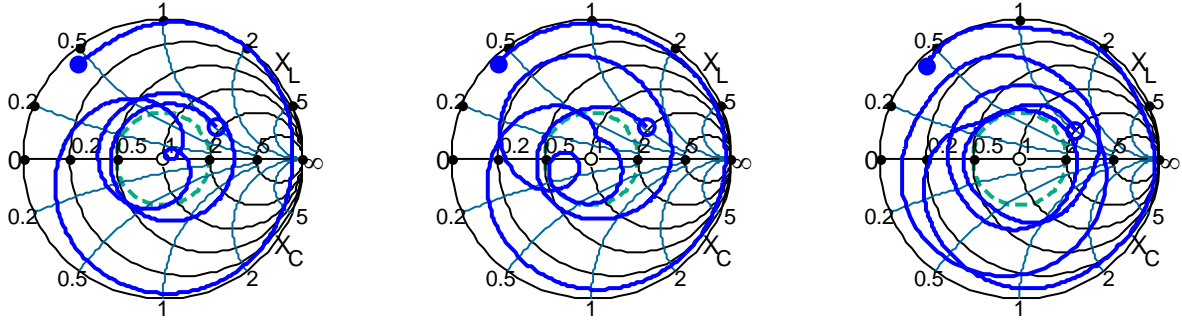
**Figure 3.3 Impedance loci of different aperture width  $A_W$  (a)  $A_W = 0.5$  mm (b)  $A_W = 0.6$  mm (c)  $A_W = 0.7$  mm**

#### 3.2.4.2 Influences of the upper ( $L_2$ ) and lower aperture length ( $L_1$ )

It was found that both the upper and lower patch widths do not play an important role on the impedance locus, while the upper and lower patch length has a greater influence on the impedance locus. This is because the current distribution on the patches is mainly along the length direction. Therefore, the patches lengths control the mutual resonance between the patches and the resonance frequency. The influences of the upper and lower patch lengths on the impedance locus are shown in Figure 3.4 and Figure 3.5.

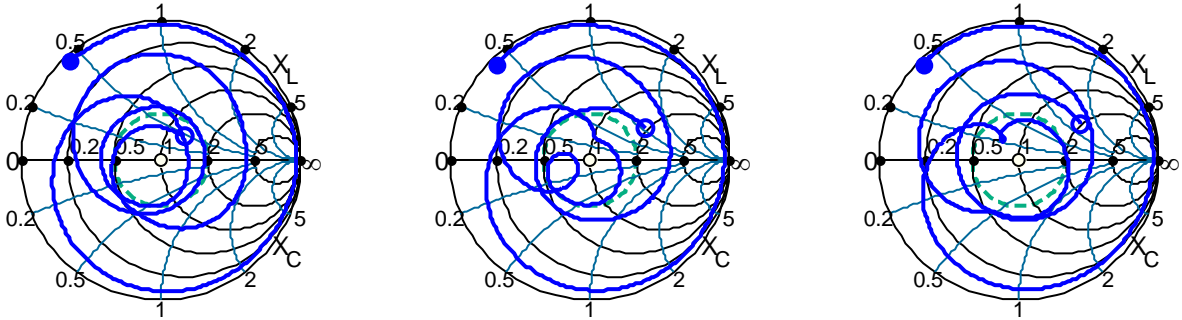
By increasing the  $L_2$  from 3.6 mm to 4.6 mm, the first loop shifts towards higher frequencies, and at the same time the second loop starts to form at lower frequencies. When the  $L_2$  increases to 5.6 mm, both loops grow larger and both are outside the VSWR=2 circle. However, we observed an opposite impedance locus behavior when  $L_1$  increases. When  $L_1$  is increases from 3.5 mm to 5.5 mm, the loops becomes smaller (see Figure 3.5). These findings gave us two important conclusions:

- 1) The similarities of Figure 3.4 (a) and Figure 3.5 (c) and Figure 3.4 (c) and Figure 3.5 (a) indicate that it is not the absolute dimensions of each patch that governs the impedance behavior, but the relative size of each patch to the other that is important.
- 2) To have large impedance bandwidth, the length of upper and lower patch should be of similar size to have balanced coupling between the patches and the patch to the aperture.



(a) Impedance locus of  $L_2 = 3.6$  mm (b) Impedance locus of  $L_2 = 4.6$  mm (c) Impedance locus of  $L_2 = 5.6$  mm

**Figure 3.4 Impedance loci of antenna with different upper patch length  $L_2$  (a)  $L_2 = 3.6$  mm (b)  $L_2 = 4.6$  mm (c)  $L_2 = 5.6$  mm**



(a) Impedance locus of  $L_1 = 3.5$  mm (b) Impedance locus of  $L_1 = 4.5$  mm (c) Impedance locus of  $L_1 = 5.5$  mm

**Figure 3.5 Impedance loci of the antenna with different lower patch length  $L_1$  (a)  $L_1 = 3.5$  mm (b)  $L_1 = 4.5$  mm (c)  $L_1 = 5.5$  mm**

#### 3.2.4.3 Influences of the feeding fork length ( $L_s$ ) and separation ( $F_s$ )

As the feeding fork does not involve in the coupling process between the aperture and the patches, its variation has a very limited influence on the loops. The major influence of the variation of  $L_s$  and  $F_s$  on the impedance locus is the distance between the two loops. The shorter the feeding stub length  $L_s$ , the closer the two loops (Figure 3.6). The fork separation  $F_s$  does not influence the distance between two loops or the size of the loops, but increasing the fork distance and rotates the position of these loops counterclockwise (Figure 3.7). This demonstrates that the variation of the feeding fork dimension mainly controls the impedance match, which has been claimed in section 3.2.1.

#### 3.2.5 Interim conclusions

The parametric study in section 3.2.4 showed that the bandwidth of the ASP antenna is mainly determined by the coupling between the aperture and the lower patch, and the resonance between the lower patch and the upper patch. On the

impedance locus, these two resonances correspond to impedance loops. To obtain large impedance bandwidth, the aperture size and the patch size need to be carefully adjusted such that the two loops are tightly located at the center of the Smith chart. The feeding stub length and feeding fork separation provided additional degree of freedom to adjust the position of the loops. Due to the high interdependency between the parameters, it was difficult to obtain the desired impedance matching by manually adjust the parameters only. Thus, optimization algorithm (particle swarm optimization (PSO) [14]) was used to adjust and optimize the parameters:  $W_1$ ,  $L_1$ ,  $W_2$ ,  $L_2$ ,  $A_i$ ,  $L_s$ , and  $F_s$ . The initial values and ranges of the parameters were obtained from the parametric study. We have used FEKO built-in PSO procedure to optimize the antenna parameters. Due to time limitation, maximum iteration of 500 was set. The optimized antenna parameters obtained by PSO are listed in appendix C. Comparing with the original geometry, an impedance matching improvement of 4 GHz was achieved (from 11.74 GHz-17.9 GHz to 9.95 GHz-20 GHz) in this study.

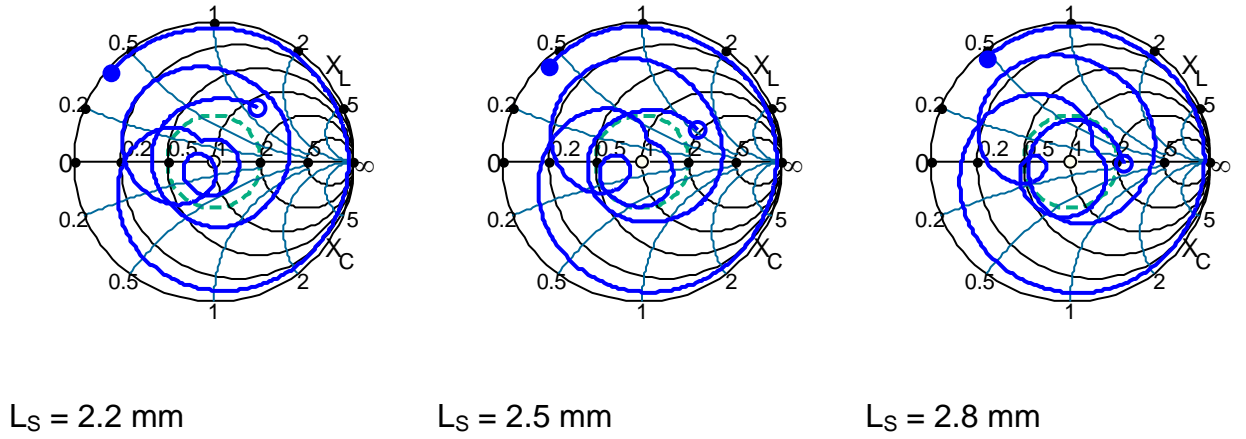


**Figure 3.6 Impedance loci of different feeding stub length (a)  $L_s = 2.2 \text{ mm}$  (b)  $L_s = 2.5 \text{ mm}$  (c)  $L_s = 2.8 \text{ mm}$**

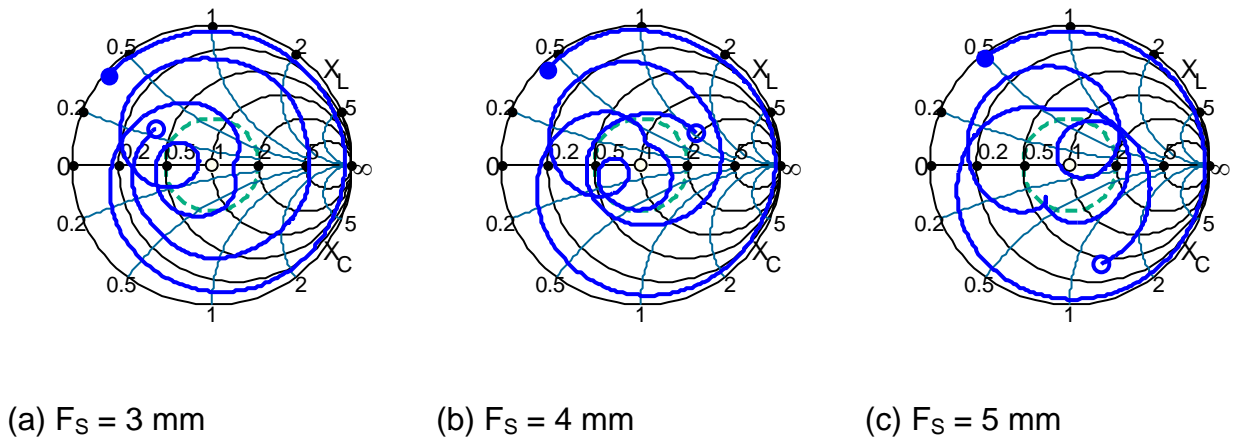


**Figure 3.7 Impedance loci of different fork separation distance (a)  $F_s = 3 \text{ mm}$  (b)  $F_s = 4 \text{ mm}$  (c)  $F_s = 5 \text{ mm}$**



### 3.3 Antenna performance analysis

The optimized antenna was fabricated for experimental verification (Figure 3.8). The feed substrate was extended 2.5 mm along the patch length direction in order to make the ground plane accessible to the connectors. The final dimensions of the antenna are 23 mm x 17 mm x 3.8 mm. These dimensions are small enough for our array application since the final array is a sparse array (see Chapter 6).

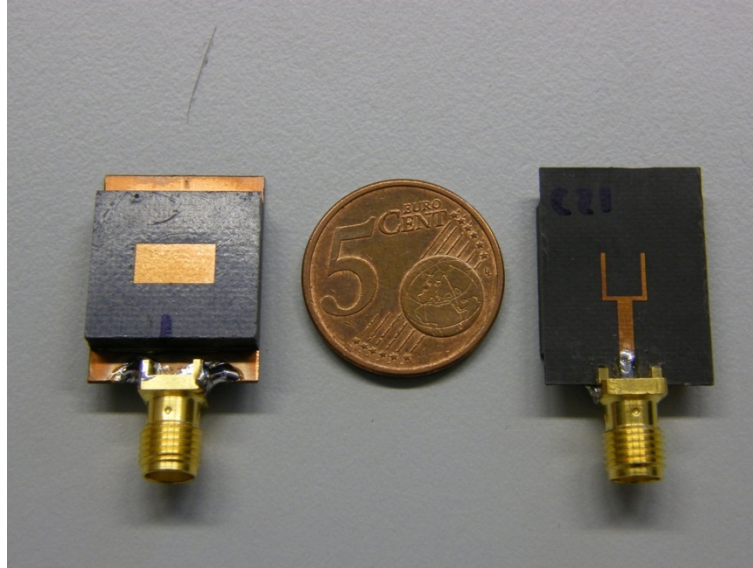
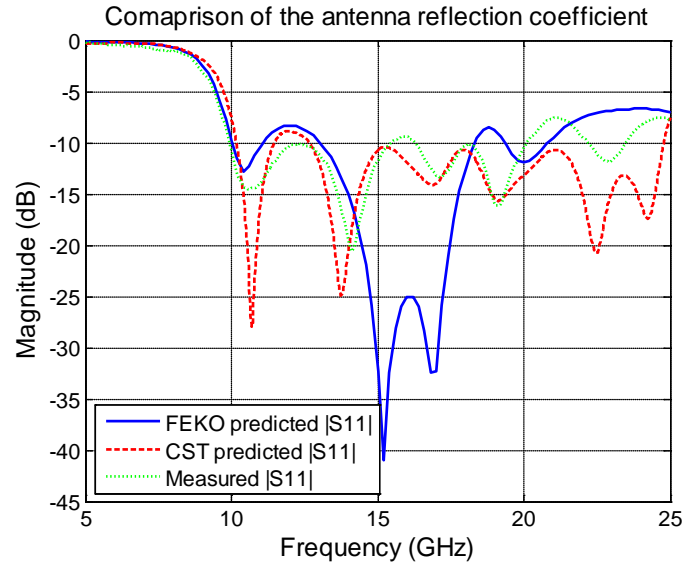


Figure 3.8 Fabricated ASP antenna

#### 3.3.1 Reflection coefficient analysis

The predicted and measured antenna reflection coefficients are illustrated in Figure 3.9. Reasonable agreement was observed between the predicted reflection coefficients (in FEKO and CST) and the measured reflection coefficient. But the reflection coefficient predicted by FEKO has deeper resonance around 14 GHz to 18 GHz. This difference was mainly due to the effect of source modeling. The FEKO model is excited by a microstrip line source, whereas the CST model is excited by a coaxial waveguide which models the connector. The similarity of reflection coefficients validates the numerical models. The measured -10 dB impedance bandwidth is essentially from 9.95 GHz to 20 GHz, which is more than the design requirement (10 GHz to 18 GHz).





**Figure 3.9 Predicted and measured reflection coefficient of the antenna**

### 3.3.2 Radiation patterns analysis

The antenna radiation patterns and gain had been measured in the anechoic chamber of IRCTR (DUCAT) described in Chapter 2 section 2.3.1. The radiation patterns were measured from 10 GHz to 18 GHz. The measurement setup is shown in Figure 3.10 where the antenna was mounted on the rotational cylinder 3.5 m against the GZD standard gain horn.

The measured gain is compared against the predicted gain (Figure 3.11 (a) and (b)). The antenna gain is calculated by the three-antenna method described in Chapter 2 section 2.5.1. The measured and the predicted broadside gain are in good agreement with each other. The broadside gain is about 5 dBi to 10 dBi in the operational frequencies. On the other hand, both FEKO and CST predicted backside gains qualitatively resemble the measured gain, but there is about 2 dB deviation between the measured and predicted backside gains. This might due to the measurement inaccuracy and numerical error. Nevertheless, the FBR is at least 10 dB. The antenna is vertically polarized with co-polar gain more than 20 dB higher than the cross-polar gain (Figure 3.11 (c)). Simulated result indicated that the antenna has a total efficiency larger than 90% within the operational band.

The normalized simulated and measured antenna radiation patterns at 10 GHz, 12 GHz, 15 GHz, and 18 GHz at the E- and H-plane are shown in Figure 3.12. The antenna radiation patterns at the H-plane are symmetric, but the radiation patterns at the E-plane are asymmetric due to the presence of the connector and the supporting structures, as Figure 3.10 (a) shows. Figure 3.13 shows the normalized radiation patterns at the E- and H-plane. The -3 dB beamwidth at the H-plane is of about 60°, while the -3 dB beamwidth at the E-plane is only about 40° because the antenna is larger along the E-plane.

To evaluate the pulse distortion with respect to radiation angle, we have used the FEKO to simulate radiated pulse at different angles at the E- and H-plane (Figure 3.14 (a) and (b)). Only  $E_y(x, y, z)$  component is compared because it is the dominate component. Due to good agreement of the FEKO simulated gain and the

measured gain, we have confidence that the FEKO simulated pulse is well representing the reality. The radiated pulses are similar in the waveform, with only difference in the amplitude. To quantitatively evaluate the dispersion of the antenna with respect to different angles, we have calculated the fidelity function of the antenna as a function of angle. The fidelity function is defined as [15]

$$F(\theta, \phi) = \max_{\tau} \left( \int_0^{T_{ref}} \hat{E}_y(\theta, \phi, t + \tau) \hat{r}(t) dt \right) \quad (3.1)$$

where  $F(\theta, \phi)$  is the value of the fidelity function,  $\hat{r}(\theta, \phi, t)$  is the normalized reference signal, defined as:

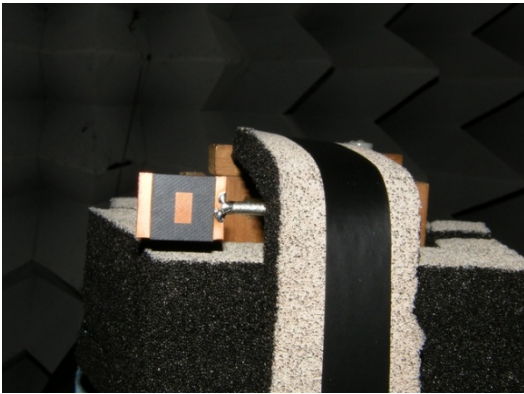
$$\hat{r}(t) = \frac{r(t)}{\sqrt{\int_0^{T_{ref}} |r(t)|^2 dt}} \quad (3.2)$$

and  $\hat{E}_z(\theta, \phi, t)$  is the normalized radiated E-field, defined as:

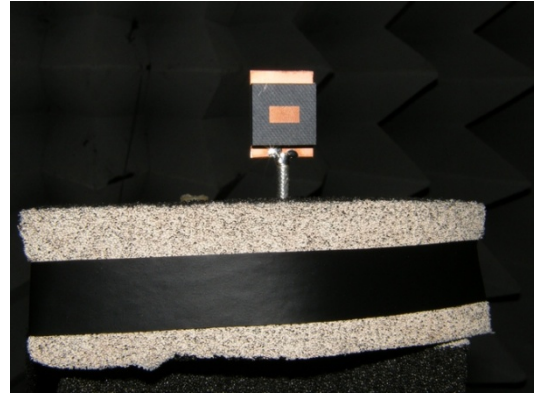
$$\hat{E}_y(\theta, \phi, t) = \frac{E_y(\theta, \phi, t)}{\sqrt{\int_0^{T_{sim}} |E_y(\theta, \phi, t)|^2 dt}} \quad (3.3)$$

where  $T_{ref}$  is the length of the reference signal and  $T_{sim}$  is the total simulation time.

The radiated pulse at the broadside was taken as the reference signal. The calculated  $F(\theta, \phi)$  is shown in Figure 3.14 (c). As the figure shows, within the area of interest ( $\theta \leq \pm 30^\circ$ ,  $\phi \leq \pm 30^\circ$ ), the value of fidelity function is larger than 0.9. This indicates that the antenna dispersion is small with respect to different angle.

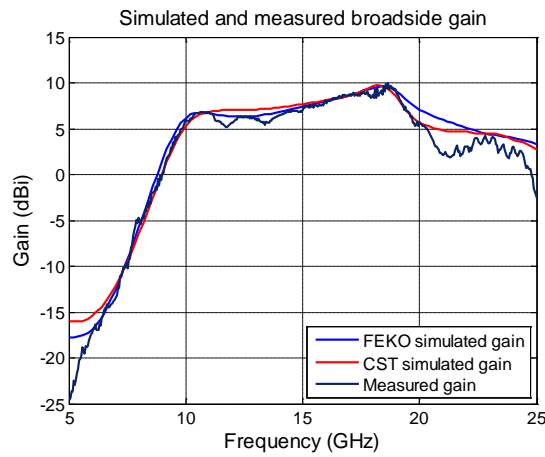


(a) E-plane

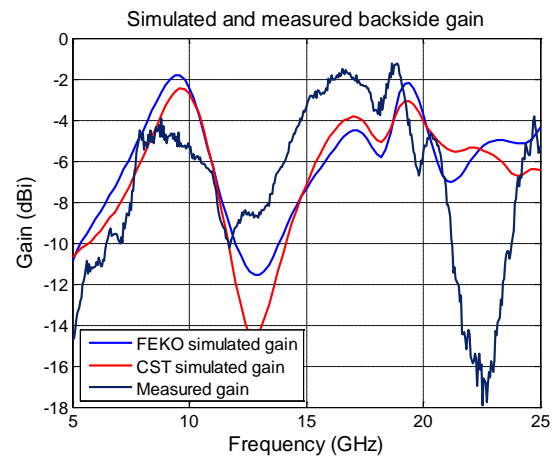


(b) H-plane

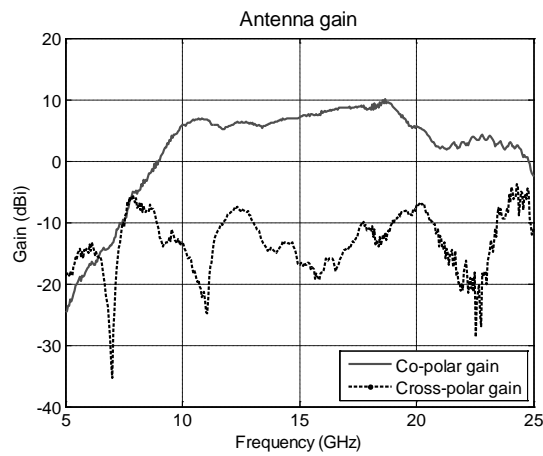
**Figure 3.10 Antenna radiation pattern measurement (a) E-plane (b) H-plane**



(a) Measured and predicted antenna broadside gain

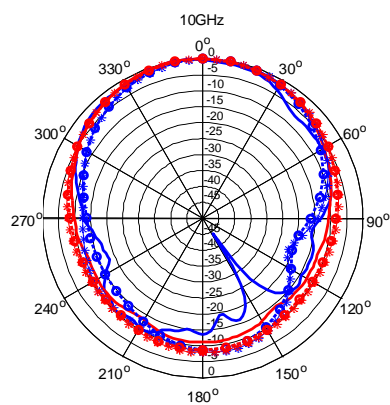


(b) Measured and predicted antenna backside gain

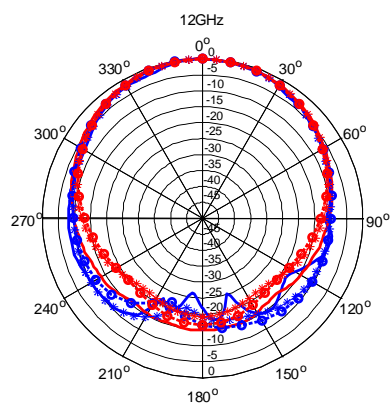


(c) Measured antenna co-polar and cross-polar gain

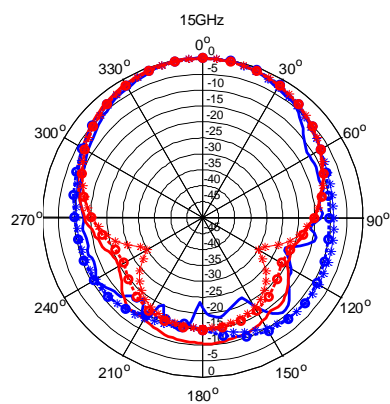
**Figure 3.11 Measured and predicted antenna gain (a) broadside gain (b) backside gain (c) co-polar and cross-polar gain**



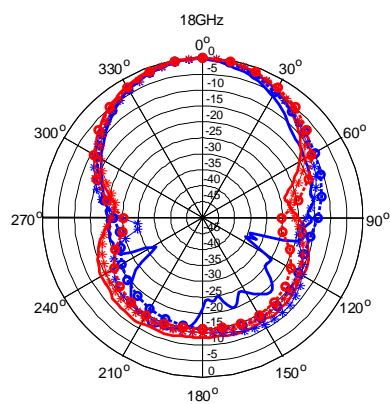
(a) 10GHz



(b) 12GHz

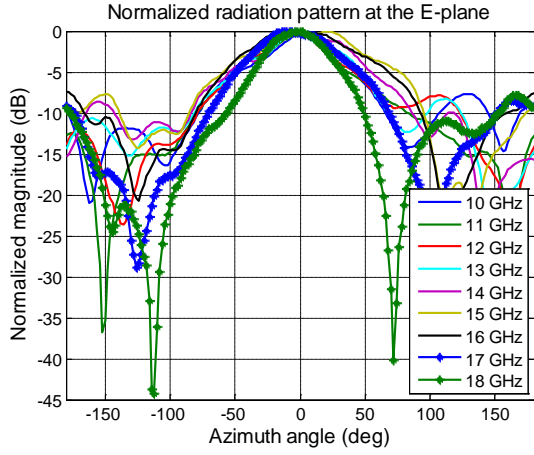


(c) 15GHz

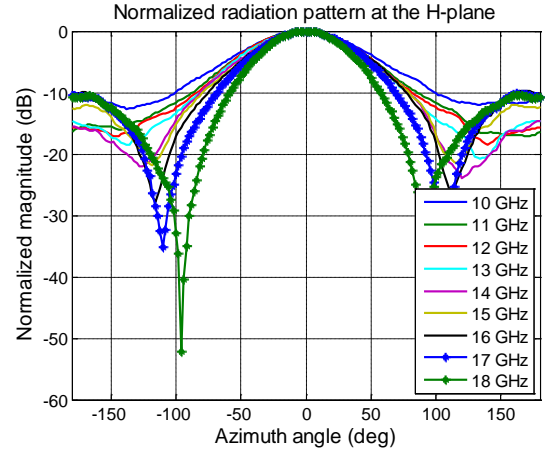


(d) 18GHz

**Figure 3.12 Predicted and measured normalized radiation pattern. Blue lines denote the E-plane radiation patterns, and red lines denote the H-plane radiation patterns. The solid lines are measured radiation patterns, “-\*-“ lines are CST predicted patterns, and “-o-“ lines are FEKO predicted patterns. (a) 10 GHz (b) 12 GHz (c) 15 GHz (d) 18 GHz**

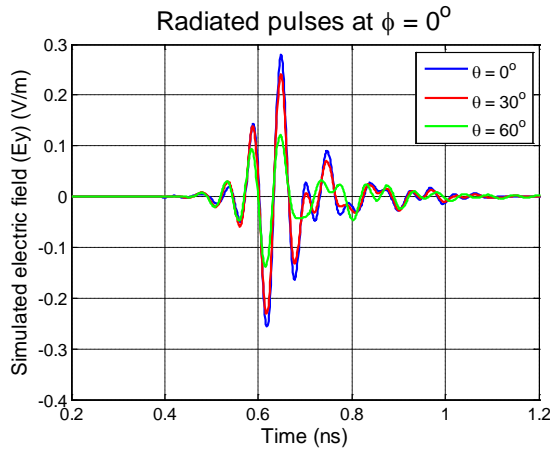


(a) Normalized radiation patterns at the E-plane

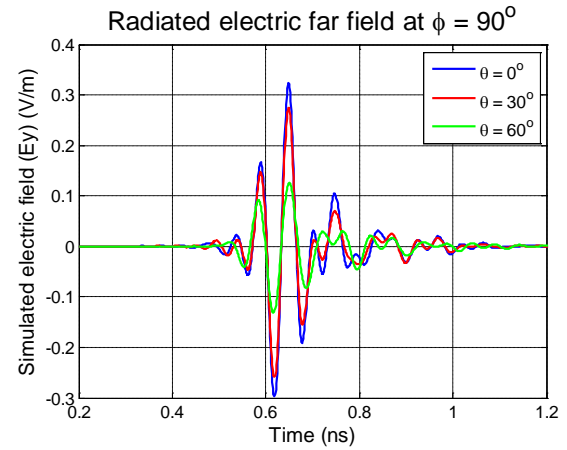


(b) Normalized radiation patterns at the H-plane

**Figure 3.13 (a) Normalized radiation patterns at the E-plane (b) Normalized radiation patterns at the H-plane**

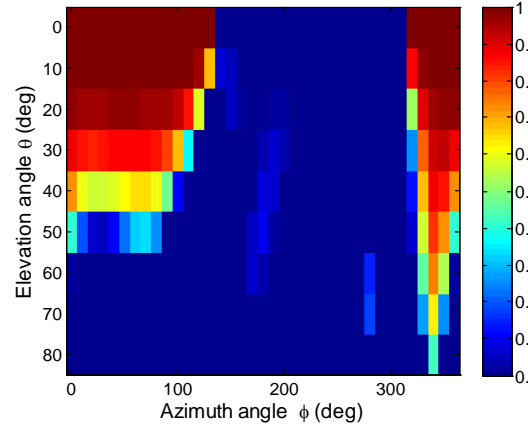


(a) E-plane ( $\Phi=0^\circ$ )



(b) H-plane ( $\Phi=90^\circ$ )

Fidelity function of the radiated pulses at different angles



(c) Fidelity function value of the radiated pulses at different angles

**Figure 3.14 Radiated pulses at different angles in the E- and H- plane and the fidelity function as a function of angle (a) E-plane (b) H-plane (c) Fidelity function value**

### 3.3.3 Time domain behavior analysis

To determine the antenna time domain behavior, the field radiated by the designed antenna (antenna under test, AUT) has been measured with the standard gain horn at each frequency as the transmission coefficient  $S_{21}$ . After that, the measured frequency domain response  $S_{21}$  has been transferred to time domain using the inverse Fourier Transform. Then we deconvolve the impulse response of the standard gain horn from the time domain  $S_{21}$  signal to obtain the impulse response of the AUT. The obtained impulse response of the AUT is shown in Figure 3.15. The  $1/e$  pulse width is about 200 ps (which is less than  $2/BW$ ) and only small ringing is observed. This is considered short pulse. Figure 3.16 shows the simulated and measured group delay of the AUT. The simulated and measured group delay show reasonable agreement, except the measured group delay has ripples due to the deconvolution. The group delay is less than 100 ps within the operational band. This indicates that the dispersion of this antenna is low and this antenna is suitable for the time domain UWB applications.

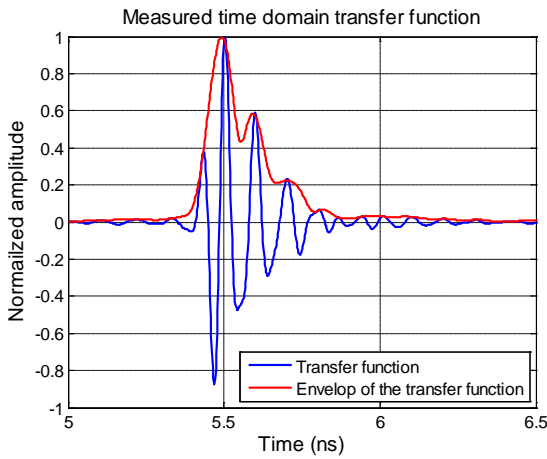


**Figure 3.15** Normalized radiated pulse of the antenna

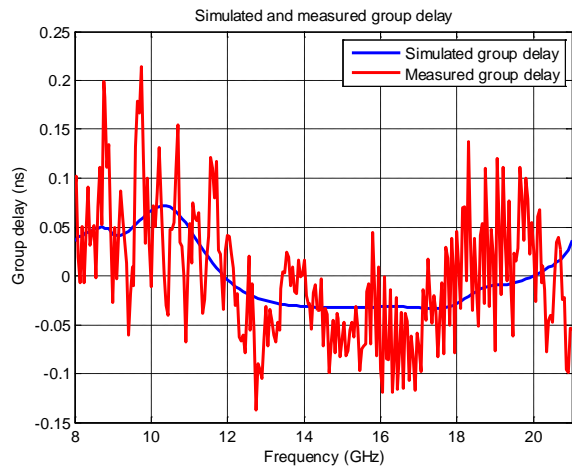


**Figure 3.16** Measured group delay of the antenna

## 3.4 Antenna coupling

### 3.4.1 Antenna coupling measurement setup

As we found in [13] (which will be described in more detail in chapter 6) that the antenna interaction in an UWB near-field imaging array causes extra late time ringing and alters the array footprint. As a result, the antenna coupling behavior is an important factor when analyzing the antenna performance. So, we analyzed the antenna coupling behavior at the H-plane (Figure 3.17 (a)) and E-plane (Figure 3.17 (b)).

The minimum separation along the H-plane is 2 cm (due to antenna physical size) and the minimum separation along the E-plane is 6 cm (due to the presence of the connector). Two different types of coupling were analyzed with respect to each plane. The first type of coupling is “antenna cross talk”, which is the leakage from the transmit antenna to the receive antenna. The setup for this coupling is shown in Figure 3.18 (a). One antenna acts as the transmit antenna and the other antenna acts as the receive antenna. The second coupling is the “scattering coupling”, which

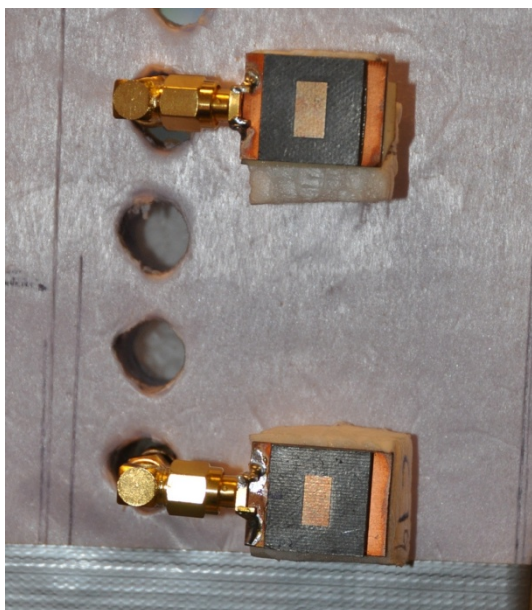
is the coupling between two receive antennas. In this measurement setup, one antenna acted as the receive antenna, and the other antenna was loaded with a matched load ( $50\Omega$  in this case). A third antenna was used as the transmit antenna, as shown in Figure 3.18 (b).

### **3.4.2 Antenna cross-talk analysis**

The measurements of antenna frequency domain cross talk are shown in Figure 3.19 (a) and (b). When the antennas are at minimum separation (2 cm along the H-plane), the maximum coupling is less than -20 dB. It can be also seen from both figures that when the antenna separation is larger than 4cm, the coupling level is linearly decreasing with distance. This indicates that the coupling before 4cm is due to antenna near-field, but the coupling after 4 cm is mainly caused by antenna far-field. By comparing both figures in respect to element spacing, it can be seen that the E-plane coupling is slightly higher than the H-plane coupling. By examine the measured and simulated coupling (Figure 3.20 (a) and (b)), we can conclude that there are two reasons that make the coupling at the E-plane stronger than that at the H-plane. The first reason is that since the current is mainly distributed along the E-field, so the E-field coupling is stronger. The other reason is that the connector also plays a role in antenna coupling, especially in the E-plane. From Figure 3.20 (a) one can observe the simulated coupling is almost identical with or without coupling. But from Figure 3.20 (b) it can be seen that the presence of connector has significant influence on the coupling especially between 10 GHz to 12 GHz. This is because when antennas are aligned along their E-plane, one antenna will be very close to the connector of the other antenna, even if antenna spacing is 6 cm.

The envelop of the time domain cross talk signal in both antenna alignments was further investigated and shown in see Figure 3.21. The antenna distance is 6 cm. Due to the UWB nature of the antenna, the cross talk only occurs in a limited time, whilst in the NB array case the cross talk occurs all the time. For the antennas which aligned along the E-plane, the cross talk decreased 33 dB/ns; and for the antennas aligned along the H-plane, the cross talk decreased 38.7 dB/ns. Both cross talk levels decreased to the noise level before 2 ns which is much earlier than the target response arrival. Since the array is mainly worked in sequential data acquisition mode (see Chapter 6), the influence of the antenna cross talk can be eliminated using time gating technique.



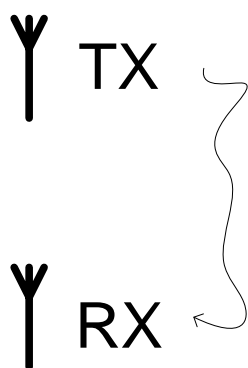


(a) Antennas aligned along the H-plane

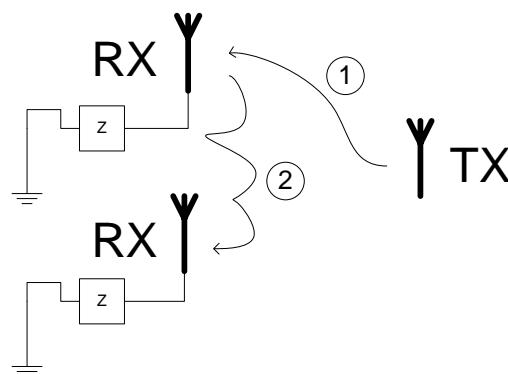


(b) Antennas aligned along the E-plane

**Figure 3.17 Measurement setup for antenna aligned along their H-plane or E-plane (a) antenna aligned along the H-plane (b) antenna aligned along the E-plane**



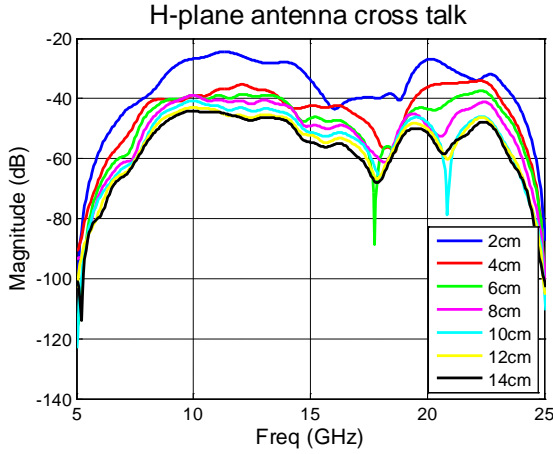
(a) Antenna cross talk measurement setup



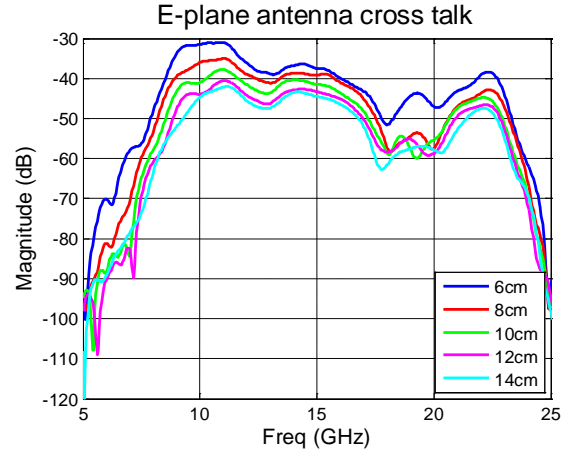
(b) Scattering coupling measurement setup

**Figure 3.18 Measurement setup of the antenna cross talk and scattering coupling (a) Antenna cross-talk measurement setup (b) Scattering coupling measurement setup**



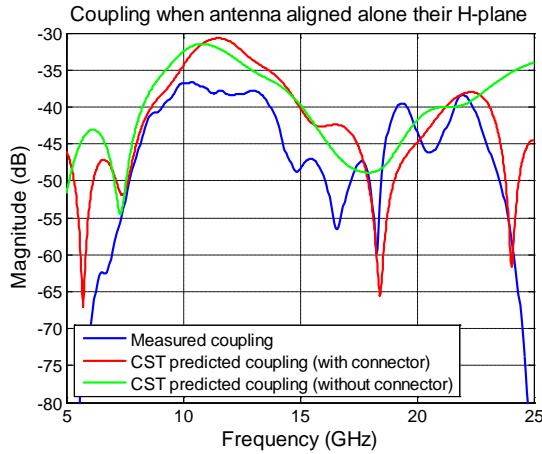


(a) H-plane antenna cross talk

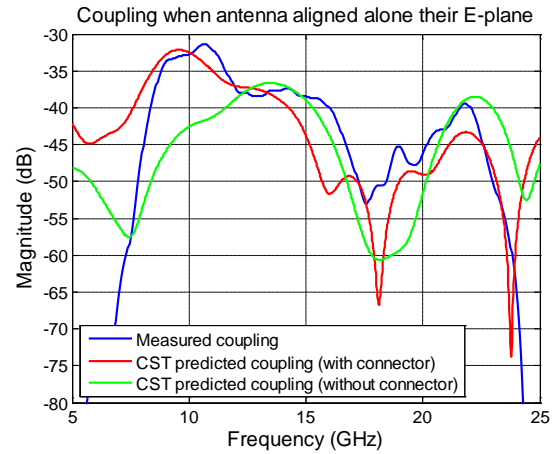


(b) E-plane antenna cross talk

**Figure 3.19 Measured antenna cross talk level (a) Antennas are aligned along the H-plane (b) Antennas are aligned along the E-plane**



(a) Measured and simulated coupling when antennas were aligned along their H-plane



(b) Measured and simulated coupling when antennas were aligned along their E-plane

**Figure 3.20 Measured and simulated antenna coupling when antennas were aligned along their H-plane and E-plane (a) Antennas were aligned along their H-plane (b) Antennas were aligned along their E-plane**

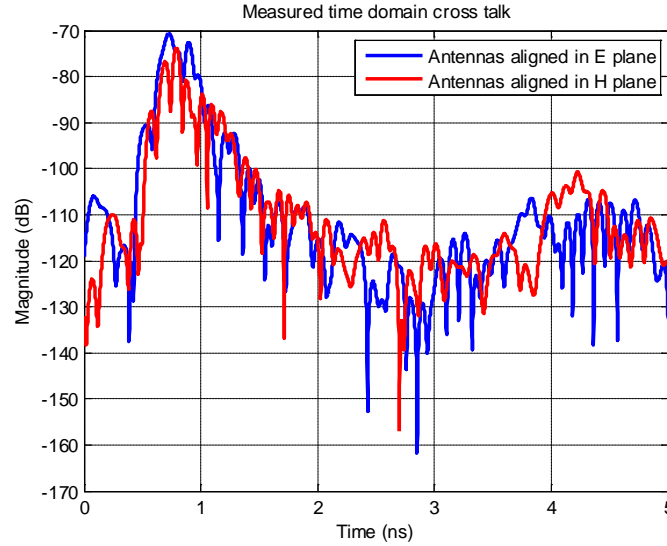
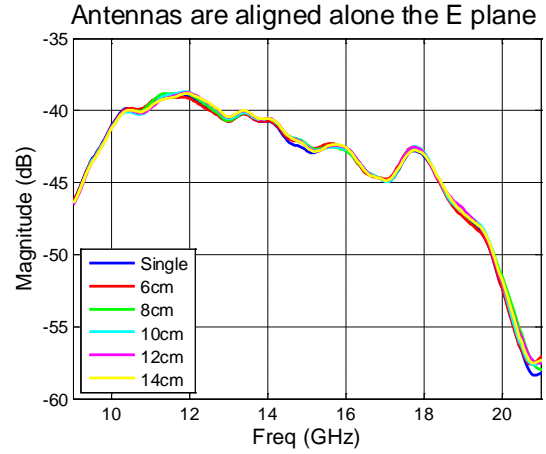
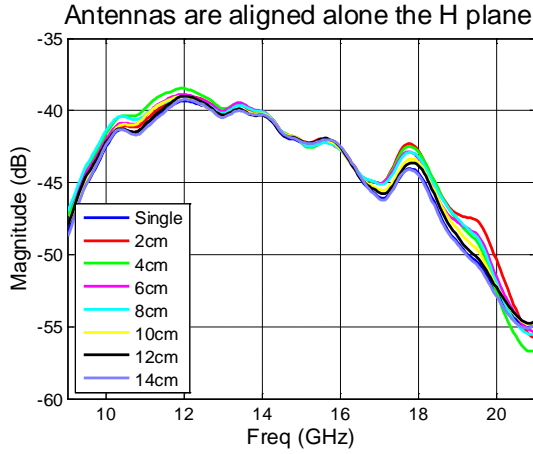


**Figure 3.21 Envelop of time domain cross talk**

### 3.4.3 Antenna scattering coupling

When an EM wave impinging on an element in an antenna array, part of the energy will be absorbed by the load and the other part will be re-scattered into free space, and picked up by adjacent elements. We defined this as “scattering coupling”. In UWB near-field imaging array, this type of coupling may alter the footprint and cause after time ringing as we found in [13]. In this research, such coupling is more important than “antenna cross talk” coupling because the latter can be eliminated by time gating when the target is sufficiently far away from the array. On the other hand, the scattering coupling (which is very close to the target response) is not possible to eliminate. Although background subtraction may alleviate the scattering coupling, due to system stability the scattering coupling cannot be completely subtracted.

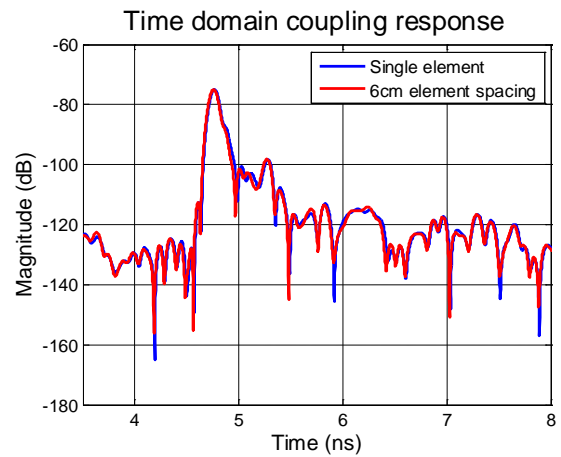
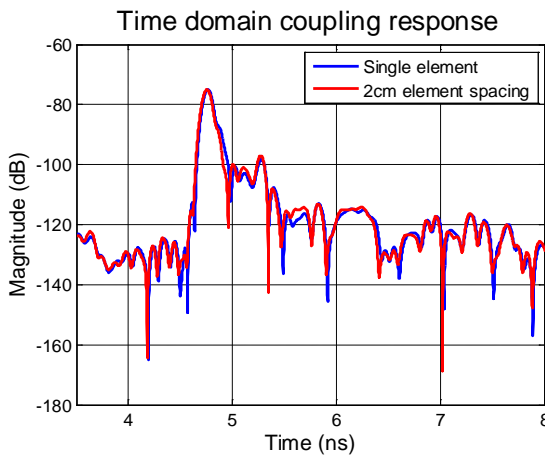
Figure 3.22 shows the antenna frequency domain sensitivity function which is obtained by operating the antenna in receive mode. We found that the received signal does not change even when the antenna is in near vicinity of other antennas. More importantly, there is no spike in the sensitivity function. The spike in the sensitivity function is the main cause of the after time ringing, thus a relatively flat sensitivity function such as Figure 3.22 will not cause long after-time ringing in time domain. Figure 3.23 demonstrates that the time domain antenna received signal does not have significant change when the antenna is in the vicinity of another antenna. As a result, it can be concluded that the coupling of this antenna is weak, and we do not expect severe performance degradation by using this antenna as element for array developed in Chapter 6.



(a) Antennas are aligned along the H-plane

(b) Antennas are aligned along the E-plane

**Figure 3.22 Scattering coupling when the antennas are aligned along the E- and the H-plane (a) Antennas are aligned along the H-plane (b) Antennas are aligned along the E-plane**



(a) Time domain received signal of a single element and two elements separated 2cm apart along their H-plane.

(b) Time domain received signal of a single element and two element separated 6cm apart along their E-plane

**Figure 3.23 Time domain received signal with vicinity of another antenna (a) Antennas are aligned along their H plane, antenna separation = 2 cm (b) Antennas are aligned along their E plane, antenna separation = 6 cm**

### 3.5 Conclusions

In this chapter we developed a microwave antenna element for a UWB sparse array. We developed a novel compact structure for ASP antenna. Unlike the conventional wideband ASP antennas which have many dielectric layers or complex aperture shapes to achieve large bandwidth, the proposed ASP antenna only has 3 dielectric layers and simple rectangular aperture. Although the proposed ASP antenna in this research is simplified (in respect to the layers), it still has the same operational

bandwidth. The simplified version makes the manufacturing easier and lowers the cost. To design and optimize this antenna, a combination of a parametric study and optimization algorithm approach was carried out (section 3.2). Thorough parametric study was performed over the antenna's dimensions to understand the physical behavior of the antenna as well as the relationship between each antenna dimension and the antenna performance. To perform the parametric study, accurate numerical models based on two different numerical methods were built. After the parametric study, the PSO optimization algorithm was used to perform the optimization.

The realized antenna has a -10 dB impedance bandwidth from 9.95 GHz to 20 GHz (67% fractional bandwidth), the gain is about 5 dBi to 10 dBi and total efficiency is better than 90%. The FBR is larger than 10 dB, and the -3 dB beamwidth is about  $\pm 30^\circ$  in both E and H plane. The measured antenna performance agreed well with those predicted by the numerical models. The antenna has small group delay variations in frequency domain and short impulse response in time domain. Moreover, the radiated pulse waveforms at different angles within the area of interest are similar to each other.

As the antenna element coupling within an UWB near-field imaging antenna array not only influences the element characteristic but, more importantly, causes the late-time ringing and raises the sidelobe level, the antenna coupling behavior was carefully analyzed as well. Unlike the conventional array coupling analysis which mainly focused on the coupling influence on the antenna impedance and scanning angle, the research in section 3.5 mainly focused on the antenna cross talk and coupling influence of the sensitivity function. We found that after about 2 ns, the cross-talk decays to the noise level of the receiver. Hence, if the targets are located approximately 0.5 m away the array, the cross-talk can be eliminated by using time gating. The scattering coupling, on the other hand, will always be present due to the close vicinity of the received target scattered signal and neighboring antenna scattered signal. The analysis demonstrated that the variation of the sensitivity function in frequency domain due to the scattering coupling is less than 2 dB. No late time ringing can be observed on the time domain signal.

Therefore, the findings show that this antenna element is suitable for implementing in impulse UWB imaging array.

## References

- [1] D. M. Pozar (May 1996), "A Review of Aperture Coupled Microstrip Antennas: History, Operation, Development, and Applications", Available: <http://www.ecs.umass.edu/ece/pozar/aperture.pdf>
- [2] S. D. Targonski, R. B. Waterhouse, and D. M. Pozar, "Design of Wide-band Aperture-Stacked Patch Microstrip Antennas", *IEEE Trans. on Antenna and Propagation*, Vol. 46, No. 9, pp. 1245-1251, Sep. 1998.
- [3] R. Erickson, R. Gunnarsson, T. Martin, L.-G. Huss, L. Pettersson, P. Andersson, and A. Ouacha, "Wideband and Wide Scan Phased Array Microstrip Patch Antennas for Small Platforms", *Proc. of 2<sup>nd</sup> EuCAP*, 2007.

- [4] D. Tallini, A. Galli, M. Ciattaglia, L. Infante, A. De Luca, and M. Cicolani, "A New Low-profile Wide-scan Phased Array for UWB Applications", *Proc. of 2<sup>nd</sup> EuCAP*, 2007.
- [5] R. Nilavalan, I. J. Craddock, A. Preece, J. Leendertz, and R. Benjamin, "Wideband Microstrip Patch Antenna Design for Breast Cancer Tumour Detection", *IET Microwaves, Antennas and Propagation*, Vol. 1, pp. 227-281, April 2007.
- [6] S. C. Gao, L. W. Li, M. S. Leong, T. S. Yeo, "Wide-band Microstrip Antenna With an H-shaped Coupling Aperture", *IEEE Trans. on Vehicular Technology*, Vol. 51, No. 1, pp. 17-27, January 2002.
- [7] K. P. Ray, P. V. Anob, R. Kapur, and Girish. Kumar, "Broadband Planar Rectangular Monopole Antennas", *Microwave and Optical Technology Letters*, Vol. 28, No. 1, pp. 55-59, 2005.
- [8] G. Kumar and K.P. Ray, *Broadband Microstrip Antennas*, Norwood, MA: Artech House, 2003, pp. 357-378
- [9] C. A. Balanis, *Antenna Theory: Analysis and Design*, 2<sup>nd</sup> ed., New York: John Wiley & Sons Inc., 1997, ch. 8.
- [10] <http://www.feko.info>
- [11] T. Weiland, "A Discretization Method for the Solution of Maxwell's Equations for Six-Component Fields", *Electronics and Communications (AEUE)*, vol. 31, no. 3, pp. 116–120, 1977.
- [12] <http://www.cst.com>
- [13] B. Yang, A. G. Yarovoy, and L. P. Ligthart, "Performance Analysis of UWB Antenna Array for Short-range Imaging", *Proc. 2<sup>nd</sup> EuCAP*, 2007.
- [14] J. Kennedy and R. Eberhart, "Particle Swarm Optimization", *Proc. of IEEE International Conference on Neural Networks*, p.p. 1942-1948, 1995
- [15] J. Bourqui, M. Okoniewski, and E. C. Fear, "Balanced Antipodal Vivaldi Antenna for Breast Cancer Detection", *Proc. 2<sup>nd</sup> EuCAP*, 2007.



## **4. K-band LTCC differentially-fed UWB antenna analysis and development**

### **4.1 Introduction**

In this chapter we investigate the challenges of using Low Temperature Co-fired Ceramic (LTCC) technology in mm-wave UWB antennas for ultra-high resolution imaging applications. LTCC technology has been selected for manufacturing the M-band (60 GHz to 100 GHz) imaging array. One of the reasons for this choice was intention to integrate the MMIC chips with the antenna in a single package to reduce the system cost and size. LTCC technology is considered to be suitable for this purpose [1]. LTCC technology is a multilayer technology which enables integration of passive components including antennas and filters with the MMICs. The multilayer nature of the LTCC technology also enables the possibility to realize complex 3-D structures such as vias or cavities. The LTCC materials exhibits low dielectric loss, and the low co-firing temperature (850°) makes the use of low conduction loss material such as silver or gold possible. An introduction of the LTCC technology is given in [2] and summarized in appendix B. Nevertheless, high dielectric constant of LTCC materials (typically ranging from 5 to 8) makes it difficult for UWB antenna design. The non-standardized LTCC manufacturing procedures and limitations also makes the realization of the LTCC antenna difficult. Due to these challenges, it is risky to directly design an M-band LTCC UWB antenna. Therefore, we firstly design an antenna working at lower frequency, such as at the K-band (20 GHz to 40 GHz), to evaluate possible difficulties related to the design and manufacture of the UWB LTCC antenna. This can reduce the risk of develop and manufacture the M-band LTCC UWB antenna.

The Chapter starts with discussion of the K-band antenna concepts (Section 4.2). The antenna analysis and optimization using full-wave numeric model are presented in Section 4.3. Section 4.4 describes the experimental analysis and verification of the antenna. Since the LTCC technology is not standardized yet, we have evaluated its deviation in Section 4.5. Section 4.6 draws the conclusions.

### **4.2 Antenna concepts**

#### **4.2.1 Initial antenna concepts**

There are several integrated UWB LTCC antennas described in the literature [1][3][4][5][6]. They are all omni-directional antennas while in many applications (especially in radar ones) radiation in a single hemisphere is required. Known flat antennas with low backward radiation are either narrow-band ones or use absorbing shielding to increase the bandwidth. LTCC technology however does not allow for use of absorbers. Furthermore, the majority of known antennas are single-fed antennas. Due to technological advantages in symmetric layouts of amplifier stages, differential circuit layout has become popular into the micro- and mm-wave range. The differential architecture permits several advantages such as higher linearity, lower offset, and immune to power supply variations and substrate noise [7].

Therefore, differentially-fed antennas are also become more of interest nowadays because they can directly integrated with the differential circuits.

As a starting point we took an in-house developed cavity-backed, differentially-fed elliptical dipole antenna working from 4.5 GHz to 10 GHz (Figure 4.1) [8], denoted as the “original antenna”. This antenna utilizes a multi-stair case back-shield to reduce the antenna back radiation as well as protect the antenna from external environment. It was demonstrated that this antenna has a flat gain of about 7 dBi to 12 dBi, and the FBR is larger than -10 dB. It was also shown that the radiation patterns did not change even if there were some large metal objects in the vicinity of the antenna back side. The antenna exhibits low dispersion and short after time ringing. Due to these good properties, it was desired to use this type of antenna as the base antenna for the K-band LTCC UWB antenna. Nonetheless, it is very challenging to re-design such a shielded antenna using the LTCC material.

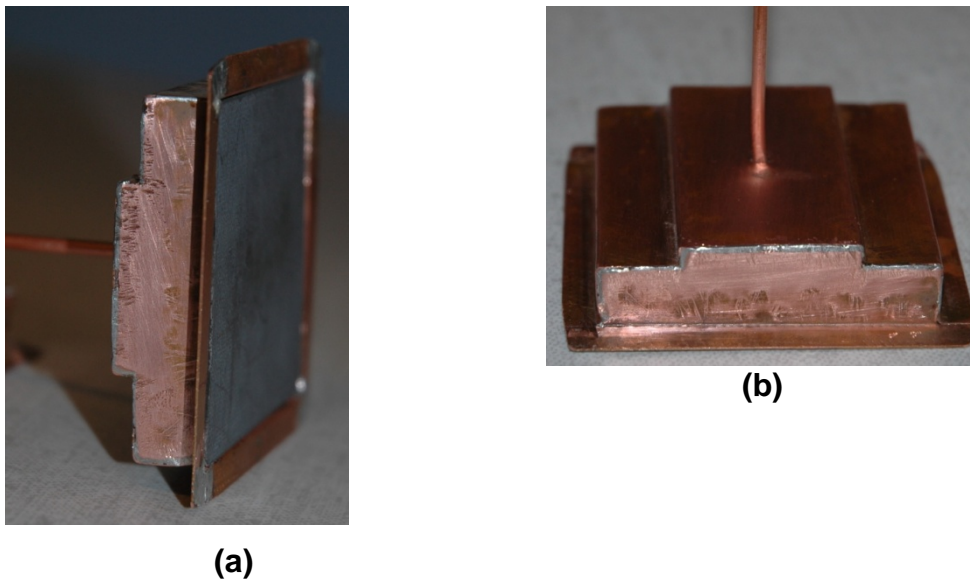


**Figure 4.1 Shielded butterfly-dipole antenna (a) Side view of the shielded antenna (b) Top view of the shielded antenna (Courtesy of [9])**

#### 4.2.2 K-band LTCC antenna concepts

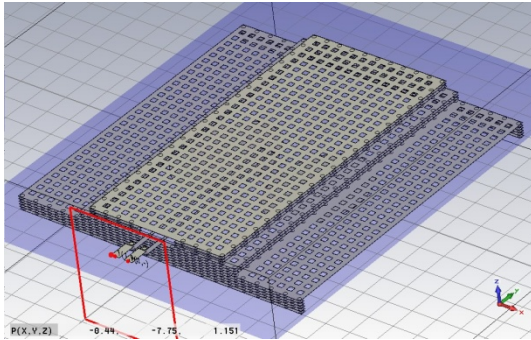
The substrate of the original antenna is very thin and has low relative permittivity ( $\epsilon_r = 2.3$ ) comparing to the LTCC material ( $\epsilon_r = 7.54$ ). Besides, the cavity was filled with air. The low material relative permittivity and air-cavity greatly reduces the impact of the material to the antenna performance. Unfortunately this is not the case for the K-band LTCC antenna. Although drilling air cavities inside the LTCC material is possible, it is difficult and expensive and is undesired to do so. Thus, the cavity will be filled with dielectric. As a result, the influence of the material of the LTCC antenna is greater than that of the original antenna, and should be carefully investigated. Additionally, due to LTCC technology manufacturing limitations, it is not possible to realize solid metal shield as the original antenna. Another challenge is the antenna feeding design. The original antenna was fed by coaxial cables passing through the metal shield. It is impossible to do so in the LTCC antenna,



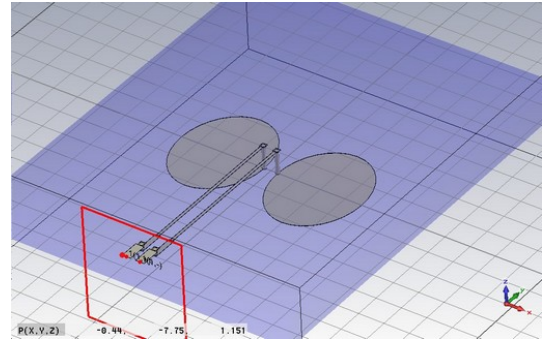
therefore, different feeding structure should be designed to properly feed the antenna.

The proposed design of K-band differentially-fed LTCC antenna is shown in Figure 4.2. Figure 4.2 (a) shows a solution to realize the metal shield in the LTCC material. The solid metal shield plate is emulated by a dense metal grid plane, and the vertical metal wall is realized by using dense via walls. In general if the grid size and the via pitch is smaller than  $\lambda_g/10$  where  $\lambda_g$  is the wavelength of the highest frequency in the LTCC material, the metal grid and the via fence can be viewed as solid metal plate and metal wall.

The concept of the antenna feeding structure is illustrated in Figure 4.2 (b). Since it is not possible to use coaxial cable to feed the elliptical dipole as it has been done in the original antenna, the feeding has been replaced by a parallel-wire transmission line passing through the top of the shield to feed the dipole. However, the simulation results showed that strong reflection occurred when the parallel wires pass through the shield. Therefore, a novel feeding concept has been proposed. In the new design, the parallel-wire transmission line did not go through the top shield, but it connected to a coplanar stripline with ground (CPSWG) where the top shield act as the ground plane of this transmission line. The CPSWG then passes through the side shield and connected to the top of the antenna with a short parallel-wire transmission line and finally connected to a coplanar stripline (CPS) as the antenna feeding. Simulation results demonstrated that by doing so the antenna can be properly excited (see section 4.3.5).



(a) Antenna shield



(b) Antenna feeding structure

**Figure 4.2 The K-band antenna concept structure (a) Antenna shield concept. (b) Antenna feeding concept**

### 4.3 Antenna investigation and optimization

Due to the complexity of the antenna structure and large bandwidth required, full-wave numerical models based on time domain Finite Integral Technique (FIT) [10] were used to perform the antenna analysis and optimization. These models were solved by commercially available software CST MWS [11]. The models were verified internally by comparing the simulated reflection coefficients with different segmentation. The impact of the LTCC material to the antenna characteristics is discussed in section 4.3.1. The analysis and optimization of the elliptical dipole is presented in section 4.3.2. The investigation of multi-stair case shield profile is presented in section 4.3.3. Realization of the metal shield is discussed in section 4.3.4, and the design of the novel feeding structure is presented in section 4.3.5.

#### 4.3.1 Impact of the LTCC material to the antenna radiation

The high relative dielectric constant of the LTCC material has significant influence on the antenna behavior. It acts like a high Q resonator, trapping the field inside the substrate instead of radiating the field out. This is illustrated in Figure 4.3, which shows the normalized absolute value of the E-field of an elliptical dipole in free space, on PCB (Roger RT/5880,  $\epsilon_r=2.2$ ), and on LTCC ( $\epsilon_r=7.54$ ), at 25 GHz. The E-field of the antenna in free space is evenly radiated towards the forward side and backward side of the antenna (Figure 4.3 (a)). Conversely, for antenna on dielectric substrates (Figure 4.3 (b) and (c)), the E-field is more concentrated into the substrate than into the free space. The major difference between Figure 4.3 (b) and (c) is that for Figure 4.3 (b), the E-field radiated into free space and substrate does not differ much, but for Figure 4.3 (c), the E-field is largely concentrated in the substrate. This demonstrated that high dielectric permittivity will distort the E-field of the antenna, thus alter the antenna radiation characteristics.

Next we compare the reflection coefficient of these antennas. When the relative permittivity of the substrate increases, the Q factor increases. This shrinks the bandwidth of the antenna first resonance. In addition, the high relative permittivity makes the antenna electrically larger, thus the first resonance frequency shifts towards lower frequencies (Figure 4.4).

The influence of the substrate thickness to the reflection coefficient of the antenna on the LTCC substrate is illustrated in Figure 4.5. Reduce the substrate thickness shifts the first resonance towards higher frequency, which is similar to the effect of lowering the relative permittivity. In addition, the width of the first resonance increases, which indicates an increase bandwidth. This behavior can be explained by the microstrip line theory. The effective relative permittivity of the microstrip line is positively related to the substrate thickness. Therefore, reduce the substrate thickness equivalently reduces the effective relative permittivity.

Figure 4.6 shows the reflection coefficient of the antenna on the LTCC substrate with different size. Shrinking the substrate size also moves the first resonance towards higher frequency, which is similar to the effect of reducing the substrate height. However, they have different physical mechanisms. This can be illustrated by comparing the normalized E-field distribution of the antenna with thin substrate and small substrate (Figure 4.7). The field structure of Figure 4.7 (a) and Figure 4.7 (b) are similar, giving similar reflection coefficient behavior. However, reducing the height of the substrate effectively decreases the relative permittivity, but shrinking the substrate size does not change the effective relative permittivity but alters the E-field structure within the substrate.

Therefore, to obtain a large bandwidth, the substrate should be thin and small. However, the shield size is solely depended on the substrate size, and small cavity will reduce the antenna bandwidth. Therefore, good balance between the substrate size and the shield size should be achieved to obtain large bandwidth.

These analyses demonstrate that the LTCC material may limit the antenna impedance bandwidth, generate high level of surface wave, and the thickness cannot be adjusted arbitrarily.

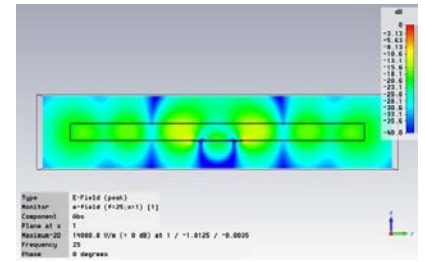
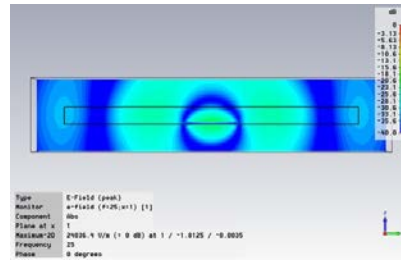


**Figure 4.3 Normalized E-field distribution of the antenna on different substrates. Frequency 25 GHz. Absolute value. (a) Antenna in the free space (b) Antenna on Roger the RT/5880 substrate (c) Antenna on the LTCC substrate**

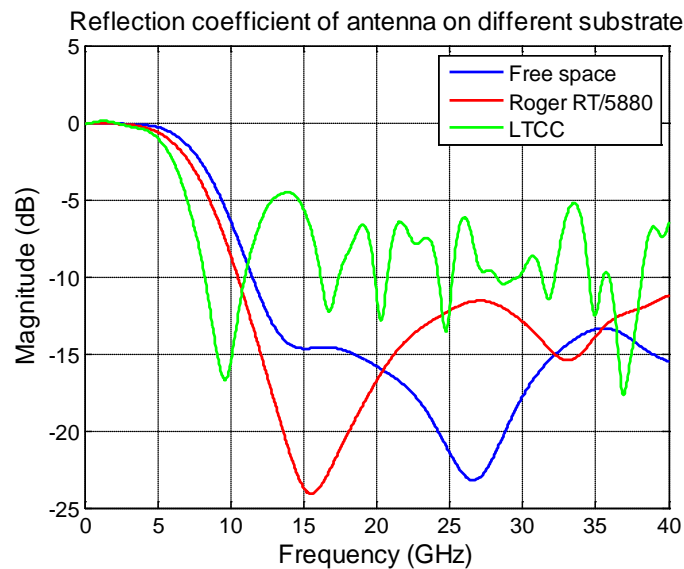


**Figure 4.4 Reflection coefficient of the antenna on different substrates**

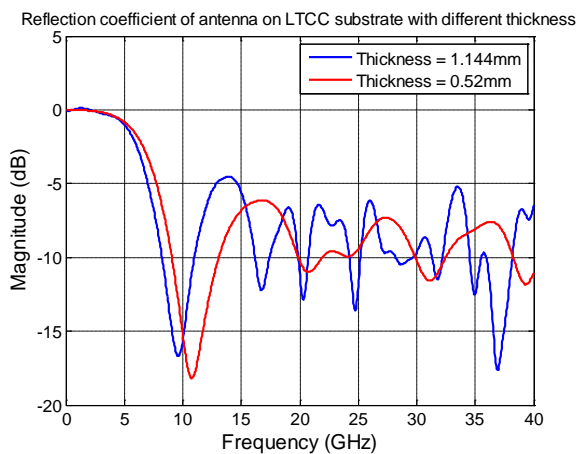


### Figure 4.5 Reflection coefficient of the antenna on LTCC substrate with different thickness

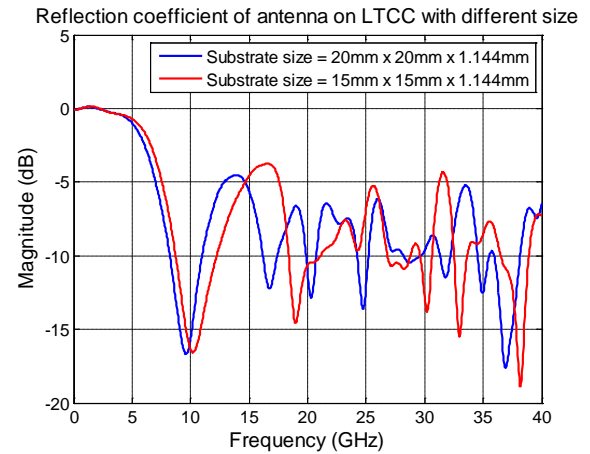
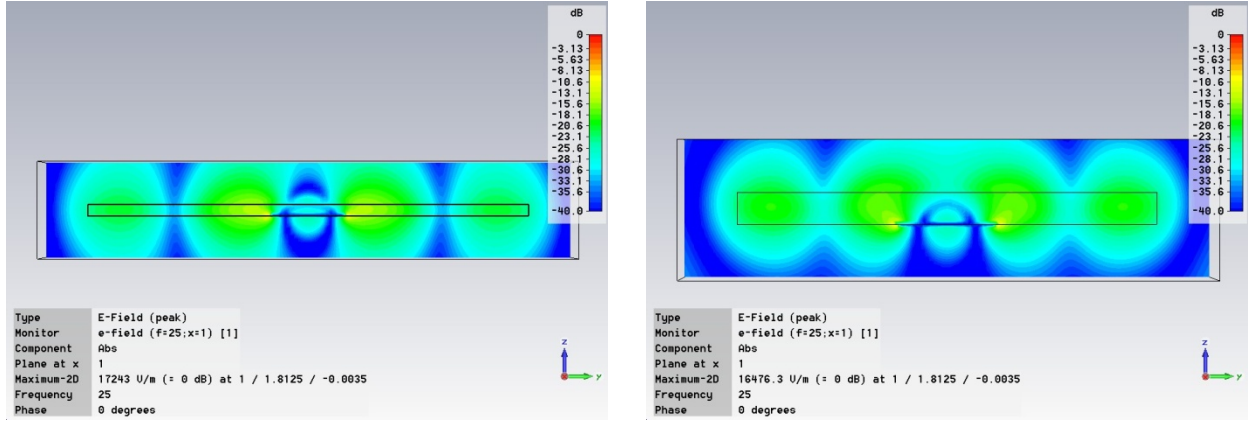


**Figure 4.6 Reflection coefficient of the antenna on LTCC substrate with different size**



(a) Normalized E-field distribution of the LTCC antenna with large, thin substrate (20 mm x 20 mm x 0.52 mm)

(b) Normalized E-field distribution of the LTCC antenna with small, thick substrate (15 mm x 15 mm x 1.144 mm)

**Figure 4.7 Normalized E-field distribution of the LTCC antenna with thin substrate and small substrate (a) Normalized E-field distribution of the LTCC antenna with thin substrate (b) Normalized E-field distribution of the LTCC antenna with small substrate. Frequency 25GHz, absolute value of the total electric field.**

#### 4.3.2 Influence of the elliptical dipole axis and separation

The first step to optimize the antenna is to understand the influence of the antenna parameters such as elliptical dipole dimensions or the shield profile. Firstly we investigate how the elliptical dipole dimensions influence the antenna performance. The Layout of the dipole is shown in Figure 4.8. The influence of the X-axis and the Y-axis length to the reflection coefficient are shown in Figure 4.9 (a) and (b). The X-axis mainly controls the resonance frequency, and the length of the Y-axis mainly controls the level of the resonance. This is because the length of the X-axis determines the resonance frequency, while the flare width (the length of the Y-axis) mainly determines the impedance of the flare.

The impedance loci of different antenna flare are shown in Figure 4.10. Enlarging the flare separation has a profound influence on the antenna input impedance. Enlarge the flare separation causes the impedance locus rotates clockwise, indicates increment in both the antenna resistance and reactance.

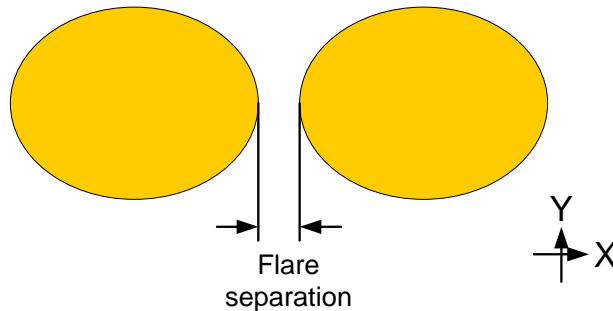


**Figure 4.8 Layout of the elliptical dipole**

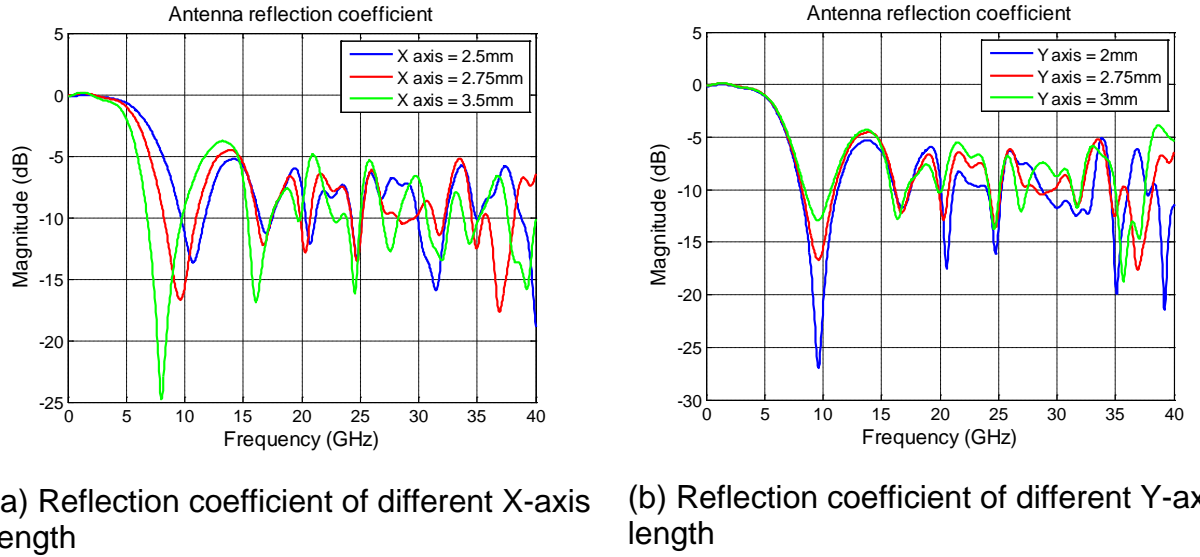


**Figure 4.9 Antenna reflection coefficient of different dipole dimensions (a) Reflection coefficient of different X axis length (b) Reflection coefficient of different Y axis length**

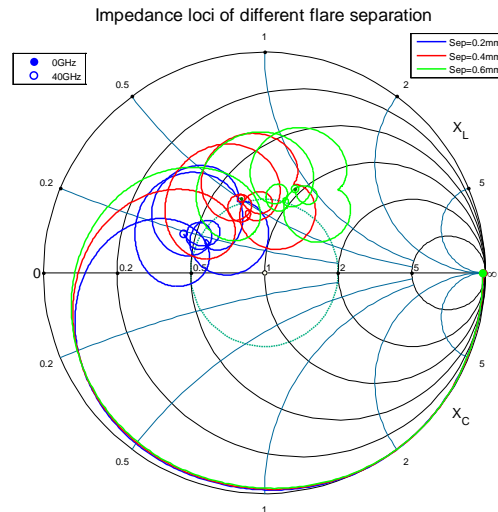


**Figure 4.10 Impedance loci of different antenna flare separation**

#### 4.3.3 Study on the multi-stair case shield

In order to achieve a uni-directional radiation and enlarge the antenna bandwidth, a multi-staircase shield (Figure 4.11) has been adopted. An investigation on how the shield profile influences the reflection coefficient is shown in Figure 4.12. Single-stair shield profile creates isolated strong narrow band resonance, because single-stair shield profile can be viewed as a high Q cavity resonator which greatly limits the antenna bandwidth. Multi-staircase shields, on the other hand, create close multiple resonances inside the shield, which increases the bandwidth of the antenna. One interesting thing to note is that the resonances of the 2-staircase profile (see Figure 4.12) are at lower frequencies, but those of the 3-staircase and 4-staircase profiles are at higher frequencies. In addition, 3-staircase profile and 4-staircase profile have

similar results. Thus, we decided to use 3-staircase profile as the basic staircase profile.

The major purpose of the shield for the original antenna is to reduce the back radiation and increase the forward radiation while keeping the dipole antenna performance [8]. For the LTCC shielded antenna, the shield has another important role. Since the relative permittivity of the LTCC material is high, high level of the surface wave will be excited. As a result, the structure will mainly radiate from the edge of the substrate instead of the antenna itself, as Figure 4.13 (a) shows. In addition, the substrate size will have profound influence on the antenna radiation patterns and gain, which makes the antenna design difficult. By adding the shield, the influence of the surface wave radiation is greatly reduced, and the antenna radiation becomes controllable, which is shown in Figure 4.13 (b).

#### 4.3.4 Realization of the metal shield

As mentioned in section 4.2.2, to realize solid metal shield in the LTCC substrate is impossible. There are two technical issues regarding this. Firstly, solid metal plates may cause camber problems. To solve this, the metal plate should be replaced by metal grids. A rule of thumb grid size is of about  $\lambda_g/10$ , where  $\lambda_g$  is corresponding to the wavelength at the highest frequency in the substrate. Therefore, we have selected the grid size as 200  $\mu\text{m}$ , which is sufficiently small ( $\lambda_g/10$  at 30 GHz is about 364  $\mu\text{m}$ ). Secondly, it is impossible to realize vertical metal walls in LTCC substrate. The vertical walls can only be realized by via fences. To perfectly emulate the solid wall, the via pitch should be as dense as possible. However, dense via fences will severely weaken the structure. As a result, the minimum via pitch should be at least 200  $\mu\text{m}$  [2], and thicker via should have larger via pitch. In addition, even though punching via usually does not take much time, too many vias still leads to long process time and higher cost (due to lower yield rate and more source of error). As a result, number of vias should be limited. To reduce number of vias and enlarge the via pitch, a connected interleaved via fence is proposed (Figure 4.14). It was demonstrated that by using this technique, the via pitch is increased from 360  $\mu\text{m}$  ( $\lambda_g/10$  at 30 GHz) to 590  $\mu\text{m}$  without compromising performance.

Figure 4.15 demonstrates that with the proposed shield realization technique, the antenna reflection coefficient only has minor change. The comparison of the forward and backward gain of the realistic shield antenna and the solid shield antenna is shown in Figure 4.16. The level of radiation of both antennas at the front side and the back side are similar. In addition, Figure 4.17 gave an example of the comparison of the radiation patterns of the antenna with solid metal shield and realistic shield at 26 GHz. It can be seen that the radiation patterns of the antenna with solid metal shield and realistic shield are almost identical. This verifies the proposed techniques and demonstrated that the via fences can be simplified by using the connected interleaved via fences.



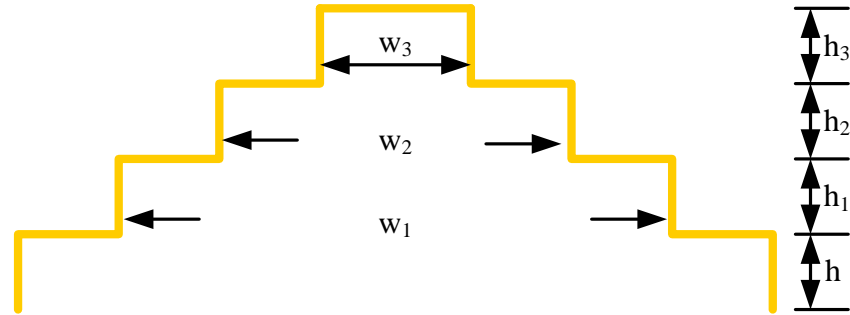


Figure 4.11 Multi-staircase shield profile

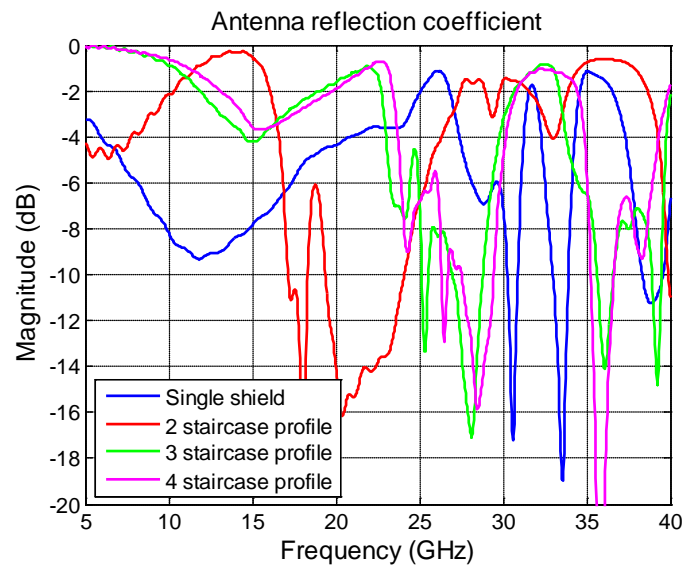


Figure 4.12 Reflection coefficient of antennas with different shield profiles

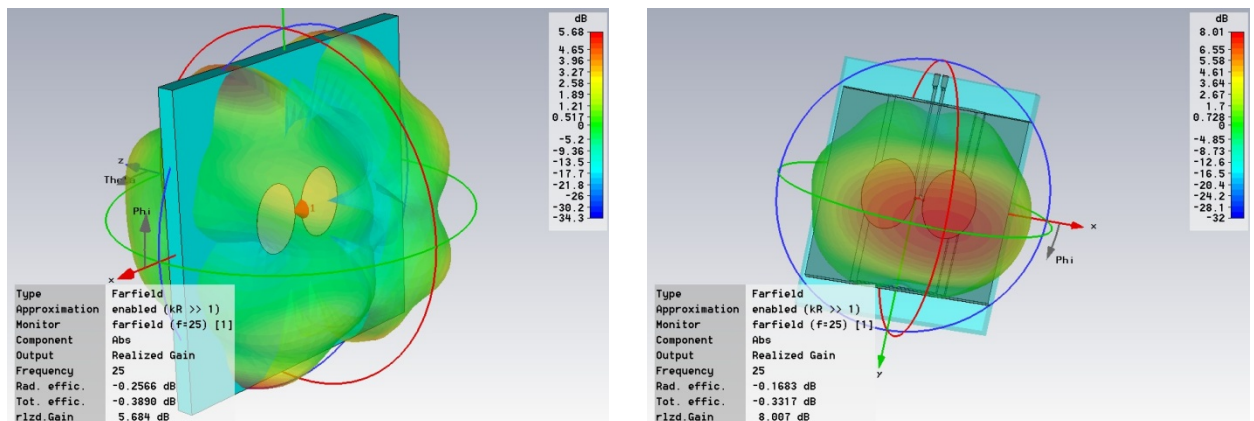
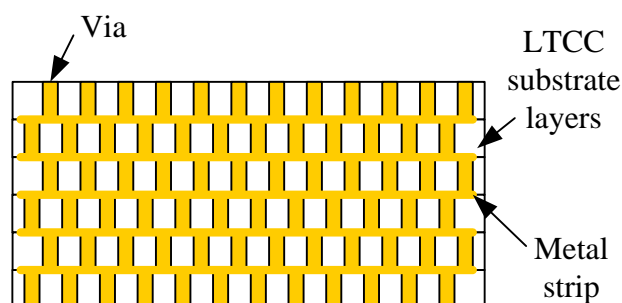
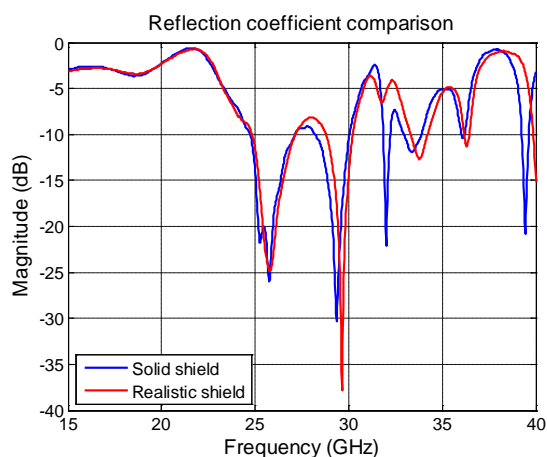


Figure 4.13 3D Radiation pattern of the antenna with and without shield at 25GHz (a) Antenna without shield (b) Antenna with shield



**Figure 4.14 Interleaved via fence**



**Figure 4.15 Reflection coefficient comparison of the antenna with solid metal shield and realistic metal shield**

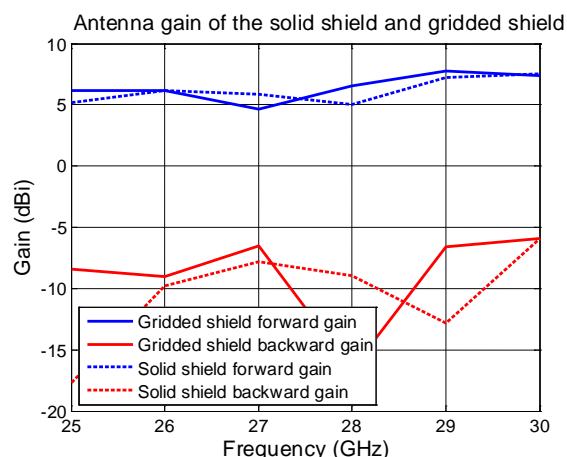
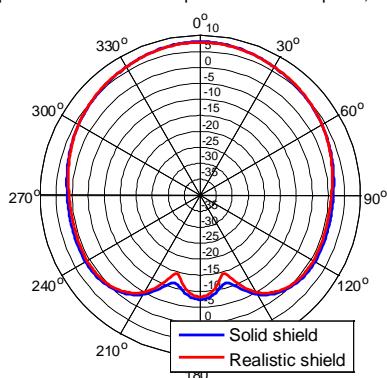


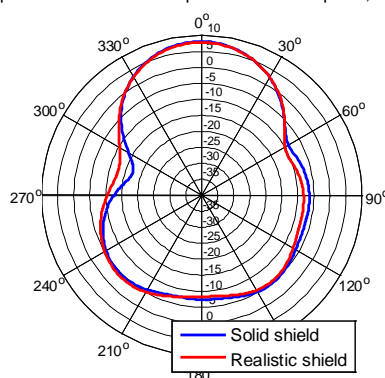
**Figure 4.16 Antenna gain of the gridded shield and solid shield**

Comparison of the radiation patterns at the E plane,  $f=26\text{GHz}$



(a) Radiation patterns comparison of the antenna with solid shield and realistic shield, E-plane, frequency = 26 GHz

Comparison of the radiation patterns at the H plane,  $f=26\text{GHz}$



(b) Radiation patterns comparison of the antenna with solid shield and realistic shield, H-plane, frequency = 26 GHz

**Figure 4.17 Radiation patterns comparison of the antenna with solid metal shield and realistic metal shield in the E- and the H-plane, frequency = 26 GHz**  
(a) E-plane (b) H-plane



#### 4.3.5 Feeding network design

As mentioned in section 4.2.2, the feeding of the antenna is done by concatenating several different types of transmission lines with the same characteristic impedance, which is shown in Figure 4.2 (b). Since the antenna is designed to be integrated with differential MMICs, the system impedance is defined as  $100\Omega$ . The feeding part is constructed as following: firstly the antenna flares are connected to a parallel-wire transmission line. The parallel-wire transmission line is then connected to a CPSWG transmission line where the top shield acted as the ground. When the CPSWG line passes through the side wall of the shield, the CPSWG line becomes CPS line. This CPS line then connects to a pair of vias to the surface of the antenna with another pair of CPS line. The CPS line on the surface serves as the final input of the antenna. The MMIC chips can then be directly connected to this CPS line using the flip-chip technique. Figure 4.18 shows the reflection coefficient comparison of the antenna with and without the feeding structure. The antenna without feeding structure is fed by an ideal source with internal impedance of  $100\Omega$  between the two flares. The simulation result demonstrated that by adding the proposed feeding structure, the antenna reflection coefficient is still mainly below  $-10$  dB within 25 GHz to 30 GHz, except from 27.1 GHz to 28.8 GHz where the reflection coefficient raised to about  $-8$  dB. The reason of this raise in reflection coefficient is due to the common mode introduced by the long CPSWG line. Despite this, the proposed feeding structure can successfully deliver most of the energy from outside the shield to the antenna flares and thus can be used to excite the antenna.

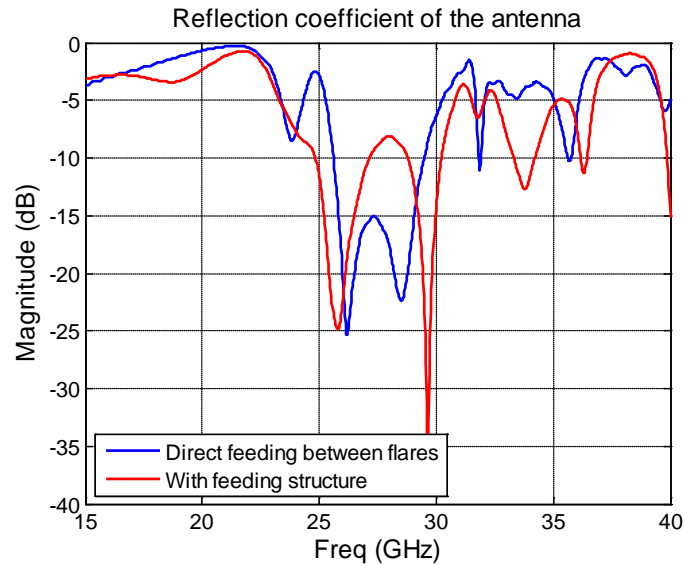


**Figure 4.18 Reflection coefficient of the antenna with and without feeding structure**

#### 4.3.6 Interim conclusion

In this section we have investigated the influence of the LTCC substrate and the influence of the elliptical dipole antenna dimensions and shield profile. 3-staircase profile has been selected as the basic shield profile to provide sufficient bandwidth at the desired frequency band. The final antenna schematic is shown in Figure 4.19

Figure 4.19, and the dimensions of the antenna are given in appendix C. In addition, to increase the antenna beamwidth, the shield wall along the Y-direction has been

removed. It was demonstrated that removing the Y-direction wall does not influence the impedance matching but widens the beamwidth at the E plane. However, this cannot be applied to the X-direction wall. Thus the antenna has wide radiation pattern at the E-plane but narrower radiation pattern at the H-plane. The metal shield has been realized with metal grids and connected interleaved via fences. With these techniques the antenna is realizable without changing performance. The simulation results showed that the final optimized antenna has a -10 dB impedance bandwidth from 25 GHz to 30 GHz (except from 27.1 GHz to 28.8 GHz where the reflection coefficient raised to about -8 dB).

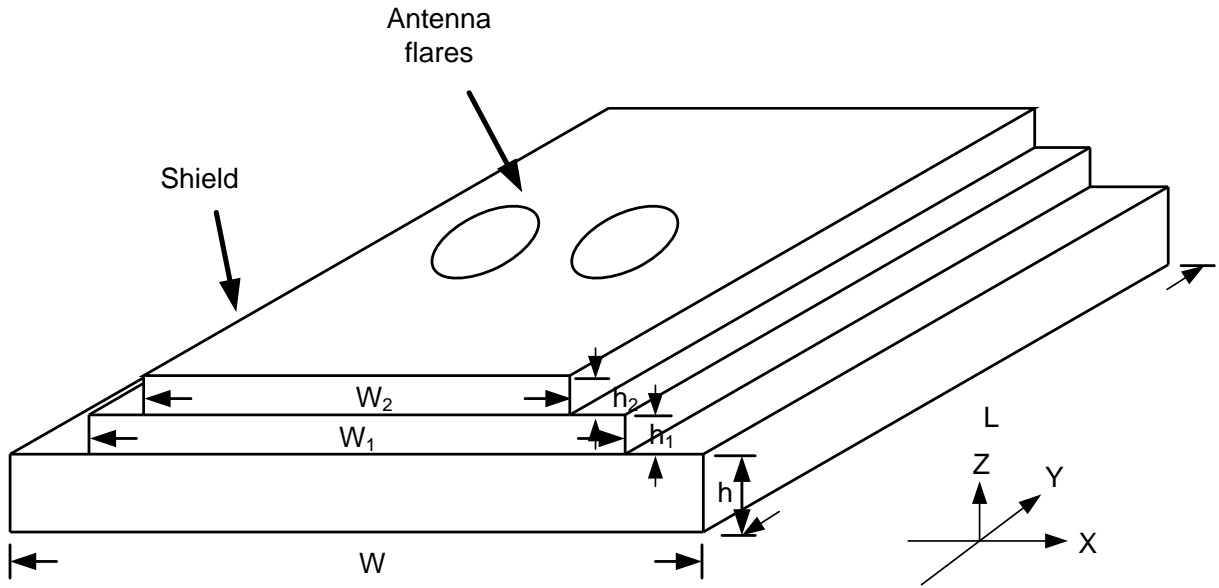


Figure 4.19 Antenna schematic

## 4.4 Experimental verifications

The proposed antenna has been manufactured and measured to experimentally verify the numerical model and evaluate the impact of LTCC process. Firstly the measurement setup is presented in section 4.4.1. The antenna reflection coefficients, gain and radiation patterns, and time domain behavior were measured and the results are discussed in section 4.4.2, 4.4.3, and 4.4.4, respectively.

### 4.4.1 Antenna connectorization

As discussed in Section 2.2, mm-wave antenna measurement is not an easy task. We have chosen to use coax-connector to measure the antenna, but it is not possible to directly connectorize the antenna. Therefore two structures were designed to enable antenna connectorization, and they are presented in the following sections.

#### 4.4.1.1 CPS-Microstrip line transition

To measure the antenna differentially, we have to connect the antenna CPS input port to connectors separately. The smallest commercially-available connector we can find has a dimension of 4.4 mm x 4.4 mm (mini-smp connector). But the input CPS line only has a separation of 0.2 mm and line width of 0.34 mm, so direct connectorization is not possible. The initial design to make connectorization possible

was to taper the CPS and enlarge the line separation large enough for the connectors. Nevertheless, due to the large CPS separation, the CPS line width will be very wide and the CPS line does not behave like a CPS line anymore. To solve this, an auxiliary ground plane was inserted at 1 layer (0.104 mm) below the surface and the transition became a CPS-CPSWG with ground (CPSWG)-microstrip line transition, as Figure 4.20 shows. The proposed transition can provide lower than -20 dB reflection coefficient and less than -0.5 dB insertion loss (Figure 4.21). The distance between connectors is 5.6 mm, which is actually still small for two adaptors to connect together. Therefore we customized a mini-SMP to 2.4 mm adapter (see appendix A) which is a concatenation of a mini-smp semi-rigid cable and a 2.4 mm connector. This enables us to connect the differentially-fed antenna to the PNA.

#### 4.4.1.2 Balun design

We have also developed a dedicated UWB balun solely for the measurement purpose. By comparing the measurement results of the differentially-fed antenna and the balun-fed antenna, we can evaluate the performance of the balun. This design of balun is necessary for the future M-band antenna measurement.

The developed balun consists of 3 major sections. First there is a Chebyshev multi-section impedance transformer to transform the 50 $\Omega$  microstrip line to a power combiner which has 25 $\Omega$  impedance. This power combiner combines 2 microstrip lines with 50 $\Omega$  impedance and 180° phase difference. Finally these 2 microstrip lines connect to the CPS line of the antenna input via a CPSWG line (Figure 4.22). The balun provides less than -15 dB reflection coefficient and smaller than -0.5 dB insertion loss (Figure 4.23 (a)), and the phase difference is 180° $\pm$ 14° from 25 GHz to 30 GHz (Figure 4.23 (b)).

To examine the impact of the proposed CPS-MS line transition and balun to the antenna reflection coefficient, we have compared the reflection coefficients of the antennas with original feeding (as shown in Figure 4.2 (b)), with the CPS-MS line transition, and with the balun (Figure 4.24). By adding the extra feeding network, the -10 dB impedance bandwidth and resonances do not change much, but the “bump” between two resonances becomes slightly higher, from -8 dB to -5.5 dB. The realized antenna with balun and differential-feeding are shown in Figure 4.25. This is due to extra common mode excited by the feeding network.

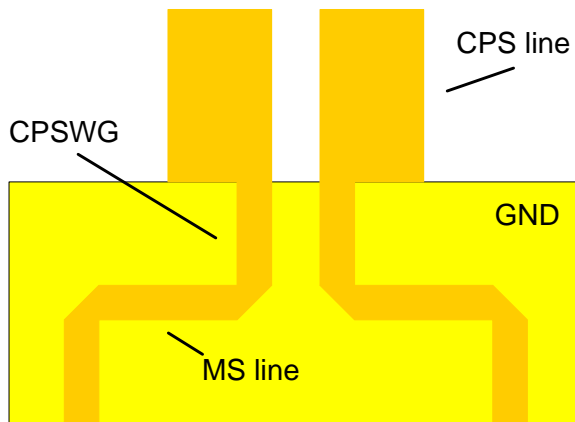


**Figure 4.20 CPS-CPSWG-MS line transition**

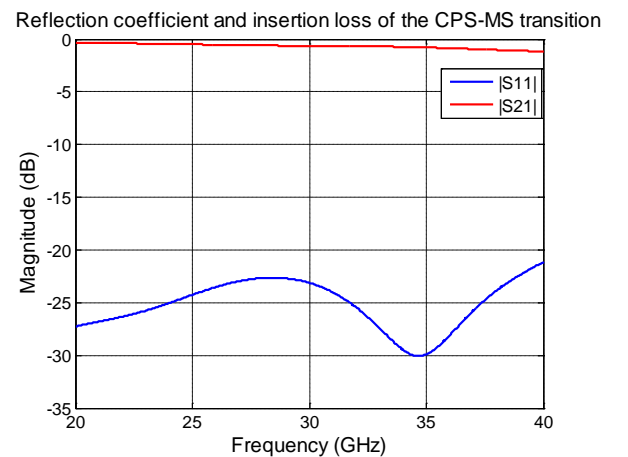


**Figure 4.21 Reflection coefficient and insertion loss of the CPS-CPSWG-MS**

### line transition

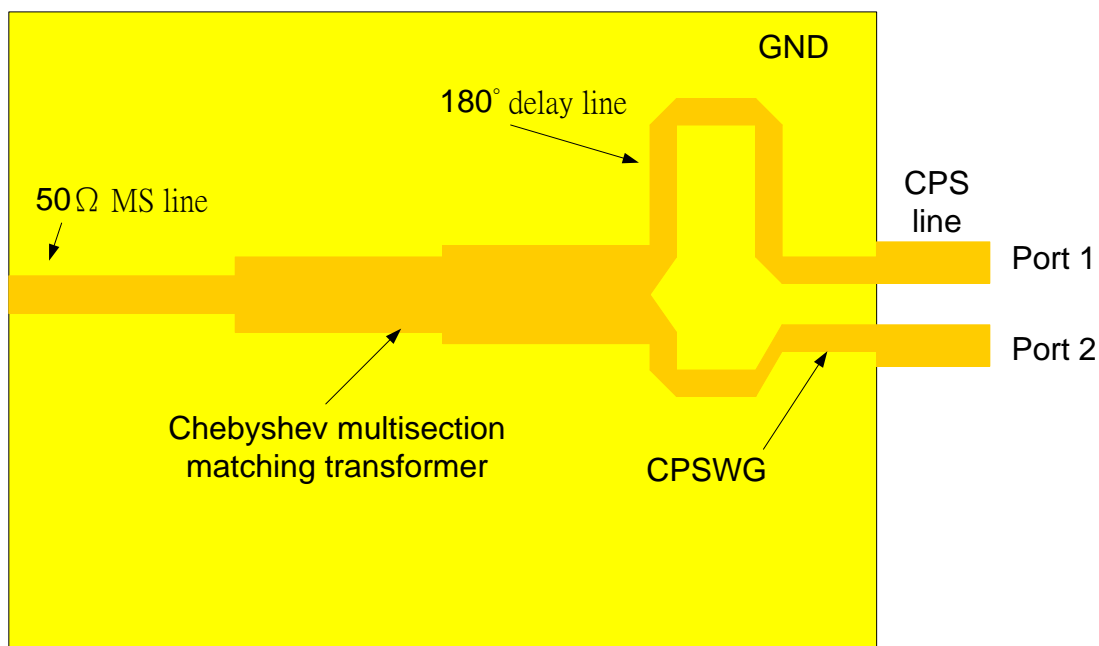
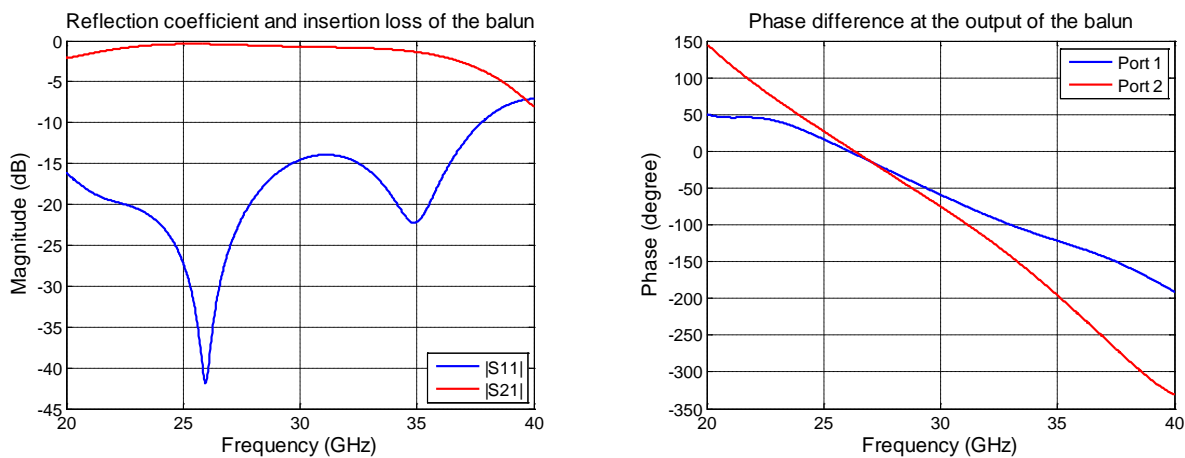
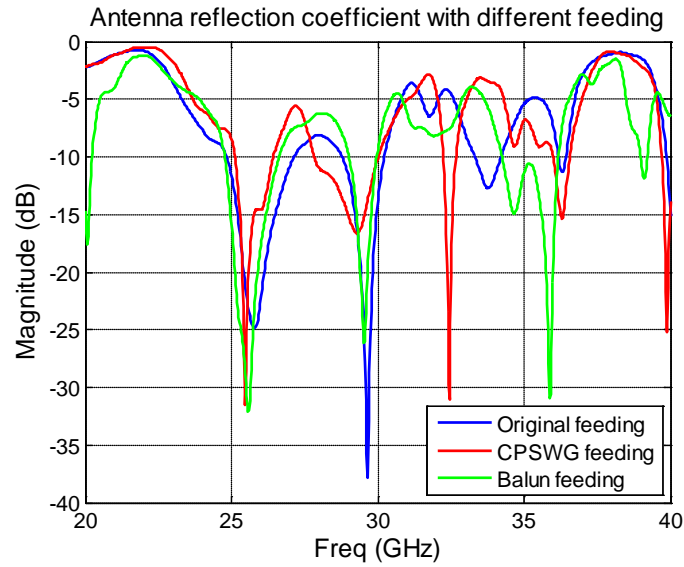


Figure 4.22 Layout of the balun

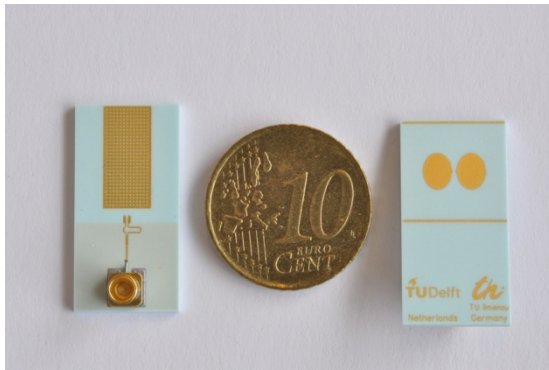


(a) Reflection coefficient and insertion loss of the balun (b) Phase of port 1 and port 2 (inversed)

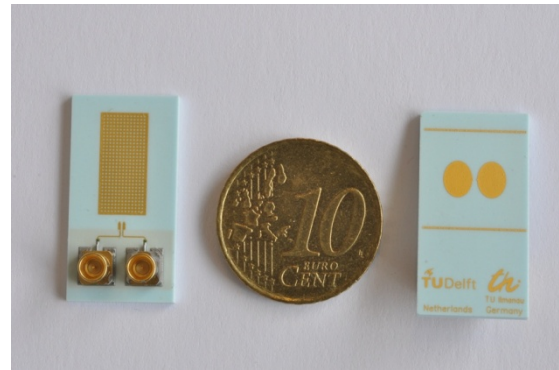
Figure 4.23 Balun performance (a) Reflection coefficient and insertion loss (b) Phase difference



**Figure 4.24 Simulated reflection coefficients of the antennas with different feeding**



(a) Antenna with balun-fed



(b) Antenna with differential-fed

**Figure 4.25 Realized antenna (a) Antenna with balun-fed (b) Antenna with differential-fed**

#### 4.4.2 Reflection coefficient analysis

Firstly the antenna reflection coefficients were measured and compared to the results predicted. Two different calibration techniques have been used to de-embed the system error. The first technique is the SOLT calibration technique, where the system error is calculated by measuring a well-defined known short, open, load, thru standards. The second technique is the TRL calibration technique, where the system error is calculated by measuring a thru, a line, and a reflect standards. The detailed discussions of these two techniques can be found in Chapter 2 section 2.4.

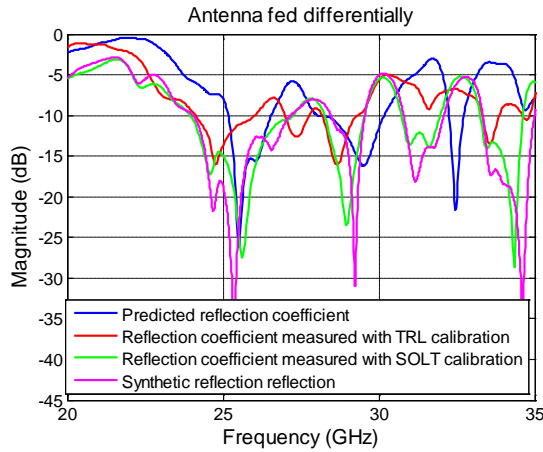
The comparison of the predicted and measured reflection coefficient of the differentially-fed antenna can be observed in Figure 4.26 (a). Two approaches were used to measure the differentially-fed antenna. Firstly the antenna was connected to a 4-port PNA and the differential mode reflection coefficient was directly obtained. With this approach both SOLT and TRL calibration were used. The other approach was to treat the differential feeding as a two port device and synthesize the differential reflection coefficient using the technique described in Chapter 2 section

2.5.2. The synthesized differential reflection coefficient measurement is calibrated with SOLT standards. All the measured reflection coefficients have similar behavior, except the one measured with 4-port PNA and TRL calibration (Figure 4.26 (a)). The similarity between the SOLT calibrated reflection coefficient and synthesized reflection coefficient verified the synthetic technique described in Chapter 2. The difference of the TRL calibrated results and other results might due to the imperfection of the differential TRL calibration standards. The measurement showed that the antenna has a -10 dB impedance bandwidth from 24.15 GHz to 29.35 GHz except from 25.8 GHz to 27 GHz (with TRL calibration) or 27 GHz to 28.5 GHz (with SOLT calibration), where the reflection coefficient is about -8 dB. The -10 dB bandwidth of all the measured results has a negative frequency shift of about 1 GHz comparing to the predicted result. This negative frequency shift behavior is also seen in the balun-fed antenna measurement results.

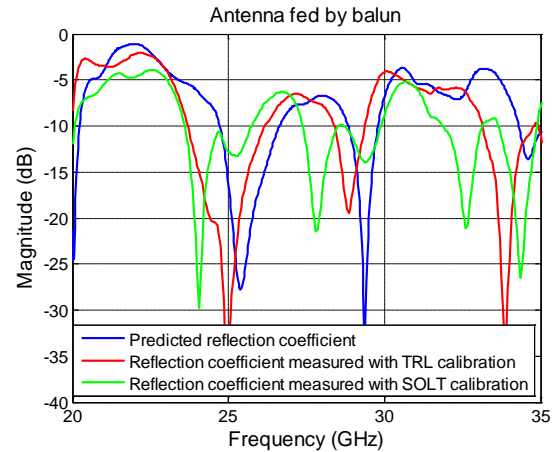
The comparison of the predicted and measured reflection coefficient of the balun fed antenna is presented in Figure 4.26 (b). The TRL calibrated reflection coefficient is well matched to the predicted one with a negative frequency shift of about 400 MHz, while the SOLT calibrated reflection coefficient has larger deviation comparing to the predicted one. The good similarity between the TRL calibrated result and the predicted result indicates that the TRL calibration can successfully de-embed the effect of the connector.

To evaluate the performance of the balun, we have compared the reflection coefficient of the differentially-fed antenna and the balun-fed antenna, as shown in Figure 4.27. Good agreement has been observed between these two results. This indicates the balun can successfully deliver out of phase field to the antenna.

The comparison of the synthetic differential mode and common mode reflection coefficient is shown in Figure 4.28 (with SOLT calibration). The result showed that when the differential reflection coefficient is above -10 dB (from 25.8 GHz to 28 GHz), the common mode reflection coefficient is lower than -10 dB. In addition, when the differential mode reflection coefficient increases, the common mode reflection coefficient decreases. This indicates that the antenna actually does not operate solely in differential mode, at certain frequencies the common mode is stronger than the differential mode, thus increase the differential mode reflection coefficient.



(a) Antenna fed differentially



(b) Antenna fed by balun

**Figure 4.26 Measured antenna reflection coefficient (a) Antenna fed differentially (b) Antenna fed by balun**

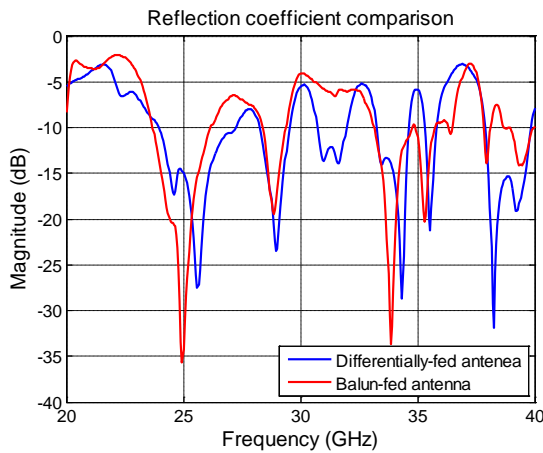


**Figure 4.27 Reflection coefficient comparison of the differentially-fed and balun-fed antenna**

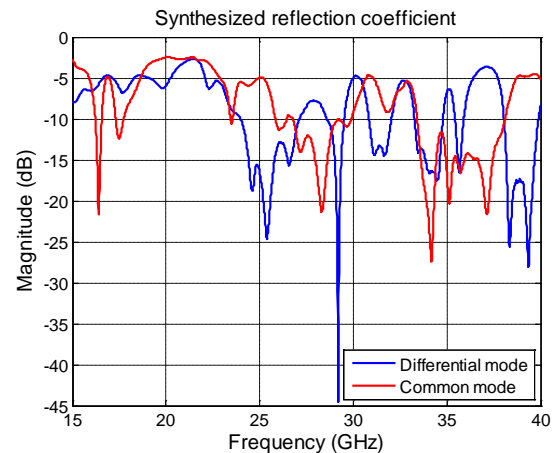


**Figure 4.28 Differential mode and common mode reflection coefficient**

### 4.4.3 Gain and radiation patterns analysis

#### 4.4.3.1 Gain measurement and analysis

The antenna gain is measured by using 3-antenna method. A WR 28 waveguide has been used as the third antenna. The predicted and measured antenna broadside and backside gain is illustrated in Figure 4.29. The model used to simulate the antenna gain is antenna with balun but without connector. Figure 4.29 (a) shows the comparison of the predicted antenna gain, measured balun-fed antenna gain, and measured differentially-fed antenna gain at broadside. Firstly, good agreement between the predicted gain and the measured balun-fed antenna gain is observed, which verifies the correctness of the model. Secondly, the gain of the differentially-fed antenna is slightly higher than that of the balun-fed antenna before 24.5 GHz (maximum about 4 dBi differences). And from 24.5 GHz to 30 GHz the gain of the balun-fed antenna and the gain of the differentially-fed match well.

The deviation of gain might due to the deviation in the reflection coefficient, since the differentially-fed antenna has about 4 dB lower reflection coefficient in the region of 22GHz to 24 GHz. The broadside gain of both balun-fed and differentially-fed antenna is of about 5 dBi to 7 dBi from 24.6 GHz to 30 GHz. On the other hand, the backside gain (shown in Figure 4.29 (b)), has larger deviations between the three results. The predicted back radiation is mainly below -5 dBi while both measured backward gain of the balun-fed antenna and differentially-fed antenna are between -5 dBi and 0 dBi. The difference is due to that the simulation model does not include the mini-SMP to 2.4 mm adaptor. This demonstrated that the connector and adaptor indeed increased the backward radiation level. Nevertheless, the FBR of about 5 dB to 10 dB is still maintained in most of the operational frequency band (25 GHz to 30 GHz). In addition, the antenna is designed to be directly integrated with the MMICs, therefore, an operational antenna would not have a connector. Simulation result showed that the antenna has good polarization purity, with co-polar gain about 30 dB higher than cross-polar gain (Figure 4.29 (C)).

Simulation result indicated that the radiation efficiency of the balun-fed antenna<sup>1</sup> is about -0.3 to -0.45 dB (96% ~ 95%) from 25 GHz to 30 GHz.

#### 4.4.3.2 Radiation patterns measurement and analysis

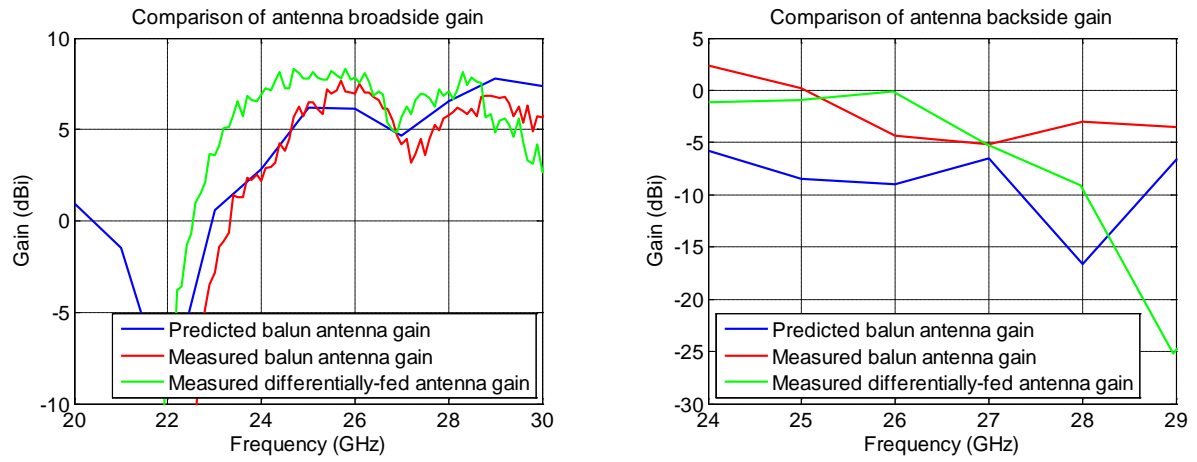
The radiation patterns analysis not only indicates how the antenna radiates, but also gives valuable information on how the feeding structure influences the antenna radiation. We have measured the radiation patterns from 25 GHz to 30 GHz for both balun-fed antenna and differentially-fed antenna, but only 25 GHz and 28 GHz are shown here.

Figure 4.30 (a) to (d) show the balun-fed antenna radiation patterns at 25 GHz and 28 GHz at the E-plane and the H-plane. At the antenna front side, the measured radiation patterns and the predicted ones agreed with each other at both E- and H-plane. However, at the antenna back side, the antenna measured radiation patterns have higher radiation level comparing to the simulated one. This indicates that the shield has good protection of the antenna flares, so the antenna front radiation is irrelative to whatever behind the antenna. The connector only influences the backward radiation but has nothing to do with the front radiation. The radiation patterns at the E-plane are wide, with a -3 dB beamwidth larger than  $\pm 30^\circ$ . This is because the shield wall along the Y-direction is removed. The radiation patterns at the H-plane are narrower due to the presence of the X-direction wall. Furthermore, due to presence of the connector, the antenna structure is not symmetric at the H-plane. Consequently, the radiation patterns at the H-plane are less symmetric comparing to those at the E-plane.

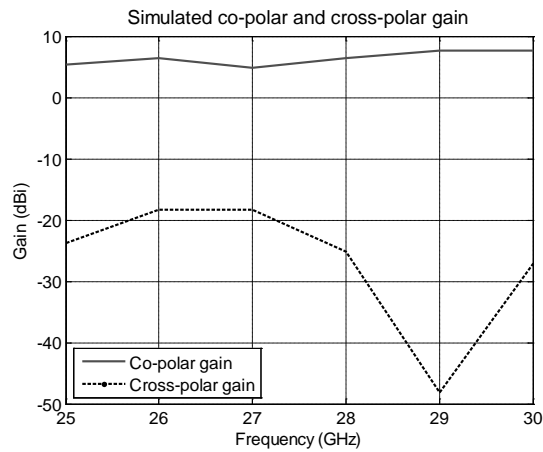
---

<sup>1</sup> CST cannot simulate the antenna efficiency of the differential antenna





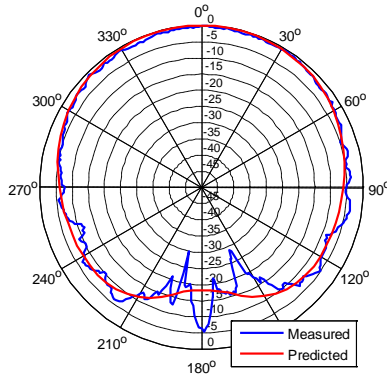
(a) Comparison of the broadside gain of different antennas (b) Comparison of the backside gain of different antennas



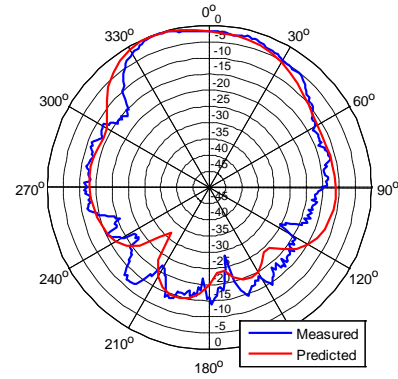
(c) Comparison of co- and cross-polar gain of the balun-fed antenna

**Figure 4.29 Antenna broadside and backside gain (a) Comparison of broadside gain (b) Comparison of backside gain (c) Comparison of co- and cross-polar gain**

Balun-fed antenna radiation pattern at 25GHz, E-plane



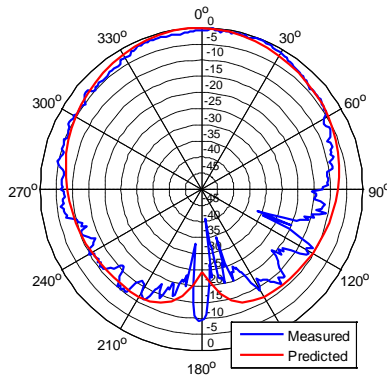
Balun-fed antenna radiation pattern at 25GHz, H-plane



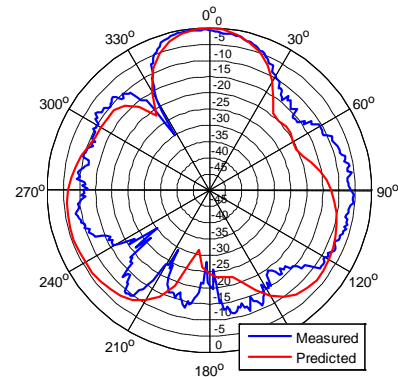
(a) Balun-fed antenna radiation patterns at 25GHz at the E-plane

(b) Balun-fed antenna radiation patterns at 25GHz at the H-plane

Balun-fed antenna radiation pattern at 28GHz, E-plane



Balun-fed antenna radiation pattern at 28GHz, H-plane



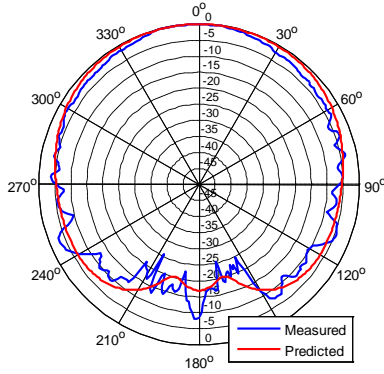
(c) Balun-fed antenna radiation patterns at 28 GHz at the E-plane

(d) Balun-fed antenna radiation patterns at 28 GHz at the H-plane

**Figure 4.30 Balun-fed Antenna radiation patterns at the E-and the H-plane (a) 25 GHz, E-plane (b) 25 GHz, H-plane (c) 28 GHz, E-plane, (d) 28 GHz, H-plane**

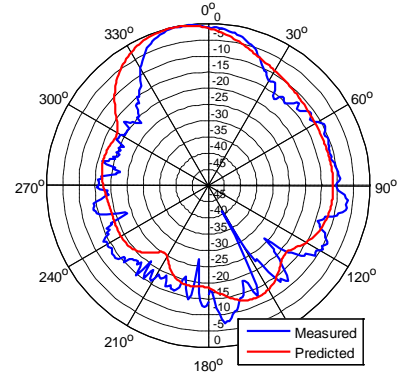
Figure 4.31(a) to (d) show the measured differentially-fed antenna radiation patterns and the predicted differentially-fed antenna radiation patterns. Although in general the simulated patterns and measurement patterns agreed with each other, the deviation is larger than that of the balun antenna. This is because the radiation patterns of the differentially-fed antenna were obtained by firstly loading the port 2, and measuring the patterns of the antenna excited by the port 1. Then port 1 is loaded, and the patterns are measured while the antenna excited by the port 2. The total antenna radiation pattern is then calculated by subtracting both patterns. This requires not only accurate magnitude measurement (which is only required for one-port antenna radiation patterns measurement), but also accurate phase measurement. Unfortunately at K-band the phase is susceptible to antenna positions, and it is quite easy to have some displacement when swapping the connection to port 1 and port 2. Since the phase is more sensitive to movement at higher frequencies, the measured radiation patterns at 25 GHz matched better with the simulated ones in both E- and H-plane, but the patterns have larger deviation at 28 GHz for both E- and H-plane

Differentially-fed antenna radiation pattern at 25 GHz, E-plane



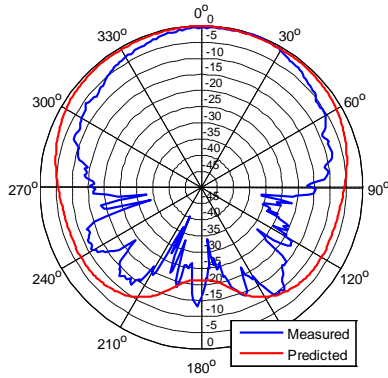
(a) Differentially-fed antenna radiations patterns at 25 GHz at the E-plane

Differentially-fed antenna radiation pattern at 25 GHz, H-plane



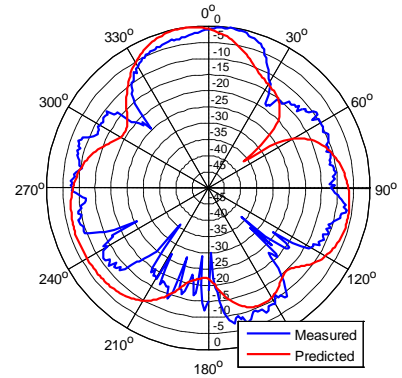
(b) Differentially-fed antenna radiations patterns at 25 GHz at the H-plane

Differentially-fed antenna radiation pattern at 28 GHz, E-plane



(c) Differentially-fed antenna radiations patterns at 28 GHz at the E-plane

Differentially-fed antenna radiation pattern at 28 GHz, H-plane



(d) Differentially-fed antenna radiations patterns at 28 GHz at the H-plane

**Figure 4.31 Differentially-fed antenna radiation patterns at the E- and the H-plane (a) 25 GHz, E-plane (b) 25 GHz, H-plane (c) 28 GHz, E-plane (d) 28 GHz, H-plane**

Next we compare the measured balun-fed antenna and differentially-fed antenna radiation patterns (Figure 4.32) to examine the impact of feeding method to the radiation patterns. Good agreement has been observed between the radiation patterns of the two antennas. This indicates that different feeding structure does not have substantial influence to the antenna radiation characteristics.

Based on the analysis above, we can conclude that both differential feeding structure and balun can successfully excite the antenna, and there is no significant difference between the two approaches. This conclusion indicates that we may be use the same balun design in the M-band to excite the antenna since it is not possible to measure the M-band antenna differentially.

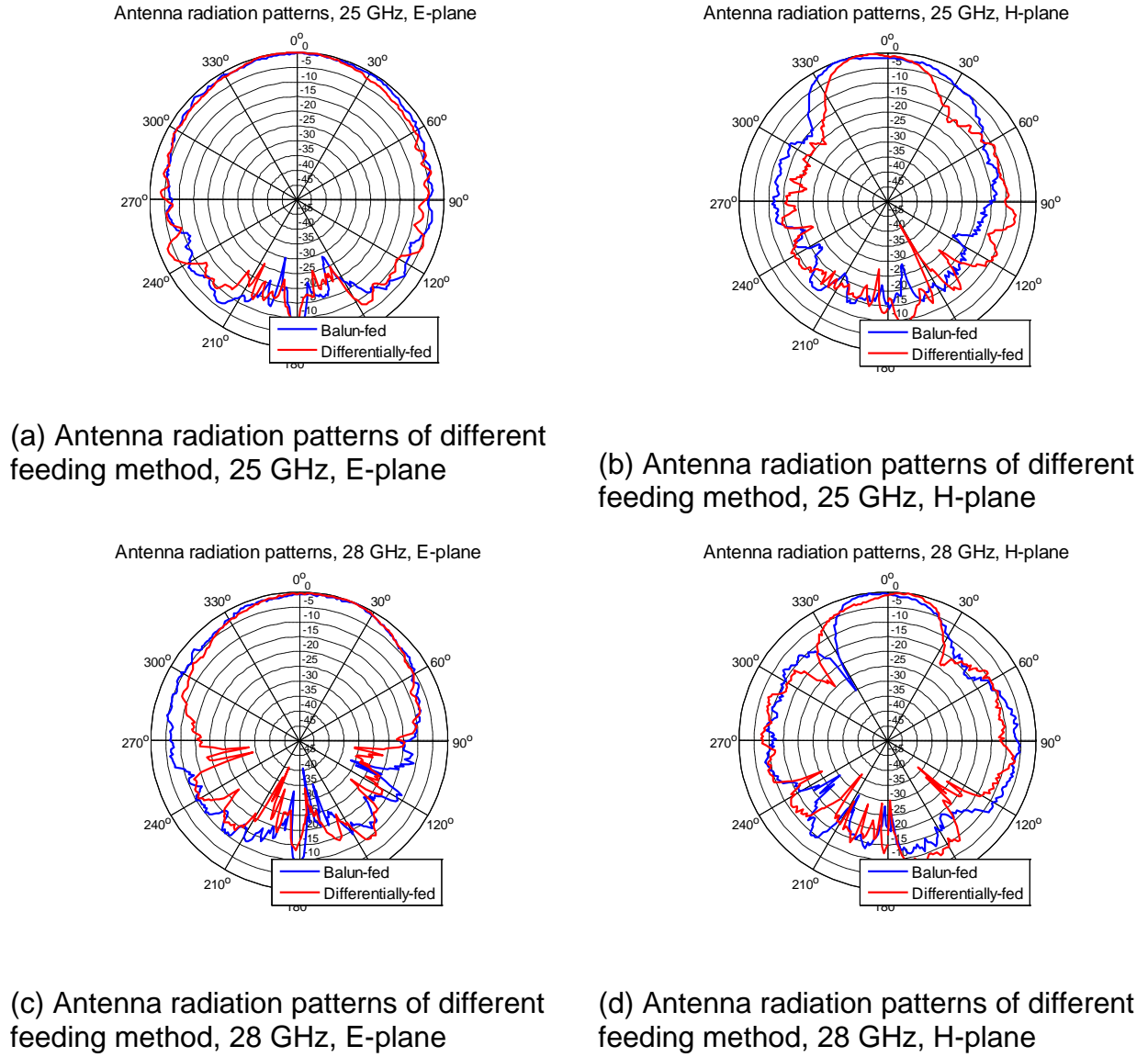


**Figure 4.32 Comparison of the antenna radiation patterns with different feeding**

#### 4.4.4 Time domain analysis

The time domain transmission response of a face-to-face TX-RX antenna pair is shown in Figure 4.33. The antennas used were balun-fed antennas, and the antenna distance is of about 25 cm. The impulse response has a  $1/e$  pulse width of about 218ps, but it has a late-time ringing of about 1ns. Figure 4.34 shows the group delay of a TX-RX antenna pair. The group delay is within 350ps, which is of the same order of magnitude as duration of the pulse. This shows that this antenna may not be suitable for time domain UWB application as the late-time ringing is too long. This late-time ringing is due to the multiple resonances in the shield. If this antenna shall be used for time domain UWB application, the time-domain property shall be further investigated and optimized.

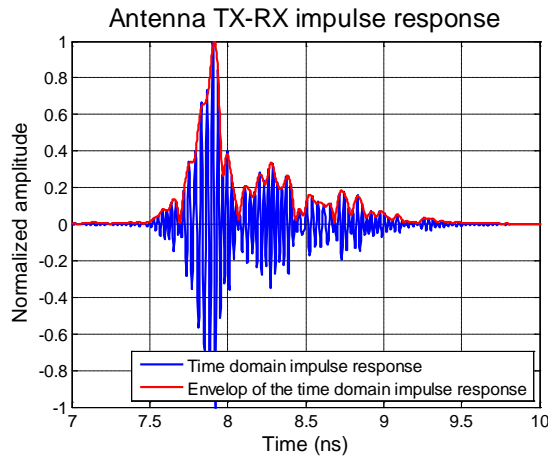


**Figure 4.33 Antenna TX-RX impulse response**

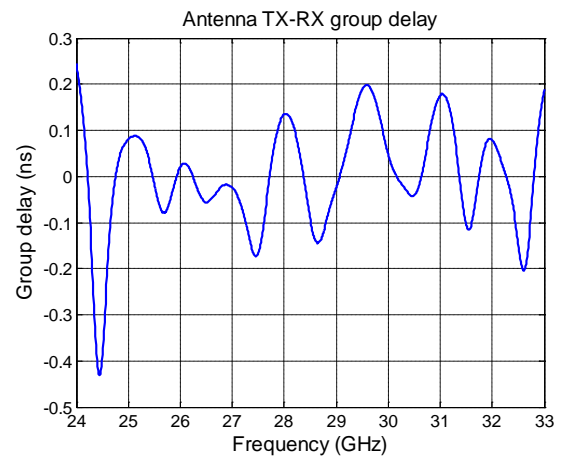


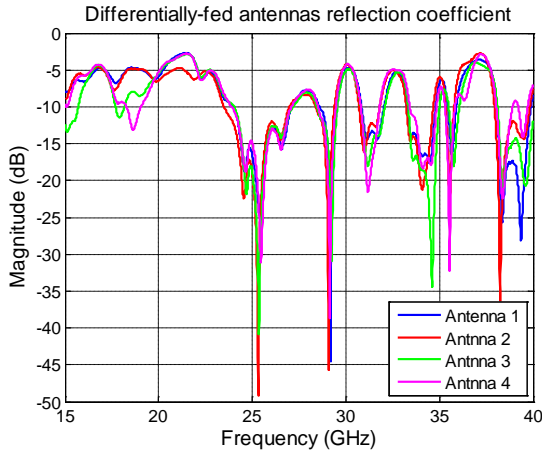
**Figure 4.34 Antenna TX-RX group delay**

## 4.5 Manufacturing variation analysis

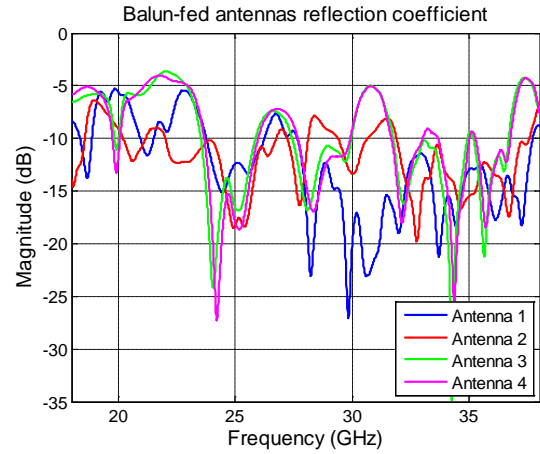
Since the LTCC process is not standardized yet, it is important to evaluate the influence of the different types of process variation to the performance of the antenna. The process variation, the material variation, and the substrate height variation were analyzed and presented in the following sections.

### 4.5.1 Process variation

Firstly we evaluate the stability of the LTCC process. To this end four balun-fed antennas and four differentially-fed antennas have been manufactured. The measured reflection coefficient of these antennas can be found in Figure 4.35 (a) and (b). For the differentially-fed antennas, all four antennas have almost identical results. On the other hand, only two balun-fed antennas have similar performance, and the other two balun-fed antennas behave very differently. This is because some steps LTCC processes are done manually, thus the yield rate cannot be guaranteed. However, comparing the success antennas, the variations are small.



(a) Reflection coefficient of the differentially-fed antennas



(b) Reflection coefficient of the balun-fed antennas

**Figure 4.35 Reflection coefficient of manufactured antennas (a) Differentially-fed antennas (b) Balun-fed antennas**

#### 4.5.2 Variation of the relative permittivity

Figure 4.36 shows the comparison of the predicted reflection coefficient simulated with nominal relative permittivity ( $\epsilon_r=7.4$ ) from the material data sheet [12], maximum measured relative permittivity provided by the manufacturer ( $\epsilon_r = 7.55$ ), and measured antenna reflection coefficient. The increasing of the relative permittivity slightly shifts the reflection coefficient curve towards lower frequencies, but the change is relative small. Therefore, the variation of the LTCC relative permittivity does not have large influence on the antenna performance.

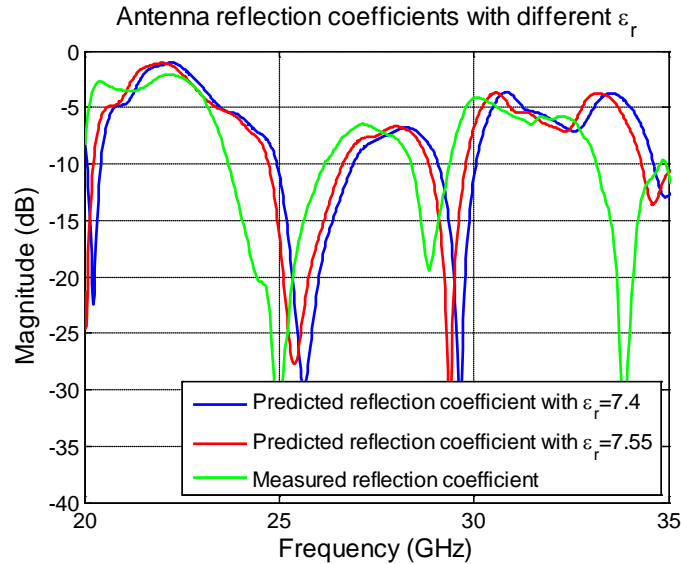


**Figure 4.36 Antenna reflection coefficients with respect to different relative permittivity**

### 4.5.3 Variation of the substrate height

The nominal substrate thickness of 1 layer from the data sheet is of about  $127 \pm 9 \mu\text{m}$  with about  $10.3\% \pm 0.5$  shrinkage after co-firing [12]. According to the manufacturer, the substrate thickness of 1 layer after co-firing is about  $104 \mu\text{m} \pm 10\%$ . To evaluate the variation of the thickness, we have simulated the antenna with layer thickness of  $100\mu\text{m}$ ,  $104\mu\text{m}$ , and  $110\mu\text{m}$ . The results are shown in Figure 4.37. The variation in thickness does not have influence on the structure of the reflection coefficient, but cause a negative frequency shift on the resonances. This is coincide with the analysis in section 4.3.1 that thicker substrate increases the effective relative permittivity and causes a negative frequency shift.

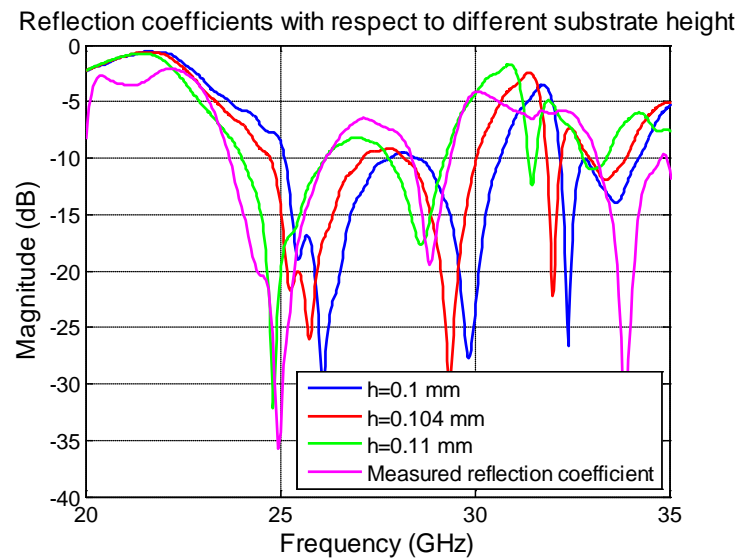


**Figure 4.37 Antenna reflection coefficients with respect to different substrate thickness**

### 4.5.4 Interim Conclusion

The process stability analysis demonstrated that unfortunately the LTCC process yield rate may not be as high as the PCB process, especially for this shielded antenna where many vias are needed, which is a major source of error. However, for the successfully manufactured antennas, the performances are quite stable. In addition, from the analysis above we can conclude that the negative frequency shift of the measured reflection coefficient is a joint effect of the variation in relative permittivity and substrate thickness. Nevertheless, the frequency shift is small (about 1.6%) comparing to the PCB materials (e.g., about 6% in [13]). As a result, the numerical analysis can provide trustful results for expected antenna performance.

## 4.6 Integrated LTCC antenna

The designed antenna has been intended to be integrated with MMICs (LNA, mixer, and LO). Figure 4.38 shows the layout of the proposed antenna integrated with the MMIC. Unfortunately the conductive glue used was too lossy at mm-wave frequency, thus the MMICs were unable to connect to the antenna. Therefore, no measurement results were available.



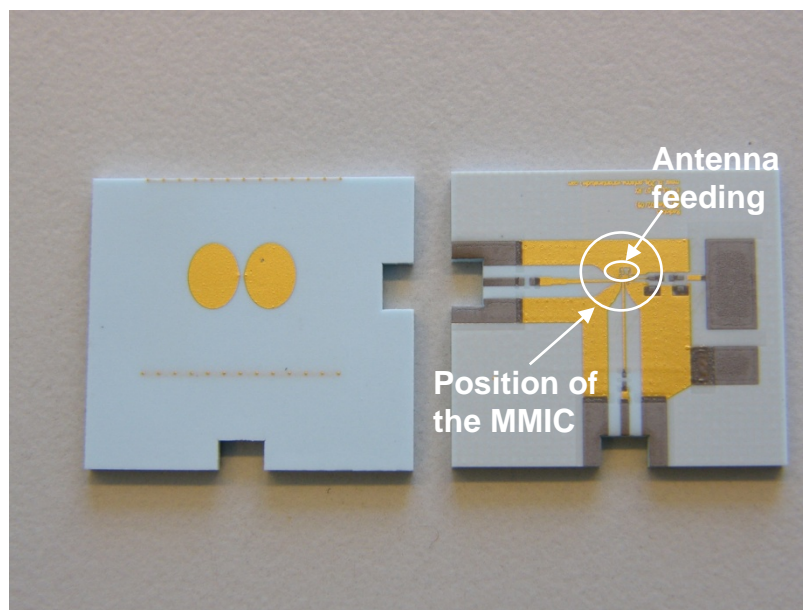


**Figure 4.38 Layout of the integrated antenna**

## 4.7 Conclusions

In this chapter we investigated the challenges of using LTCC technology in mm-wave UWB antennas on an example of K-band differentially-fed antenna. The basic antenna concept is adopted from a previously developed cavity-backed, differentially-fed elliptical dipole antenna working from 4.5 GHz to 10 GHz. Numerous changes have been made in order to realize the concept in LTCC technology resulting in development of a novel UWB antenna for K-band.

I investigated the influence of the LTCC substrate on the performance of elliptical dipole. It was found that due to high relative permittivity, the substrate act as a high Q resonator, which limits the bandwidth of the antenna. Moreover, the LTCC substrate creates strong surface wave, altering the antenna radiation pattern. By adding the shield to the antenna, the surface wave influence is reduced, and the antenna radiation patterns became controllable. Both achievements are very important for the integrated antenna design as integration the antenna with MMICs and other components will inevitably alter the substrate size. With the shielded antenna design, the antenna can be directly integrated with other components without any modification or re-optimization for different substrate size.

To overcome the difficulty of realizing shield in LTCC, I used metal grid and via fence to emulate the metal shield. However, dense via fence will weaken the structure and raise cost, thus we have proposed connected interleaved via fence. By this technique I can enlarge the via pitch by 2 while keeping the original performance. This experience is important for M-band LTCC antenna development.

The antenna feeding is done by concatenating several different transmission lines with same characteristic impedance. Two approaches were developed to experimentally verify the designed antenna. The first approach is by developing a differential feeding transition to measure the antenna differentially. The second approach is to measure the antenna with a balun. Comparison of both approaches allowed me to verify the balun design and evaluate the influence of the balun on



antenna performance. This information will be used for the M-band antenna development and measurement.

The investigations described above resulted in development of a novel K-band, cavity-backed, differentially-fed UWB antenna. The simulations have been experimentally verified. The antenna has a -7.5 dB (VSWR = 2.5:1) impedance bandwidth from 24 GHz to almost 30 GHz. No existing LTCC antenna working at the K-band has such large bandwidth. Good agreement between antennas with different feeding methods and simulated results has been observed. This agreement between numerical and experimental results validates both antenna and the balun designs.

The antenna gain is approximately from 5 dBi to 7 dBi from 24.6 GHz to 31 GHz with good efficiency (>95%). The radiation patterns analysis indicates that due to the protection of the shield, the forward radiation patterns are very stable and very similar to the simulated ones. However, due to the presence of the feeding structure such as balun or differential feeding transition and the adaptor, the backward radiation level is slightly higher than the predicted ones.

Since the LTCC process is not standardized, several antennas to evaluate the process variation were manufactured. Since the LTCC process is not fully automatic and several steps are done manually, the yield rate is not 100%. 2 out of 4 balun-fed antennas were failed. Nevertheless, the variations between successfully manufactured antennas are very small. After co-firing, the LTCC substrate shrinks and the substrate permittivity has slight deviation with respect to the value provided in the specifications. Due to these uncertainties, the measured results have small deviations comparing to the simulated results. However, these deviations are small (about 1.6%) comparing to the mm-wave antennas using the PCB material such as in [13], whose deviation is almost 6%. Thus it can be concluded that with the current LTCC technology the deviation of the predicted antenna performance is smaller than that of the PCB technology.

The novelty aspects of the research described in this chapter can be summarized as follows. Due to a new concept of the shield, new feeding techniques and optimization of the radiating element geometry for a substrate with a high dielectric permittivity, the research described above has resulted in a development of a novel antenna. Realization of the via fence in LTCC technology suggested by me is also novel. The UWB balun design on LTCC substrate is novel. Theoretical and experimental analysis of the manufacturing tolerances on the LTCC antenna performance is also new. Finally, to perform experimental verification of the differentially-fed antenna, new measurement techniques have been developed.

The knowledge gained from development of K-band antenna will be used to reduce the risk of the development of the M-band antenna.

## References

- [1] A. Panther, A. Petosa, M.G. Stubbs, and K. Kautio, "A Wideband Array of Stacked Patch Antennas Using Embedded Air Cavities in LTCC", *IEEE Microwave and Wireless Component Letters*, Vol. 15, pp. 916-918, 2005.
- [2] Available on line: <http://www.ltcc.de/en/home.php>

- [3] T. Seki, N. Honma, K. Nishikawa, and K. Tsunekawa, "Novel Microstrip Antenna Employing Stacked Rings on Multi-Layer Cermic Substrate for mm-Wave Applications", *IEEE Microwave Symposium Digest*, p.p. 1405-1408, 2005.
- [4] E. Tentzeris, R. L. Li, K. Lim, M. Maeng, E. Tsai, G. DeJean, and J. Lasker, "Design of compact Stacked-patch Antennas on LTCC Technology for Wireless Communication Applications", *IEEE Antennas and Propagation Society International Symposium*, Vol. 2, p.p. 500-503, 2002.
- [5] S. Wi, Y. Sun, I. Song, S. Choa, I. Koh, Y. Lee, and J. Yook, "Package-level Integrated Antennas Based on LTCC Technology", *IEEE Trans. on Antennas and Propagation*, Vol. 54, No. 8, p.p. 2190-2196, 2006.
- [6] G. Brezezina, L. Roy, and L. MacEachern, "Planar Antennas in LTCC Technology With Transceiver Integration Capability for Ultra-wideband Applications", *IEEE Trans. on MTT*, Vol. 54, No. 6, p.p. 2830-2839, 2006.
- [7] M. Sun, Y.P. Zhang, K.M. Chua, L.L. Wai, D. Liu, and B. P. Gaucher, "Integration of Yagi Antenna in LTCC Package for Differential 60-GHz Radio", *IEEE Trans. on Antennas and Propagation*, Vol. 56, No. 8, August 2008.
- [8] A. Vorobyov, "Planar Elliptically Shaped Dipole Antenna for UWB Impulse Radio", Ph. D dissertation, IRCTR, Delft University of Technology, The Netherlands, 2008
- [9] A. Vorobyov, "Report on Antenna Back Side Shield Optimization for Elliptically Shaped Dipole Antenna", IRCTR Internal report.
- [10] T. Weiland, "A Discretization Method for the Solution of Maxwell's Equations for Six-Component Fields", *Electronics and Communications (AEUE)*, vol. 31, no. 3, pp. 116–120, 1977.
- [11] Available online: <http://www.cst.com>
- [12] Available on line:  
[http://www2.dupont.com/MCM/en\\_US/assets/downloads/prodinfo/943LowLossTape.pdf](http://www2.dupont.com/MCM/en_US/assets/downloads/prodinfo/943LowLossTape.pdf)
- [13] J. A. G. Akkermans, R. van Dijk, and M. H. A. J. Herben, "Millimeter-wave Antenna Measurement", *Proc. of the 37<sup>th</sup> EuMC*, pp. 83-86, Oct. 2007.

## 5. M-band differentially-fed UWB antenna analysis and development

### 5.1 Introduction

The antenna working at the M-band (60 GHz to 100 GHz) is of great interest nowadays and has many applications such as high data-rate short-range communications, collision avoidance radar, or mm-wave ultra-high resolution near-field imaging radar. These applications have motivated many studies in the 60 GHz systems, especially in the integrated 60 GHz front end. In this chapter we address the problem of an integrated UWB M-band differentially-fed antenna development.

The antenna in mind is intended for ultra-high resolution near-field imaging radar. Therefore, it has to meet strict requirements similar to those in Chapter 3 such as large impedance bandwidth ( $> 10$  GHz), stable gain within the operational bandwidth, and near omni-directional radiation patterns at the broadside. The antenna is designed to be integrated with the differential MMICs, thus it has to be differentially-fed.

Using experience learned in Chapter 4, in this chapter I am going to develop M-band antenna which has:

- Large bandwidth: The antenna is intended to be used for 3-D ultra-high resolution imaging radar, thus large bandwidth ( $\sim 10$  dB impedance bandwidth at least larger than 10 GHz) is required. Although 10 GHz bandwidth at the M-band has relative narrow fractional bandwidth (about 17%), most of existing M-band antennas do not have this fractional bandwidth. Therefore, develop such a wideband antenna is challenging.
- Reasonable radiation characteristics: The antenna should not only have large impedance bandwidth, but also reasonably good radiation characteristic. We aimed to deal with small M-band antenna, and the antenna radiation characteristic should have moderate gain (about 5 dBi) and broadside radiation. The radiation pattern is desired to have broad beamwidth, for example,  $90^\circ$   $\sim 10$  dB beamwidth.
- Integration with MMICs: The antenna is expected to be integrated with the RF MMICs to reduce the loss, size, and cost of the RF front-end. In addition, direct integration with MMIC can reduce the complexity of designing the interface between the antenna and the RF MMIC. The MMIC that will be integrated with the antenna has differential feeding; therefore the antenna should also have differential feeding. This makes the antenna measurement challenging since we do not have equipment that can directly measure differential antenna at the M-band.
- Stable performance within LTCC manufacturing tolerances: Challenges of realizing antennas with the LTCC material in the mm-wave region are related to fabrication accuracy (which has higher impact on M-band antenna performance

in comparison with K-band antenna) and limitations on structures such as lines, metal plates, or vias. In addition, high relative permittivity of the LTCC material may limit the bandwidth of the antenna and supports excitation of the surface waves in the substrate, which will degrade the antenna radiation performance.

I expect that the findings from this study will give better insight into the application of the LTCC technology in the mm-wave antenna design.

The antenna concept is discussed in Section 5.2. Analyses an optimization of the antenna is presented in Section 5.3. The balun design and the antenna shield design are discussed in Section 5.4. Experimental analysis and verification of the antenna design are presented in Section 5.5, while conclusions are drawn in section 5.6.

## 5.2 Antenna concept

In previous chapters we have investigated an ASP antenna and a multi-stair case shielded dipole antenna. The advantage of the ASP antenna is its simplicity and large bandwidth. In addition, the ASP antenna has good radiation characteristics and good time domain behavior. However, based on the analysis in Chapter 4, the high dielectric constant of the LTCC material greatly limits the bandwidth of the microstrip type of antenna. More importantly, the severe surface wave will degrade the antenna radiation and matching characteristics. The other draw back of the ASP antenna is that conventional ASP antennas are all singly-fed, but the antenna is required to have differential feeding to be directly integrated with differential MMICs. These are all challenges for the M-band ASP antenna.

The multi-staircase shielded antenna, on the other hand, has much less surface wave problem thanks to the shield, and it is a differentially-fed antenna. Nevertheless, the shield realization involves large numbers of vias and metal grid, which is expensive and difficult to realize in the M-band due to the precision it needs. Therefore, to realize this type of antenna in the M-band would be extremely difficult and expensive.

Therefore, we have adapted the ASP antenna as radiator and designed a simplified version of shield to alleviate the surface wave influence. The proposed antenna concept is shown in Figure 5.1 (a) to (d). The antenna is based on an ASP antenna with modified feeding structure and simplified shield to prevent the propagation of the surface wave. The antenna has an H-shaped aperture to couple the energy from the feeding line to the patches. The H-shaped aperture is able to provide more design of freedom (comparing to the rectangular shaped aperture) and reduce the back radiation level [1]. The differential feeding is done by replacing the microstrip with two feeding probes located symmetrically on either side of the center aperture, which forms a parallel-wire transmission line (Figure 5.1 (b)). This type of feeding has been proven to provide good radiation patterns, apart from offering a wide bandwidth of operation [2]. The parallel-wire transmission line excites the aperture, from where the energy gets coupled to the patches above.

The proposed antenna has several distinctive features comparing with existing M-band antennas. Most existing UWB LTCC antennas use air cavity [3][4] or punch holes [5] to reduce the effective relative permittivity and enlarge the bandwidth. However, these techniques will increase the complexity of the structure and

increase the cost of the antenna. The proposed antenna, on the other hand, avoids any complex structures, which is favorable for manufacturing.

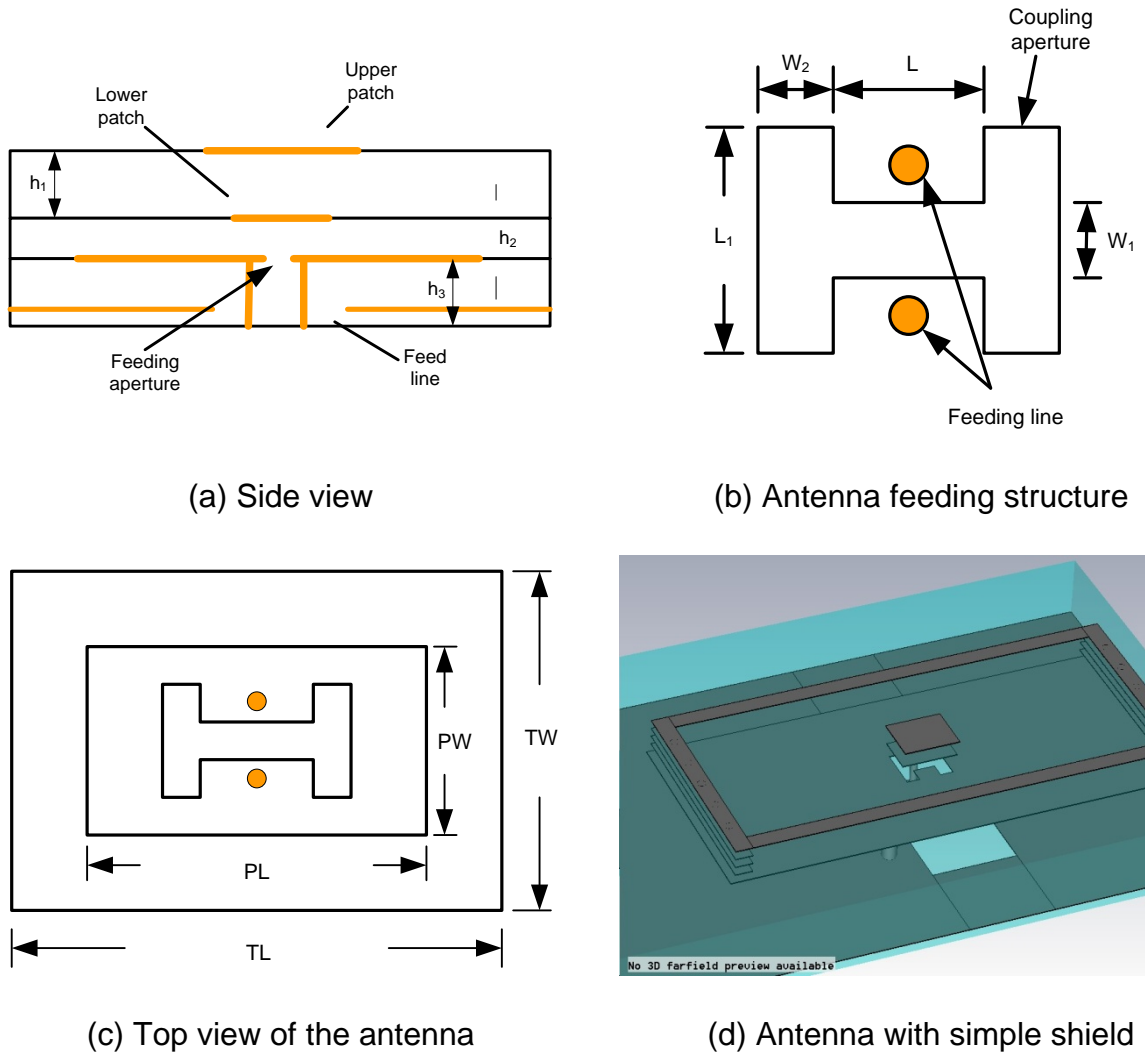


**Figure 5.1 The conceptual M-band differentially-fed LTCC antenna (a) Side view (b) Feeding aperture (c) Top view (d) Antenna with simple shield**

### 5.3 Antenna investigation and optimization

We have developed numerical models to perform investigation and optimization of the proposed antenna. Due to the complexity of the antenna structure and large bandwidth required, the numerical model is based on time domain finite integral technique (FIT), and is solved by commercially available software CST MWS. We tried to build the antenna model as realistic as possible; however, due to lack of accurate connector model, all the models were without connector. We have firstly optimized the dimensions of the ASP antenna, and then investigated the effect of the shield.

The basic working principles of ASP antenna has been investigated in Chapter 3. It was concluded that to obtain large (impedance) bandwidth, tightly coupled loops should appear at the center of the impedance locus when plotted on the Smith chart. Therefore, we examine the impedance locus behavior to determine the optimal parameters that can give large impedance bandwidth. The initial antenna

parameters are listed in appendix C. The impedance locus of the initial antenna is shown in Figure 5.2. There are 3 loops on the impedance locus, and these loops are very far from each other. This indicates the coupling between the aperture and the lower patch and the resonance between the two patches are weak. Thus, the initial antenna cannot provide proper matching. Comparing this impedance locus to the impedance loci in Chapter 3, this impedance locus has 3 loops instead of 2, which is result from the H-shaped aperture.

Firstly we reduce the patch size to examine the change of the impedance locus (Figure 5.3). By doing so we see that the loops are moving towards the center of the Smith chart, but the size of the loops are still small. This indicates that shrinking the patches moves the resonances towards higher frequencies, which is logical, but the coupling aperture is too small thus the coupling between the feeding line and the radiating patches is too weak. Therefore, at the next step we fix the size of both patches to 0.65 mm x 0.65 mm, and vary the aperture dimensions to increase the coupling between the feeding line and the aperture.

By enlarging the H-aperture length  $L_1$  to 0.3 mm and 0.5 mm, the loops, especially the first loop, are considerably increased (Figure 5.4). Therefore, we can identify that the first loop is mainly caused by the coupling between the aperture and the patches. The second loop size also increased considerably when  $L_1$  increased from the initial value to 0.3 mm, but when  $L_1$  changed from 0.3 mm to 0.5 mm, the second loop size only increased slightly. This indicates that the second loop is mainly due to the mutual resonance between the upper and the lower patch. Enlarging  $L_1$  increases the coupling between the aperture and the lower patch and consequently increases the mutual coupling between the patches. However when  $L_1$  increases to a certain degree the mutual resonance is then dominated by the relative size of the patches, thus the influence of  $L_1$  becomes insignificant. The change of center aperture length (Figure 5.5), on the other hand, does not have substantial influence to the impedance locus.

The influence of the center aperture width  $W_1$  and arm aperture width  $W_2$  are shown in Figure 5.5 and Figure 5.6, respectively. Enlarging both widths do not change the loops size, but rotate the position of the loops. By enlarging  $W_1$ , the second loop rotates counter clockwise, whereas enlarging  $W_2$ , the second loop rotates clockwise. This means that  $W_1$  and  $W_2$  do not influence the coupling level, but they play important role in impedance tuning.

Since the field distribution is mainly along the patch width direction, the variation of the patch width will have profound influence on the impedance locus, while the variation of the patch length will not have significant influence to the impedance locus. The influence of the upper patch width  $TW$  and lower patch width  $PW$  are shown in Figure 5.8 and Figure 5.9. The influence of the upper and lower patch widths is mainly on the size of the second loop, the position of the second loop, and the third loop. When Top patch width is smaller than the lower patch width, the mutual resonance becomes weak, thus the second loop size reduces. The third loop size, on the other hand, increases as long as the upper patch width and lower patch width are not the same.

From the analysis above it was found that the length of the H-shaped aperture arm determines the coupling between the aperture and the lower patch, which corresponds to the first loop of the impedance locus. The center aperture width and

the arm aperture width can be used to adjust the impedance matching. The patch width controls the resonance between the two patches, which is corresponding to the second loop on the impedance locus. The third loop is influenced by the center aperture length and the patch width. However, the third loop is located outside the band of interest, thus it is not important.

The optimized antenna parameters are listed in appendix C.

The simulated antenna reflection coefficient and gain at the broadside are shown in Figure 5.10. The antenna has a -10 dB impedance bandwidth from 50 GHz to 78 GHz (44%), which, to the authors' best knowledge, has never been reported in the literature, especially for LTCC antennas. The antenna gain at the broadside is decreasing as the frequency increases, which contradict to normal small antenna gain behavior. This is because at lower frequencies, the antenna is small or comparable to the wavelength, thus the antenna behaves like a small antenna which has a hemisphere uni-directional radiation pattern. When the frequency increases, the antenna electrical size increases as well. Therefore, the radiation patterns are not hemisphere-like anymore, but sidelobes start to build up, which decreases the gain at the broadside.

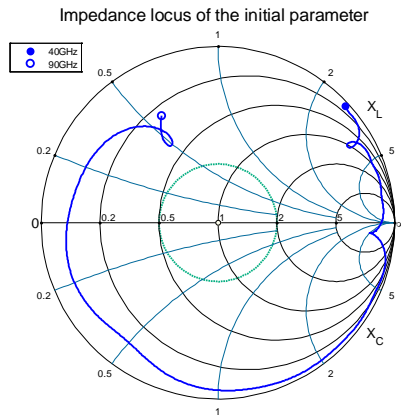


**Figure 5.2 Impedance locus of the initial values**

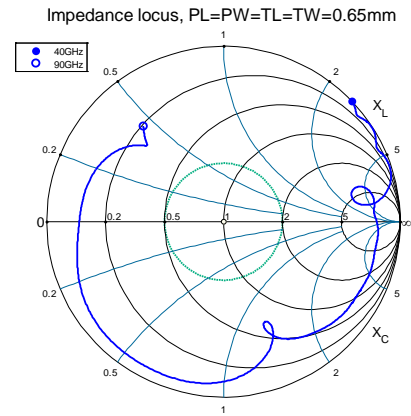


**Figure 5.3 Impedance locus of TL=TW=PL=PW=0.65mm**

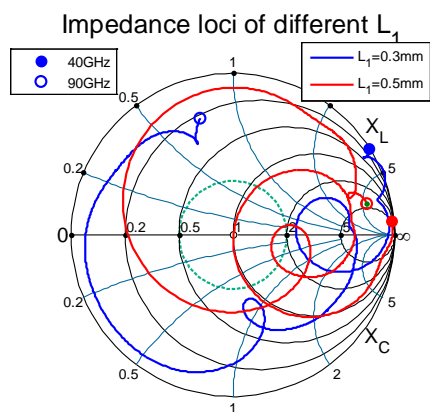


**Figure 5.4 Impedance loci of different  $L_1$**

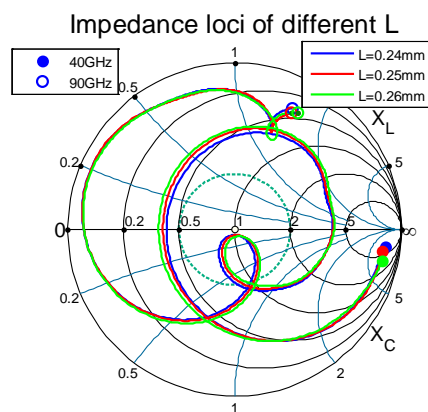


**Figure 5.5 Impedance loci of different  $L$**

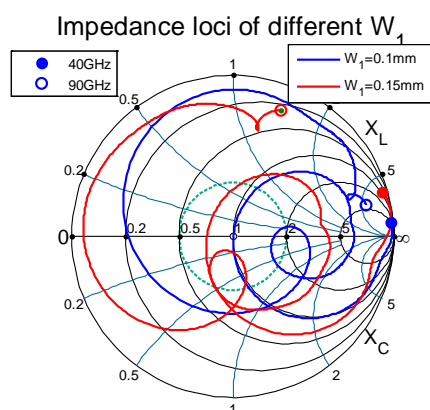


**Figure 5.6 Impedance loci of different  $W_1$**

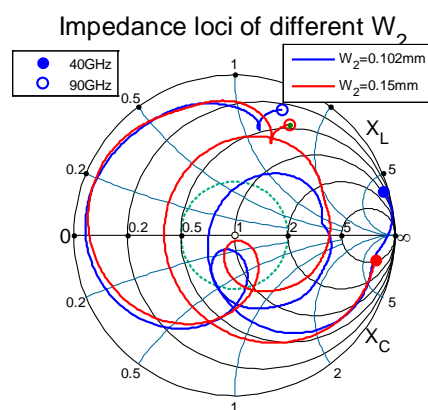


**Figure 5.7 Impedance loci of different  $W_2$**

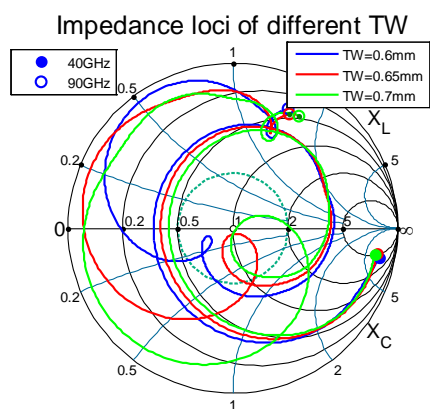


**Figure 5.8 Impedance loci of different  $TW$**

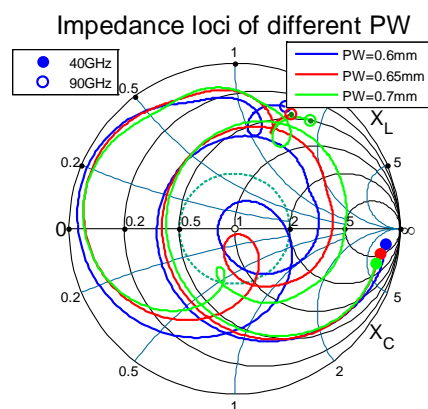
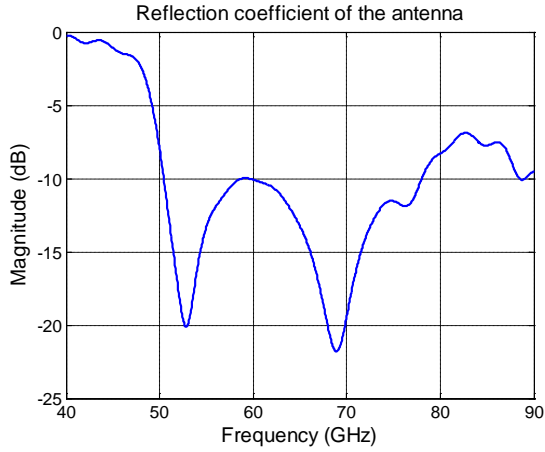
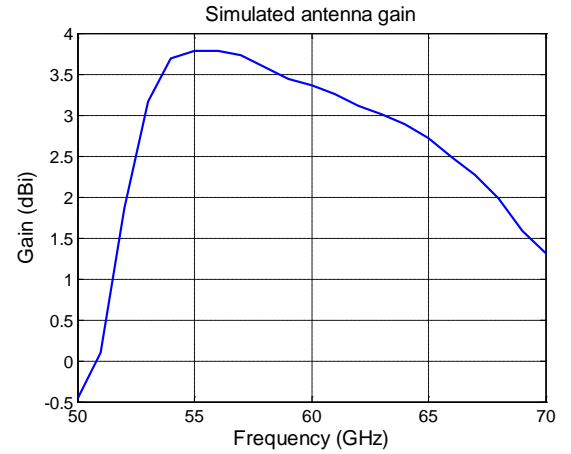


**Figure 5.9 Impedance loci of different  $PW$**





(a) Simulated reflection coefficient of the antenna



(b) Simulated gain of the antenna

**Figure 5.10 Simulated antenna reflection coefficient and gain (a) Simulated reflection coefficient (b) Simulated gain**

## 5.4 Antenna balun and shield design

### 5.4.1 Antenna balun design

Although the differentially-fed antenna is advantageous for the integrated systems, it is difficult to experimentally verify the differentially-fed antennas directly as most of the available measurement equipment working at mm-wave frequencies can only measure two-port devices but not four-port devices. As a result, a dedicated balun is designed to measure the proposed antenna with the available measurement equipment.

The design concept of the balun is the same as that in Chapter 4. The balun consists of a  $50\Omega$  microstrip line input, and then the  $50\Omega$  MS line connects to a 2 section Chebyshev impedance transformer to transform the impedance from  $50\Omega$  MS line to a  $25\Omega$  power combiner. The power combiner combines two  $50\Omega$  MS lines with  $180^\circ$  phase difference. The two  $180^\circ$  phase difference lines are then connect to a coplanar strips with ground (CPSWG) transmission line which connects to the antenna input (Figure 5.11).

To realize the balun, a ground plane is necessary. The antenna itself has a ground plane at 4 layers ( $0.416$  mm) below the feeding surface ( $h_3$  in Figure 5.1 (a)), so ideally this ground plane should also be the ground plane of the balun. Unfortunately,  $0.416$  mm substrate thickness will lead to wide microstrip line width (about  $0.683$  mm for a  $50\Omega$  MS line), and with this line width the  $180^\circ$  delay line will occupy a large area, which is a much undesired feature. As a result, we inserted an auxiliary ground plane at 1 layer ( $0.104$  mm) below the feeding surface, thus the microstrip line width can be thinner ( $50\Omega$  MS line width reduces to  $0.124$  mm) and consequently the balun can occupy less space. By adding this auxiliary does not introduce any negative feature.

The simulated reflection coefficient and insertion loss (differential mode and common mode) of the balun is shown in Figure 5.12. The balun provides less than  $-15$  dB reflection coefficient and less than  $-1$  dB differential mode insertion loss within

the operational band. The common mode insertion loss, on the other hand, is larger than -10 dB in the operational band. This demonstrated that most of the energy will be converted into the differential mode. The phase difference is  $180^\circ \pm 30^\circ$  between 55 GHz to 65 GHz. The effect of this phase difference is that not only pure differential mode is excited, but also some common mode is excited. This result in the maximum radiation not radiated exactly at the broadside but lean towards end-fire direction.

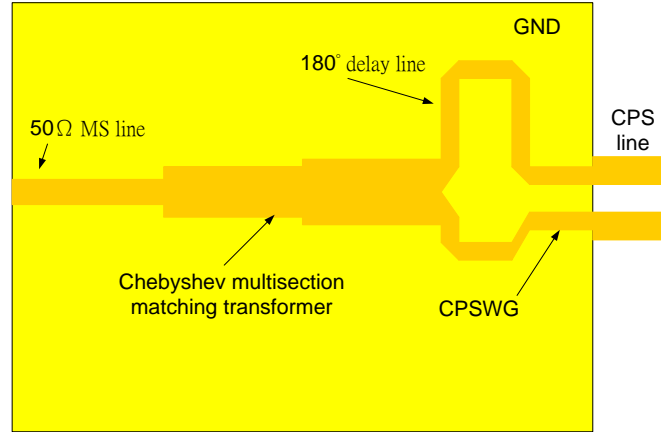


**Figure 5.11 Balun layout**

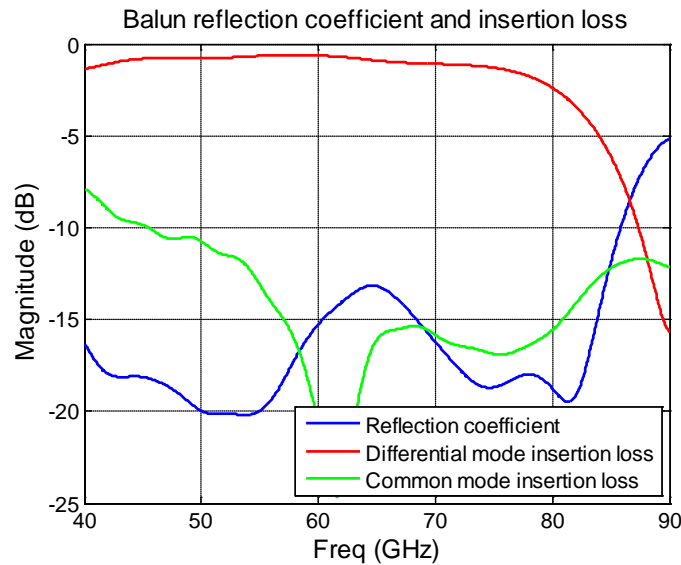


**Figure 5.12 Reflection coefficient and the insertion loss of the balun**

#### 5.4.2 Antenna shield design

It is well known that for the patch type antenna, the radiation characteristics can be significantly degraded by the diffraction of surface waves at the edge of the substrate, especially when the  $\epsilon_r$  of the substrate is high or the substrate size is large [8]. However, integrating the antenna with MMICs or adding structures such as balun for measurement purpose (Figure 5.11) will inevitably increase antenna size. This will cause the antenna radiation characteristics to degrade due to the strong surface wave.

To alleviate this problem, we have adopted the shield idea from Chapter 4. In Chapter 4, we have demonstrated that the metal shield can reduce the surface wave and protect the antenna. Therefore, here we also proposed to use a shield to surround the antenna and prevent the surface wave to propagate, or to control the propagation of the surface wave such that the variation of the substrate size will not influence the surface wave propagation around the antenna.

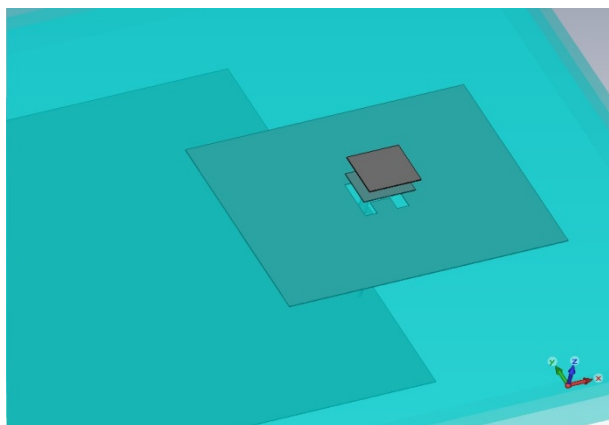
The antenna with and without the shield are illustrated in Figure 5.13 (a) and (b). Unlike the complex multi-staircase shield profile proposed in Chapter 4, the shield proposed here is very simple. The back shield is simply the extension of the auxiliary ground plane of the balun, with a sufficiently large hole to allow the parallel-wire transmission line to pass through. The side walls of the shield is realized by the connected interleaved vias same as in Chapter 4. The via wall is only at the H-plane, while at the E-plane there are only two metal strips connecting the two via walls.

To better demonstrate the effect of the shield, we have simulated the E-field at the surface of the antenna. Simulation results (Figure 5.14 (a) and (b)) showed that with this rectangular shield, the E-field is effectively confined within the shield. Thus, the edge diffraction effect of the surface wave on the gain and the radiation patterns can be alleviated.

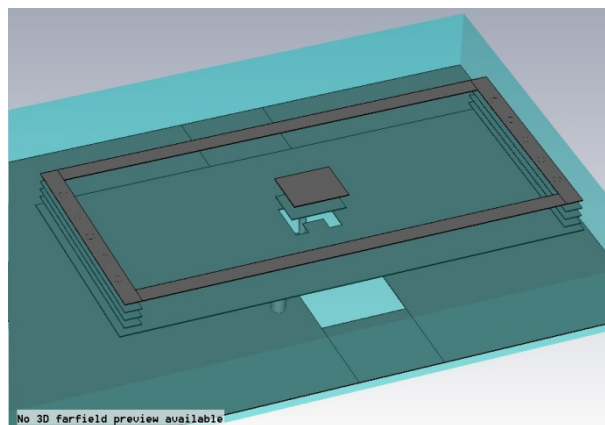
To further investigate the influence of the shield, we have simulated the reflection coefficient, the broadside gain, and the radiation patterns for the two antennas with different substrate size. The small antenna size is 6.6 mm x 5 mm, and the large size is 11.6 mm x 5 mm. The comparison of the reflection coefficient of the antennas with and without shield with different size can be observed in Figure 5.15. Firstly it can be seen that the antenna with shield has better reflection coefficient behavior. Without the shield, the reflection coefficient is influenced by the surface wave, thus the resonance frequencies are not stable. Some resonance frequencies happen in the antenna with smaller substrate, but they disappeared when the substrate size increases. The shield antenna, on the other hand, has more identical reflection coefficient behavior. The resonance frequencies are identical, and the level of the reflection coefficient is less than that of the antenna without shield.

The comparison of the antenna broadside gain with different configurations is demonstrated in Figure 5.16. The gain variation between the small and large unshielded antenna (Figure 5.16 (a)) is considerably larger than that of the shielded antenna (Figure 5.16 (b)). This demonstrated that due to the surface wave, the substrate size change will have profound influence on the unshielded antenna broadside gain but only minor influence to the shielded antenna gain. This is because when the substrate size increases, the sidelobes will build up, and the antenna maximum radiation does not close to the broadside anymore. The variation between the small antenna and the large antenna of the shielded antenna is less than 1 dBi.

Therefore, these analyses proved that the shield indeed alleviated the influence of the surface wave to the antenna radiation, and makes the antenna characteristic stable with regards to variation of the substrate size.

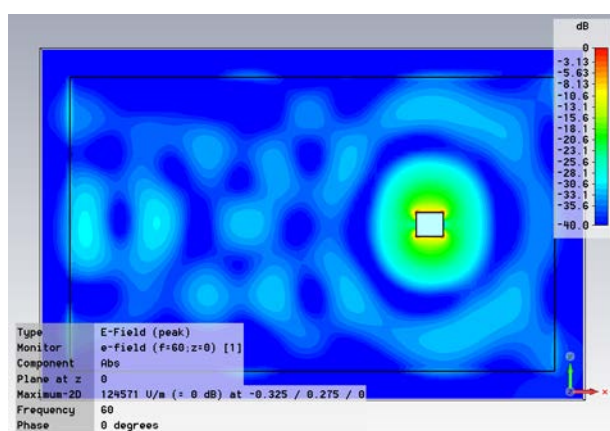


(a) Antenna with balun but without shield

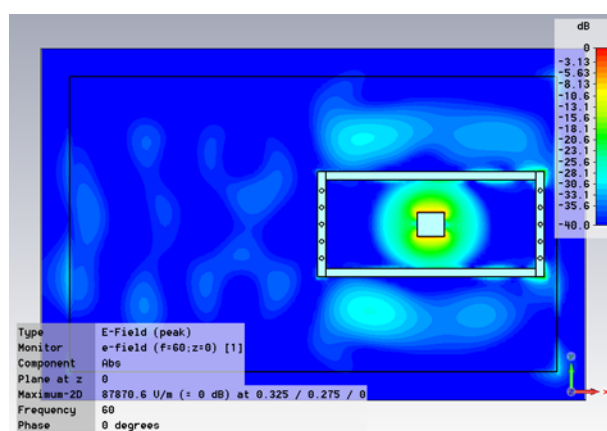


(b) Antenna with balun and shield

**Figure 5.13 Antenna with and without shield**

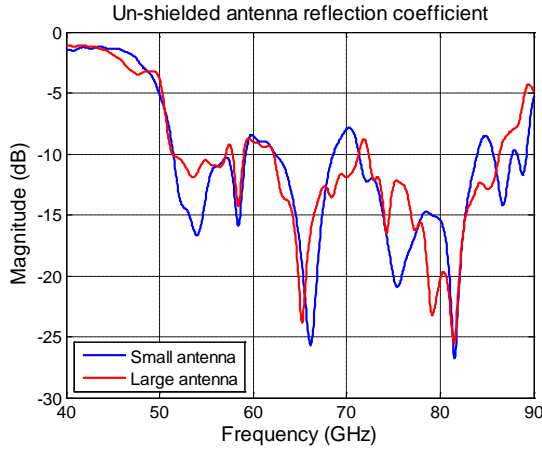


(a) Simulated E-field at the antenna surface of the unshielded antenna at 60 GHz

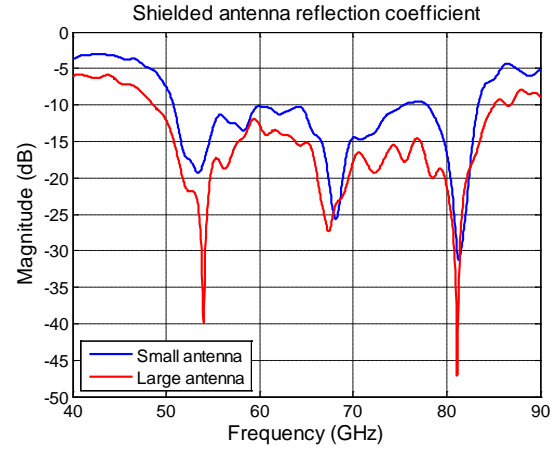


(b) Simulated E-field at the antenna surface of the shielded antenna at 60 GHz

**Figure 5.14 Simulated E-field at the antenna surface at 60 GHz (a) Antenna without shield (b) Antenna with shield**

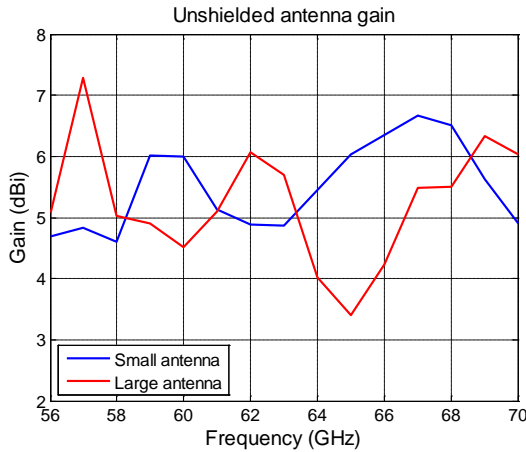


(a) Simulated reflection coefficient of the unshielded antenna with different size

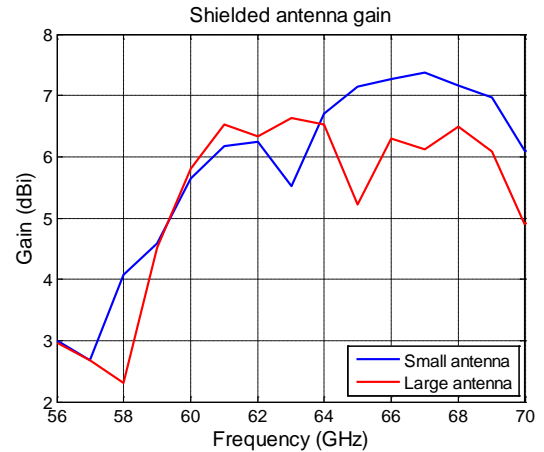


(b) Simulated reflection coefficient of the shielded antenna with different size

**Figure 5.15 Simulated reflection coefficient of the antenna with and without shield with different size (a) Simulated reflection coefficient of the unshielded antenna with different size (b) Simulated reflection coefficient of the shielded antenna with different size**



(a) Simulated unshielded antenna gain



(b) Simulated shielded antenna gain

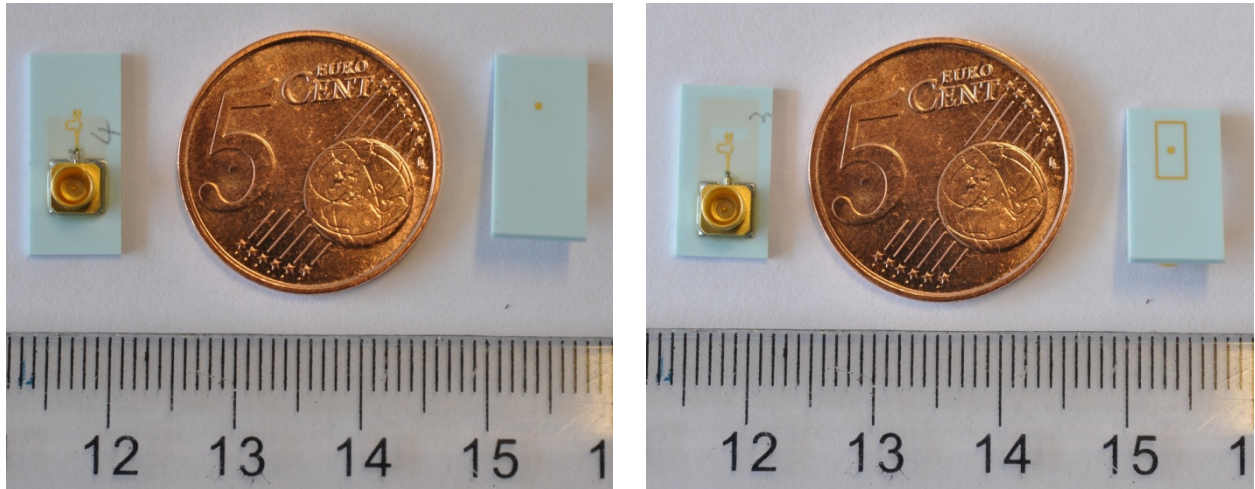
**Figure 5.16 Simulated broadside antenna gain of the antenna with and without shield**

## 5.5 Experimental verification and analysis

### 5.5.1 Manufactured antenna

The developed antennas have been manufactured to experimentally verify the simulated results and analyze impact of manufacturing tolerances such as uncertainty of the material and process as well as imperfection of connectors. To keep the dielectric loss low, a material system optimized for high frequency applications was employed, DuPont DP943<sup>®</sup> with  $\tan\delta = 0.002$  specified for 40 GHz [6]. The measurement performed by the manufacturer, Ilmenau University of Technology, revealed that the material has the real part of the dielectric permittivity of  $\epsilon_r = 7.54$  and indicated an upper limit of  $\tan\delta = 0.01$  at 60 GHz [7]. Figure 5.17 (a)

and (b) show the manufactured unshielded and shielded antenna. Due to manufacturing limitations, the ground plane of the balun has been realized using a 150  $\mu\text{m}$  grid, but the ground plane of the antenna as well as the antenna patches are realized using solid metal to ensure proper operation of the antenna.



(a) Manufactured unshielded antenna

(b) Manufactured shielded antenna

**Figure 5.17 Manufactured unshielded and shielded antenna (a) Manufactured unshielded antenna (b) Manufactured shielded antenna**

### 5.5.2 Antenna reflection coefficient measurement and analysis

To measure the antenna (which is connectorized by a mini-smp connector) using the network analyzer (which has 2.4mm coaxial connector), we have used a mini-smp to 2.92 mm adaptor, then used a 3.5 mm to 2.4 mm adaptor to connect to the network. Although this is not an ideal set up as the 2.92 mm standard only specified to 40 GHz and we measured the antenna up to 67 GHz, we had to use this configuration due to equipment limitations. Firstly, we measure the antenna reflection coefficients using the SOLT calibration standards, shown in Figure 5.18. The results for both antennas with and without shield are very different from the predicted results, and they have periodic resonance behavior. To investigate the deviation, we measured the reflection coefficient of the manufactured TRL thru calibration standard to examine the transition from the connector to the microstrip line (Figure 5.19). Similarity between the reflection coefficient of the antennas and that of the TRL was observed. This indicates that the measured reflection coefficient may actually be dominated by the reflection from the connector to the microstrip line (MS line) transition. To probe further, we examine the time domain TRL thru reflection coefficient by using inverse Fourier Transform (Figure 5.20). Four distinctive reflections can be identified. The first two reflections are coming from the mini-smp to 2.92 mm adaptor and 3.5 mm to 2.4 mm adaptor. The third reflection is from the connector to MS line transition, which dominates the reflection. The fourth reflection is the reflection from the other port. Due to the third large reflection, the actual antenna reflection is masked and is difficult to be accurately measured. Note that the reflections from the mini-smp to 2.92 mm adaptor and 3.5 mm to 2.4 mm adaptor are small in comparison to the reflection of the connector to MS line and the antenna reflection. Therefore the adaptors will not generate dominate reflections and thus are able to be used in this measurement.



To calibrate and eliminate the reflection from the connector to the MS line, we have used two approaches. The first approach is that we directly use the manufactured TRL calibration standards to calibrate the network analyzer (Figure 5.21). The other approach is that we transform the frequency domain reflection coefficients to time domain, and then use time gating technique to gate out the reflection from the adaptors and connectors to get the reflection of the antenna. Figure 5.22 shows the time domain reflected signal of the unshielded and shielded antenna before time gating and the time gate. The time gate is designed in such a way that it filters out the reflections from the connectors as much as possible and preserves all reflections from the antenna. Figure 5.23 shows the comparison of the filtered measured reflection coefficient and the predicted reflection coefficient.

The reflection coefficients obtained from both approaches still have some deviations comparing to the predicted results. To figure out possible reasons of the deviation, we have investigated each antenna's time domain reflection coefficient after correction (Figure 5.24). Firstly it can be seen that for both approaches, the reflections from the connectors to the microstrip line were not completely removed. The TRL calibration approach leaves more residues comparing to the time gate approach, which is due to the high reflection from the connector-MS line transition. As to the time gating technique, the reflection from adaptor 1 and 2 are completely removed, but due to the proximity of the connector-MS line reflection and antenna reflection, it is not possible to completely filter out the reflection from the connector-MS line transition. These residues give error in the measurement and cause the deviations. Nevertheless, by comparing the measurement results obtained using these two approaches it is still possible to conclude that the antennas, especially the shielded one, have a -10 dB impedance bandwidth from about 50 GHz to over 65 GHz. This gives us confidence that the antenna may work up to 78 GHz, as predicted.

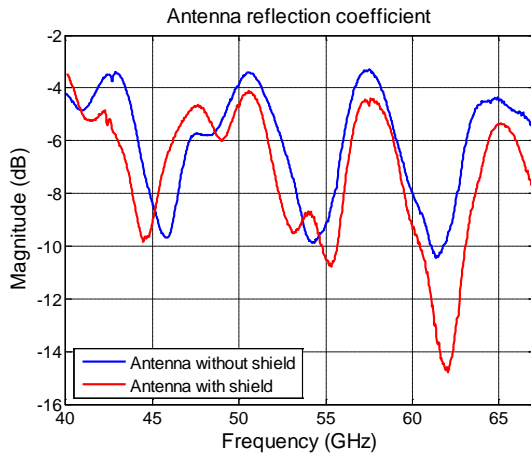


**Figure 5.18 Measured antenna reflection coefficient using the SOLT calibration standards**

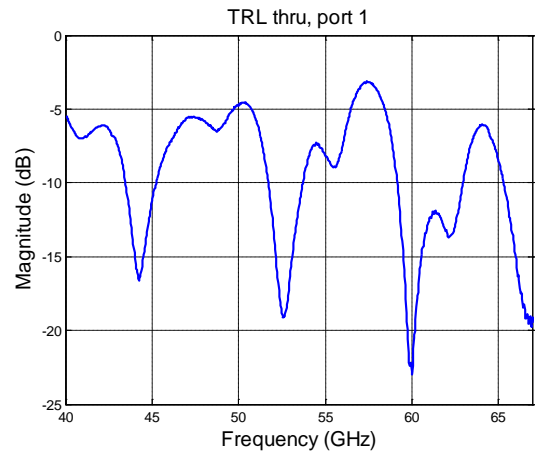


**Figure 5.19 Reflection coefficient of the TRL thru standard port 1**

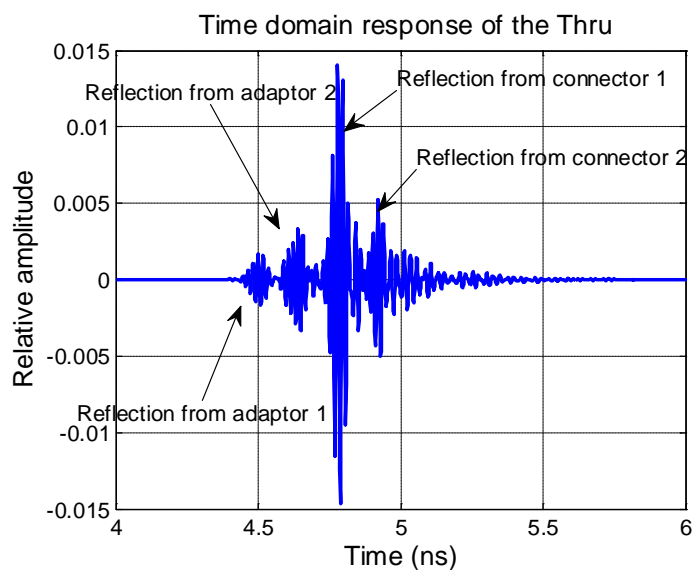
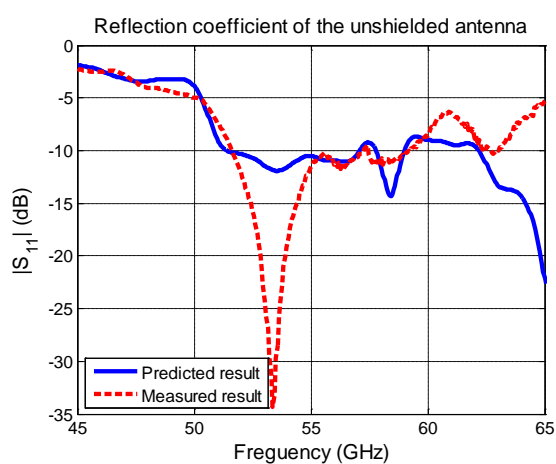
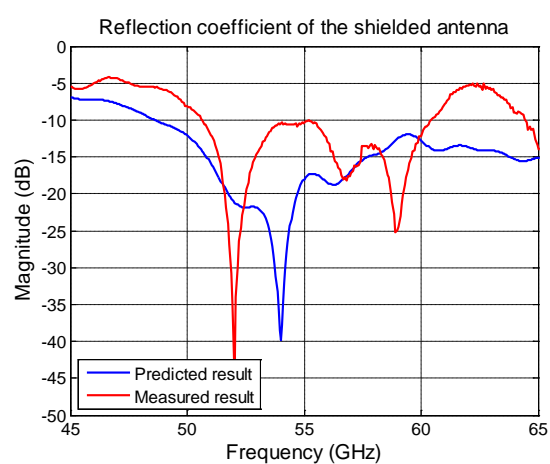


Figure 5.20 Time domain response of the TRL thru standard



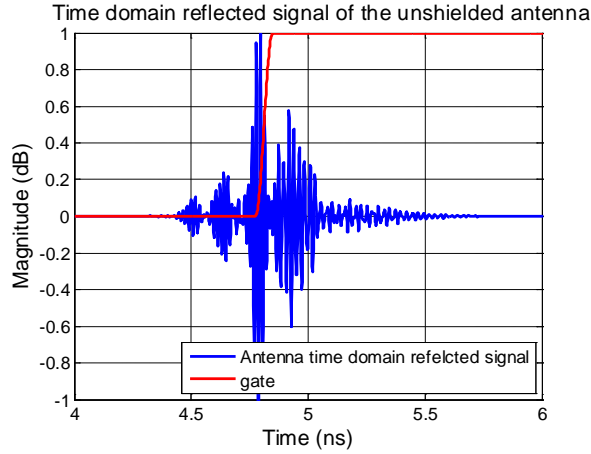
(a) Reflection coefficient of the antenna without shield



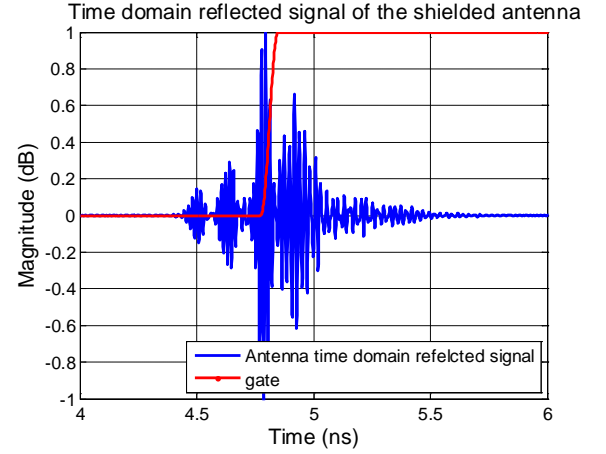
(b) Reflection coefficient of the antenna with shield

Figure 5.21 Reflection coefficient of the antenna with and without shield calibrated by TRL calibration (a) antenna without shield (b) antenna with shield



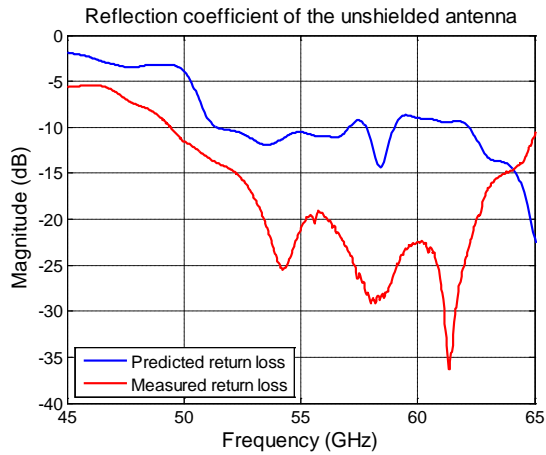


(a) Time domain reflected signal of the unshielded antenna before time gating and the gate

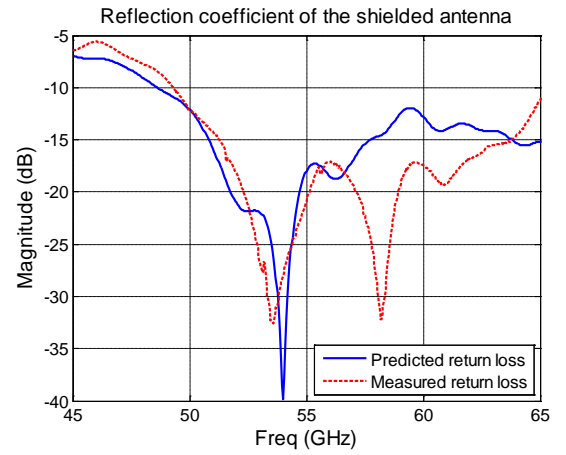


(b) Time domain reflected signal of the shielded antenna before time gating and the gate

**Figure 5.22 time domain reflected signal of the unshielded and shielded antenna measured using SOLT calibration (a) Unshielded antenna (b) Shielded antenna**

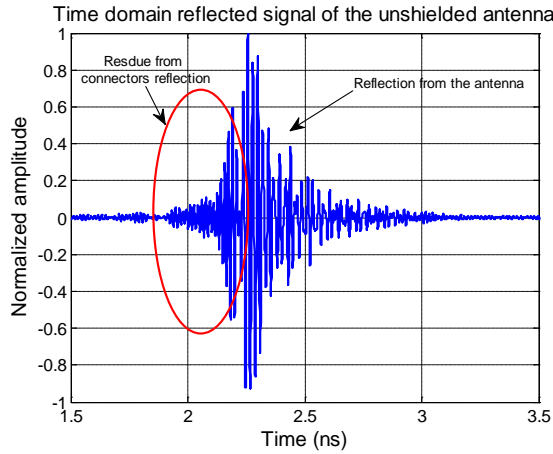


(a) Reflection coefficient of the unshielded antenna after time gating

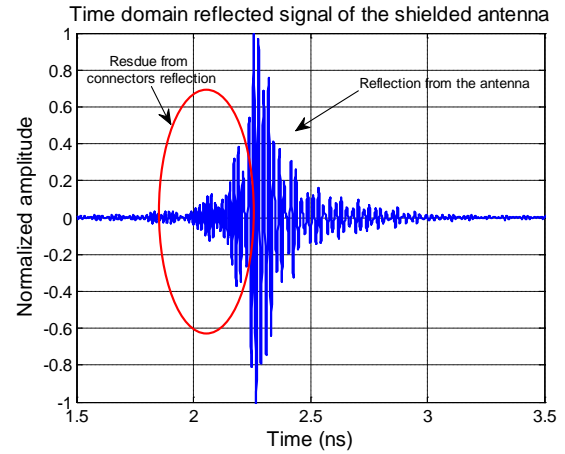


(b) Reflection coefficient of the shielded antenna after time gating

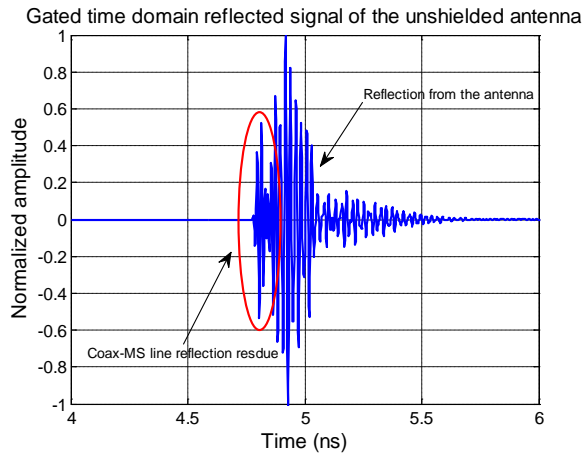
**Figure 5.23 Comparison of gated antenna reflection coefficient and the predicted antenna reflection coefficient (a) Unshielded antenna (b) Shielded antenna**



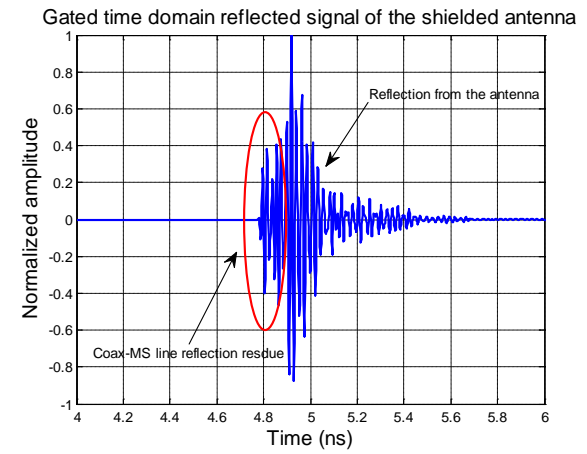
(a) Time domain reflected signal of the unshielded antenna using the TRL calibration



(b) Time domain reflected signal of the shielded antenna using the TRL calibration



(c) Time domain reflected signal of the unshielded antenna using the time gating



(d) Time domain reflected signal of the shielded antenna using the time gating

**Figure 5.24 Antennas time domain reflection coefficient after calibration (a) Unshielded antenna measured using the TRL calibration (b) Shielded antenna measured using the TRL calibration (c) Unshielded antenna measured using the SOLT calibration and time gating (d) Shielded antenna measured using the SOLT calibration and time gating**

### 5.5.3 Antenna broadside gain measurement

The antenna gain is calculated by the 3-antenna approach described in Chapter 2 section 2.5.1. A standard-gain-horn is used as reference. We have measured the gain in an anechoic chamber (see Chapter 2 section 2.3.1) and in free space (see Chapter 2 section 2.3.2).

The measured antenna broadside gains of the shielded and unshielded antenna in free space are shown in Figure 5.25 (a) and (b), respectively. The gain plots of these two antennas measured in anechoic chamber are shown in Figure 5.25 (c) and (d). Analyzing both measured results showed that the gain of the shielded antenna is in the region from 0 dBi to 8 dBi in the band from 50 GHz to 60 GHz. For

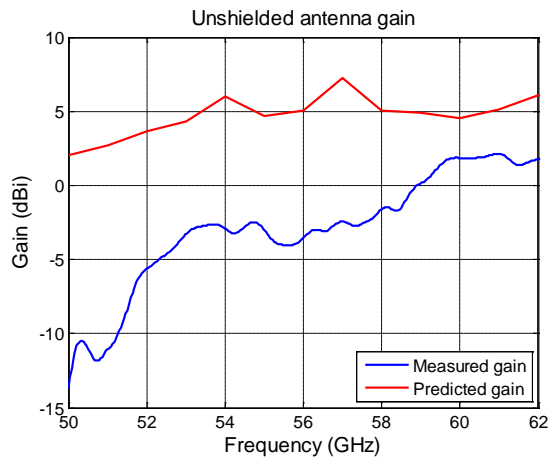
the free-space gain measurement, only SOLT calibration was performed, and for the anechoic chamber measurement, full TRL calibration was carried out. Thus, the strong reflection from the connector-MS line (Figure 5.18) was not calibrated out. This may explain why there are ripples in the measured gain in Figure 5.25 (b), and the gain measured in anechoic chamber is higher than that measured in free-space. The gain of the unshielded antenna is about 2 dBi lower than that of the shielded antenna in both measurement cases. This demonstrates that with the shield, the antenna mainly radiates towards the broadside, while the maximum radiation direction of the unshielded antenna is unpredictable due to the influence of the surface wave. This statement is further justified by examining the antennas' radiation patterns, which is shown in the next sub-section. The antenna has good polarization purity, which is illustrated in Figure 5.26.

To verify the antenna gain measurement, we have compared the standard-gain-horn gain measured in free space and anechoic chamber and its nominal gain, shown in Figure 5.27. It can be observed that the gain measured in anechoic chamber matches the nominal gain well, while the gain measured in free space is about 2 dBi lower than the nominal gain. The reason that the free space measured gain is lower may due to antenna misalignment, since it is very difficult to align the antennas in free space. The good agreement between the measured gain and the nominal horn gain verified the correctness of the gain measurement.

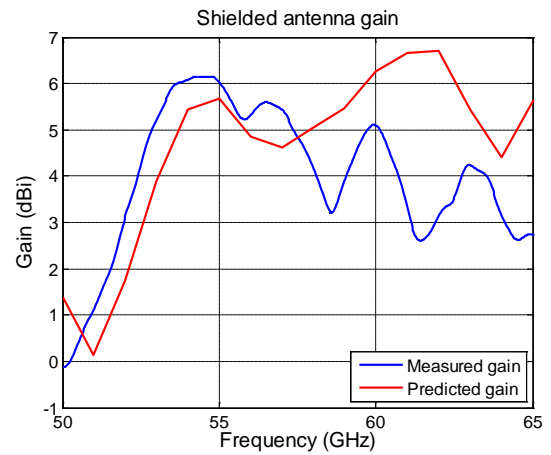
Simulated result indicated that the antenna has a radiation efficiency of about -2 dB (80%). Comparing with the K-band antenna, the radiation efficiency of the M-band antenna is lower, which is due to higher loss tangent of the material (0.01 @ 60 GHz comparing to 0.002 @ 40 GHz), and surface wave loss.

#### **5.5.4 Antenna radiation patterns measurement**

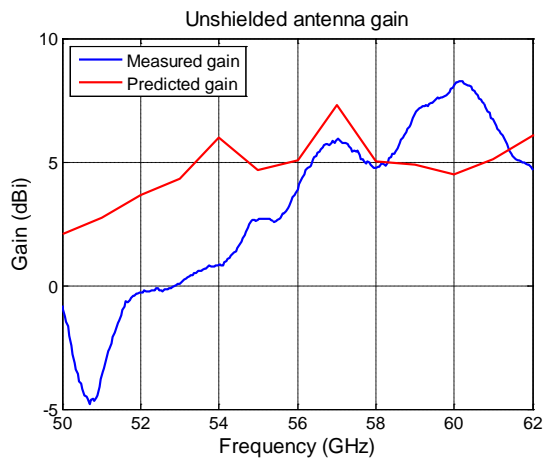
The antenna radiation patterns were measured in the anechoic chamber with a rotating rod described in Chapter 2 section 2.3.1. Unfortunately the rotating rod can only rotate from -90° to 90° due to the cable length limitation, thus the antenna back radiations were unable to measure. Figure 5.28 and Figure 5.29 show the measured shielded and unshielded antenna radiation patterns at 50 GHz, 56 GHz, and 62 GHz, at their E-plane and H-plane, respectively. For the shielded antenna, there is mainly one main lobe which radiates towards the broadside in both E-plane and H-plane and the radiation patterns were stable across the operational frequency band. For the unshielded antenna, the antenna radiates not towards the desired broadside direction but towards the side of the antenna and the radiation patterns were not similar at each frequency. This is especially seen at the H-plane, because the antenna is greatly extended in the H-plane to accommodate the balun, thus the influence of the surface wave was stronger. This demonstrates that with the shield, the antenna radiation patterns can be protected from the negative influence of the surface wave. The shielded antenna achieves a -10 dB beamwidth more than 90° for both E-plane (approximately from -60° to 60°) and H-plane (approximately -45° to 45°) within the operational frequency band.



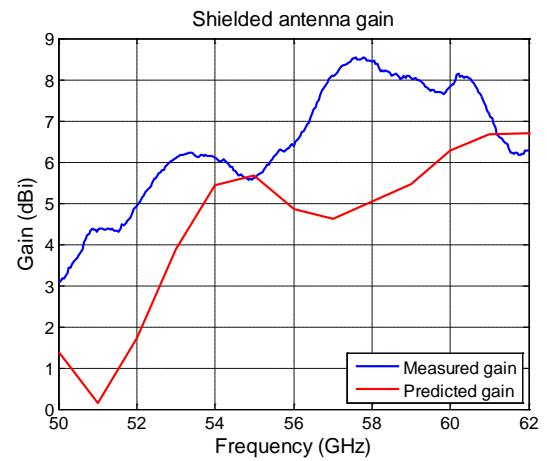
(a) Measured unshielded antenna gain in free space



(b) Measured shielded antenna gain in free space



(c) Measured unshielded antenna gain in anechoic chamber



(d) Measured shielded antenna gain in anechoic chamber

**Figure 5.25 Measured and predicted gain of the antenna with and without the shield (a) Unshielded antenna measured with the SOLT calibration (b) Shielded antenna measured with SOLT calibration (c) Unshielded antenna measured with the TRL calibration (d) Shielded antenna measured with the TRL calibration**

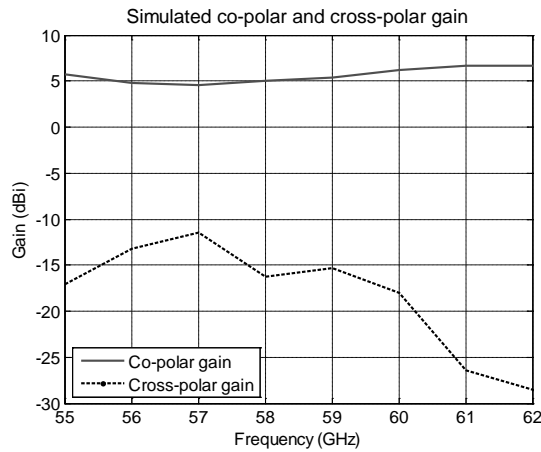


**Figure 5.26 Predicted co- and cross-polar gain**

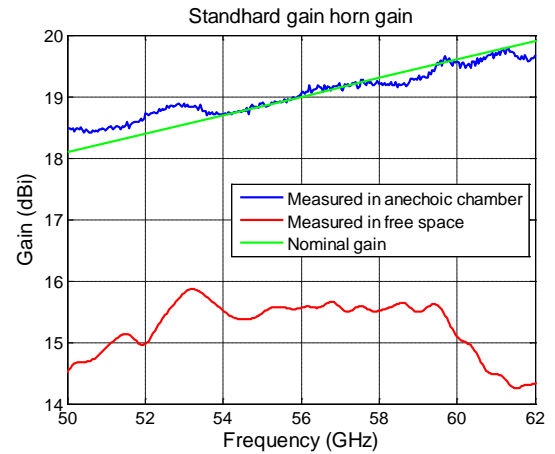
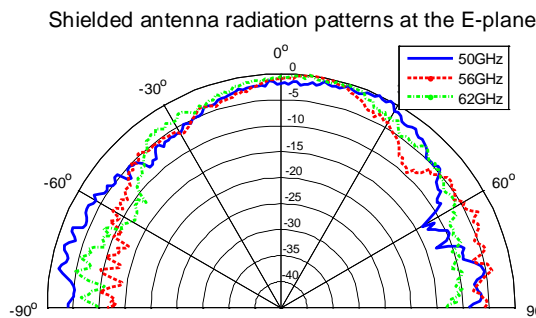
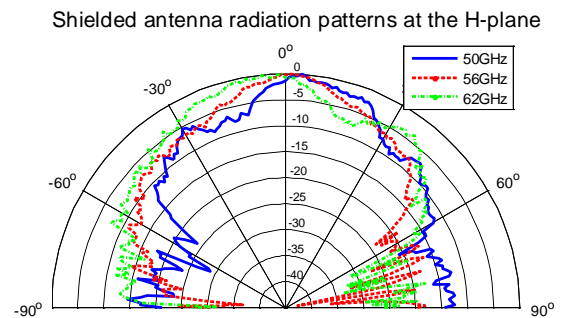


**Figure 5.27 Measured and nominal standard-gain-horn gain**

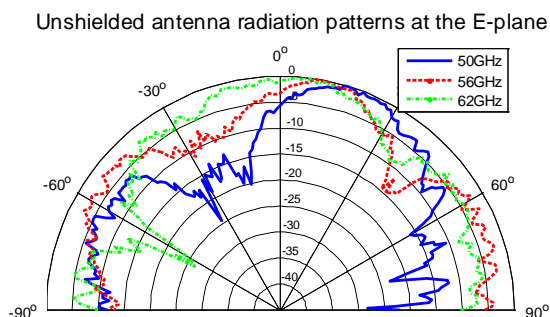


(a) Shielded antenna radiation patterns at the E-plane

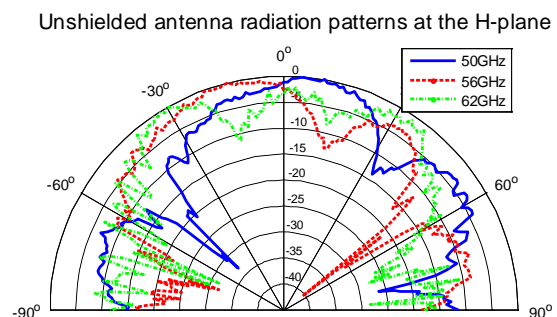


(b) Shielded antenna radiation patterns at the H-plane

**Figure 5.28 Radiation patterns of the shielded antenna at the E-plane and the H-plane (a) E-plane (b) H-plane**



(a) Unshielded antenna radiation patterns at the E-plane



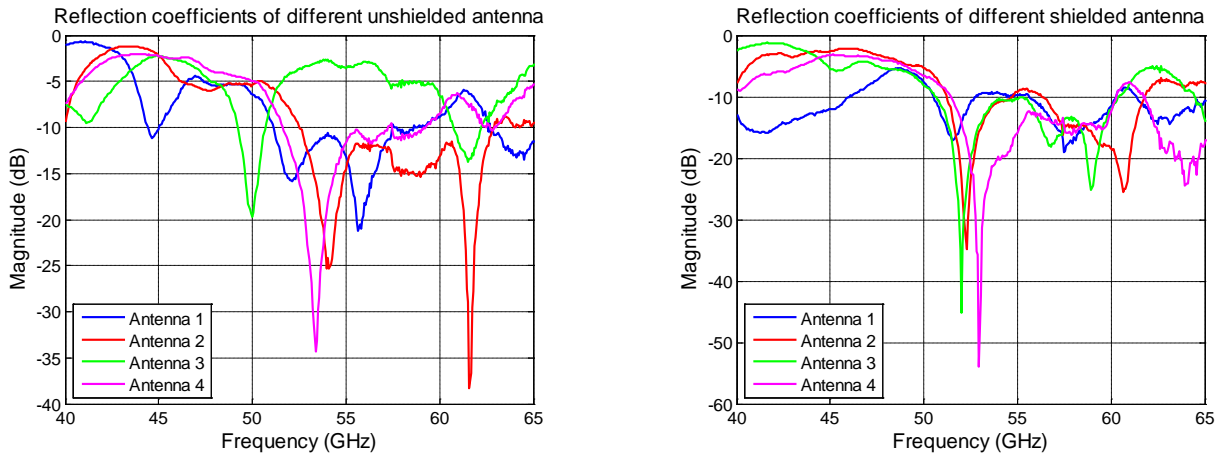
(b) Unshielded antenna radiation patterns at the H-plane

**Figure 5.29 Radiation patterns of the unshielded antenna at the E-plane and the H-plane (a) E-plane (b) H-plane**

### 5.5.5 Manufacturing variations

Four identical antennas were manufactured for both unshielded and shielded antenna and their reflection coefficients are compared in Figure 5.30. The variation between the reflection coefficients of the unshielded is larger than that of the shielded antenna. For the unshielded antennas, only the antenna 2 and antenna 3 have similar performance. For the shielded antennas, only reflection coefficient of antenna 1 has different behavior because the connector was not properly soldered to the antenna 1. Comparing Figure 5.30 to Figure 4.34, it can be observed that at the M-band the antenna reflection coefficient is quite sensitive to the processing variations comparing to the antennas in the K-band. One reason is that the wavelength in the M-band is very short thus small variation in physical dimensions will cause larger electrical dimension change at the M-band. The other reason is that the LTCC material is only specified up to 40 GHz. Therefore the LTCC material manufacturer does not guarantee the stability of the material at the M-band.

Another observation is that the behavior of the reflection coefficients of the shielded antennas is more stable than that of the unshielded antennas. This may suggest that by adding the shield, the antenna performance is less sensitive to the manufacturing process.



(a) Reflection coefficients of different unshielded antennas

(b) Reflection coefficients of different shielded antennas

**Figure 5.30 Reflection coefficients of different unshielded and shielded antennas measured using the TRL calibration (a) Reflection coefficients of different unshielded antennas (b) Reflection coefficients of different shielded antennas**

## 5.6 Integrated antenna design

The designed antenna has been intended to be integrated with MMICs (Figure 5.31). The package is a TX-RX radar head. Unfortunately the conductive glue used was too lossy at mm-wave frequency, thus the MMICs were unable to connect to the antenna. Therefore, no measurement results were available.

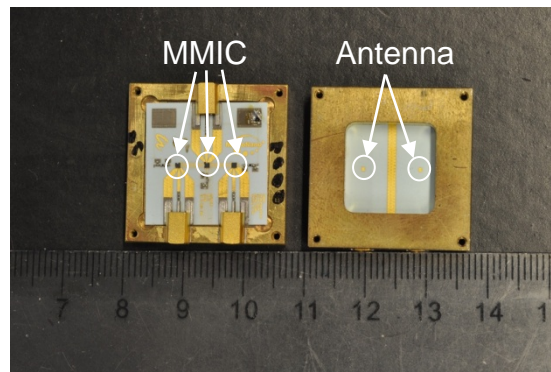


**Figure 5.31 Manufactured integrated M-band antenna with MMICs**

## 5.7 Conclusions

In this chapter I developed a M-band differentially-fed, UWB antenna using the LTCC technology. Several challenges associated with this problem such as how to achieve large impedance bandwidth, how to obtain good radiation characteristics, and how to realize the antenna using the LTCC technology were analyzed. The analysis and optimization of radiating element geometry resulted in a development of a novel antenna. The large antenna bandwidth is achieved by utilizing ASP antenna architecture with H-shaped aperture. The H-shaped aperture is excited by a parallel-transmission line. By using this feeding technique the antenna can have a -10 dB impedance bandwidth from 50 GHz to 78 GHz (44%) with very simple antenna architecture. The parallel-transmission line served as differential input which can be directly integrated with differential MMICs.

Since the antenna architecture is very simple, realizing such antenna with the LTCC technology faces much less trouble comparing to the antenna proposed in Chapter 4. Nevertheless, the high relative permittivity of the LTCC material induces severe surface waves which substantially degrade the antenna radiation characteristics. To solve this issue, a novel simple rectangular-shaped shield is added to surround the antenna. Simulation results showed that this shield can effectively reduce and confine the surface wave and consequently improve the antenna performance. The proposed antenna can be easily integrated with differential MMICs. The simplified shield demonstrated that by adding extra structures behind the antenna (whether it is a balun or differential MMIC) or change the substrate dimensions, the antenna reflection coefficient, gain, and radiation patterns will not be significantly influenced. This is an important feature and assures the antenna performance in the integrated environment.

Dedicated version of the antenna (with integrated balun) has been manufactured and experimentally verified to examine the theoretical model. The measured reflection coefficient is qualitatively matches the predicted one. The deviation is mainly from the high reflection of the connector to the microstrip line transition, which is difficult to be removed. The measurements demonstrated that the proposed antenna has a -10 dB impedance bandwidth from 50 GHz to over 65 GHz, which has never been report in the literature. The antenna gain varies from 3.5 dBi to 8 dBi with about 80% efficiency within this frequency range, and the -10 dB beamwidth is at least from -45° to 45° for both E- and H-planes.

## References

- [1] Shi-Chang Gao, Le-Wei Li, Mook-Seng Leon, and Tat-Soon Yeo, "Wide-band Microstrip Antenna With an H-shaped Coupling aperture", *IEEE Trans. on Vehicular Technology*, vol. 51, p.p. 17-26, 2002
- [2] Quan Xue, Xiu Yin Zhang and Ching-Hong K.Chin, "A Novel Differential-fed Patch Antenna", *IEEE Antennas and Wireless Propagation Letters*, vol. 5, p.p. 471-474, 2006.
- [3] A. E. I. Lamminen, J. Säily, and A. R. Vimpari, "60-GHz Patch Antennas and Arrays on LTCC With Embedded-Cavity Substrates", *IEEE. Trans. on Antennas and Propagation*, Vol. 56, No. 9, pp. 2865-2874, September 2008.
- [4] A. Panther, A. Petosa, M. G. Stubbs, and K. Kautio, "A Wideband Array of Stacked Patch Antennas Using Embedded Air Cavities in LTCC", *IEEE Microwave and Wireless Components Letters*, Vol. 15, No. 12, December 2005.
- [5] Y. Venot, K. Schuler, and W. Wiesbeck, "Tapered Slot Antenna for LTCC Multilayer Substrate Integration in mm-Wave Applications', *INICA-2003 ITG-conference on Antennas, ITG-Fachbereich*, pp. 49-52, Germany, Spetember 17-19, 2003.
- [6] DuPont Microcircuit Materials: 943 low-loss green tape [Online]. Available: [http://www.dupont.com/MCM/en\\_US/PDF/datasheets/943.pdf](http://www.dupont.com/MCM/en_US/PDF/datasheets/943.pdf)
- [7] L. Alhourri, S. Rentsch, R. Stephan, J.F. Trabert, J. Müller, and M. Hein, "60 GHz Patch Antennas in LTCC Technology for High Data-Rate Communication Systems", *INICA '07*, Munich, 28-30 March 2007, pp. 186-189
- [8] R. Li, G. DeJean, M. M. Tentzeris, J. Papapolymerou, and J. Laskar, "Radiation-Pattern Improvement of Patch Antennas on a Large-Size Substrate Using a Compact Soft-Surface Structure and Its Realization on LTCC Multilayer Technology", *IEEE Trans. on Antennas and Propagation*, vol. 53, No. 1, pp. 200-208, 2005.



## **6. UWB MIMO Sparse Arrays for Near-Field Imaging**

### **6.1 Introduction**

In this chapter we address development of UWB antenna arrays for high-resolution near-field imaging radar applications such as concealed weapon detection (CWD). These radars are aimed to produce 3-D images with fine cross- and down-range resolution as well as low sidelobe level, while having antenna arrays with small aperture size and small number of elements.

High performance requirements contradict to the requirement of a small element number, so development of antenna arrays for such radar is very challenging. As discussed in Chapter 1, the state-of-the art UWB antenna arrays for imaging radar are mostly 1-D arrays with mechanical scanning or 2-D arrays with non-optimum topology. Thus they cannot fulfill the requirements mentioned above (especially fast data acquisition time and small number of elements). We propose to make a step beyond the state-of-the-art towards MIMO arrays and demonstrate that by separating the antenna array into a transmit antenna sub-array and receive antenna sub-array, it is possible to achieve 2-D sparse real-aperture array with fine cross-range resolution and a reduced antenna aperture size.

The chapter is organized as follows. The performance of a UWB array evaluation is discussed in Section 6.2. Then we discuss possible approaches to realize such array in Section 6.3. Section 6.4 discusses the 1-D UWB antenna array design in general. Section 6.5 discusses MIMO antenna array design. Section 6.6 demonstrates how we use the proposed approaches for application-driven 2-D UWB MIMO antenna array designs. The experimental verification of the designed array is shown in section 6.7. The conclusions are given in section 6.8.

### **6.2 UWB array performance evaluation and presentation**

#### **6.2.1 UWB antenna array pattern calculation**

To design and investigate the properties of the UWB antenna array, we use theoretical model of antenna array with isotropic radiators and ignore the interaction between the elements. The antenna performance is evaluated by the point spread function (PSF), which is the image of a point-like scatterer. This makes the analysis easier and we can focus on the impact of antenna topology on the PSF. In addition, by comparing the measured PSF and simulated PSF enables us to evaluate the impact of real element and element interaction to the array performance. Classical algorithm to calculate the PSF such as diffraction stack is by propagating each collected time-domain range profile backward in reverse time. This will move the observed events from the data acquisition position to their true spatial position and generates the image of the targets. Although the formulation of the diffraction stack algorithm is simple and versatile, the fact that it is not based on rigorous wave theory causes high sidelobe level in the image. A wave-equation-based successor of the diffraction stack algorithm, Kirchhoff algorithm, delivers significantly higher image quality and lower sidelobe level. However conventional Kirchhoff migration algorithm only applicable either to an array with a number of identical transmit-

receive antenna pairs (or common-offset data gather) or to Synthetic Aperture Radar (SAR) [7]. Therefore, a modified Kirchhoff migration algorithm was proposed to incorporate multi-static scenarios [7]. Due to the better result from modified Kirchhoff migration, in this thesis the PSF will be mainly calculated by using modified Kirchhoff migration.

## 6.2.2 UWB antenna array PSF representation

An example of a 1-D UWB antenna array PSF calculated by the modified Kirchhoff migration is shown in Figure 6.1. The PSF has two spatial dimensions (cross-range in the horizontal plane and down-range), and it has no time dimension since the time dimension has been migrated by the modified Kirchhoff migration. The PSF is a 3-D presentation (cross-range, down-range, and power of each pixel), thus it is difficult to analyze and compare the array beam pattern by directly using this representation. Since the down-range resolution is mainly determined by the bandwidth and has less relevance to the array topology, while the cross-range resolution and sidelobe structure are closely related to the array topology, we are going to collapse the down-range dimension and keep the cross-range dimension only.

There are many ways to collapse the down-range dimension. The simplest way is to take a single cut through the center of the point-like scatterer. However, as one can see in Figure 6.1, the PSF is spread over a certain range, and selecting a single cut only through the center of the scatterer will inevitably miss some high sidelobes which exist outside the cut, thus mislead the results. Another approach to collapse the down-range is by taking an average cut within a range  $[R_1, R_2]$ , as Figure 6.2 (a) shows. The averaged PSF (Figure 6.2 (b)) is then calculated as:

$$avg\_PSF(\phi) = \sum_{r=R_1}^{R_2} PSF(\phi, r) / (R_2 - R_1) \quad (6.1)$$

Although this approach takes the sidelobes within a range into account, the drawback is that it overlooks sidelobe level. For example, the maximum sidelobe level of the average cut in Figure 6.2 (b) is about -11.58 dB at  $\pm 44^\circ$ , but Figure 6.2 (a) shows that all the level of the sidelobes are actually below -25 dB. This is because by summing the PSF cuts from  $R_1$  to  $R_2$ , the sidelobes will be built up mistakenly. In addition, by taking different  $R_1$  and  $R_2$ , the averaged sidelobe level will also be different. Larger range may results in higher sidelobe level while smaller range may result in smaller sidelobe level.

To find a proper way to collapse the down-range, we have examined Figure 6.3 which is an example of a 3-D PSF. We observed that the clutter is caused by the maximum value of a sidelobe, rather than the average value. Thus, a proper method to examine the PSF is the maximum projection method. This method collapses the down-range dimension onto its angular dimensions and treats the maximum envelop of this projection as a radiation pattern (Figure 6.2 (c)). This projection shows the maximum energy envelop of the PSF, and shows the maximum angular side energy that would produce artifacts in the image as well as the maximum angular bandwidth.

The PSF of the 2-D antenna array has three- dimensional support: cross-range in both horizontal and vertical plane and the down-range, while the PSF value shows

the power level of each voxel. Similarly, maximum projection method is used to analyze such PSF. However, the 3-D maximum projection method collapses the maximum of the 3D image onto three 2-D cut planes: The XZ-plane (Figure 6.4 (a)), the YZ-plane (Figure 6.4 (b)), and the XY-plane (Figure 6.4 (c)). The projection on the XZ-plane provides information regarding horizontal cross-range resolution and sidelobe structure. The projection on the YZ-plane provides information regarding vertical cross-range resolution and sidelobe structure. The projection on the XY-plane provides information regarding down-range resolution and sidelobe structure.

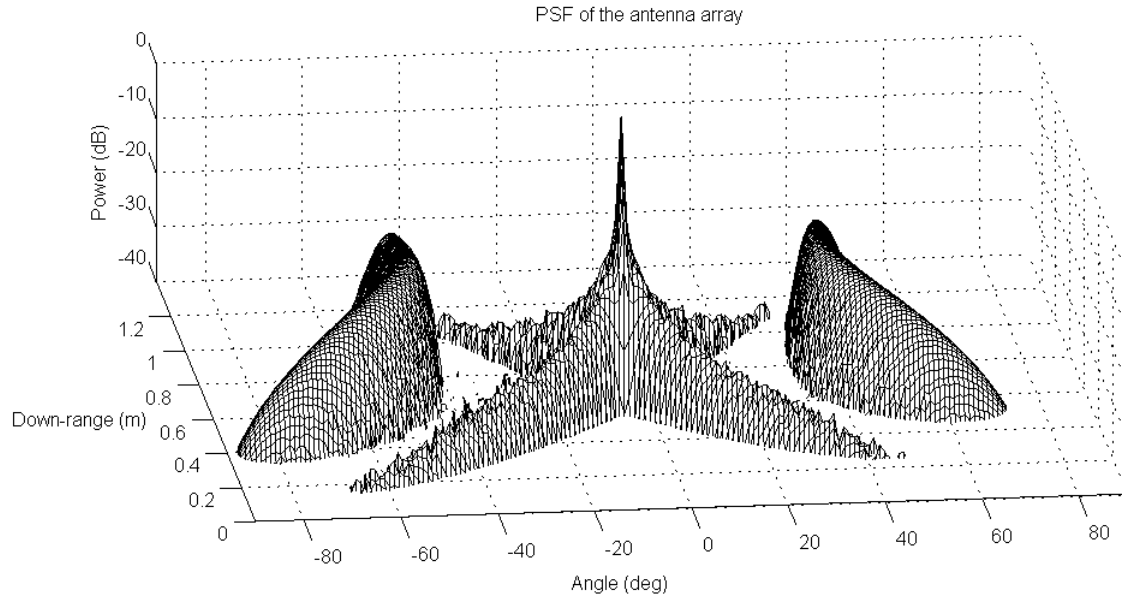
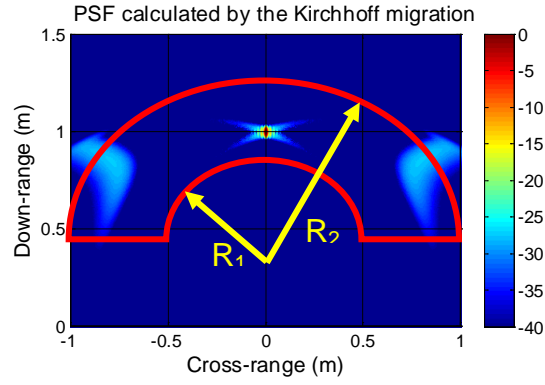
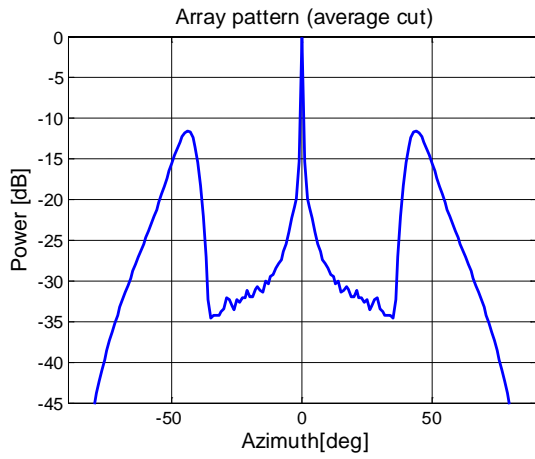


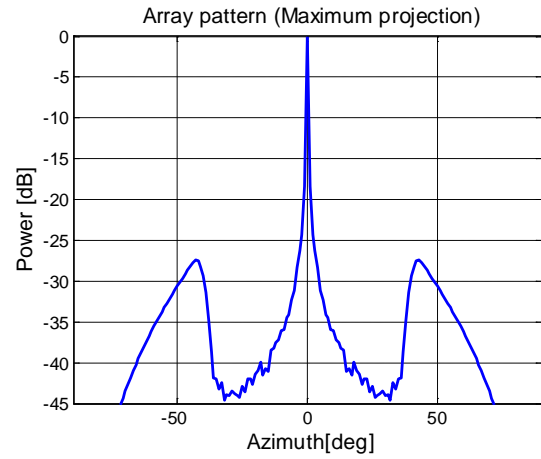
**Figure 6.1 Example of a 1-D UWB antenna array PSF calculated by the modified Kirchhoff migration**



(a) Range used to calculate the averaged PSF



(b) Averaged PSF of a 1-D array



(c) Maximum projected PSF of a 1-D array

**Figure 6.2 Different PSF representation of a 1-D array (a) Range used to calculate the averaged PSF (b) Averaged PSF of a 1-D array (c) Maximum projected PSF of a 1-D array**

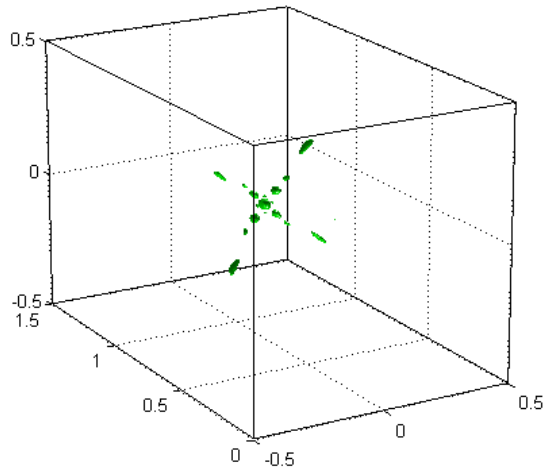
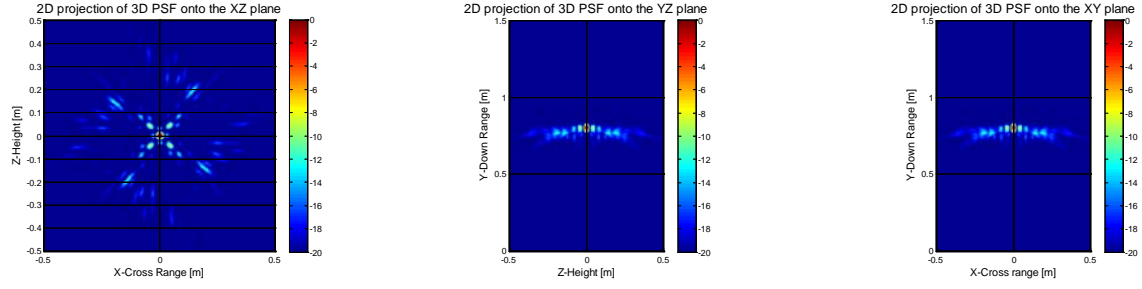


**Figure 6.3 An example of a 3-D PSF of a 2-D array**



(a) 2-D projection of 3-D PSF onto the XZ plane

(b) 2-D projection of 3-D PSF onto the YZ plane

(c) 2-D projection of 3-D PSF onto the XY plane

**Figure 6.4 2-D projections of the 3-D PSF onto different planes (a) Projection onto the XZ plane (b) Projection onto the YZ plane (c) Projection onto the XY plane**

### 6.3 Existing 2-D imaging array design approaches

To obtain a 3-D image, both down-range and cross-range resolution are important. While fine down-range resolution can be achieved due to a large operational bandwidth [1], the cross-range resolution is mainly realized by the array aperture size [2]. The most common way to realize large array aperture (thus fine cross-range resolution) is synthetic aperture radar (SAR) [3]. This well-developed technique is a side looking radar system scanned over a long linear aperture using the motion of a host aircraft or satellite. For the near-field imaging system, SAR is done by spatially sample the echoes in the target(s) area using a mechanical scanner. The echoes received at different positions are then post-processed to resolve the target(s) image [4]. Although SAR is a simple, versatile, and well-developed technique, it can only be implemented by moving one or more antennas over relatively immobile targets. To increase the data acquisition speed, 2-D real-aperture array is an essential step towards high-resolution real-time imaging applications. In general, to avoid high sidelobes in the resulting image, the antenna element spacing within an array should be less than half-wavelength. However, this dense spacing will lead to large number of elements, which causes several problems such as high cost, heavy weight, complex electronics design, large data flow, and severe coupling between elements.

A compromise between SAR and densely spaced 2-D array is by using a single-transmit multiple-receive (SIMO) 1-D array to electrically scan one dimension and use a mechanical scanner to scan another dimension [5]. This approach was demonstrated effectively to provide high quality image with reasonably fast data acquisition time and cost. Nevertheless, this approach still requires mechanical scanning, which is a bottle neck of the scanning speed.

In recent years the multiple-input multiple-out (MIMO) array has attracted attentions in both communication and radar applications. MIMO configuration uses different transmit antennas and receive antennas, and is able to provides design diversity of transmit/receive antennas and waveforms. This design diversity and freedom enable superior capabilities for imaging. By exploiting MIMO configuration, it is possible to achieve fine cross-range resolution with relative small elements and large element spacing [8][11]. This leads to better clutter suppression, faster data acquisition rate, and improved target shape reconstruction. As a result, 2-D real-aperture MIMO

array configuration is considered as one of the promising solutions for real-time high quality imaging radar applications.

In this chapter the main attention will be given to UWB MIMO array design.

## 6.4 Investigation of UWB antenna array behavior

Before investigating the MIMO array configuration, we firstly investigated two important array properties of UWB array for imaging: sidelobe behavior with respect to element spacing and impact of the mutual coupling on the image quality.

### 6.4.1 Sidelobe behavior with respect to element spacing

In narrow band (NB) phased array, if the element spacing is larger than half wavelength, grating lobe will occur [1]. The grating lobes cause severe problems to radar image such as clutter and even fake target image. It was demonstrated in [8] that UWB arrays have a very distinctive feature comparing to the conventional NB phase array that the radiation patterns of the UWB antenna arrays do not have any behaviors similar to grating lobes.

However, the condition and the algorithm to derive the beam pattern in [8] is not the same as in this research. To examine the applicability of this distinctive UWB feature to the application in mind (described in Section 6.6), we have calculated several PSFs with relative bandwidth of about 57% (which is defined by the application requirements) and with different element spacing using modified Kirchhoff migration. The results are shown in Figure 6.5, where  $\lambda$  is the wavelength at the central frequency. This figure clearly indicates that there is only one mainlobe even the element spacing is as large as  $2\lambda$ , and no sidelobe plateau such as [8] thanks to the rigorous full-wave-equation based formulation. However, by increasing the element spacing, the sidelobe level increases and the maximum sidelobe peak shifts towards the mainlobe. When the element spacing increased from  $\lambda/2$  to  $\lambda$ , the sidelobe moves into the visible region and a substantial increase of the maximum sidelobe level is observed (from below -50 dB to -27.4 dB). When the element spacing increases from  $\lambda$  to  $2\lambda$ , the maximum sidelobe peak moves towards the mainlobe and its magnitude increases. However, both the increment of sidelobe level and the approaching speed of the sidelobe to mainlobe decreases. This indicates that the influence of element spacing is decreasing when the element spacing increases.

As a result, although the UWB antenna array does not have grating lobe problem as the narrow band arrays have, and large element spacing does not raise the sidelobe level much, it is still desired to keep the element spacing as small as possible to not only keep the sidelobe outside the area of interest but also reduce the sidelobe level.

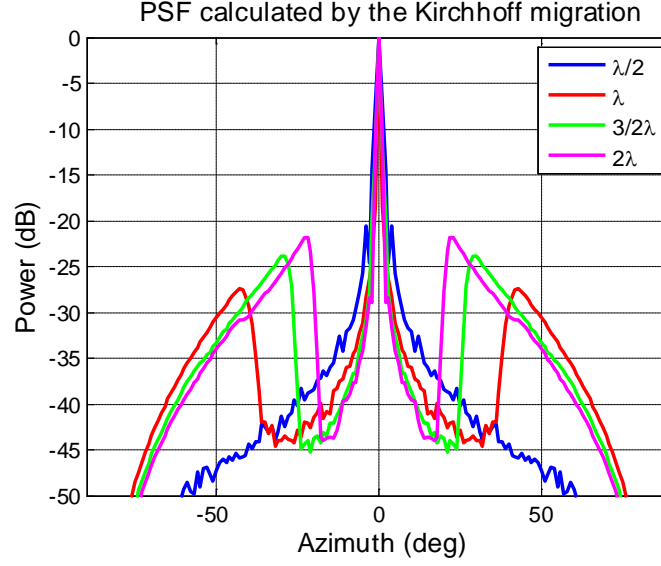


**Figure 6.5 PSF of one-dimensional equally spaced antenna array with different element spacing, fractional bandwidth = 57%**

#### 6.4.2 Impact of antenna mutual coupling

To evaluate the impact of antenna mutual coupling on the antenna array imaging performance, we have considered model shown in Figure 6.6. The model consists of 7 shielded loop antennas with diameter of 3 cm [9] aligned along their H-plane with separation of 7 cm. The antennas are modeled using the Pocklington integral equation [1], and were solved by commercially available EM solver FEKO [17]. This model is computationally simple thus we can concentrate on the influence of the antenna mutual coupling.

Firstly we investigate the sensitivity function of each element. The sensitivity function is defined as the induced voltage of an element when the array is impinged by a plane wave. The result showed that the sensitivity function of a loop within the array has a spike at around 3.6 GHz while in single loop does not have such spike (Figure 6.7). To investigate the cause of the spike, we have calculated the scattered E-field when a plane wave impinging on a single loop at 3.6 GHz (Figure 6.8 (a)). The cut-plane of this scattered field at different frequencies at the X-axis (Figure 6.8 (b)) showed that the scattered  $|E|$  field has oscillating behavior, and at the frequency of 3.6 GHz the local maximum of the scattered field is situated at 7 cm – at the position of a neighboring loop within the array. Therefore, at 3.6 GHz the coupling is strongest for array with element spacing of 7 cm and causes a distinctive spike in the sensitivity function.

This spike in the sensitivity function has a profound effect on the array near-field footprint. Both frequency domain and time domain footprint have been examined. The frequency domain footprint is obtained by first excite each loop separately with 1V to get the individual transfer function  $F_i(x, y, z, f)$ , then the focused footprint is calculated by [10]

$$F(x, y, z, f) = \sum_{i=1}^7 F_i(x, y, z, f) p(f) \exp(-j2\pi f \tau_i) \quad (6.2)$$

where  $F(x, y, z, f)$  is the focused frequency domain footprint,  $p(f)$  is the probing pulse which a second derivative Gaussian pulse with -10 dB bandwidth from 300 MHz to 3.3 GHz, and  $\tau_i$  is the time of flight from the  $i^{th}$  loop to the focused point and is given by

$$\tau_i = \frac{d_i}{c} \quad (6.3)$$

where  $d_i$  is the distance from the  $i^{th}$  loop to the focused point and  $c$  is the speed of light. Therefore,  $p(f)\exp(-j2\pi f\tau_i)$  is nothing more than the Fourier transform of  $p(t - \tau_i)$ . In other words, the footprint is obtained by applying time delayed pulse to each loop where the delay corresponds to the time needed for a pulse to travel from each loop to the focused point. The time domain footprint  $F(x, y, z, t)$  is then the Fourier transform of the frequency domain footprint  $F(x, y, z, f)$ .

Figure 6.9 (a) and (b) show the frequency domain footprint of the array with and without the element interaction, respectively. The focus point is located at 12 cm in front of the antenna array. We can observe that the element interaction results in widening of the mainlobe and deepening the nulls between mainlobe and sidelobes, and most of all, destroying the footprint after 3.6 GHz.

The focused time domain footprints of the array with and without element interaction are shown in Figure 6.10 (a) and (b). The size of focused time domain footprints is similar in both figures, but with element interaction, the footprint has about almost 1.5 ns long after-time ringing. This after-time ringing corresponds to the 3.6 GHz spike in the sensitivity function, and it will obscure small objects behind large objects.

Figure 6.11 shows the focused time domain footprint with and without element interaction, where the black circle is the -10 dB contour, and blue circle is -3 dB contour. We can clearly observe that without element interaction, the sidelobe of the footprint is slightly above -10 dB. However, with element interaction, the sidelobe level drastically increased to above -3 dB. This will drastically increase the clutter and deteriorate the image quality.

In conclusion, the antenna coupling has a profound influence on the near-field footprint of an antenna array. The major influence of the coupling is that it will alter the sensitivity function of the each element. If this change causes some frequency to have larger response than others, i.e., a spike in the sensitivity function, the focused footprint will have long after-time ringing and the sidelobe will be considerably increased. To avoid this effect, it is important to either design an element that will not have such coupling behavior, or arrange the element in such a way that the coupling will not cause a spike in the sensitivity function.



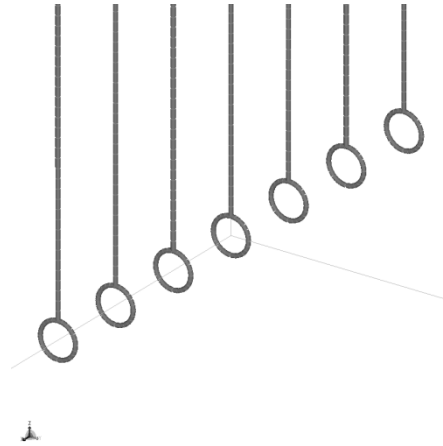


Figure 6.6 Antenna array model considered for mutual coupling analysis

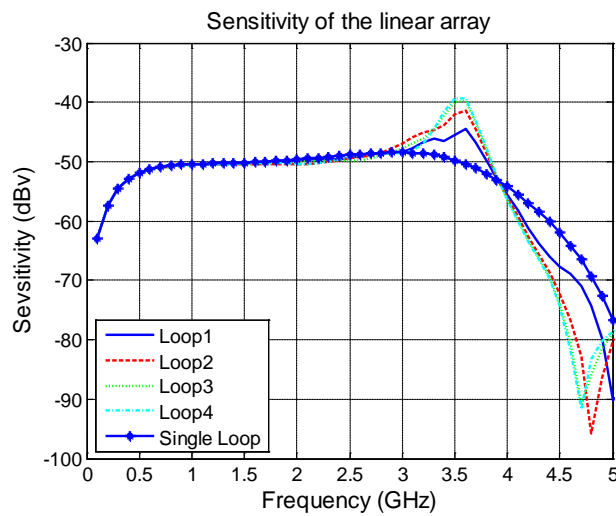
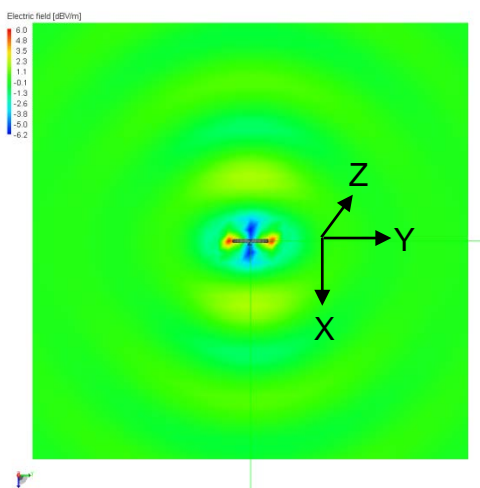
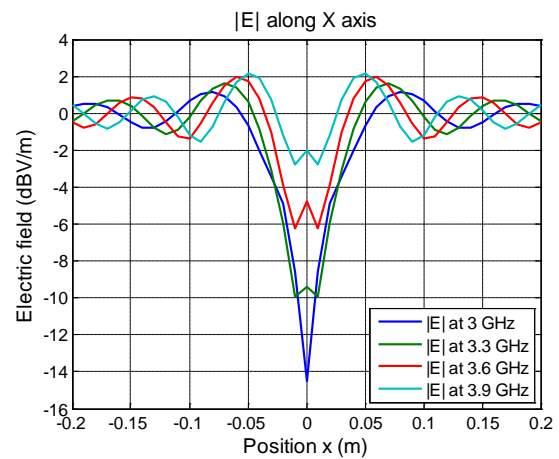


Figure 6.7 Sensitivity function of each loop

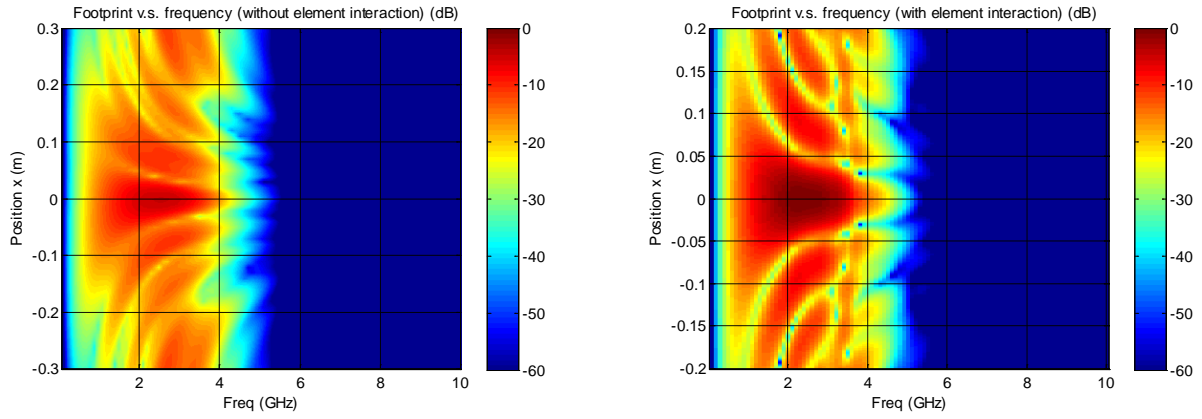


(a) 2-D E-field distribution at 3.6GHz



(b)  $|E|$  field at X-cut plane

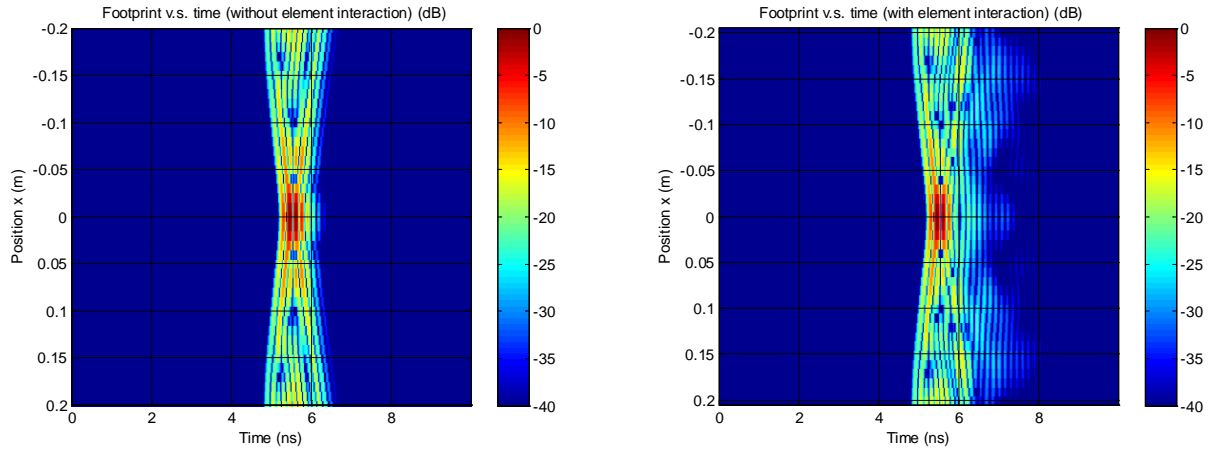
Figure 6.8 Distribution of total electrical field around a single loop at 3.6 GHz



(a) Frequency domain footprint of the array without element interaction

(b) Frequency domain footprint of the array with element interaction

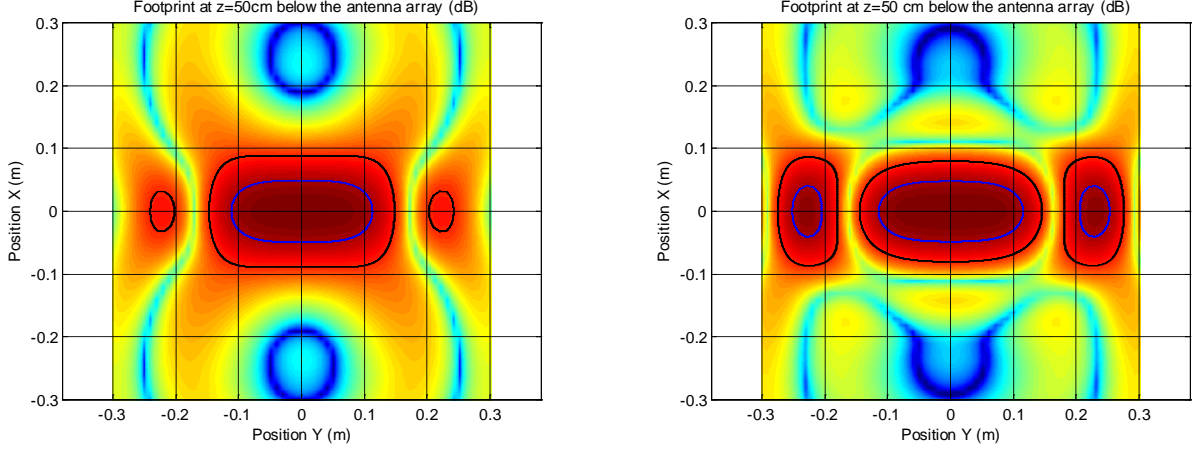
**Figure 6.9 Frequency domain footprint of the array with and without element interaction (a) With element interaction (b) Without element interaction**



(a) Time domain footprint without element interaction

(b) Time domain footprint with element interaction

**Figure 6.10 Time domain footprint of the array with and without element interaction (a) Without element interaction (b) With interaction**



(a) Focused time domain footprint without element interaction

(b) Focused time domain footprint with element interaction

**Figure 6.11 Focused time domain footprint with and without element interaction (a) Without element interaction (b) With element interaction, blue line indicates -3 dB contour and black line indicates -10 dB contour**

## 6.5 MIMO antenna array design

As discussed in section 6.3, MIMO array configuration is one of the most promising solutions for 2-D sparse real-aperture UWB antenna array applied in high quality imaging radar. Due to high dimensionality of 2-D MIMO arrays, direct design is almost impossible. So, we used rotational 1-D array analysis approach (see section 6.5.3) to reduce the problem into 1-D MIMO array design.

We have applied two different approaches to design 1-D MIMO arrays. The first design approach is based on linear uniformly spaced effective array, and the second approach is based on stochastic optimization algorithm. These two approaches are discussed in the first two sub-sections. Section 6.5.3 discusses how to design the 2-D MIMO array using the rotational 1-D array analysis.

### 6.5.1 Linear MIMO array design based on linear uniformly spaced effective array approach

There is no straightforward approach to synthesize a MIMO array topology from a desired PSF as SIMO array has. As a result, we have utilized effective array approach to design the MIMO array.

The UWB effective array  $E_{UWB}(\mathbf{r})$  can be expressed as the spatial convolution of the transmit sub-array aperture  $w_{Tx}(\mathbf{r})$  and the receive sub-array aperture  $w_{Rx}(\mathbf{r})$  as [11]:

$$\begin{aligned} E_{UWB}(\mathbf{r}) &= \int_{\{\mathbf{r}_{Tx}\}} w_{Tx}(\mathbf{r}_{Tx}) \cdot \delta(|\mathbf{r} - \mathbf{r}_{Tx}|) d\mathbf{r}_{Tx} * \int_{\{\mathbf{r}_{Rx}\}} w_{Rx}(\mathbf{r}_{Rx}) \cdot \delta(|\mathbf{r}_{Rx} - \mathbf{r}|) d\mathbf{r}_{Rx} \\ &= w_{Tx}(\mathbf{r}) * w_{Rx}(\mathbf{r}) \end{aligned} \quad (6.4)$$

The effective array approach enables the possibility to firstly design a SIMO array with desired PSF, and then factorize the SIMO array to obtain the MIMO array. Note

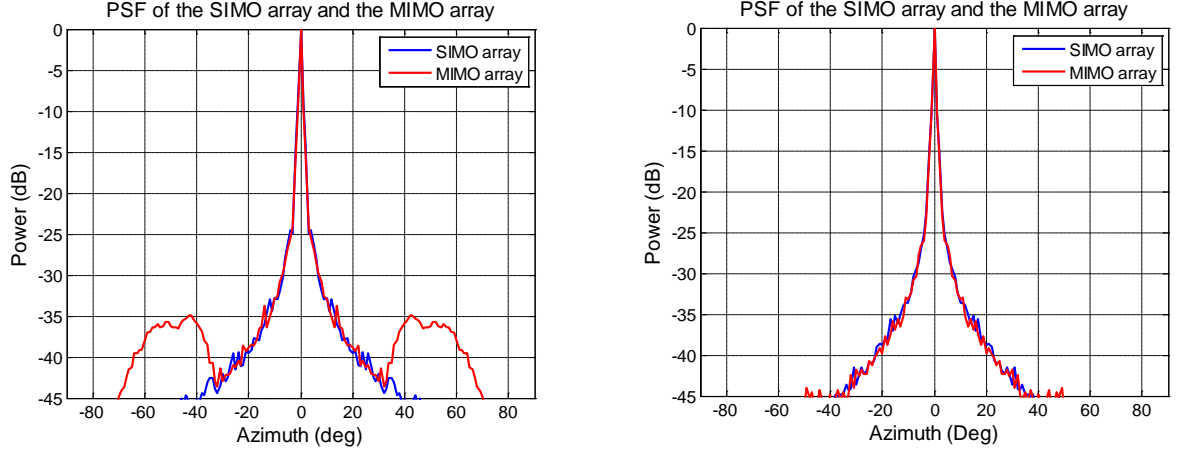
that the effective array relationship is derived under the far-field assumption, thus this relation is only exact when the target is in the far-field region of the array. Figure 6.12 (a) and (b) show the comparison of PSFs of a MIMO array and its equivalent SIMO array calculated when a point-like scatterer is located at 1 m ( $50 \lambda_c$ ) and 4 m ( $200 \lambda_c$ ). The results showed that the sidelobe of the PSF of the MIMO array is different than that of the equivalent SIMO array (-35 dB vs. below -45 dB) when the scatterer is at 1 m. But the PSF of the MIMO array approaches its counterpart of the equivalent SIMO array when the scatterer moves away from the array. When the scatterer is further than 4 m, the PSFs of the MIMO array and its equivalent SIMO array are identical in the region of interest (above -45 dB). Nevertheless, for the mainbeam region the PSFs of the MIMO array and its effective SIMO array are identical whether the scatterer is in the near-field region or far-field region. This is because the mainbeam region of a UWB array is called “interference region” and it has far-field zone behavior [8]. Although in the near-field region the PSFs of the MIMO array and its equivalent SIMO array are not identical, we still consider the PSF of the effective array is a good approximate to the PSF MIMO array to reduce the complexity of designing a MIMO array with desired PSF.

The design approach using the effective array method is as following: firstly the number of effective array antenna elements  $N_E$  is determined either by the requirement of the minimum sidelobe level or by the system requirement. After this the required cross-range resolution  $\delta_{cr}$  determines the effective array aperture size  $L_{eff}$  by [2]

$$L_{eff} = \frac{R}{\delta_{cr}} \cdot \lambda_c \quad (6.5)$$

where  $R$  is the possible target range and  $\lambda_c$  is the wavelength at the center frequency. Next, the element number of the transmit array and the receive array is chosen under the relation  $N_E = N_{Tx} \cdot N_{Rx}$  (the total number of the antenna elements is then  $N_{total} = N_{Tx} + N_{Rx}$ ). As a result, a uniformly spaced linear SIMO array with aperture size  $L_{eff}$  and element number  $N_E$  is obtained with desired PSF properties.

After the effective SIMO array is obtained, it should be factorized into the desired MIMO array using eq. (6.4). However, the factorization of a SIMO array into an MIMO array is not unique. A detailed strategy of how to factorize a SIMO array into an MIMO array is not the scope of this thesis and can be found in [11], Chapter 3.



(a) Target located at 1 m

(b) Target located at 4 m

**Figure 6.12 PSF of the MIMO array and its equivalent SIMO array for target at different range (a) target located at 1 m (b) target located at 4 m**

### 6.5.2 Linear MIMO array design based on optimization algorithm

Another approach to design a linear MIMO array is by using the optimization algorithms such as particle swarm optimization (PSO) or genetic algorithm (GA) to directly search possible transmit and receive sub-array configurations that can give desired PSF. PSO has been chosen to optimize the MIMO antenna array topology. PSO is a robust stochastic evolutionary optimization method benefiting from the movement and intelligence of swarms [12][13], and is proposed by Kennedy and Eberhart in 1995 [12]. It has been successfully applied in solving practical electromagnetic applications such as antenna shape design and optimization in Chapter 3 and in [13][14][15]. The main algorithm of PSO can be expressed as

$$\mathbf{v}_{n+1} = w * \mathbf{v}_n + c_1 * \mathbf{r}_1 * (\mathbf{p}_{best,n} - \mathbf{x}_n) + c_2 * \mathbf{r}_2 * (\mathbf{g}_{best,n} - \mathbf{x}_n) \quad (6.6)$$

$$\mathbf{x}_{n+1} = \mathbf{x}_n + \Delta t * \mathbf{v}_{n+1} \quad (6.7)$$

where  $w$  is inertia weights,  $\mathbf{x}$  is the matrix of the particles' positions,  $\mathbf{v}$  is the velocity of the particles,  $c_1$  and  $c_2$  are acceleration constants,  $\mathbf{r}_1$  and  $\mathbf{r}_2$  are two random vectors with uniform distribution over  $[0,1]$ ,  $\mathbf{p}_{best}$  is the best position of each particle, and  $\mathbf{g}_{best}$  is the best position of the entire swarm.  $\Delta t$  is the unit time step. The goodness of each particle's position is evaluated by a scalar fitness function. This fitness function takes the position in the solution space and returns a single number representing the value of this position. To obtain good results, the definition of the fitness function is extremely important and difficult. It directly influences the final imaging capability of the array.

The goal of the optimization is to find the TX array topology and RX array topology that provides required cross-range resolution and sufficient low sidelobe level. To achieve this, we proposed to define the fitness function  $f$  as following

$$f = \sum_{\phi_i=-90^\circ}^{90^\circ} a(\phi_i) [(\text{PSF}(\phi_i) - \text{mask}(\phi_i))] \quad (6.8)$$

where  $a(\phi_i)$  is a weighting function and  $\text{mask}(\phi_i)$  is the PSF mask which can be viewed as the desired PSF. The weighting function controls the weight of the difference between the PSF and the mask at different angle. For example, if the cross-range is most important, then we can set the weighting function near the mainbeam to 1 and the weighting function outside the mainbeam area to a lower value, such as 0.5 or 0.1, depending on the requirement. We can also set the weighting function at the sidelobe area to 1 and at the mainbeam a lower value. This enables us to tradeoff between the cross-range resolution and the sidelobe level. The target of the optimization is to find a TX array topology and a RX array topology which minimize the fitness function. The TX antenna elements positions and RX antenna elements positions together form the particle position vector  $\mathbf{x}$ . The flow chart of using the PSO to find the optimum MIMO array topology is shown in Figure 6.13.

An example of MIMO array design using PSO can be found in section 6.6.3.

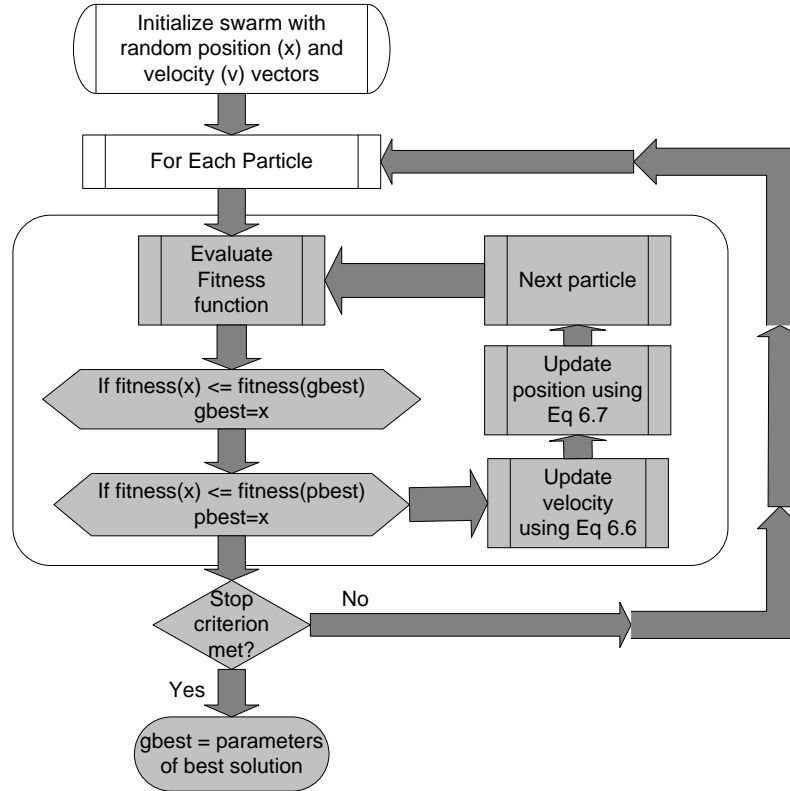


Figure 6.13 Flow chart of PSO method

### 6.5.3 Two-dimensional MIMO antenna array design

To obtain 3-D near-field images, a 2-D real-aperture antenna array is desired because it potentially can provide 3-D images within a snap shot, thus real-time imaging is possible. However, conventional 2-D real-aperture array topologies such as rectangular topology normally requires large aperture size with element spacing less than  $\lambda_c/2$  to provide low sidelobe level and fine cross-range resolution. This

will lead to enormous number of elements. Large number of elements increases cost and weight, as well as data flow. In addition, dense element spacing makes element interaction strong. MIMO array topology combined with UWB provides a good solution to reduce number of elements and enlarge the element spacing while keeping the sidelobe level low and cross-range resolution fine. Therefore, it is desired to design two-dimensional array topology also using UWB MIMO configuration. Due to high dimensional nature of two-dimensional array, it is challenging to use stochastic optimization approach to obtain array topology that has desired PSF. Therefore, deterministic approach is preferred. We have used rotational 1-D array analysis approach which is based on the projection slice method to design the 2-D array. The projection slice method [8] states that the pattern of a 2-D array at any  $\Phi$ -cut plane can be found by calculating the pattern of the equivalent 1-D array at that specific cut plane. The equivalent 1-D array is the projection of the 2-D array onto that specific  $\Phi$ -cut plane.

The rotational 1-D array analysis approach actually utilizes the projection slice method in an “inverse” way. The design approach starts with a design of a 1-D MIMO array with a desired PSF. Then we select two orthogonal cut planes, for example, the X- and Y- cut planes or diagonal cut planes, and lay the designed 1-D MIMO array on these two axes as an equivalent array. This will form a grid as Figure 6.14 shows in the array plane. Next is to select which grid points should we put the elements. This is done by selecting the grid points that causes as minimum element shadowing [8] as possible in all cut planes. If the element number is small, it is possible to elaborate all possible array topologies and compare their PSFs to find the optimum configuration. If the element number is large which prevents from elaborate all possible topologies, arranging the elements in spiral or curvilinear may provide better PSF than other configurations such as square or cross configurations [8][11].

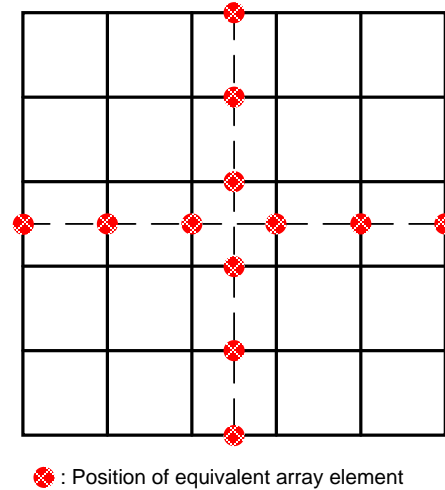


**Figure 6.14 Example of a grid in 2D array plane formed by placing the equivalent array at the vertical and horizontal axes.**

## 6.6 Application-driven UWB antenna array design

We have applied the above mentioned strategy to design prototypes of antenna arrays and evaluated their imaging capabilities as well as impact of real elements on the image quality. The application is microwave imaging radar for concealed

weapon detection. The system specification is given in section 6.6.1. The design of 1-D MIMO array which serves as the equivalent array using deterministic and stochastic approach are described in section 6.6.2 and section 6.6.3, respectively. The 2-D MIMO array design is described in section 6.6.4.

### 6.6.1 System specifications

The array specifications have been set by the system designers. Due to the limitation of available components such as connectors, cables, and switches, the upper frequency was limited to 18 GHz. The required -10 dB down-range resolution is 2 cm. The required antenna array should have -10 dB 5 cm cross-range resolution at a distance of 1 m. These specifications can be translated to a -10 dB beamwidth of 3°. The maximal acceptable level of the sidelobes has not been specified. However, due to the hardware limitations it has been decided that the array can consists from 4 TX antennas and 16 RX antennas. This determines the effective element number to be equal to 64.

The down-range resolution  $\delta_d$  is directly related to the bandwidth by the following relationship [2]:

$$\delta_d = \frac{c}{2B} \quad (6.9)$$

where  $c$  is the speed of light in free space, and  $B$  is the bandwidth. The demand of 2 cm down-range resolution can be thus translated into a bandwidth of 7.5 GHz. Having in mind the upper frequency limit the antenna array operational frequency has been selected from 10 GHz to 18 GHz with center frequency of 14 GHz.

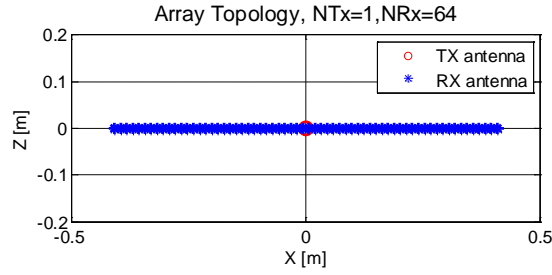
### 6.6.2 One-dimensional MIMO array design using the effective array approach

The effective array aperture length is calculated by eq. (6.5), which gives the aperture size of 0.82 m. This leads to element spacing of the effective array approximately 13 mm ( $0.87\lambda$  where  $\lambda$  is the wavelength at 20 GHz). The effective SIMO array topology is shown in Figure 6.15 (a). The MIMO array is then factorized from this SIMO effective array. The factorization is not unique. Figure 6.15 (b) and (c) show two possible different 1-D linear MIMO factorizations which give the same effective array. Figure 6.15 (b) shows the array with transmit antennas located at the edge of the array (1-D MIMO array 1), whereas Figure 6.15 (c) shows the array with transmit antennas located at the center of the array (1-D MIMO array 2). When the transmit antennas are located at the edge of the array, the total array size is smaller, thus it may be favorable to locate the transmit antennas at the edge. Although both array topologies result in the same effective array, the PSFs of these MIMO arrays are slightly different at the sidelobe region due to the target position in the near-field of the array (Figure 6.16). The PSF of 1-D MIMO array 1 has better performance in terms of lower sidelobe level.

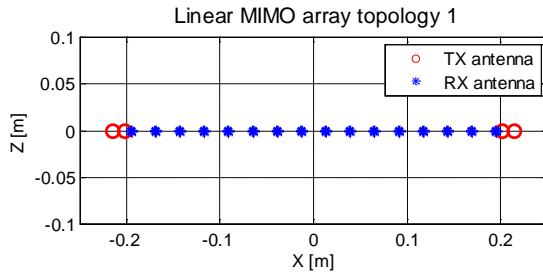
In addition, there are two more advantages to select the transmit antennas at the edge of the array. Firstly, if the transmit antennas are closely located at the center of the array as MIMO array 2, the active coupling level between the transmit antennas will dramatically increase and may deteriorate the array performance. Secondly, we found by experiments that locating the transmit element at the center of the array



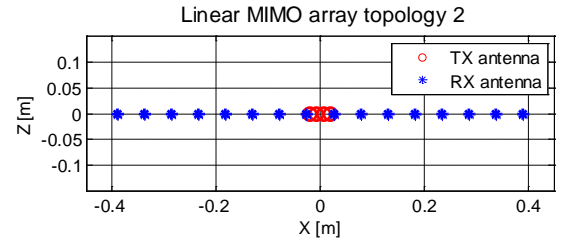
causes severer element shadowing effect for the transmit sub-array. Therefore, it is desirable to select 1-D MIMO array1 configuration.



(a) Effective SIMO array topology



(a) TX antennas located at the edge of the array



(b) TX antennas located at the center of the array

**Figure 6.15 Different linear MIMO array configuration (a) TX antennas located at the edge of the array (b) TX antennas located at the center of the array**

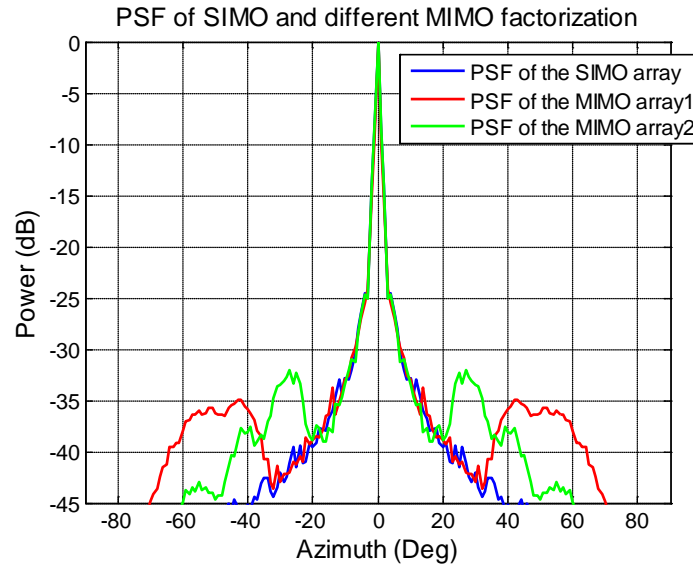


**Figure 6.16 PSF of the effective SIMO array and different factorized linear MIMO configuration**

### 6.6.3 One-dimensional array design using the optimization algorithm approach

We have also used the PSO approach to directly optimize a MIMO array topology that is able to deliver the desired PSF. As mentioned before, to achieve desired cross-range resolution, the -10 dB beam width is of about 3°. The ideal sidelobe level ISL of the effective SIMO array with  $N$  elements is obtained by

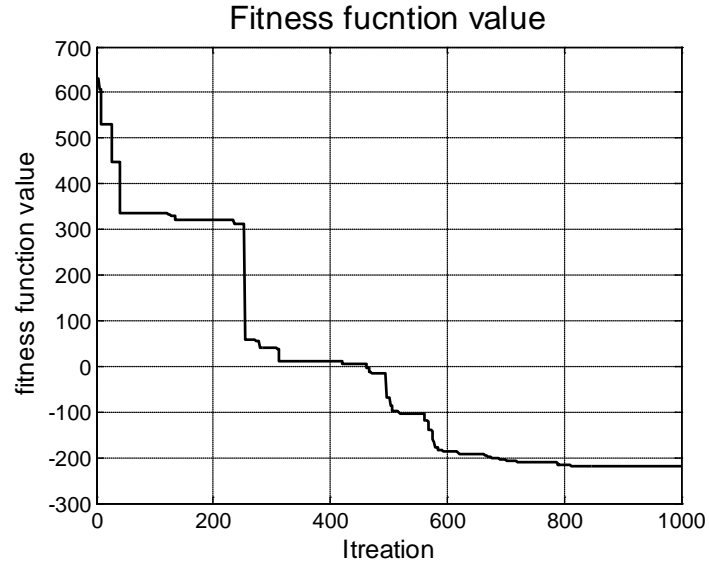
$$ISL = 20\log_{10}(N) \quad (6.10)$$

which is about -36 dB. As a result, we set the desired sidelobe level to -35 dB. The weight function is designed such that from -30° to 30° the weight is 1. This is because the target is assumed to be mainly located within the  $\pm 30^\circ$ , therefore, it is important that the PSF in this area is strictly below the mask. From  $\pm 30^\circ$  to  $\pm 45^\circ$ , the weight is set to 0.25 because we assume the region from  $\pm 30^\circ$  to  $\pm 45^\circ$  is less important than the region within  $\pm 30^\circ$ , but we would still like to keep the sidelobe level low within this region to reduce the possible influence of clutter. We assume the interference from  $\pm 45^\circ$  to  $\pm 90^\circ$  region is less likely to happen, thus we relief the constraint by setting the weight to 0.1.

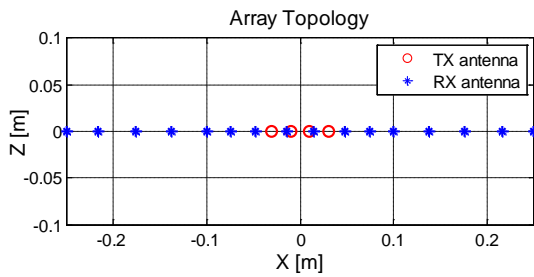
The antenna array is forced to be symmetric because we want to image the object in both left and right side of the antenna. Thus, there are 2 positions for the transmit antennas and 8 positions for the receive antennas to be determined, which means the dimension of the solution space is 10. Moreover, we constrain the maximum size of the antenna to be 50 cm so the final system is possible to be handheld. Therefore, the boundary of the solution space is set to [0m, 0.25m] for all particles. The number of particles is chosen to be 20. We have run the optimization for 2000 iterations, and the trace of the fitness function is shown in Figure 6.18. The initial fitness function is 553.9, and after 1239 iterations the fitness function value converges to -620.4.

Figure 6.18 shows the PSO optimized MIMO array topology, and Figure 6.19 shows the beam pattern of the optimized array (named PSO array), the beam pattern of the array obtained from the deterministic approach (named deterministic array), and the mask. Comparing the beam pattern of the PSO array and the deterministic array, the most distinctive difference happens in the region  $\pm 10^\circ$  to  $\pm 90^\circ$ . The mainlobe of the beam pattern of the deterministic array gradually decreased to -43 dB at about  $\pm 32^\circ$ , and then the sidelobe happens with maximum level of -35 dB at  $\pm 42^\circ$ . On the other hand, the main lobe of the beam pattern of the PSO array sharply dropped to below -50 dB at about  $\pm 20^\circ$ , and then raised back to about -30 dB at about  $\pm 33^\circ$ . Since we have set the weight within  $\pm 30^\circ$  to 1, and the weight from  $\pm 30^\circ$  to  $\pm 45^\circ$  to 0.25, the PSO tries to confine and minimize the beam pattern level within  $\pm 30^\circ$ , and does not care much about the sidelobe level behind  $\pm 30^\circ$ . As a result, the very low value within  $\pm 10^\circ$  to  $\pm 30^\circ$  dominates the fitness function value, and PSO thinks this is a good beam pattern because the value is minimal. The deterministic array beam pattern, on the other hand, is above the mask from  $\pm 3^\circ$  to  $\pm 12^\circ$ , and slightly below (maximum 10 dB below) the mask from  $\pm 12^\circ$  to  $\pm 60^\circ$ . The value above the mask is in the dominant area (weight = 1), therefore, this leads to large fitness function value (-127.8430). Thus, due to the weighting function, the PSO favors beam pattern with narrow main beam and low dip between main beam and sidelobe, rather than slightly wider main beam and low sidelobe. It can be concluded that PSO does provide a direct method to design array topology, and the PSO optimized array topology indeed provided “desired” beam pattern. In addition, one may trade the

mainbeam width and sidelobe level by adjusting the mask and weighting function. However, it actually transfers the design difficulties from “designing the topology” to “designing a good mask and weighting function”, which requires further investigation. In addition, PSO requires long computation time (in this thesis one PSO simulation took about 3 days), so it may not be very efficient. A summary and comparison of the advantages and disadvantages of the deterministic approach and stochastic approach is given in Table 6-1.



**Figure 6.17 Fitness function value trace of the PSO**



**Figure 6.18 PSO optimized MIMO array topology**

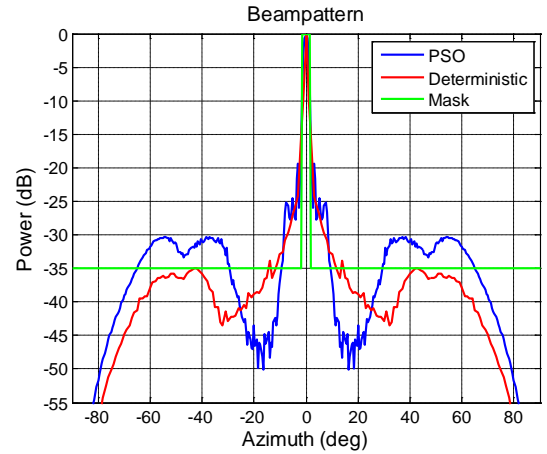


**Figure 6.19 PSF of the PSO optimized MIMO array and the mask.**

**Table 6-1 Advantages and disadvantages of the deterministic approach and stochastic approach**

	Advantages	Disadvantages
Deterministic approach	<ul style="list-style-type: none"> <li>● Fast</li> <li>● Can already deliver good beam pattern</li> </ul>	<ul style="list-style-type: none"> <li>● Inflexible</li> </ul>
Stochastic approach	<ul style="list-style-type: none"> <li>● Topology can be directly obtained</li> <li>● Flexible</li> </ul>	<ul style="list-style-type: none"> <li>● Design the mask and weighting function is not trivial</li> <li>● Requires long computation time</li> </ul>

#### 6.6.4 Two-dimensional UWB antenna array design

The approach to extend the one-dimensional array to 2-D array has been discussed in section 6.5.3. We have selected the X- and Y- axes as the principal axes. Thus, the 2-D array topology should have equivalent array on the X- and the Y- axes same as the designed 1-D MIMO array. This forms a 2-D grid on the array plane as Figure 6.20, and the elements should be located on the grid point in order to have the equivalent array on the principal axes. The arrangement of the element in this 2-D grid is not unique; many different topologies can result in the same equivalent array on the principal axes. As discussed in section 6.5.3, the element arrangement should avoid element shadowing as much as possible. Since the element number is small, we have elaborated all possible element arrangements and examined their PSFs to determine which one is the optimal element arrangement.

The best two possible element arrangements are shown in Figure 6.21 (a) and (b). Both arrays are sparse with minimum element spacing larger than 3.5 wavelengths at the highest frequency. Both arrays have the same mainlobe width, but the maximum sidelobe level of array 2 (-12.58 dB, see Figure 6.22 (b)) is considerably lower than that of array 1 (-8.3 dB, see Figure 6.22 (a)). This is because for array 1, the elements are located too close to the diagonal axes; therefore, at the diagonal axes the sidelobe level is high. The antenna elements of array 2 are more evenly spread over the whole aperture, thus the element shadowing effect is less, and consequently, the maximum sidelobe level is lower. Note that both arrays have their maximum sidelobe level near the diagonal axes. This is because at these two axes, the transmit antennas are shadowed to each other thus the number of TX antennas reduced from 4 to 2. As a result, at these axes the number of effective array elements is two times less than that at other axes, which leads to higher sidelobe level. The highest sidelobe level in both arrays is much higher than that in the original 1-D MIMO array.

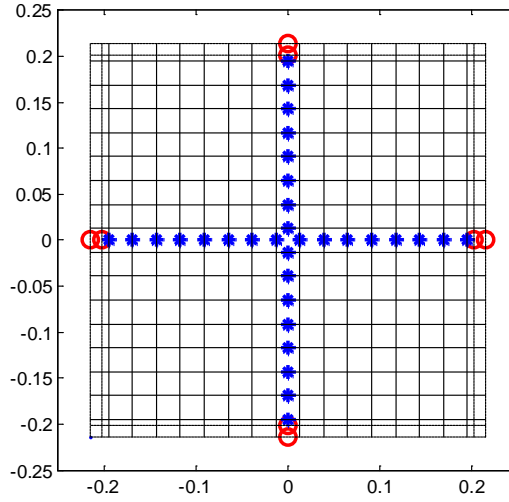
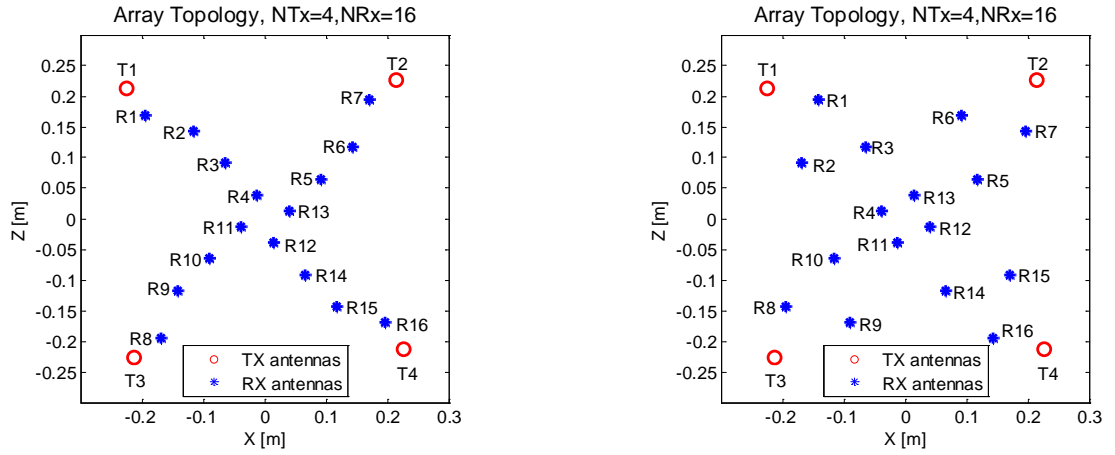


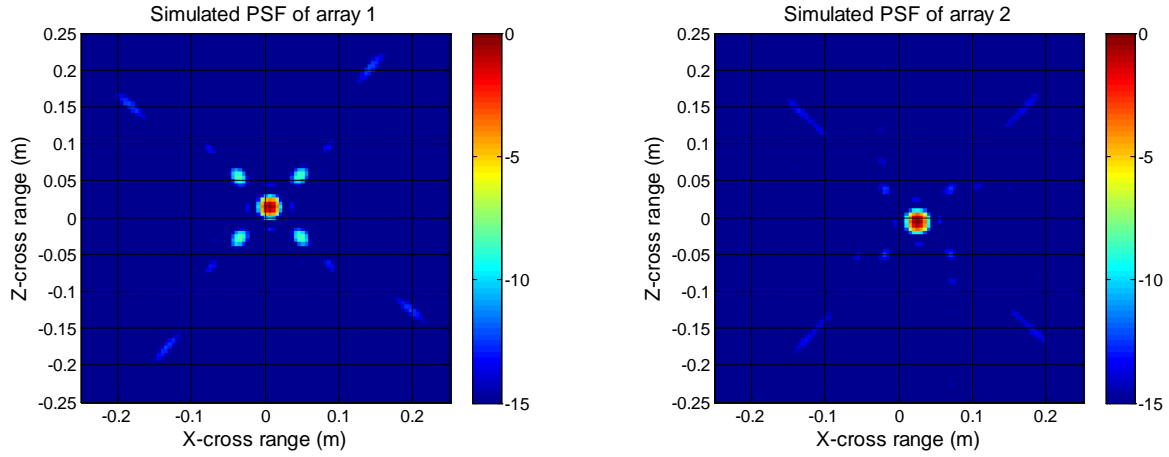
Figure 6.20 Grid of antenna positions



(a) Topology of array 1

(b) Topology of array 2

Figure 6.21 Designed 2D MIMO antenna topologies (a) Array topology 1 (b) Array topology 2



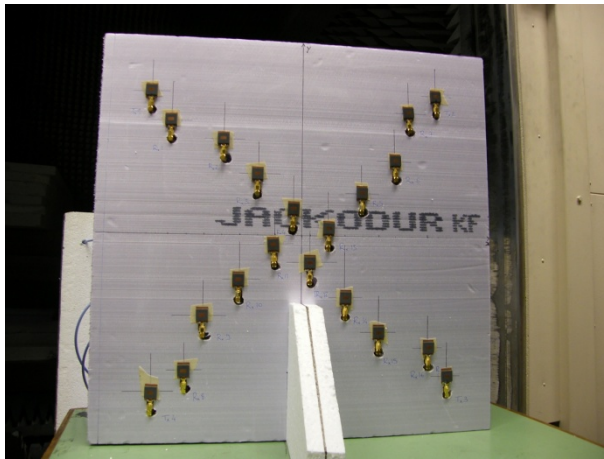
(a) Simulated PSF of array 1

(b) Simulated PSF of array 2

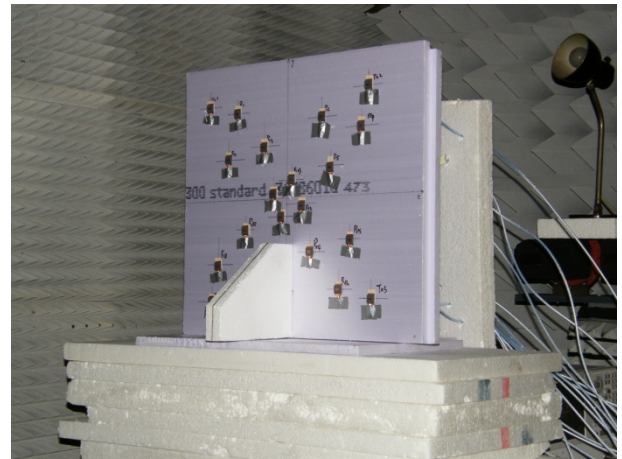
**Figure 6.22 Simulated PSF of array topology 1 and array topology 2 (a) Simulated PSF of array 1 (b) Simulated PSF of array 2**

## 6.7 Experimental verification

Deterministic 1-D MIMO array topology and both 2-D MIMO array topologies have been manufactured. The antenna element used is ASP antenna described in Chapter 3. The discussion of the experimental verification on the 1-D array can be found in Appendix E and [4]. Figure 6.23 shows the prototype of two proposed antenna. Although the array and elements are designed for time-domain UWB system, we have used network analyzer and performed measurement in frequency-domain due to better dynamic range and stability of PNA. The transmit antennas and the receive antennas are sequentially transmit and receive the data by using a mechanical switch. Full port calibration of the network analyzer, switch, and cables are performed before the measurement. Background subtraction is performed to remove the antenna cross-talk and clutters from the raw data, and then time window is applied to the background-subtracted data to further remove the residues from the background subtraction. The pre-processed data is then focused using the modified Kirchhoff migration to obtain the image.



(a) Prototype of array 1



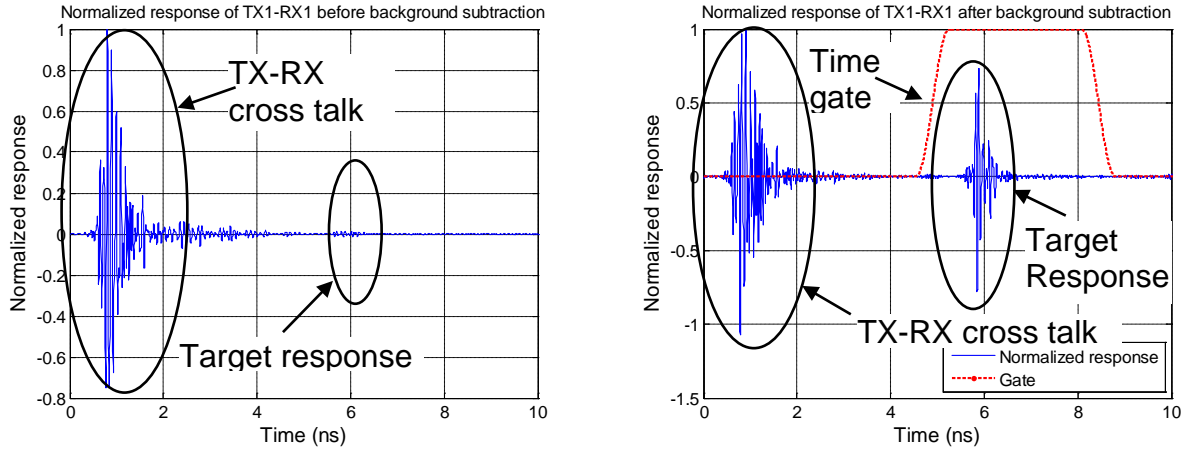
(b) Prototype of array 2

**Figure 6.23 Manufactured prototypes of array 1 and array 2 (a) Prototype of array 1 (b) Prototype of array 2**

### 6.7.1 Coupling behavior analysis

Due to the operational principle of the array, there are mainly two different types of coupling exist in the designed array. The first type is the cross talk between TX antennas and RX antennas, and the second type is the “scattering coupling” between RX antennas. The active coupling TX antennas were ignored because TX antennas were located at corner of the array and were far from each other. Thus we do not expect any coupling between TX antennas.

Figure 6.24 (a) shows the time domain target response between T1 and R1 (the most adjacent TX-RX pair located at the most upper left corner in both array 1 and array 2). Due to the close vicinity of this TX-RX pair, the cross talk level is much stronger than the target response. Thus, it is not possible to identify the target response with the naked eye. However, after the background subtraction, as Figure 6.24 (b) demonstrates, the cross talk is considerably reduced and the target response can be easily identified. Nevertheless, there is still residue of the cross talk which will cause strong artifact in the image. According to the analysis in Chapter 3, the cross talk will decrease to the noise level after about 2 ns. As a result, the residue of the cross talk can be completely removed by the time gating. In summary, the background will firstly be subtracted from the measured raw data to remove most part of the cross talk and static reflection from the environment. Then time gating will be applied to the subtracted data to further remove the residue of the cross talk and other signals that are not from the target. As a result, the cross-talk has very limited influence to the image quality.



(a) Response of T1-R1 before background subtraction

(b) Response of T1-R1 after background subtraction

**Figure 6.24 Target response between T1 and R1 before and after background subtraction (a) Response of T1-R1 pair before background subtraction (b) Response of T1-R1 pair after background subtraction**

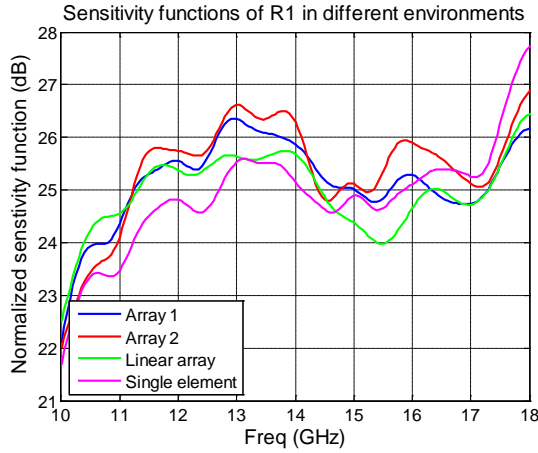
The scattering coupling, as discussed in section 6.4.2, may have significant influence to the image quality if it alters the receive antennas' sensitivity function, causing late-time ringing and raising sidelobe level. To evaluate how the antennas' sensitivity function behaves in the array environment, we have illuminated the arrays with a standard gain horn whose 3 dB beamwidth is of about  $20^\circ$  and measured all elements sensitivity function. To ensure all the elements are within the 3 dB beamwidth, the distance between the standard gain horn and the array is 2.9 m. These measured sensitivity functions are then compared with their counter parts when the elements are not in an array environment and when the elements are in linear array environment.

The frequency domain sensitivity functions of R1 and R11 in different environments are shown in Figure 6.25 (a) and (b), respectively. Compare Figure 6.25 (a) and Figure 6.25 (b), it can be seen that the sensitivity functions of R1 in the environment of array1, array 2, and linear array are very similar. On the other hand, the sensitivity functions of R11 in linear array environment has larger deviation than that when R11 in array 1 or array 2 environment. This is because R1 is the element at edge, and R11 is the element at the center of the array. Array1 and array2 are sparse array, so the sensitivity functions of R1 and R11 are similar. However, in a linear array environment, the element spacing is dense, so the mutual coupling influence is larger and the sensitivity function has larger deviation from others. Nevertheless, the sensitivity functions of R1 and R11 in different array environments and in single element environment are very similar. The deviation is within 2 dB. Therefore, we do not expect severe influence from mutual coupling.

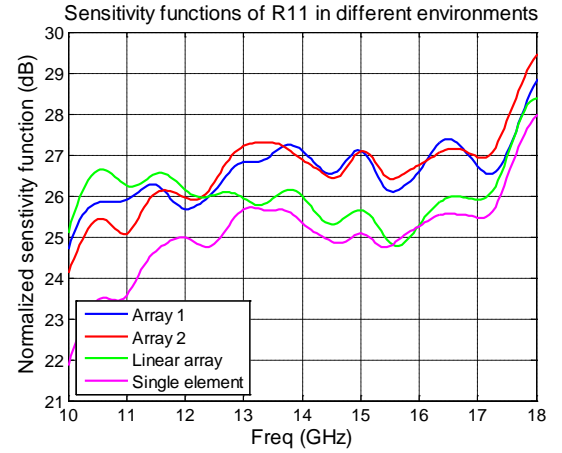
Analysis in section 6.4.2 also demonstrated that the scattering coupling will also cause late time ringing and may obscure small targets behind large targets. Therefore, we have also examined the time domain sensitivity function to see if the coupling will cause after time ringing or not. The time domain sensitivity function of R1 and R11 are shown in Figure 6.26 (a) and (b). To better visualize the time domain ringing, we have plotted the envelop of the time domain sensitivity function



in dB scale. The sensitivity functions of R1 showed that there is no much difference before -20 dB level for the antenna in different environments, and below -20 dB level the antenna in the array 2 environment has slightly higher ringing than the antenna in other environments. This difference is quite small, thus we can conclude that for R1 the scattering coupling does not cause extra ringing. The time domain scattering response of R11 in different environments are also very similar except for the linear array environment. As a result, we can conclude that for the 2-D arrays, the coupling would not cause a severe problem. This is expected since the 2-D arrays are sparse arrays, so the element coupling is weak between elements.



(a) Sensitivity functions of R1 in different environments



(b) Sensitivity functions of R11 in different environments

**Figure 6.25 Frequency domain sensitivity function of R1 and R11 in different environments (a) Sensitivity function of R1 in different environments (b) Sensitivity function of R11 in different environments**

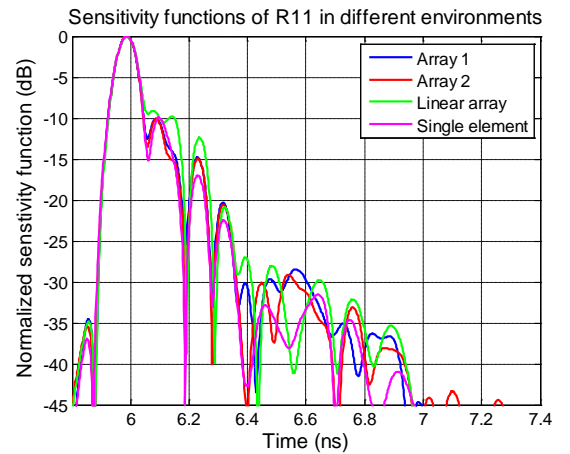
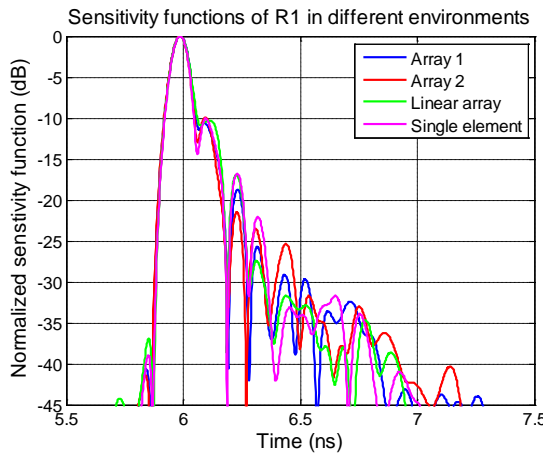


**Figure 6.26 Time domain sensitivity function of R1 and R11 in different environments (a) Sensitivity function of R1 in different environments (b) Sensitivity function of R11 in different environments**

### 6.7.2 Measured PSF

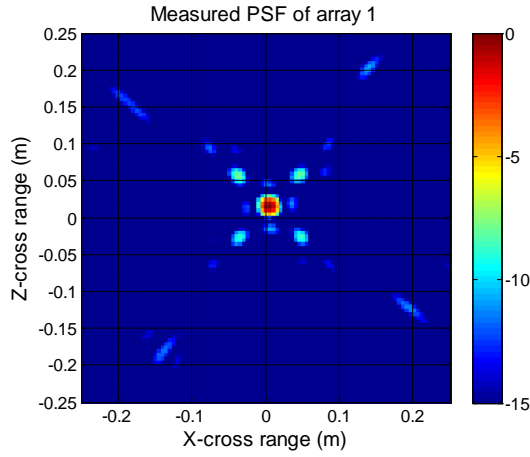
Figure 6.27 (a) and (b) show the measured PSF of array 1 and array 2, respectively. The target is a metal ball with 2cm diameter located at about 0.8m from the center of both arrays.

Comparing the measured PSFs with the simulated PSFs (shown in Figure 6.22), they are very similar except slightly higher sidelobe level for the measured PSFs. For array 1, the difference between the maximum sidelobe levels is about 0.4 dB, while for array 2 this difference is about 2.62 dB. The reason that deviation of array 2 is larger than that of array 1 may be because the sidelobe level of array 2 is quite low, thus it is more susceptible to measurement errors. Other than the difference in the maximum sidelobe level, the measured PSFs have more clutter comparing to the simulated PSFs. Several reasons cause these deviations. One of the reasons may be the element mutual coupling. However, as discussed before, since the mutual coupling is weak, it may not be the main reason of this deviation. Another reason, which we think is more dominant, is the instability of the system. It was found that the system was not time-invariant; the background measured at different time has some deviations. This causes errors when performing the background subtraction and introduces artifacts to the image.

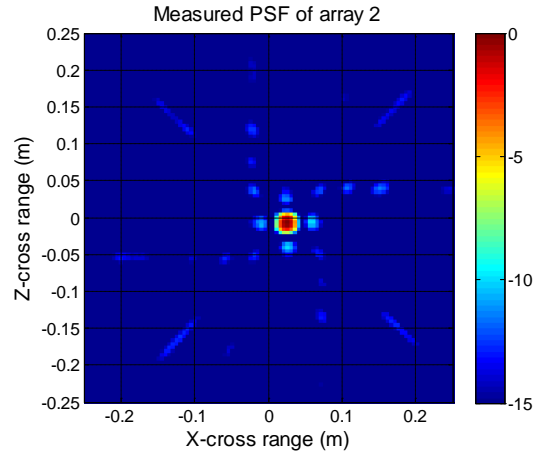
Since the target is not possible to be always at the center of the array, we have also measured the PSF when the target is off the center of the array, and the results are shown in Figure 6.28. The target is located at (250, -250) mm off the array center, which is at the lower right corner of the array. Both results showed that the PSF of the target at off center position is almost identical to the PSF where the target is at the center of the array. This demonstrated that the imaging capability of the array is almost identical whether the target is at the center of the array or at the edge of the array.

The cross-range resolution measurements of both arrays are shown Figure 6.29. The targets are two metal balls with diameter of 2 cm and a separation of 5 cm (center to center). It can be clearly seen that two targets can be resolved at -10 dB level for both antenna arrays. The results for both arrays are very similar because the two arrays both give the same effective 1-D MIMO array along the principle axis.

The down-range resolution measurements of both arrays are shown in Figure 6.30. The targets are also 2 metal balls with 2 cm diameter placed 5 cm apart (center to center). Although the second target response is weaker than the first target for both array case, it can still be clearly identified there are two targets. This measurement result clearly showed that for both arrays, the two targets could be separated at -10 dB level. The results for both arrays are very similar, because the down-range resolution is mainly determined by the bandwidth. The down-range and cross-range measurements verified that the -10 dB cross-range and down-range resolution of the both antenna arrays are better than 5cm at 0.8 m.



(a) Measured PSF of array 1



(b) Measured PSF of array 2

**Figure 6.27 Measured PSF of array 1 and array 2 when the target is located at center (a) Measured PSF of array 1 (b) Measured PSF of array 2**

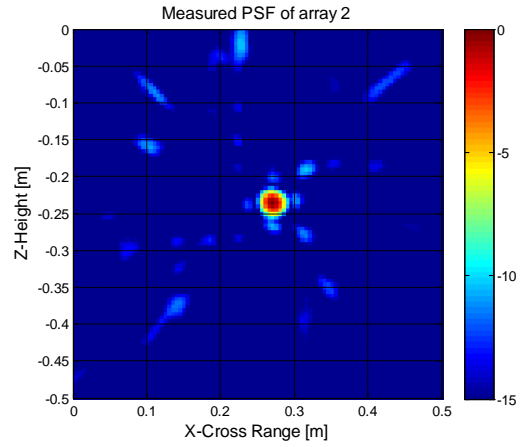
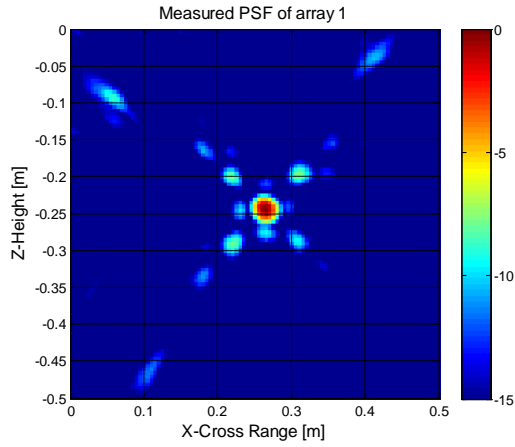


**Figure 6.28 Measured PSF of array 1 and array 2 when the target is located at (-250,-250) (a) Measured PSF of array 1 (b) Measured PSF of array 2**

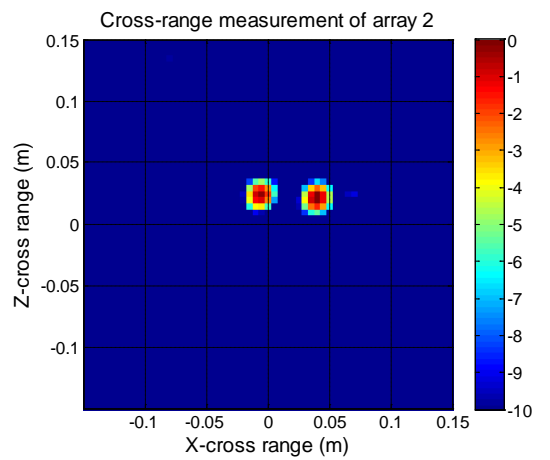
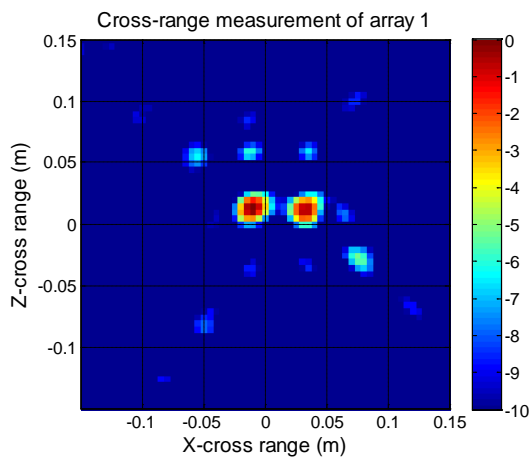
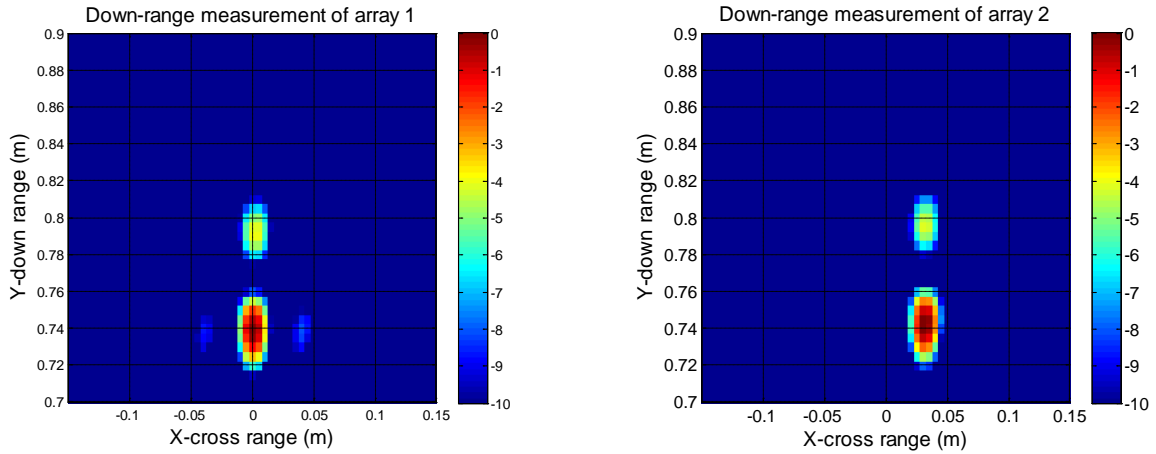


**Figure 6.29 Cross-range measurement of array 1 and array 2 (a) Cross-range measurement of array 1 (b) Cross-range measurement of array 2**



(a) Down-range measurement of array 1      (b) Down-range measurement of array 2

**Figure 6.30 Down-range measurement of array 1 and array 2 (a) Down-range measurement of array 1 (b) Down-range measurement of array 2**

### 6.7.3 Image of distributed targets in free space

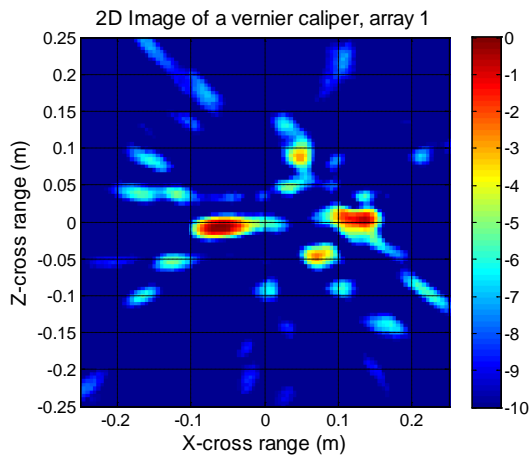
In reality a target is never a single point-like scatterer but many scatterers distributed in space. To evaluate the imaging capability of the proposed array topologies for distributed targets, we have used two targets to test. A vernier caliper (Figure 6.31 (a)) and a pistol (Figure 6.32 (a)) have been used as test targets. The vernier caliper is positioned horizontally with its outside jaw opened 5cm wide. This is to test the arrays' cross-range resolution, down-range and dynamic range. Figure 6.31 (b) and (c) show the two-dimensional image from both arrays at -10 dB level. Unfortunately both arrays only can present the body part of the vernier caliper but failed to resolve the outside jaws and inside jaws. The reason may not because the arrays do not have sufficient resolution, but the main body created strong artifacts which interact with the reflection from the outside jaws and inside jaws constructively or destructively. As a result, the outside jaws and inside jaws are not able to be presented in the image. The sidelobe level of array 1 is stronger than that of array 2, therefore, it can be seen that the center part of the vernier caliper is disappeared due to destructive interaction. Figure 6.31 (d) and (e) are the 3-D image of the vernier caliper. Besides the clutter, at the center of the image there is something with a thickness of 5 cm and length of 25cm which barely can be identified as a vernier caliper.

Figure 6.32 shows images of a pistol as a realistic target. The pistol is vertically positioned at 0.8 m range distance from the center of the arrays (Figure 6.32 (a)). The 2-D images imaged by both arrays are shown in Figure 6.32 (b) and (c), respectively. Unlike the vernier caliper case, both arrays can give reasonable reconstruction of the shape of the pistol. Comparing the images from array 1 and array 2, the image of array 1 has less clutters but part of the gun barrel is missing. The image generated by array 2 gives better reconstruction of the gun but with slightly more clutters. This may be that the sidelobe structure from the gun body created by array 1 destructively interacted with the reflection from the barrel and the gun butt, which makes the shape of the gun break-up.

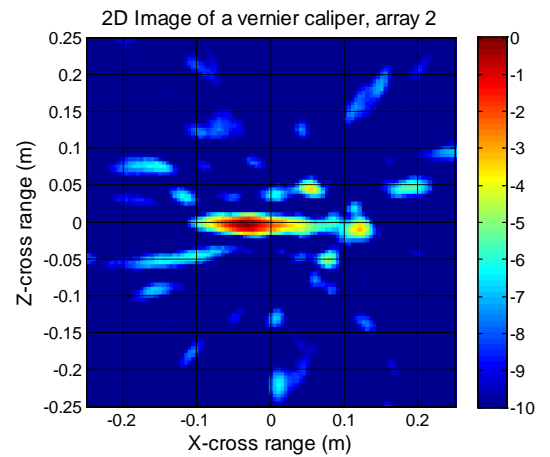
The measurement results showed that in principle both arrays can deliver images of targets in free space. However, due to higher sidelobe level of array 1, the shape reconstruction of both vernier caliper and pistol are slightly inferior to that of array 2. However, it can be foreseen that if targets is not in free space but on a large reflecting body such as human body, the interference from the sidelobe from the reflecting body may severely degrade the shape of the target. Thus, further optimization of the array topology to reduce sidelobe is necessary to provide better image of targets and enable the capability to image targets on large reflecting body.



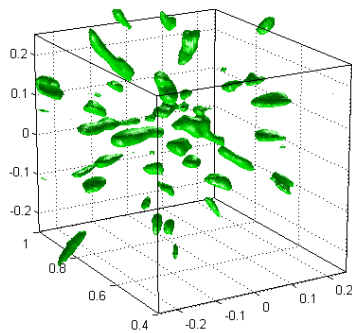
(a) Vernier caliper in horizontal position



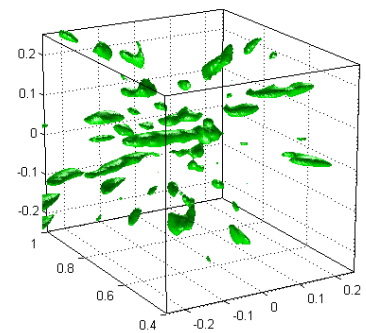
(b) 2D image of a vernier caliper from array 1



(c) 2D image of a vernier caliper from array 2



(d) 3D image of a vernier caliper from array 1

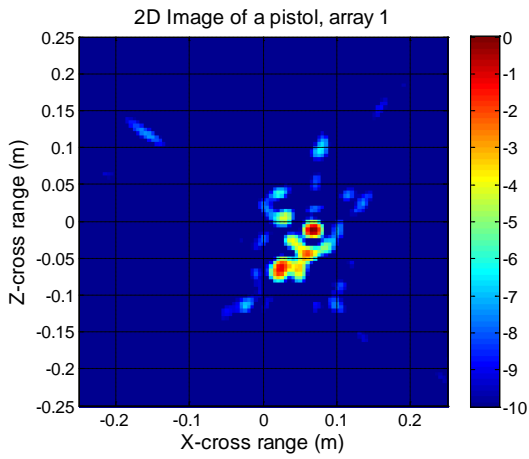


(e) 3D image of a vernier caliper from array 2

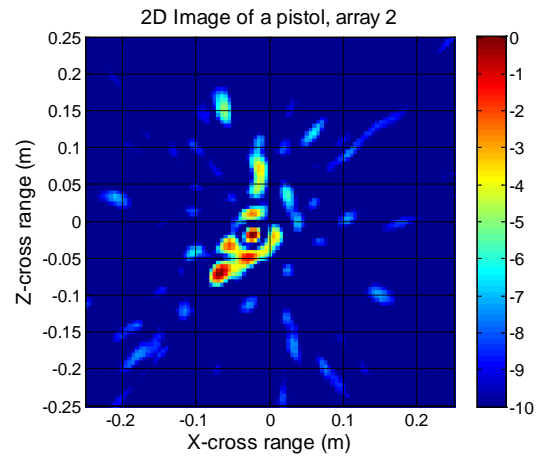
**Figure 6.31 2D and 3D images of a vernier caliper (a) Position of the vernier caliper (b) 2D image generated by array 1 (c) 2D image generated by array 2 (d) 3D image generated by array 1 (e) 3D image generated by array 2**



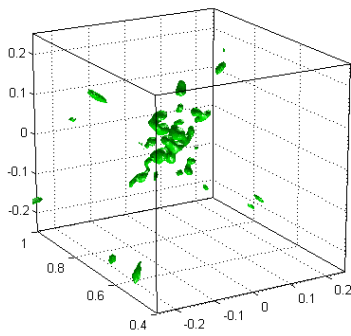
(a) Pistol in vertical position



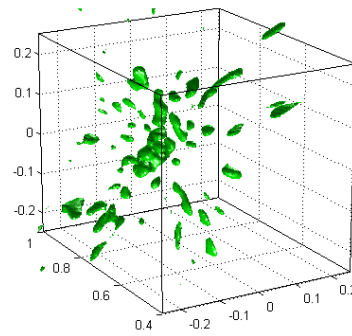
(b) 2D image of the pistol from array 1



(c) 2D image of the pistol from array 2



(d) 3D image of a pistol, array 1



(e) 3D image of a pistol, array 2

**Figure 6.32 2D and 3D images of a pistol (a) Position of the pistol (b) 2D image generated by array 1 (c) 2D image generated by array 2 (d) 3D image generated by array 1 (e) 3D image generated by array 2**

## 6.8 Conclusions

In this chapter we have discussed development of UWB sparse arrays for near-field high resolution imaging.

In order to come to universal design criteria of UWB arrays, I have decided to characterize the overall performance of an UWB imaging array by means of the Point Spread Function (PSF). I have investigated properties of PSF of UWB sparse array calculated by using modified Kirchhoff migration. It was demonstrated that the PSF of an UWB sparse array has no grating lobes, but the sidelobe level increases as the element spacing increases. In addition, the sidelobe position occurs closer to the mainlobe when the element spacing increases. This study demonstrated that it is possible to use UWB sparse array configuration to obtain sharp PSF with low sidelobe level.

The influence of coupling to the array performance has also been examined. It was shown that the most profound influence of coupling is that the scattered wave will alter the sensitivity function of each element. If this alteration caused a narrow band spike in the sensitivity function, extra ringing in time domain signal will occur which may mask smaller target behind a large target. In addition, the coupling may also raise the PSF sidelobe level considerably. Therefore, it is important to control the element coupling in such a way that there is no narrow band spike in the sensitivity function and the PSF sidelobe level remains under the specifications.

I have demonstrated that among three possible approaches (i.e., conventional dense array, SIMO and MIMO) the UWB MIMO is the most attractive one as it allows for fine cross-range and down-range resolution with low sidelobe level using a small number of elements.

I have proposed a design approach for 2-D MIMO arrays. The approach is separated into two steps.

Firstly, a 1-D MIMO array with desired PSF properties is designed. We have investigated a deterministic and a stochastic approach to design the 1-D MIMO array. The deterministic approach is based the effective aperture principle. This approach firstly designs a SIMO array with desired PSF properties, and then factorizes the SIMO array into the MIMO array. The stochastic approach is to use optimization algorithm such as PSO to directly optimize 1-D MIMO array topology that can give desired PSF. It was found that the result of the stochastic approach is not better than that of the deterministic approach because the stochastic approach actually transfer the design difficulty to the design of the fitness function.

Secondly, the 1-D MIMO array developed in the first step is used as an equivalent topology at two orthogonal cut planes of the 2-D array. The 2-D array topology can then be constructed in such a way that its projections to the both orthogonal cut plains resemble the 1-D topology. This process results in multiple topologies. The topology which is characterized by minimal shadowing at other cut planes is the preferable one.

Two 2-D MIMO arrays for CWD application working in microwave range have been developed using the above-mentioned approach and experimentally verified to examine how the real element influence the array performance. Both arrays have the same mainlobe width, but the maximum sidelobe level of array 2 (-12.58 dB) is

lower than that of array 1 (-8.3 dB). The coupling analysis demonstrates that the sensitivity function of any element in the array only differs from that of a single element because of the sparse nature of the designed array topology. Therefore, no severe consequence due to coupling is expected. The simulated and measured PSFs are resemble to each other except the measured PSFs have slightly higher sidelobe level and more clutter which may due to system instability. A vernier caliper and a pistol have been used as distributed targets to evaluate the imaging capability of the designed arrays. It was demonstrated that array 2 with distributed element arranging in comparison to the array 1 can provide better target shape reconstruction due to its lower sidelobe level. However the sidelobe level of both arrays has been found not sufficient for high-quality imaging of small targets (like a pistol) having a large target (such as human body) at the background. It was also found that the sidelobe level is one of crucial specifications of the array, which should be specified by system designers in order to achieve proper performance of the whole imaging system. The 3-D imaging results proved high potential of using microwave 2-D UWB sparse MIMO array in real-time short-range high-resolution imaging applications.

## References

- [1] A. Yarovoy, "Ultra-wideband radars for high-resolution imaging and target classification", in *Proc. European Radar Conference (EuRAD) 2007*, pp. 1-4, 10-12 Oct. 2007.
- [2] A. G. Yarovoy, X. Zhuge, T. G. Savelyev, L. P. Ligthart, "Comparison of UWB Technologies for Human Being Detection with Radar", in *Proc. European Microwave Conference (EuMC)*, pp. 1574-1577, Oct. 2007.
- [3] D. L. Mensa, *High Resolution Radar Cross-Section Imaging*. Norwood, MA: Artech House, 1991.
- [4] T. Savelyev, X. Zhuge, B. Yang, P. Aubry, A. Yarovoy, L. Ligthart, and B. Levitas, "Comparison of 10-18 GHz SAR and MIMO-Based Short-Range Imaging Radars", *International Journal of Microwave and Wireless Technologies*, Available on CJO 08 Jan, 2010, doi: 10.1017/S1759078710000383.
- [5] A. Yarovoy, T. Savelyev, P. Aubry, P. Lys, and L. Ligthart, "UWB Array-Based Sensor for Near-field Imaging", *IEEE Transl. Microwave Theory and Technology*, vol. 55, p.p. 1288-1295, (2007)
- [6] W.A. Schneider, "Integral Formulation of Migration in Two and Three Dimensions", *Geophysics*, Vol. 43, No. 1, pp. 49-76, 1978
- [7] X. Zhuge, A. G. Yarovoy, T. Savelyev, and L. P. Ligthart, "Modified Kirchhoff Migration for UWB MIMO Array-Based Radar Imaging", *IEEE Trans. on Geoscience and Remote Sensing*, Vol. 48, No. 6, June 2010
- [8] J. L. Schwartz, *Ultrasparse, Ultrawideband Time-Steered Arrays*, Ph. D Dissertation, Dept. Elect. Eng., University of Pennsylvania, PA, 1996
- [9] A. Yarovoy, R. de Jongh, and L. Ligthart. "Ultra-wideband sensor for electromagnetic field measurements in time domain", *Electronics Letters*, vol 36, pp. 1679-1680, 2000.



- [10] A. Yarovoy, P. Lys, P. Aubry, T. Savelyev, and L. Ligthart, "Near-field focusing within a UWB antenna array," In H. Lacoste & L. Ouwehand (Eds.), *Proceedings of the European Conference on Antennas and Propagation: EuCAP 2006*. Nice, France: European Space Agency, pp. 1-6, 2006.
- [11] X. Zhuge, *Short-Range Ultra-Wideband Imaging with Multiple-Input Multiple-Output Arrays*, Ph.D Dissertation, Dept. Elect. Eng., Delft University of Technology, 2010
- [12] J. Kennedy and R. Eberhart, "Particle Swarm Optimization", *Proc. of IEEE International Conference on Neural Networks*, p.p. 1942-1948, 1995
- [13] J. Robinson and Y. Rahmat-Samii, "Particle Swarm Optimization in Electromagnetics", *IEEE Trans. on Antennas and Propagation*, Vol. 52, No. 2, p.p. 397-407, Feb. 2004
- [14] M. Fernández Pantoja, A. Rubio Bretones, F. García Ruiz, S. G. García, and R. Gómez Mattín, "Particle-swarm Optimization in Antenna Design: Optimization of Log-periodic Dipole Arrays", *IEEE Antenna and Propagation Magazine*, Vol. 49, No. 4, p.p. 34-47, August 2007.
- [15] P. Cerny, J. Nevrlý, and M. Mazanek, "Planar UWB Dipole Antennas Optimization Using PSO Method", *Proc. of 2<sup>nd</sup> EuCAP*, 2007.
- [16] C. A. Balanis, *Antenna Theory: Analysis and Design*, 2<sup>nd</sup> ed., New York: John Wiley & Sons Inc., 1997, ch. 8.
- [17] Available online: <http://www.feko.info>



## 7. Conclusions and recommendations

Array-based UWB short-range imaging system exhibits several distinctive advantages and draw considerable attention recently. One of important parts of any array-based UWB imaging system is its array subsystem. This explains importance of studies on UWB imaging array. An integral part of an array study is study on an array element including development of elements with dedicated performance and interaction with neighboring elements.

In this thesis several research activities have been performed in order to develop a design approach for 2-D UWB antenna arrays for short-range high-resolution imaging. Behavior and properties of UWB 2-D sparse antenna array have been studied. UWB antenna elements working at microwave and mm-wave range have been developed and analyzed. Experimental verifications of the developed elements as well as array topology have been performed. In addition, measurement and calibration techniques as well as data post-processing technique have been developed for the array experimental verification. With these activities we have developed understanding of performance and approaches of how to develop UWB antenna elements for array application and 2-D UWB sparse array topologies.

### 7.1 Results and novelties of this research

The major results achieved this research can be summarized as follows:

- A number of novel UWB antenna elements to be used in UWB imaging arrays have been developed. In particular,
  - I have developed a novel aperture stacked patch (ASP) antenna element operating within the frequency band from 9.95 GHz to 20 GHz . The dimension of the developed antenna is only 23 mm x 17 mm x 3.658 mm. The gain varies from 5 dBi to 10 dBi and the -3 dB beamwidth is of about 60°. The antenna possesses almost 67% fractional impedance bandwidth with only 3 layers, which is the best-known result for given limitations of geometry and specifications. In addition, the antenna has a gain of about 5 dBi to 10 dBi within this bandwidth and total efficiency larger than 90%. The antenna has a good time domain characteristic: the group delay is about 100ps, and the impulse response has 1/e pulse width of about 200ps. This demonstrates that the pulse distortion is small and the pulse ringing is short and is very suitable for time domain operations. Moreover, the antenna has low mutual coupling, thus it is suitable for the array application. The developed antenna has been successfully applied in UWB near-field imaging radar prototype.
  - I have developed a novel K-band differentially-fed, shielded elliptical dipole antenna using the LTCC technology. Numerical models based on time domain Finite Integral Technique (FIT) have been developed to optimize the antenna flares' size, ellipticity, separation, and shield profile. The antenna developed is characterized by -7.5 dB impedance bandwidth from 24 GHz to 30 GHz, about 5 dBi gain and larger than 95% radiation efficiency, and -3 dB gain bandwidth within the operational bandwidth. The

3 dB beamwidth at the E-plane is of about  $60^\circ$  and  $30^\circ$  at the H-plane. Such performance has never been achieved previously according to the available literature. The knowledge obtained by developing this antenna is used to reduce the risk of developing future M-band UWB LTCC antenna.

- I have developed a novel UWB differentially-fed aperture stack patch antenna in LTCC technology operating from 50 GHz to 78 GHz. The achieved gain is about 3 dBi to 8.5 dBi from 55 GHz to 62 GHz with about 80% efficiency. In comparison of other LTCC antennas working at the same band, this antenna has larger operational bandwidth (23 GHz, or 44% fractional bandwidth), stable over frequency radiation pattern, and simpler structure.
- I showed that the substrate has a significant impact on the radiation pattern due to surface wave. Different size of substrate will have very different radiation patterns due to spurious radiation caused by the surface wave. This makes the antenna working differently than expected when larger substrate is used for the purpose of connectorization or integration with the MMICs, or manufacture many antennas on a single substrate for array purpose. A multi-stair case shield has been proposed for the K-band antenna to decrease the influence of the surface wave and protect the antenna. However this shield is very complicated to manufacture and is not suitable for the M-band antenna. For the M-band antenna a simplified shield has been proposed to suppress the surface wave. It was shown that the proposed simple shield can alleviate the surface problem. By adding the shield the radiation patterns can be significantly improved, the broadside gain is increased by 2 dB ~ 4 dB and the impedance bandwidth is not decreased.
- Based on studies on the properties of sparse UWB antenna arrays a number of novel 1-D and 2-D UWB sparse arrays for high resolution imaging radar exploiting the MIMO concept has been developed. In particular,
  - I have investigated properties of PSF of UWB sparse array calculated by using modified Kirchhoff migration. It was demonstrated that the PSF has no grating lobes, but the sidelobe level increases as the element spacing increases. In addition, the sidelobe position occurs closer to the mainlobe when the element spacing increases. This study demonstrated that it is possible to use UWB sparse array configuration to obtain sharp PSF with low sidelobe level.
  - I have studied impact of antenna coupling on the imaging quality via a 1-D loop array. It was found that strong mutual coupling will cause long after time ringing, which will obscure small targets behind big targets. Moreover, strong mutual coupling will also raise the sidelobe level of the PSF.
  - I have exploited potential of MIMO array configuration. It was demonstrated that with the MIMO array configuration, one can achieve sharp PSF with very low PSF by using very few number of elements and small array aperture. Therefore the MIMO array configuration is very attractive and has strong potential to be used for short-range high resolution imaging radar system. Based on the research performed I have suggested two

approaches for deriving 1-D MIMO array topology from given performance specifications: deterministic and stochastic one. Furthermore, an approach to derive 2-D MIMO array topology from given performance specifications has been suggested.

- I have developed two 2-D MIMO sparse arrays based on same 1-D uniform MIMO array with 20 elements and compared their performance theoretically and experimentally. These two arrays have same cross-range resolution and same sidelobe level at X- and Y- axes, but due to different element arrangement, one array has lower sidelobe levels at other axes than the other array. Both arrays are used to image distributed targets in free space. The target can be identified in the image for both arrays with presences of clutters. This demonstrated the feasibility of using the 2-D MIMO sparse array for imaging application, but to obtain better image
- I have investigated possibilities to realize UWB mm-wave antennas in LTCC technology. The major challenges are the high relative permittivity of the substrate (in this case, the relative dielectric permittivity equals 7.54), stronger than for PCB-based antennas influence of the surface wave on antenna performance and not-standardized yet manufacturing process with manufacturing tolerances which are much larger than those of PCB technology. A novel K-band differentially-fed LTCC antenna developed by me has been used to assess and familiarize the techniques and limitations of the LTCC technology. I have suggested a novel realization of the via fence in LTCC technology and the novel UWB balun design on LTCC substrate. Finally, I have performed theoretical and experimental analysis of the manufacturing tolerances on the LTCC antenna performance.
- I have developed novel measurement and calibration techniques to accurately measure the reflections and radiation from mm-wave differentially-fed LTCC antennas. In particular, I have developed a coax-to-microstrip transition for the M-band antenna, calibration procedure and coax calibration standards for SOLT and TRL measurements (I have used SOLT calibration for micro-wave range measurement while both SOLT and TRL calibration were used for mm-wave range calibration) and several data post-processing technique used throughout this work. The most important technique is the time domain gating technique. By using the time domain gating technique we can gate out undesired noise or interference, and “clean” the measured data for further processing. The second most important one is mixed-mode S-parameter measurement technique, which was used for the differentially-fed antenna measurements.

## **7.2 Dissemination and utilization of the results**

The results achieved have been mainly utilized within Radiotect project. The developed 10 GHz – 18 GHz 1-D MIMO array has been integrated into a prototype of the imaging system for concealed weapon detection, which was developed by GeoZondas Ltd, Lithuania. The M-band antenna will be used by Technical University of Ilmenau in their mm-wave imaging system. Activities of integration of this antenna with MMIC front-end are continuing.

The results of this thesis have been presented and discussed at a number of top conferences in the field: the European Microwave Week 2010, the European Conference on Antenna and Propagation 2007, 2009, 2011, the European Radar Conference 2008 and 2009, and IEEE International Conference on Ultra-Wideband 2008. At all these conferences presentations have attracted attention of the audience and raised discussions after presentations. The results have also generated two Journal publications in EuMA International Journal of Microwave and Wireless Technologies.

### 7.3 Recommendations

In this section we present several recommendations for future studies as a continuation of the work presented in this thesis. The recommendations pertain to further investigation of MIMO array design principles and improvement of array performance, as described in the following.

#### Integrate developed mm-wave antennas with MMIC chips

The developed K-band and M-band antennas were successfully experimentally verified against the predicted performance. These antennas were designed to be integrated with MMIC chips and servers as mm-wave TDI radar head. They have been integrated with MMIC chips but the experiment verification was failed. It would be of great interest to design and manufacture a working prototype of integrated antenna with MMIC to evaluate the overall performance.

#### Further development of the mm-wave 2-D array

In this thesis, only mm-wave antenna prototypes have been developed but not the mm-wave array system. The design concepts developed from the microwave 2-D MIMO array should be extended to the mm-wave array for the ultra-high resolution imaging radar. It is interesting to develop 2-D mm-wave array topology and use the proposed mm-wave element to experimentally verify the designed mm-wave array. Imaging capabilities of the mm-wave array should be evaluated and compared with the microwave imaging array to evaluate the advantages and disadvantages of micro- and mm-wave imaging.

#### Further investigation on optimizing the array topology using PSO

In this thesis it has been pointed out that by using the PSO, one actually transfers the difficulty of designing a “good 1-D array topology” into designing a “good mask and weighting function”. Thus, it is important to examine the optimized beam patterns under different masks and weighting functions to determine how to design the mask and weighting function such that the optimized beam pattern is most “useful”.

#### Improvement of MIMO array design

In this thesis I have investigated the properties of UWB sparse array, and proposed approaches to develop 2-D UWB MIMO sparse array. Experimental analysis demonstrated the feasibility of using such array to obtain high resolution images. However, the approach to develop the 2-D array is not unique. If the element number increases, the approach may not be suitable as it will give too many possible solutions. Therefore, it would be interest to develop a method to

systematically obtain an optimal topology. One possible solution may be to use optimization algorithm such as PSO to obtain such topology.

During the measurement it was found that the PSF of array 2 has lower sidelobe level than that of the array 1. In addition, the measurement results from the array 2 are less susceptible to system instability than that from the array 1. Thus it would be interesting to exploit why the results obtained from array 2 are less susceptible.

The experimental results showed that objects, which can be easily imaged in free space, can be easily masked in the presence of clutter. Such clutter is due to the sidelobe of the PSF. It has been found that the sidelobe level achieved in the developed 2-D arrays is not sufficient to image small objects such as knife or pistol having larger objects such as human body in the background. Thus, it is important to improve the design by adjusting the topology and adding more elements to bring down the sidelobe level.





## **Appendix A Introduction to equipment used**

### **A.1 Programmable network analyzer**

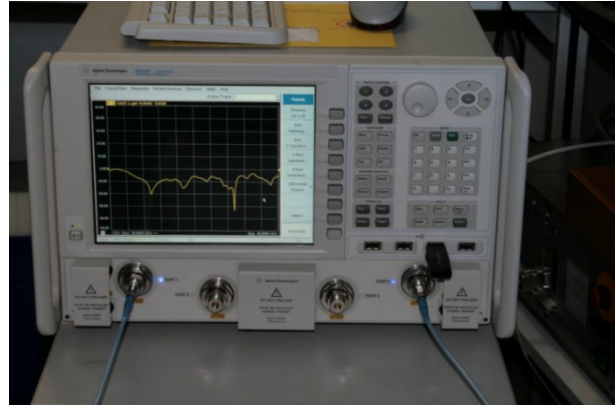
In this thesis several antennas working at different frequency bands and with different feeding methods have been developed. To measure these different antennas, several different programmable network analyzers (PNA) were used. Agilent E8364B PNA (Figure A.1 (a)), which is a 2-port PNA and operates from 10 MHz to 50 GHz, was used for microwave range measurement. This PNA is used in to measure the ASP antenna described in chapter 3, and used to obtain the array data described in Chapter 6. The antenna described in Chapter 4 is a differentially-fed antenna. Therefore, Agilent XN5245A 4-port PNA (Figure A.1 (b)) working from 10 MHz to 50 GHz was used. This PNA can configure a pair of ports into differential port, allowing us to obtain the mix-mode S-parameters. The antenna described in Chapter 5 is working from 50 GHz up to 78 GHz. To measure this antenna we have used Agilent E8361C PNA (Figure A.1 (c)) which is a 2-port PNA working from 10 MHz to 67 GHz. A typical 2-port S-parameter measurement setup is shown in Figure A.1 (d).

### **A.2 24-port switch**

Multiport mechanical switch Agilent 87050A-K24 (Figure A.2 (a)) has been used for array PSF measurement. The Agilent 87050A-K24 provides the ability to make single connection, multiple measurements of multiport devices with up to 24 ports. The operational frequency range is from 50MHz to 20GHz. The specification is shown in Table A - 1. The switch is controlled by the PNA. Before the measurement, full two-port calibrations over all the used ports were carried out. The measurement is done by sequentially switch the TX path and RX path to generate a 4x16 data streams. The array PSF measurement setup is shown in Figure A.2 (b).



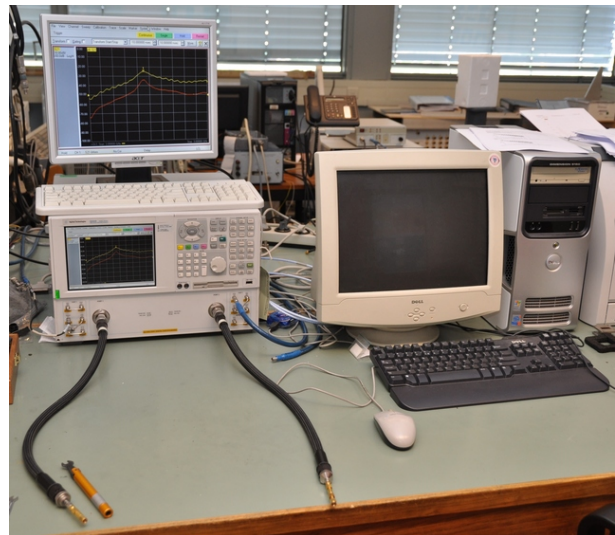
(a) 2-port network analyzer E8364B



(b) 4-port network analyzer N5245A



(c) 2-port network analyzer E8361C



(d) Typical S-parameter measurement setup with a 2-port network analyzer

**Figure A.1 PNA used in this thesis (a) E8364B (b) N5245A (c) E8361C (d) Typical S-parameter measurement setup with a 2-port network analyzer**

**Table A - 1 Agilent 87050A Option K24 Specifications**

Isolation	0.5GHz to 1.3GHz	$\geq 85\text{dB}$
	1.3GHz to 3.0GHz	$\geq 100\text{dB}$
	3.0GHz to 6.0GHz	$\geq 95\text{dB}$
Return loss	0.5GHz to 1.3GHz	$\geq 24\text{dB}$
	1.3GHz to 3.0GHz	$\geq 20\text{dB}$
	3.0GHz to 6.0GHz	$\geq 14\text{dB}$
	6.0GHz to 12.4GHz	$\geq 12\text{dB}$
	12.4GHz to 20GHz	$\geq 8\text{dB}$
Insertion loss	0.5GHz to 6.0GHz	$\leq 2.5\text{dB}$
	6.0GHz to 12.4GHz	$\leq 3.5\text{dB}$
	12.4GHz to 20GHz	$\leq 4.5\text{dB}$
Phase deviation	Reflection Port to Ports 1-24 (0.5GHz to 6.0GHz)	$\pm 10^\circ$
	Transmission Port to Ports 1-24 (0.5GHz to 6.0GHz)	$\pm 10^\circ$
	Reflection Port to Ports 1-24 (6.0GHz to 20GHz)	$\pm 35^\circ$
	Transmission Port to Ports 1-24 (6.0GHz to 20GHz)	$\pm 35^\circ$



(a) Agilent 87050A Option K24 Switch



(b) Network analyzer and switch during measurement

**Figure A.2 Agilent switch and measurement setup (a) 24-port switch (b) measurement setup**

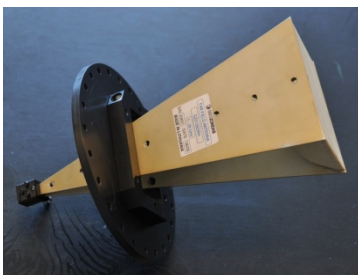
### A.3 Antenna probes

In this thesis several antennas operating at different frequency bands were analyzed, which includes the 10GHz-18GHz ASP antenna, the K-band LTCC antenna, and the M-band LTCC antenna. The numerical and experimental characterizations of these antennas are reported in Chapters 3-5. To measure the gain and radiation patterns, standard gain horns working in the corresponding frequencies were used.

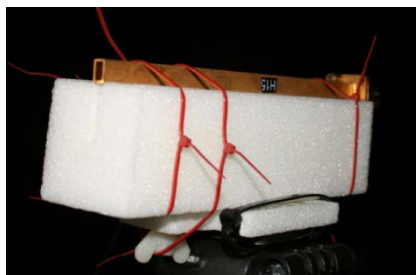
TEM horn antenna (Figure A.3 (a)) working from 1GHz to 26GHz with relatively flat gain has been used to measure the 10 GHz to 18 GHz ASP antenna gain and radiation patterns in the anechoic chamber DUCAT.

An open waveguide WR 28 (Figure A.3 (b)) was used to measure the K-band antenna. The gain of this open waveguide is about 5 dBi (Figure A.4).

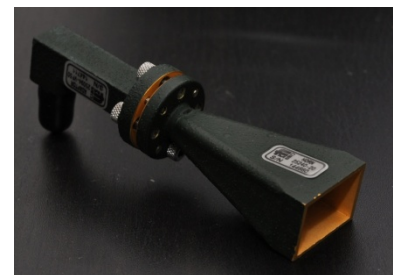
For M-band antenna standard gain horn (Figure A.3 (c)) working from 49.9 GHz to 75.8 GHz was used to measure the antenna gain and radiation patterns. The nominal gain of this standard gain horn is 18 dBi to 21.5 dBi.



(a) TEM horn



(b) WR 28 open waveguide



(c) Mm-wave standard gain horn

**Figure A.3 Antenna probes used in this thesis (a) TEM horn (b) WR 28 open waveguide (c) mm-wave standard gain horn**

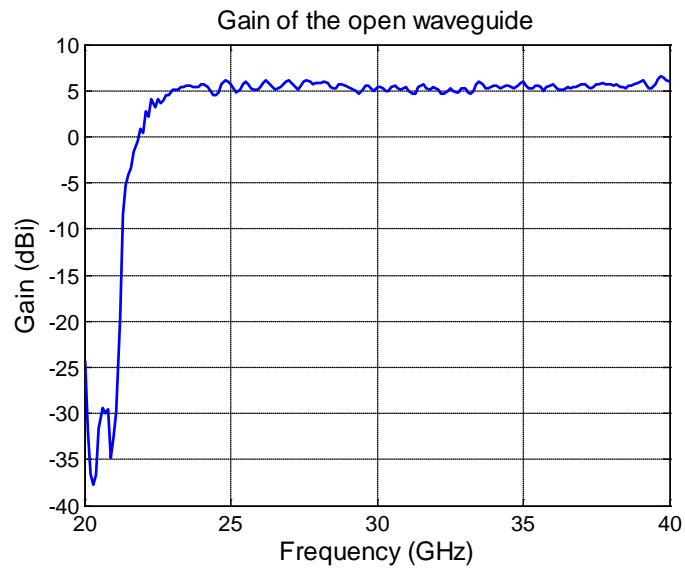


**Figure A.4 Gain of the open waveguide WR 28**

#### **A.4 Customized mini-SMP to 2.4mm adaptor**

Due to the close vicinity of two mini-SMP connectors of a differentially-fed K-band LTCC antenna, we were unable to use off-the-shelf adaptors. Therefore, we customized an adaptor, which is a mini-SMP connector connected to a semi-rigid coaxial cable, then connected to a 2.4 mm connector (Figure A.5). Figure A.6 shows the differentially-fed K-band antenna with the customized adaptor.



**Figure A.5**  
**Customized mini-SMP to 2.4 mm**  
**adaptor**

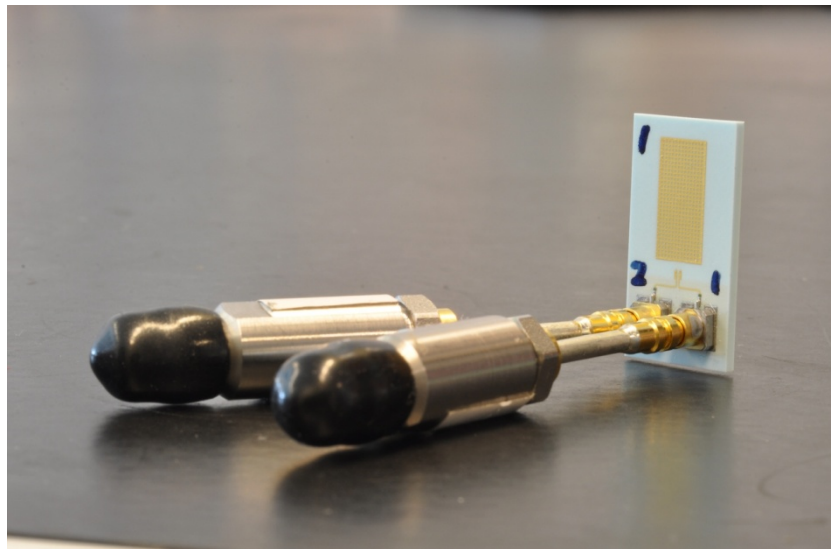


**Figure A.6 Differentially-fed K-band LTCC**  
**antenna with customized mini-SMP to 2.4 mm**  
**adaptor**



## Appendix B Introduction to LTCC<sup>2</sup>

### B.1 Introduction to LTCC technology

LTCC stands for Low Temperature Co-fired Ceramic. It can be defined as a multilayer circuit fabricated by laminating single greensheets (term for unfired tapes; Green Tape<sup>TM</sup>, Dupont) with printed conductor lines etc. on the surface on top of each other and firing them all together in one step. This process is almost similar to that of High Temperature Co-fired Ceramic (HTCC), but the big advantage of the LTCC system is the possibility to use low resistivity conductors like silver, gold, copper and alloys with palladium and platinum instead of tungsten and molybdenum; the separation between this two (different) technologies is defined with the firing temperature: in excess of 1000°C for HTCC and below for LTCC (mostly 850 to 875°C, what makes it possible to use silver for conductor lines etc.). The whole process includes several steps which are described under "LTCC Process". As a disadvantage it has to be mentioned that these ceramics provide a bad thermal conductivity (about 2.5 to 4 W/mK), what can, if it's necessary be compensated with the help of so called Thermal Vias which rise the thermal conductivity up to about 20 W/mK (70 W/mK; Source: DuPont).

It is possible to involve photo processes into the row of process steps of LTCC, but (nearly) all of them to be applied pastes are printed on the greensheet with the help of a conventional thick film technique. Standard thickfilm pastes must not be used (except for several postfire processes; depends on material); this is due to the shrinking the tape is subjected to during the firing. This shrinking is about 10 to 15 percent in x/y-axis (shrinkage of x- and y-axis may be different) and about 10 to 45 percent in z-axis.

It is also possible to integrate passive elements like resistors, capacitors and inductors into the substrate. Resistors are processed with the help of special pastes, which have to be printed on the tape just like conductor lines and have to be post- or cofired. The nowadays problem is the tolerance of buried resistors, which provide only values of about 30 percent. Capacitors and inductors are built only with the help of special forms of the conductor lines (plates, spoils); there are and there will be much more materials like ferrite pastes and high-k pastes, which offer a great range of possibilities to process such elements.

The LTCC technology avoids many disadvantages the others have and offers a couple of benefits:

- Economizes multiple steps of the manufacture process compared with the conventional thickfilm technology (parallel processing);
- Mass production methods can be really applied (several processing steps can be automated);

---

<sup>2</sup> Cited from [www.ltcc.de](http://www.ltcc.de)

- Fabrication techniques are relatively simple and inexpensive;
- Tapes of different compositions can be manufactured with desired layer properties;
- Thermo-physical properties can be modified;
- Possibility of auto-packaged devices fabrication;
- Electronic circuits can be integrated, using its hybrid nature;
- Design and manufacture 3-dimensional circuits;
- Possibility of cutting the tape / substrate into different shapes;
- Because of the possibility to bury passive components within the substrate, it reduces the size of circuits (down to about 50 percent in comparison to the PCB);
- Number of signal layers almost unlimited;
- Ability to perform at frequencies over 30GHz;
- High resistance against ambient working temperatures (up to 350°C);
- Good thermal conductivity compared to PCBs (factor 10);
- Good match to semiconductor TCEs;
- Very good hermeticity of the substrate.

## **B.2 LTCC Process**

The LTCC process is illustrated in Figure B.1. The process is separated into the following steps:

- **Slitting:**

Mostly the greensheets are shipped on a roll; the tape has to be unrolled onto a clean, stainless steel table. The sheet is cut with a razor, laser or a punch into parts (these parts have to be a little larger than the blank size, if the material needs to be preconditioned). If a laser is used it is very necessary to control the power to avoid firing of the sheets.

- **Preconditioning:**

Some tapes need to be preconditioned (e.g. Dupont GreenTape); that means the greensheet has to be baked for about half an hour at 120°C (depends on manufacturer and material). Normally the tapes are shipped with an applied foil / bake sheet, which has to be removed before lamination at the latest; some processors use this foil as a filling mask for the vias.

- **Blanking:**



A blanking die is used to create orientation marks and lamination tooling holes (and the final working dimension in case of to be preconditioned tapes).

*Note:* It is preferred to rotate the single parts in turns 90° to compensate the different x/y-shrinking of the LTCC.

■ **Forming vias:**

Vias may be punched or drilled with a laser (low power).

● **Filling vias:**

Vias can be filled with a conventional thick film screen printer or an extrusion via filler.

In the first case the tape has to be placed on a sheet of paper which lays on a porous stone; a vacuum pump holds the tape on his place and is used as an aid for via filling.

*Note:* The possibilities of this method are limited; the vias must have a larger diameter than tape thickness. The smallest possible size of vias to be filled also depends on the viscosity of the paste.

The second possibility to fill the vias is to use a special extrusion via filler that works with pressures of about 4 to 4.5 bar.

Both methods need to have a mask; this mask should be made of a 150-200mm thick stainless steel. An alternative to that is to use the (Mylar-)foil the tape usually is applied on.

For the filling of blind vias it is advisable to form the holes concerned of the masks a little smaller than the diameter of the blind vias. Otherwise there could occur problems with the filling rate.

● **Printing:**

Cofireable conductors etc are printed on the green sheet using a conventional thick film screen printer. The screens are standard (250 – 325) emulsion type thick film screens. Just like the via printing process, a porous stone is used to hold the tape in place. Printing of the conductor tends to be easier and of higher resolution than standard thick film on alumina. This is due to the flattness and solvent absorption of the tape. After printing, the vias and conductors have to be dried in an oven at 80 to 120°C for 5 to 30 minutes (depends on material); some pastes need to level at room temperature for a few minutes before drying.

*Note:* Resistors may vary their value when terminated with different conductors. With the help of a Micro-Screen printer, it is possible to print conductors with a 50mm line resolution.

● **Register for Lamination:**

Each layer is placed in turns over tooling pins.

Some processors use a heat pliers to fix the sheets in turns one on top of the other.

- **Lamination:**

There are two possibilities of laminating the tapes.

The first is named uniaxial lamination; the tapes are pressed between heated platens at 70°C, 200 bar for 10 minutes (typical values). This method requires a 180° rotation after half the time. The uniaxial lamination could cause problems with cavities / windows. This method causes higher shrinking tolerances than the isostatic lamination.

The main problem is the flowing of the tape; that results in high shrinkage tolerances (especially at the edge of the part) during the firing and varying thicknesses of single parts of each layer (causes hard problems on the high frequencies sector).

The second way is to use an isostatic press. The stacked tapes are vacuum sealed in a foil and pressed in hot water (temperature and time are just the same like using the uniaxial press). The pressure is about 210 bar.

*Note:* deep cavities and windows need to have an inlay during lamination.

- **Cofiring:**

Laminates are fired in one step on a smooth, flat setter tile. The firing should follow a specific firing profile, what causes the need of a programmable box kiln.

A typical profile shows a (slow) rising temperature (about 2-5°C per minute) up to about 450°C with a dwell time of about one to two hours, where the organic burnout (binder) takes place; then the temperature has to be raised up to 850 to 875°C with a dwell time of about 10 to 15 minutes. The whole firing cycle lasts between three and eight hours (depends on the material; large / thick parts cause the need of a modification of the firing profile).

*Note:* especially resistor pastes need to have defined firing conditions (temperatures); Otherwise they vary enormous in value.

- **Postfiring:**

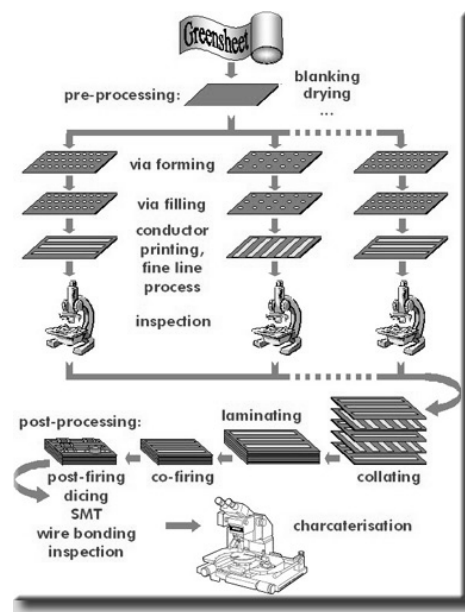
Some materials need to be postfired; that means the paste is to be applied after firing the tape and has to be fired again. The postfiring conditions depend on the used material and vary in a wide range.

*Note:* especially resistor pastes need to have defined firing conditions (temperatures); Otherwise they vary enormous in value.

- **Singulation:**

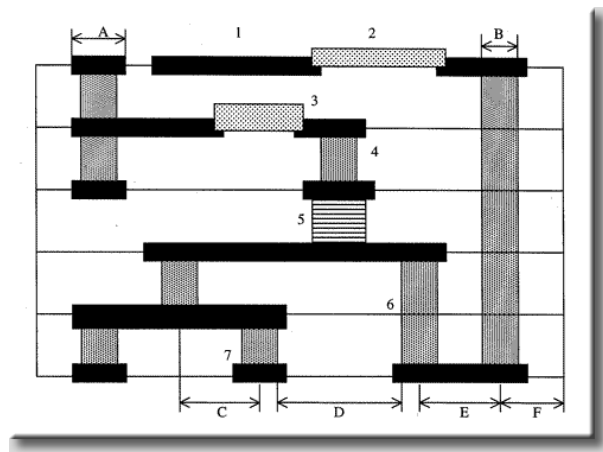
If the fired parts have to be cut into smaller pieces or other shapes, there are three different ways to realize.

The first is to use a post fire dicing saw, which is a common method and works very well for rectangular shapes; it holds tight outside dimensional tolerances and allows high quality edges.



Material	Dupont 943
Relative permittivity	7.54
Loss tangent	0.001 @ 50GHz
Layer thickness after shrinkage	104um
Metal thickness	7um
Surface roughness	1~3um
Size of a substrate	50mm x 50mm

## B.4 LTCC manufacturing terminology



1 : Top Side External Conductor

2 : Cofired or Postfired Surface Resistor

3 : Buried Resistor

4 : Buried Via

5 : Buried Capacitor

6 : Stacked Vias

7 : Blind Via

A : Via Cover Pad

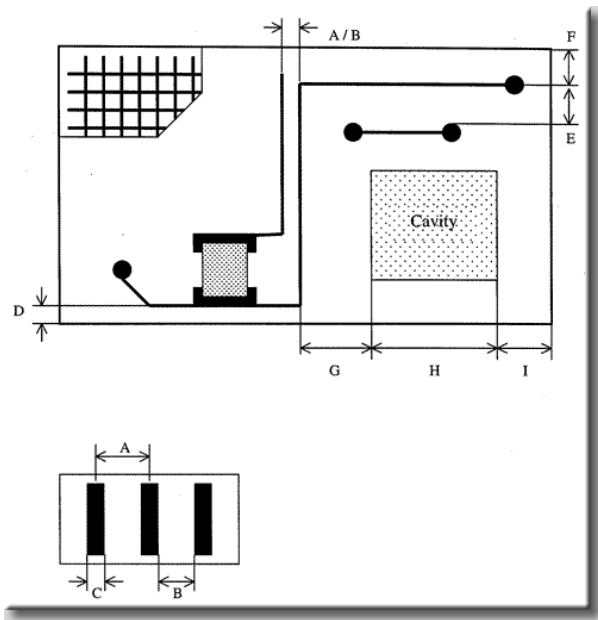
B : Via Diameter

C : Via Stagger

D : Via Spacing

E : Via Pitch

F : Via Center To Part Edge



A : Line Pitch

D : Conductor To Part Edge / Edge To Feature

G : Line To Cavity Wall Spacing

B : Line Spacing

E : Via To Conductor Line Spacing

H : Cavity Size

C : Line Width

F : Via Center To Part Edge

I : Cavity Wall To Part Edge Spacing

## B.5 Design rules

**Table B - 2 Design rules**

	Standard	Possible
Line width in um	80um	50um
Line spacing in um	80um, the spacing is better same as the line width	50um
Via diameter in um		75um
Via coverpad / Catchpad	200um	Same as the via diameter
Via spacing in um		200um
Via edge to part edge	400um	
Via edge to cavity edge	400um	
Line to part edge	200um	

## References

- [1] Available online: [www.ltcc.de/en](http://www.ltcc.de/en)



## Appendix C List of antennas parameters

### C.1 Microwave antenna parameters

**Table C - 1 Initial antenna parameters**

Parameter name	Description	value (mm)
$A_l$	Aperture length	6
$A_w$	Aperture width	0.4
$L_s$	Stub length	2.5
$W_1$	Width of the lower patch	6.9
$W_2$	Width of the upper patch	6
$L_1$	Length of the upper patch	4.5
$L_2$	Length of the lower patch	4.6
$F_s$	Separation of the feeding fork	4

**Table C - 2 Optimized antenna parameters**

Parameter name	Description	value (mm)
$A_l$	Aperture length	7
$A_w$	Aperture width	0.5
$L_s$	Stub length	2.2
$W_1$	Width of the lower patch	9
$W_2$	Width of the upper patch	8
$L_1$	Length of the upper patch	4.8
$L_2$	Length of the lower patch	4.3
$L_s$	Length of the stub	2.2
$F_s$	Separation of the feeding fork	4.5

### C.2 K-band antenna parameters

**Table C - 3 Optimized K-band antenna parameters**

Parameter name	Parameter value (mm)
X-axis radius	1.7
Y-axis radius	2.21
Flare separation	0.57

W	12.4
L	12
$W_1$	6.24
$W_2$	5.28
H	0.52
$h_1$	0.312
$h_2$	0.312

### C.3 M-band antenna parameters

**Table C - 4 Initial M-band antenna parameters**

Parameter name	Parameter description	Initial value (mm)
TW	Top patch width	$\lambda_d/2 = 0.85$
TL	Top patch length	$\lambda_d/2 = 0.85$
PW	Lower patch width	$\lambda_d/2 = 0.85$
PL	Lower patch length	$\lambda_d/2 = 0.85$
L	Center aperture length	$0.15*\lambda_d = 0.255$
L1	H-shaped aperture length	$0.09*\lambda_d = 0.153$
W1	Center aperture width	$0.03*\lambda_d = 0.051$
W2	H-shaped aperture width	$0.06*\lambda_d = 0.102$
r	Feeding pin radius	0.045
sep	Feeding pin separation	0.37
$h_1$	Substrate height between upper patch and lower patch	0.208
$h_2$	Substrate height between lower patch and ground	0.208
$h_3$	Substrate height from bottom of the antenna to the ground	0.416



**Table C - 5 Optimized M-band antenna parameters**

Parameter name	Parameter description	Optimized value (mm)
TW	Top patch width	0.55
TL	Top patch length	0.65
PW	Lower patch width	0.45
PL	Lower patch length	0.65
L	Center aperture length	0.25
L1	H-shaped aperture length	0.5
W1	Center aperture width	0.16
W2	H-shaped aperture width	0.15
r	Feeding pin radius	0.045
sep	Feeding pin separation	0.37
$h_1$	Substrate height between upper patch and lower patch	0.208
$h_2$	Substrate height between lower patch and ground	0.208
$h_3$	Substrate height from bottom of the antenna to the ground	0.416



## Appendix D Projection slice method and element shadowing effect

The principle of the projection slice method is illustrated in Figure D.1 using a 16-element rectangular array topology with element spacing of  $2\lambda_c$ . At the top of Figure D.1 are the 2-D array topologies with different rotation angle, and at the bottom of Figure D.1 are the corresponding equivalent one-dimensional arrays. The weight of each element in the equivalent arrays is determined by how many elements overlapping on that position. For example, the magnitude of each element in the equivalent 1-D array in Figure D.1 (a) is 4, because 4 elements are projected onto the same place. Figure D.2 shows the three-dimensional PSF of the 16-element rectangular array topology and its 2-D array pattern at three cut planes. It can be seen that the array pattern of at different  $\Phi$  cut plane is the same as their 1-D equivalent array (Figure D.2 (b), (c), and (d)).

From Figure D.2 (b), (c), and (d), it can be seen that the array pattern at different cut plane has very different sidelobe behavior.  $\Phi=\pi/8$  cut-plane has the lowest sidelobe level while  $\Phi=0$  cut-plane has the highest sidelobe level. This is due to the element shadowing effect. At  $\Phi=0$  cut-plane, the equivalent array has only four elements each with weight 4, and the spacing between elements is  $2\lambda_c$ . On the other hand, the equivalent array at  $\Phi=\pi/4$  cut-plane has seven elements with triangular amplitude taper, and the equivalent array at  $\Phi=\pi/8$  cut-plane has 16 elements with dense spacing and uniform amplitude taper. The element spacing of  $\Phi=\pi/4$  cut-plane equivalent array is slightly larger than  $\lambda_c$ , and the element spacing of  $\Phi=\pi/8$  cut-plane is about  $\lambda_c/2$ . As a result, the  $\Phi=\pi/8$  cut-plane equivalent array is the densest array which results in the lowest sidelobe level. This called element shadowing. For the  $\Phi=0$  cut-plane, four elements are overlapped with each other, thus three elements are “shadowed”.

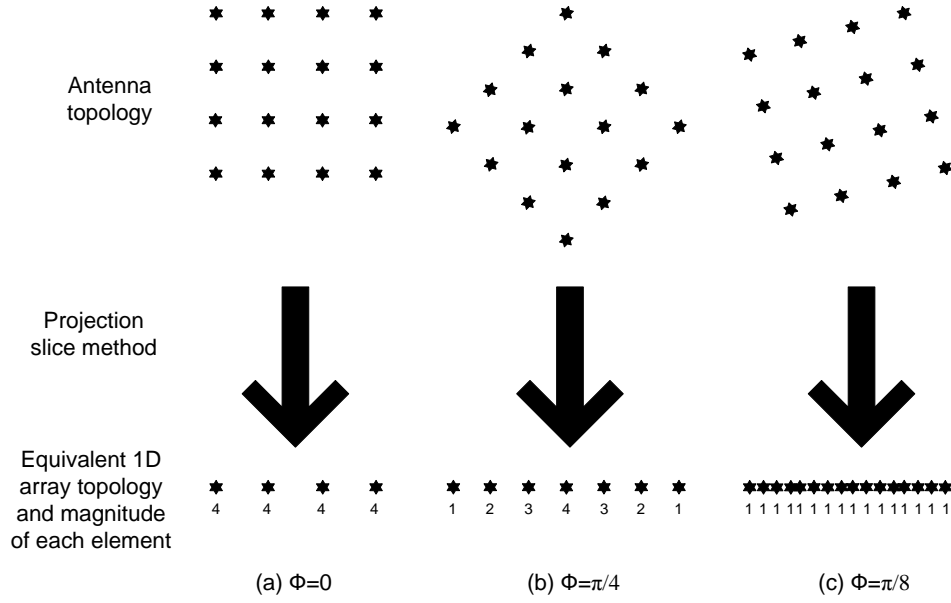
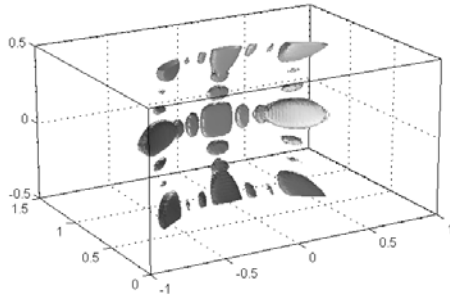
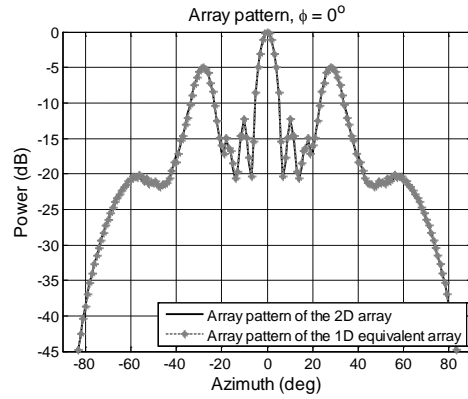


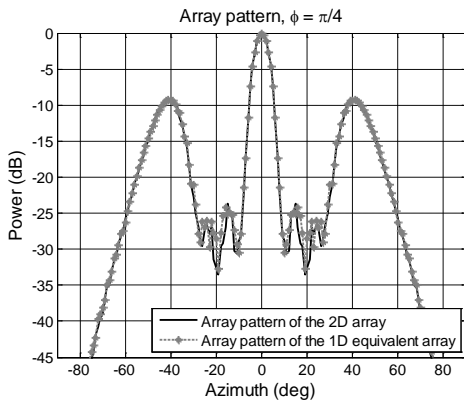
**Figure D.1 Illustration of projection slice method and element shadowing with a 16-element rectangular array topology in three cut planes (a)  $\Phi=0$  cut plane (b)  $\Phi=\pi/4$  cut plane (c)  $\Phi=\pi/8$  cut plane**



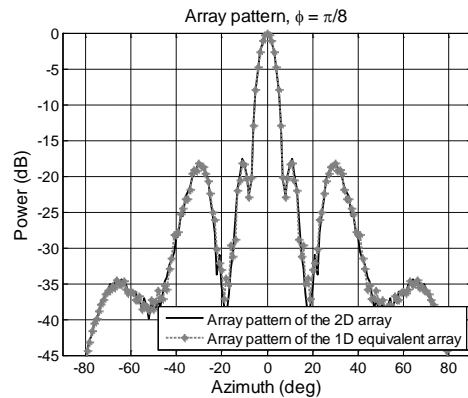
(a) 3D PSF of the array



(b) Array pattern at  $\Phi=0$  cut plane



(c) Array pattern at  $\Phi=\pi/4$  cut plane



(d) Array pattern at  $\Phi=\pi/8$  cut plane

**Figure D.2 3D PSF and 2D array pattern of the 16-element rectangular array topology at different cut planes and their equivalent 1D array**

## Appendix E Experimental verification of 1-D MIMO array

The 1-D MIMO array developed using deterministic approach (Figure 6.15 (a)) was manufactured (Figure E.1) and its imaging capability was experimentally analyzed. The 1-D MIMO array itself cannot be used for 3-D image generation because the 1-D array cannot provide a C-scan. Thus, we have combined the 1-D array with SAR to form a “MIMO-SAR” setup. The horizontal scan was done by the 1-D MIMO array electrically, while the vertical scan was done by a mechanical scanner. The scanning height was 170 cm with a step of 0.5 cm.

The measured PSF of the MIMO-SAR array from a small sphere of 3 cm diameter is shown in Figure E.2. Comparing with Figure 6.27, the PSF of the MIMO\_SAR array has much less artifact. This indicates that the artifacts appeared in the PSF of the 2-D MIMO arrays were mainly caused by the scarcity of the array, rather than the imperfection of the antenna. Figure E.3 illustrates the image of four spheres at -6 dB level. The MIMO-SAR array can successfully resolve the 4 targets.

The same pistol used in 6.7.3 was used to evaluate the imaging capability of the MIMO-SAR array of distributed target (Figure E.4 (a)), and the result is shown in Figure E.4 (b). A better image (comparing to Figure 6.32 (c) and (d)) was obtained. Although there were still some artifacts, this demonstrated that if the antenna elements are sufficient, it is possible to deliver good quality image.

The MIMO-SAR array was also used to measure a pistol on human body (Figure E.5 (a)). The scan of MIMO-SAR was 40 cm with the same 0.5 cm step. The pistol was fixed on a leg of a sitting still person, which prevented minor movements (also due to breathing) and, consequently, blurring of the image. The result is shown in Figure E.5 (b). The pistol can be clearly seen at 20 dB dynamic range. This demonstrates on one hand, the developed antenna can be successfully used for the imaging radar, and on the other hand, the MIMO-SAR approach has a serious potential for imaging of concealed weapons.



**Figure E.1 Manufactured 1-D MIMO array**

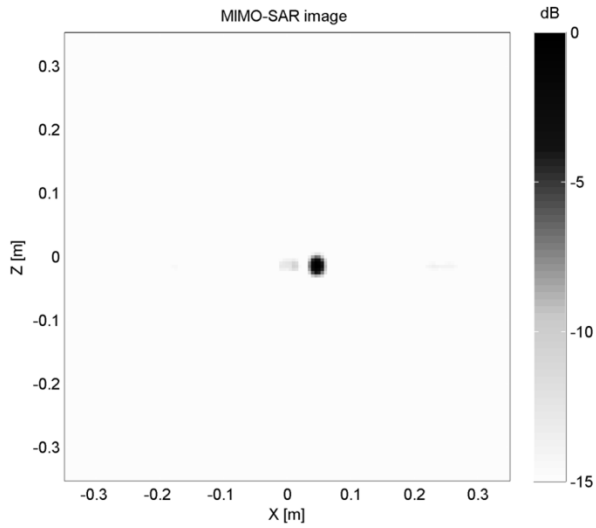


**Figure E.2 Measured MIMO-SAR PSF**

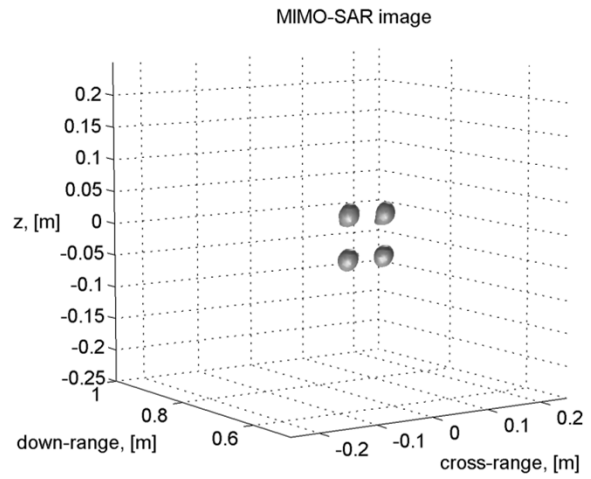
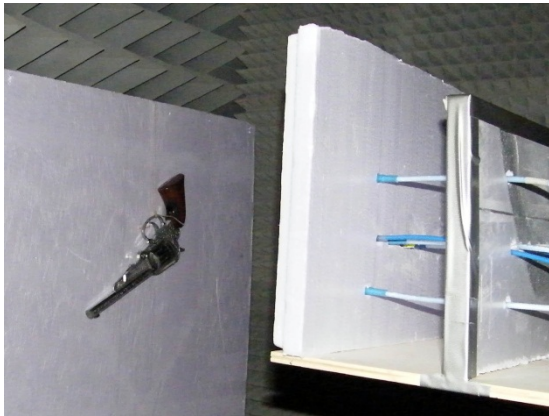
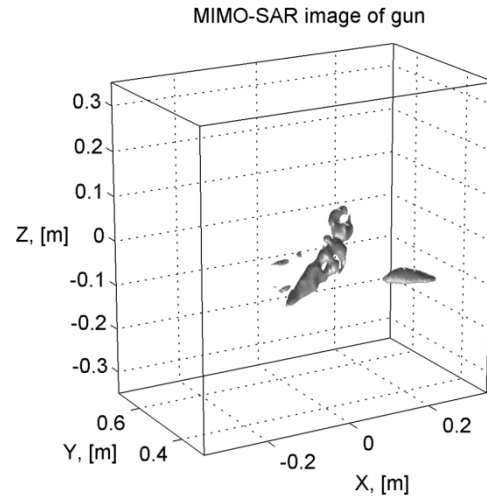


**Figure E.3 Image of 4 spheres separated by 3 cm**



**(a) Measurement setup**

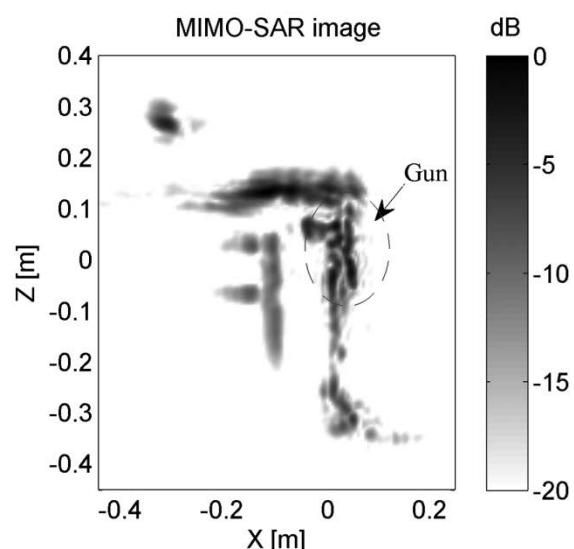


**(b) Image of the pistol**

**Figure E.4 Measurement of a pistol with the MIMO-SAR array (a) Measurement setup (b) Measured image**



(a)



(b)

**Figure E.5 Measurement of a pistol on human body with the MIMO-SAR array (a) Measurement setup (b) Measured image**





## List of Acronyms

UWB	Ultra-wide band
FCC	Federal Communications Commission
GPR	Ground penetration radar
NDT	Non-destructive testing
SAR	Synthetic aperture radar
TWI	Through-the-wall imaging
CWD	Concealed weapon detection
EM	Electromagnetic
RF	Radio-frequency
FBR	Front-to-back ratio
IRCTR	International Research Center for Telecommunications and Radar
LTCC	Low-Temperature Co-fired Ceramic
MoM	Method of Moment
FIT	Finite Integral Technique
PSF	Point Spread Function
MIMO	Multiple Input Multiple Output
PSO	Particle Swarm Optimization
ASP	Aperture-Stacked Patch
PNA	Programmable Network Analyzer
DUCAT	Delft University Chamber of Antenna Tests
FHR	Fraunhofer-Institut für Hochfrequenzphysik und Radartechnik
AUT	Antenna under test
PSF	Point Spread Function
SOLT	Short-Open-Load-Thru
TRL	Thru-Line-Reflect
MS	Microstrip
DUT	Device Under Test
FFT	Fast Fourier Transform
IFFT	Inverse Fast Fourier Transform
MMIC	Microwave Monolithic Integrated Circuits
CPS	Co-planar Strip line
CPSWG	CPS with ground



## Summary

UWB radar is the most promising radar system for the future. In addition, by combining the UWB and array signal processing, one can obtain 3-D images of the objects for classification and identification, which is very useful in many applications. To achieve high-resolution real-time 3-D imaging radar, two essential items are missing in the current technology: dedicated antenna systems for sparse C-scan acquisition and fast high-quality imaging algorithms. In this thesis we have focused on the development of dedicated sparse antenna systems, including the sparse array topology development and antenna element development, while imaging algorithm is out of scope of this research.

The main conclusions and their novelties are presented as follows:

1. *Novel microwave ASP antenna:* In this thesis a novel ASP antenna working from 10 GHz to 18 GHz has been developed. This antenna is aimed to be used for the time-domain UWB imaging array. The analysis demonstrated that the antenna not only has sufficient -10 dB impedance bandwidth from 9.95 GHz to 20 GHz, but also has good radiation characteristic within the impedance bandwidth. The antenna has gain of 5 to 10 dBi. The FBR is larger than 10 dB, and the -3 dB beamwidth is about  $\pm 30^\circ$  in both E- and H-plane. The antenna has about 100 ps group delay and the impulse response has 1/e pulse width of about 200 ps. The analysis of radiated pulse distortion with respect to angle demonstrated that the pulse is very similar within the -3 dB beamwidth. This demonstrated that the antenna has small distortion and short after-time ringing, which makes the antenna suitable for time-domain application. The antenna coupling behavior analysis showed that the coupling between elements is small. Therefore, no severe performance degradation was expected when this antenna operates in the sparse MIMO array environment.
2. *Investigation of LTCC technology:* LTCC technology has been selected to manufacture mm-wave antennas to be integrated with MMICs. The multilayer nature of the LTCC technology makes it suitable for system-in-package. However, LTCC technology is a relatively new and not-yet standardized technology and LTCC material normally possesses high dielectric constant, which makes the design of UWB antenna difficult. As a result, we have investigated the properties of LTCC material and its impact on UWB antenna design. We have also explored the manufacturing limitations of the LTCC technology, and proposed solutions to overcome these limitations. The LTCC processing variations have also been studied. It reveals that the variation of substrate height has significant influence to the antenna resonance frequency, while the variation of relative permittivity has very small impact on the antenna reflection coefficient.
3. *K-band LTCC antenna:* A novel K-band antenna using the LTCC technology has been developed. This antenna is a differentially-fed, multi-

staircase shielded elliptical dipole UWB antenna. The antenna has a novel differential feeding which enables it to be directly integrated with differential MMICs. The multi-staircase shield reduces the antenna back radiation and improves the antenna forward radiation, while keeping the antenna impedance bandwidth large. The antenna has a -7.5 dB impedance bandwidth from 24 GHz to 30 GHz, with a gain of approximately 5 dBi to 7 dBi. Thanks to the presence of the shield, the antenna radiation patterns are stable within the operating bandwidth, and the 3 dB beamwidth at the E-plane is of about 60° and 30° at the H-plane.

4. M-band LTCC antenna: A novel differentially-fed UWB antenna working at M-band using LTCC technology has been developed. The antenna is based on ASP type of antenna with novel differential feeding structure. With this feeding structure the antenna can achieve a -10 dB impedance bandwidth from 50 GHz to 78 GHz. The high dielectric constant of LTCC material induces severe surface wave which substantially degrade the antenna radiation characteristics. Although the multi-staircase shield proposed for the K-band antenna can solve this problem, it is far too complex to realize in the M-band. A novel simplified rectangular shield has been proposed to solve this. This shield does not have complex structure but can successfully confine the surface wave, thus improving the antenna radiation characteristics. The gain of the M-band antenna is from 3.5 dBi to 8 dBi from 50 GHz to 62 GHz, and the -10 dB beamwidth is at least from -45° to 45° for both E- and H-planes.
5. Element coupling investigation for imaging array: The influence of element coupling to the quality of image has been investigated. The antenna cross-talk does not pose severe threat to the image quality, because it can be eliminated by time-gating technique. The most influential coupling is the scattering coupling, which acquires fewer attentions in the antenna community. This type of coupling will alter the antenna receive sensitivity function. If at certain frequency the coupling is stronger than others, then the sensitivity function will have a spike at that frequency. This spike will cause long after-time ringing, masking small objects behind a large object. Another profound influence of scattering coupling to the image is that the scattering coupling will cause increase of sidelobe level, which increases the clutters.
6. 2-D sparse MIMO antenna array topology: Investigation demonstrated that MIMO array concept can achieve 2-D sparse real-aperture array for fine cross-range resolution and low sidelobe imaging system. The design of the 2-D MIMO array has been break down to two steps. The first step is to design a 1-D MIMO array with desired PSF properties. The next step is expand this 1-D MIMO array into 2-D array by firstly lay the designed 1-D array on two orthogonal axes, and then use the rotational 1-D array analysis to obtain the 2-D array. Two 2-D arrays based on the same 1-D array have been developed using this approach and manufactured. The measured results of small objects demonstrated that both arrays were capable to image small objects. It was also found that the sidelobe level is one of crucial specifications of the array, which should be specified by system designers in order to achieve proper performance of the whole

imaging system. The 3-D imaging results proved high potential of using microwave 2-D UWB sparse MIMO array in real-time short-range high-resolution imaging applications.



# Samenvatting

UWB radar is het meest belovende radar systeem voor de toekomst. Een van de toepassingen is bijvoorbeeld het maken van 3-D beelden van een object voor klassificatie en identificatie doeleinden, door het combineren van UWB met de signaal verwerking van een antenne-stelsel. Om hoge resolutie real time 3-D beeldweergave radar te maken, missen er tegenwoordig nog twee stukken technologieën: een antenne systeem die toegewijd is aan 'sparse C-scan' acquisitie en snelle hoge kwaliteit beeldweergave algoritmes. In dit proefschrift geven we de aandacht aan het ontwikkelen van toegewijde 'sparse' antenne systemen, waarbij zowel naar de ontwikkeling van topologie van het antenne stelsel alsmede naar de antenne elementen wordt gekeken. Beeldweergave algoritmes vallen buiten de scope van ons onderzoek.

De hoofd conclusies en hun nieuwigheden zijn als volgt:

1. Nieuwe microgolf ASP antenne: In dit proefschrift wordt een nieuwe ASP antenne die tussen 10GHz tot 18GHz werkt ontwikkeld. Deze antenne is bestemd om in tijd-domein UWB beeldweergave antenne stelsels te worden gebruikt. De analyse heeft laten zien dat de antenne niet alleen genoeg -10dB impedantie bandbreedte van 9.95 GHz tot 20 GHz heeft, maar ook een goede stralingskarakteristiek binnen de impedantie bandbreedte heeft. De antenne heeft een versterking van 5 tot 10 dBi. De voor/achter-verhouding is groter dan 10 dB, en de -3 dB bundelbreedte is ongeveer  $\pm 30^\circ$  in zowel de E- als de H-vlakken. De antenne heeft ongeveer 100 ps groepsvertraging en de impuls respons heeft een 1/e pulsbreedte van ongeveer 200 ps. De analyse van de vervorming van de uitgestraalde puls ten opzicht van de hoek, laat zien dat de puls heel gelijk blijft binnen de -3 dB bundelbreedte. Dit toont aan dat de antenne een kleine vervorming en korte na-rinkeltime heeft, die de antenne geschikt maakt voor tijd-domein toepassingen. Een analyse van het antenne koppeling gedrag laat zien dat deze koppeling tussen elementen klein is. Daarom wordt er wordt geen sterke verslechtering van prestaties van de antenne verwacht als deze in een 'sparse' MIMO antenne stelsel wordt gebruikt.
2. Onderzoek van LTCC technologie: De LTCC technologie was gekozen om millimetergolf antennes te fabriceren en met MMICs te integreren. De meerdere lagen van de LTCC technologie maakt het geschikt voor 'system-in-package' toepassing. Maar tegelijkertijd, LTCC technologie is in vergelijking een nieuwe technologie en is derhalve nog niet gestandaardiseerd. Ook bezit het LTCC materiaal meestal een hoge dielectrische constant die het ontwerpen van UWB antenne moeilijk maakt. Als resultaat hiervan hebben we onderzoek gedaan naar de eigenschappen van het LTCC materiaal en naar de consequenties daarvan op het ontwerp van een UWB antenne. We hebben ook de fabricage beperkingen van de LTCC technologie onderzocht en hebben oplossingen voorgesteld om deze beperkingen te overwinnen. De LTCC variatie tijdens fabricage is ook door

ons bestudeerd. Dit geeft aan dat de variatie van de hoogte van het substraat een significante invloed heeft op de resonantie frequentie van de antenne, terwijl de variatie van de relatieve permittiviteit een zeer kleine invloed heeft op de reflectie coëfficiënt van de antenne.

3. K-band LTCC antenne: Een nieuwe K-band antenne was ontwikkeld die gebruik maakt van de LTCC technologie. Deze antenne is een differentieel-gevoede, met meervoudig getrapte afscherming, elliptisch dipolaire UWB antenne. Deze antenne heeft een nieuwe differentiele voeding die directe integratie met differentiele MMICs mogelijk maakt. De meervoudige getrapte afscherming vermindert de straling naar achter en verbetert de straling naar voren, dit allemaal terwijl de antenne impedantie bandbreedte groot wordt gehouden. De antenne heeft een -7.5 dB impedantie bandbreedte van 24 GHz tot 30 GHz, met een versterking van ongeveer 5 dBi tot 7 dBi. Met dank aan dit schild is het antenne stralingsdiagram stabiel binnen de operationele bandbreedte, en de 3 dB bundelbreedte in het E-vlak ligt op ongeveer 60° en 30° voor het H-vlak.
4. M-band LTCC antenne: Een nieuw differentieel-gevoede UWB antenne voor de M-band was ontwikkeld met gebruik van LTCC technologie. De antenne is gebaseerd op een ASP type antenne met nieuwe differentiele voeding. Met deze voeding is de antenne in staat een -10 dB impedantie bandbreedte van 50 GHz tot 78 GHz te bereiken. De hoge dielektrische constant van het LTCC materiaal veroorzaakt ernstige oppervlakte golven die het antenne stralingsdiagram aantasten. Alhoewel het mogelijk is dat de getrapte afscherming, zoals voorgesteld voor de K-band antenne, dit probleem kan oplossen, is het veels te complex om dit te realiseren voor M-band. Een nieuwe versimpelde rechthoekige afscherming is voorgesteld om dit op te lossen. Deze afscherming heeft geen complexe structuur maar kan desondanks de oppervlakte golf met succes beperken, en daardoor de antenne stralingsdiagram verbeteren. De versterking van de M-band antenne is van 3.4 dBi tot 8 dBi van 50 GHz tot 62 GHz, en de -10 dB bundelbreedte is tenminst van -45° tot 45° voor zowel E- als H-vlak.
5. Onderzoek naar element koppeling voor imaging-array: De invloed van element koppeling op de kwaliteit van de beelden was onderzocht. De antenne overspraak heeft geen ernstige invloed op de beeldkwaliteit, omdat het door 'time-gating' technieken verholpen kan worden. De verstrooiing koppeling, die niet zoveel aandacht van de antenne gemeenschap krijgt, heeft juist het meeste invloed op de beeldkwaliteit. Als de koppeling sterker is op een bepaalde frequentie, dan ziet men een verhoogde gevoeligheid op die frequentie. Deze verhoging zal lang na-rinkelen veroorzaken en kleine objecten achter grote objecten maskeren. Een ander grote invloed van verstrooiing koppeling op de beelden is dat de zijlobben groter zullen worden, en derhalve meer ongewenste radar reflecties veroorzaken.
6. 2-D 'sparse' MIMO antenne stelsel topologie: Uitgevoerd onderzoek laat zien dat het MIMO antenne stelsel concept 2-D 'sparse real-aperture' kan bereiken om een hoge resolutie horizontale scan en lage zijlob beeldweergave systeem te maken. Het ontwerp van de 2-D MIMO reeks was gesplitst in twee stappen. De eerste stap is het ontwerpen van een 1-D



MIMO antenne stelsel met de gewenste PSF eigenschappen. De volgende stap is deze 1-D MIMO reeks naar 2-D reeks uit te breiden door middel van de ontworpen 1-D reeks op twee orthogonale assen uit te zetten, en dan de gedraaide 1-D antenne stelsel te gebruiken om het 2-D antenne stelsel te verkrijgen. Twee 2-D antenne stelsels die gebaseerd waren op eenzelfde 1-D antenne stelsel waren met deze aanpak ontwikkeld en gefabriceerd. De gemeten resultaten hebben laten zien dat beide antenne stelsels in staat zijn om kleine objecten af te beelden. Ze hebben ook laten zien dat het zijlob niveau een van de belangrijkste specificaties van het antenne stelsel is, die door de ontwerper gespecificeerd hoort te worden om de juiste prestatie van het gehele beeldweergave systeem te bereiken. De 3-D beeldweergave resultaten hebben de hoge potentie van het microgolf 2-D UWB 'sparse' MIMO antenne stelsel in real time kort-bereik hoog-resolutie beeldweergave applicaties ook bewezen.



# Author's publications

## Journals

- [1] T. Savelyev, X. Zhuge, **B. Yang**, P. Aubry, A. Yarovoy, L. Ligthart, and B. Levitas, "Comparison of 10-18 GHz SAR MIMO-Based Short-Range Imaging Radars," *International Journal of Microwave and Wireless Technologies*, Available on CJO 08 Jun. 2010, DOI: 10.1017/S1759078710000383
- [2] **B. Yang**, A. G. Yarovoy, A. Shenario Ezil Valavan, K. Buisman, and O. Shoykhetbrod, "A novel LTCC differentially Fed UWB antenna for the 60 GHz band", *International Journal of Microwave and Wireless Technologies*, Available on CJO 08 Mar. 2011, DOI: 10.1017/S1759078711000237

## Conferences

- [3] A. Chen, Li-Chun Wang, D. S.-L. Wei, K. Naik, Y. T. Su, Y. X. Zheng, **B. Yang**, "NICE - a decentralized medium access control using neighborhood information classification and estimation for multimedia applications in ad hoc 802.11 wireless," *Proc., IEEE International Conference on Communications (ICC '03)*, Volume: 1, pp. 208-212, May 2003.
- [4] R. Maaskant, **B. Yang**, "A Combined Electromagnetic and Microwave Antenna System Simulator for Radio Astronomy," *Proc. EuCAP 2006*, Nov. 2006.
- [5] **B. Yang**, M. Hajian, L.P. Ligthart, "Capacity Enhancement for Indoor Up-Link MC-CDMA in Dense-Populated Area," *Proc. of VTC 2007 Spring*, pp. 3046-3050, April 2007.
- [6] **B. Yang**, A.G. Yarovoy, L.P. Ligthart, "Performance Analysis of UWB Antenna Array for Short-range Imaging", *Proc. of 2<sup>nd</sup> EuCAP 2007*, Nov. 2007.
- [7] A.G. Yarovoy, W. Qiu, **B. Yang**, P.J. Aubry, "Reconstruction of the Field Radiation by GPR Antenna into Ground", *Proc. of 2<sup>nd</sup> EuCAP 2007*, Nov. 2007.
- [8] A.S.E. Valavan, **B. Yang**, A.G. Yarovoy, L.P. Ligthart, "An M-band Differentially Fed, Aperture Coupled Stacked Patch Antenna in LTCC", *Proc. of EuRAD 2008*, pp. 200-203, 2008.
- [9] **B. Yang**, X. Zhuge, A.G. Yarovoy, L.P. Ligthart, "UWB MIMO Antenna Array Topology Design Using PSO for Through Dress Near-field Imaging", *Proc. of EuRAD 2008*, pp. 463-466, 2008.

- [10] **B. Yang**, A. Vorobyov, A.G. Yarovoy, L.P. Ligthart, S. Rentsch, J. Muller, "A Novel Shielded UWB Antenna in LTCC for Radar and Communications Applications", *Proc. of ICUWB 2008*, pp. 117-120, 2008.
- [11] **B. Yang**, A.G. Yarovoy, P. Aubry, X. Zhuge, "Experimental Verification of 2D UWB MIMO Antenna Array for Near-field Imaging Radar", *Proc. of EuMC 2009*, pp. 97-100, 2009.
- [12] **B. Yang**, A.G. Yarovoy, L.P. Ligthart, "UWB Stacked Patch Antenna Design for Near-field Imaging Radar Antenna Array", *Proc. of 3<sup>rd</sup> EuCAP 2009*, pp. 817-821, 2009.
- [13] Shenario Ezhil Valavan A, **B. Yang**, A.G. Yarovoy, L.P. Ligthart, "Stacked Patch UWB Antenna in LTCC Technology", *Proc. of 3<sup>rd</sup> EuCAP 2009*, pp. 1467-1468, 2009.
- [14] **B. Yang**, A. G. Yarovoy, and L. P. Ligthart, "2D Antenna Array for Near-Field Imaging Applications", *URSI-Benelux 2009*, 2009.
- [15] N. Haider, **B. Yang**, D. P. Tran, A. G. Yarovoy, "UWB Antenna element for a full-polarimetric antenna array", *Proc. of 4<sup>th</sup> EuCAP 2010*, 2010.
- [16] **B. Yang**, A. G. Yarovoy, O. Shoykhetbrod, and D. Nuessler, "Experimental verification of Ka band LTCC antenna", *Proc. of EuMC*, pp. 779-782, Nov. 2010.
- [17] **B. Yang**, A. G. Yarovoy, and S. E. Amaldoss, "Novel LTCC UWB 60 GHz Semi-shielded Aperture Stacked Patch Antenna with Differential Feeding", *Proc. of 5<sup>th</sup> EuCAP 2011*, pp.1882-1885, 2011.

# Acknowledgement

A research cannot be done without other people's support. Therefore, I would like to give my sincere gratitude to those who have given their support through the journey of my Ph.D.

First of all, I would like to thank my promoter and daily supervisor Prof. Alexander Yarovoy for accepting me as his Ph.D student. I am very grateful for his supervision, advice, and proofreading of my papers, presentation slides, and several versions of thesis drafts. His truly scientist intuition, expertise, and knowledge gave me great ideas and inspirations. These inspiring discussions gave me great momentum to push my Ph.D research to the last point. He is also a warm and kind friend. Alex, it is a great pleasure being your student. Without your constant support, it is impossible for me to finish my thesis. I am indebted to you more than you know.

I would like to thank Prof. Ligthart who gave me the chance to become a Ph.D student in IRCTR. I would like to give my gratitude to Dr. Mostafa Hajian, who was my Master thesis mentor. You introduced me into IRCTR as a system administrator. Without this extraordinary chance, I would not have had the opportunity to get deeper touch with all the interesting research activities in IRCTR, which opens a wider gate of academic world to me.

It was my utmost great pleasure to work in IRCTR with many smart and friendly colleagues. I thank Pascal Aubry, who is always happy to help me doing all sorts of measurements. I thank Paul Hakkart and Johan Zijderveld for giving me technical supports. I thank Dr. Timofey Savelyev for helping me throughout the project and sharing with me his invaluable knowledge. I thank Shenario Ezhil Valavan. A, who was my Master student and helped me to develop the M-band antenna prototype. I thank Alexander Voroboyv who provided the shielded antenna idea to me for my K-band antenna development. Special thanks to Xiaodong Zhuge, whom I shared room with for the past years, for his companion as a peer researcher and a friend. We spent a lot of time bouncing ideas and support each other's research.

I appreciate the assistance of the secretaries of IRCTR, Mia van der Voort, Laura Bauman, Dominique Meijer, Wendy Murtinu-van Schagen, Majon Verkaik,-vonk, and Stefanie van Gentevoort, and financial managers: Ad de Ridder and Jeffery Ransun. They have supported me in many aspects ranging from finding a house, translating Dutch letters, arranging traveling, claiming expenses, and helping me arrange my Ph.D defense. Their professional help eased a lot of administrative things for me.

Many thanks to Alexander Schulz who helped me manufactured the K-band and M-band LTCC antenna. He helped me review the design layout of these antennas and gave me many valuable suggestions to make the antenna layout correct.

Special thanks to Alexey Shoykhetbrod and Dirk Nüssler from FHR for helping me develop antenna measurement solutions for the K-band and M-band antenna. Alexey also spent quite some time helping me to measure the K-band and M-band antennas. In addition, I would like to thank Koen Buisman from DIMES, Delft University of Technology, who helped me measured several mm-wave antennas, and helped me translate my summary!

I would like to thank all my Taiwanese friends in Delft, who enriched my leisure time. Special thanks to Jason Chiang and Nana Lin, who gave me many valuable advices regarding the daily life in Delft. Many thanks to Kai-Fan Chang who helped me to find my current job!

My deepest thanks go to my dearest parents and sister. Without their unconditional support, I would not be able to come to the Netherlands. Moreover, I would like to thank my beloved wife, Pei-Hui, and my lovely little daughter, Rozen. You are my driving force. I am very grateful to have you joined on my journey and that you are there to enrich my life!

As a famous Chinese writer said, because there are too many people to thank, so, let's thank god!

## About the Author

Yu-Che (also known as Bill) Yang was born in Taipei, Taiwan on the 2<sup>nd</sup> of April 1980. He received his B.Sc. degree in Communication Engineering from Chiao Tung University, Taiwan, in 2002, and M.Sc. degree in Delft University of Technology, the Netherlands in 2006.

In September 2006, he started his work towards Ph.D. degree at Delft University of Technology in the International Research Center for Telecommunications and Radar (IRCTR). His research interests include UWB antenna array design and signal processing for near-field imaging.

Since 1<sup>st</sup> January 2011, he started his new career as a secure evaluator at Brightsight, Delft.